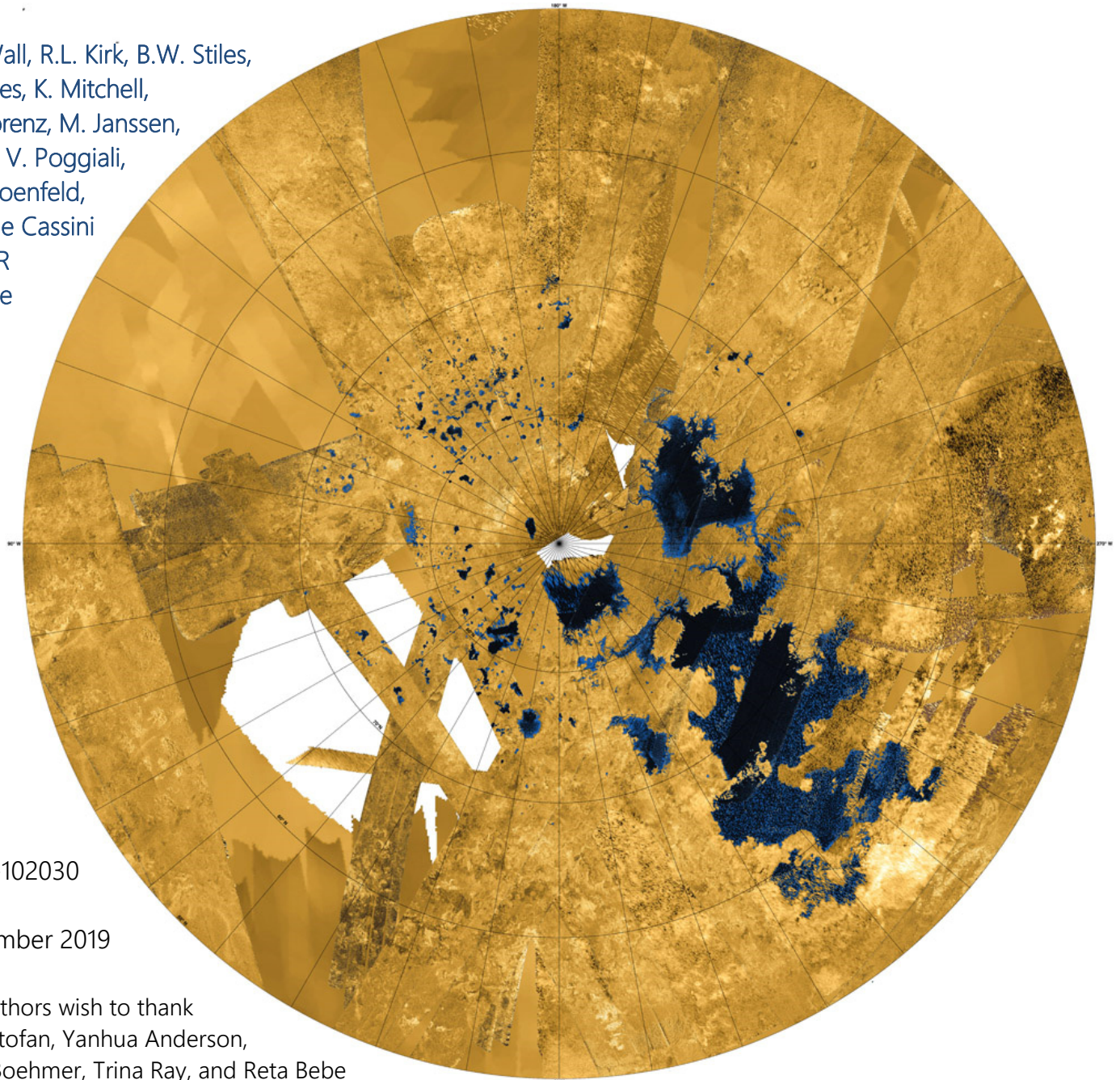




# Cassini RADAR Users Guide

## Second Edition

S.D. Wall, R.L. Kirk, B.W. Stiles,  
A. Hayes, K. Mitchell,  
R.D. Lorenz, M. Janssen,  
B. Bills, V. Poggiali,  
A. Schoenfeld,  
and the Cassini  
RADAR  
Science  
Team



JPL D-102030

September 2019

The authors wish to thank Ellen Stofan, Yanhua Anderson, Rudy Boehmer, Trina Ray, and Reta Bebe for their assistance in producing this document, and especially Charles Elachi, whose guidance and support have led us in this amazingly successful experiment. We also thank Claire Marie-Peterson for helpful comments and superb editing.

This publication was prepared for the Jet Propulsion Laboratory, California Institute of Technology, under a contract with the National Aeronautics and Space Administration.

Reference herein to any specific commercial product, process, or service by trade name, trademark, manufacturer, or otherwise, does not constitute or imply its endorsement by the United States Government or the Jet Propulsion Laboratory, California Institute of Technology.

This guide is dedicated to the memory of Bill Johnson and Steve Ostro.  
They were fundamental to the success of the Cassini RADAR,  
and we miss them not only as colleagues, but as friends.

## Contents

Preface to the Second Edition .....	1
<b>1 Introduction .....</b>	<b>2</b>
<b>2 The Cassini Spacecraft and Mission .....</b>	<b>4</b>
2.1 The Cassini Orbiter .....	5
2.2 Mission Operations.....	8
2.3 Mission Phases.....	9
<b>3 The Cassini RADAR Experiment.....</b>	<b>11</b>
3.1 Cassini RADAR Overview .....	11
3.2 Experiment Description.....	13
3.2.1 <i>RADAR Modes</i> .....	13
3.2.2 <i>Secondary RADAR Data Types</i> .....	14
3.3 Nominal RADAR Observation of Titan.....	15
3.4 RADAR Operation .....	16
3.5 Titan Coverage.....	16
3.6 Other RADAR Coverage.....	25
3.6.1 <i>Rings</i> .....	25
3.6.2 <i>Icy Satellites</i> .....	25
3.6.3 <i>Saturn</i> .....	27
3.6.4 <i>Venus, Earth, and Jupiter</i> .....	27
<b>4 RADAR Data Product Overview.....</b>	<b>29</b>
4.1 Burst-Ordered Data Products (BODPs).....	30
4.1.1 <i>Product Overview</i> .....	31
4.1.2 <i>Short-Burst Data Record (SBDR)</i> .....	31
4.1.3 <i>Long-Burst Data Record (LBDR)</i> .....	34
4.1.4 <i>Altimeter-Burst Data Record (ABDR)</i> .....	34
4.1.5 <i>Data Validation and Archiving</i> .....	35
4.2 Basic Image Data Records (BIDRs) .....	35
4.2.1 <i>Data Format and Description</i> .....	36
4.2.2 <i>Non-Titan BIDRs</i> .....	37
4.2.3 <i>Data Validation and Archiving</i> .....	39
4.3 SARTopo Products.....	39
4.4 Digital Map Products (DMPs).....	42
4.4.1 <i>Pass Radiometry Data Records (PRDRs)</i> .....	43
4.4.2 <i>Pass Scatterometry Data Records (PSDRs)</i> .....	45
4.4.3 <i>Global Radiometry Data Records (GRDRs)</i> .....	45
4.4.4 <i>Global Scatterometry Data Records (GSDRs)</i> .....	47
4.4.5 <i>Global Topography Data Records (GTDRs)</i> .....	48
4.4.6 <i>Mosaicked Image Data Records (MIDRs)</i> .....	48
4.4.7 <i>Repeat Image Data Records (RIDRs)</i> .....	50

4.4.8	<i>Digital Topographic Models (DTMs)</i> .....	51
4.4.9	<i>PDS Label Format for DMPs</i> .....	52
4.4.10	<i>Validation and Archiving of DMPs</i> .....	52
4.5	<b>Versions of Data Products and Summary of Errata</b> .....	54
4.5.1	<i>Definition of Volume Versions</i> .....	54
4.5.2	<i>Errata Overview</i> .....	55
<b>5</b>	<b>Calibration</b> .....	<b>61</b>
<b>6</b>	<b>Titan SAR Swath Summary</b> .....	<b>66</b>
6.1	Swath Descriptions .....	66
6.2	Ontario Lacus: A Case Study .....	73
6.3	Huygens Landing Site: A Case Study.....	74
<b>7</b>	<b>Data Outages, Anomalies, and Related Data Issues</b> .....	<b>76</b>
7.1	Major Data Outages and Corruption .....	76
7.1.1	<i>Dione/Mimas 00b (Total Loss)</i> .....	76
7.1.2	<i>The T7 Anomaly</i> .....	77
7.1.3	<i>The T60 Anomaly</i> .....	78
7.1.4	<i>Iapetus Pass 49 Anomaly</i> .....	78
7.1.5	<i>The T64 Anomaly</i> .....	78
7.1.6	<i>The T69 Anomaly</i> .....	79
7.1.7	<i>The T71 Anomaly</i> .....	79
7.1.8	<i>The T77 Anomaly</i> .....	79
7.1.9	<i>The T83 Anomaly</i> .....	79
7.1.10	<i>The T86 Anomaly</i> .....	79
7.1.11	<i>The T92 Anomaly</i> .....	79
7.1.12	<i>The T104 IEB Error</i> .....	79
7.1.13	<i>Rev 277 RADAR Rings Anomaly</i> .....	79
7.1.14	<i>Other Experiment Anomalies</i> .....	80
7.2	Anomaly Statistics and Review .....	80
7.3	Complexities to Consider When Interpreting SAR Images.....	81
<b>8</b>	<b>Studies in Quantitative Use of Cassini RADAR Data</b> .....	<b>83</b>
8.1	Study 1: Titan Pole and Spin-Rate Estimation.....	84
8.1.1	<i>SAR Spin-Model Estimation</i> .....	84
8.1.2	<i>Titan Spin-Model Improvements</i> .....	88
8.2	Study 2: SAR Stereo.....	96

9	Obtaining Cassini RADAR Data Products.....	100
10	Appendix 1: References and Selected Bibliography.....	103
11	Appendix 2: Acronyms .....	128
12	Appendix 3: Index to All Titan Passes.....	132
13	Appendix 4: SAR Swath Details .....	136
14	Appendix 5: Cassini RADAR Uplink/Downlink Spreadsheet through T77.....	140
15	Appendix 6: Example BIDR PDS Label, Primary Data Set, 32-Bit Data .....	154
16	Appendix 7: SAR Coverage of Titan by Feature Names .....	157
17	Appendix 8: File Names and Product IDs for Digital Map Products.....	161

## Preface to the Second Edition

The Cassini-Huygens Mission certainly belongs high on the list of NASA's most successful missions. Its spacecraft has performed exceptionally well, as have its instruments and its operations teams. The science data returned will provide material for decades of analysis, and its gallery of images and other data representations will forever stand as evidence that the Saturnian system is one of the most beautiful sites in the sky.

This volume extends and revises the first (2011) edition of the Cassini RADAR Users Guide to include all data acquired by the RADAR instrument through the end of the Cassini Mission in 2017, encompassing the Primary, Equinox, and Solstice mission phases. Where possible we have updated metadata tables to include all Titan passes and, where appropriate, moved them to appendices.

## 1 Introduction

The surface of Saturn's moon Titan, shrouded in haze, has been revealed by data returned from the Cassini Orbiter, as well as from descent and surface images from the Huygens probe. The revealed surface is far more complex than hypothesized prior to Cassini, with very few impact craters, but with abundant channels, dunes, and polar lakes (Figure 1-1). The Cassini Titan Radar Mapper (RADAR) data set,<sup>1</sup> covering approximately 46% of Titan using synthetic aperture radar (SAR) at its highest resolution<sup>2</sup>, have appealed to a wide range of researchers, from planetary scientists who study how surface processes vary from body to body across the solar system, to more terrestrially-oriented scientists who now have the opportunity to study the only other body in the solar system besides Earth with an active liquid cycle, and active lacustrine and riverine processes. Although its primary focus has been Titan, RADAR has also observed Saturn's icy satellites, rings, and Saturn itself.

In order to exploit fully the scientific information within the Cassini RADAR data, the user must understand how the data were collected, including the peculiarities of the instrument and events that might have occurred during data collection or processing. As with any NASA mission, these descriptions exist across a range of documents and locations. In Sections [2](#) and [3](#), this guide draws together the most pertinent information for future users of the RADAR data, facilitating the data access and manipulation that necessarily precede interpretation. A similar guide was put together for the Magellan Mission to Venus ([Wall et al. 1995](#)) by one of the authors of this report, and it has proven to be a useful document for users of that data set. We aim similarly to aid future users of RADAR data.

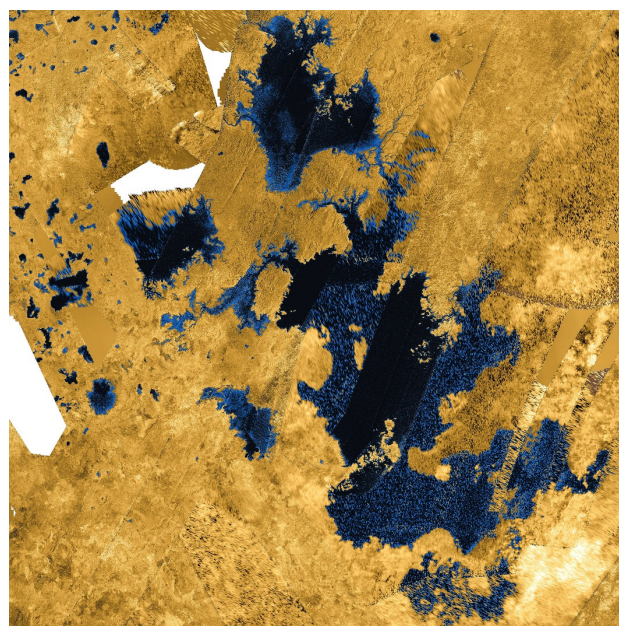


Figure 1-1. Mosaic of RADAR images of Titan's north pole, false-colored to emphasize hydrocarbon lakes and seas in blue.

Most scientific analyses of RADAR data performed to date have used SAR imagery, altimeter surface heights, scatterometer backscatter, or radiometer temperatures. These are the primary scientific measurements in the data set. The SAR imagery is contained in the Basic Image Data Record (BIDR) files. The other values are in the Burst-Ordered Data Product (BODP) files. These and other data types, including high-altitude SAR imaging (HiSAR), SAR topographical (SARTopo), and SAR-

<sup>1</sup> In this guide we distinguish between radar, a microwave sensing technique, and RADAR, an instrument aboard the Cassini spacecraft.

<sup>2</sup> In this guide we distinguish between SAR and the lower-resolution HiSAR as distinct operating modes and data types, although both employ the synthetic-aperture technique.

derived stereo, are described in [Section 4](#) of this guide. All of these data sets are archived by NASA's Planetary Data System (PDS).

RADAR operates in four modes: SAR (imaging), altimetry, scatterometry, and radiometry. While most users will likely be familiar with the imaging data, the other three RADAR data sets greatly enhance interpretation of the SAR data where they are coincident. Scatterometer and radiometer data, which cover the entire surface at widely varying resolutions, provide a background for understanding the other data as well as providing specific information about surface properties. In [Section 6.2](#) we provide an illustration of their combined use.

This guide is a compilation of previous Cassini project reports, some of which are internal to the project and some of which have been published and/or presented in popular, scientific, or engineering journals and conferences. We have tried to attribute this work accurately; any errors or omissions are the responsibility of the authors.

The true credit for the information in this report, however, goes to the many scientists and engineers from NASA, the Italian Space Agency (ASI), and numerous other organizations who have made the Cassini Mission a resounding success, and who have allowed it to continue through its Grand Finale in 2017.

## 2 The Cassini Spacecraft and Mission

The Cassini-Huygens Mission to the Saturn system was launched in October of 1997, arriving at Saturn on July 1, 2004, with the Huygens probe landing on Titan on January 14, 2005 (Figure 2-1). In this section, we briefly describe the mission and how it operates, in order to provide a framework for the more detailed descriptions of the RADAR experiment in [Section 3](#).

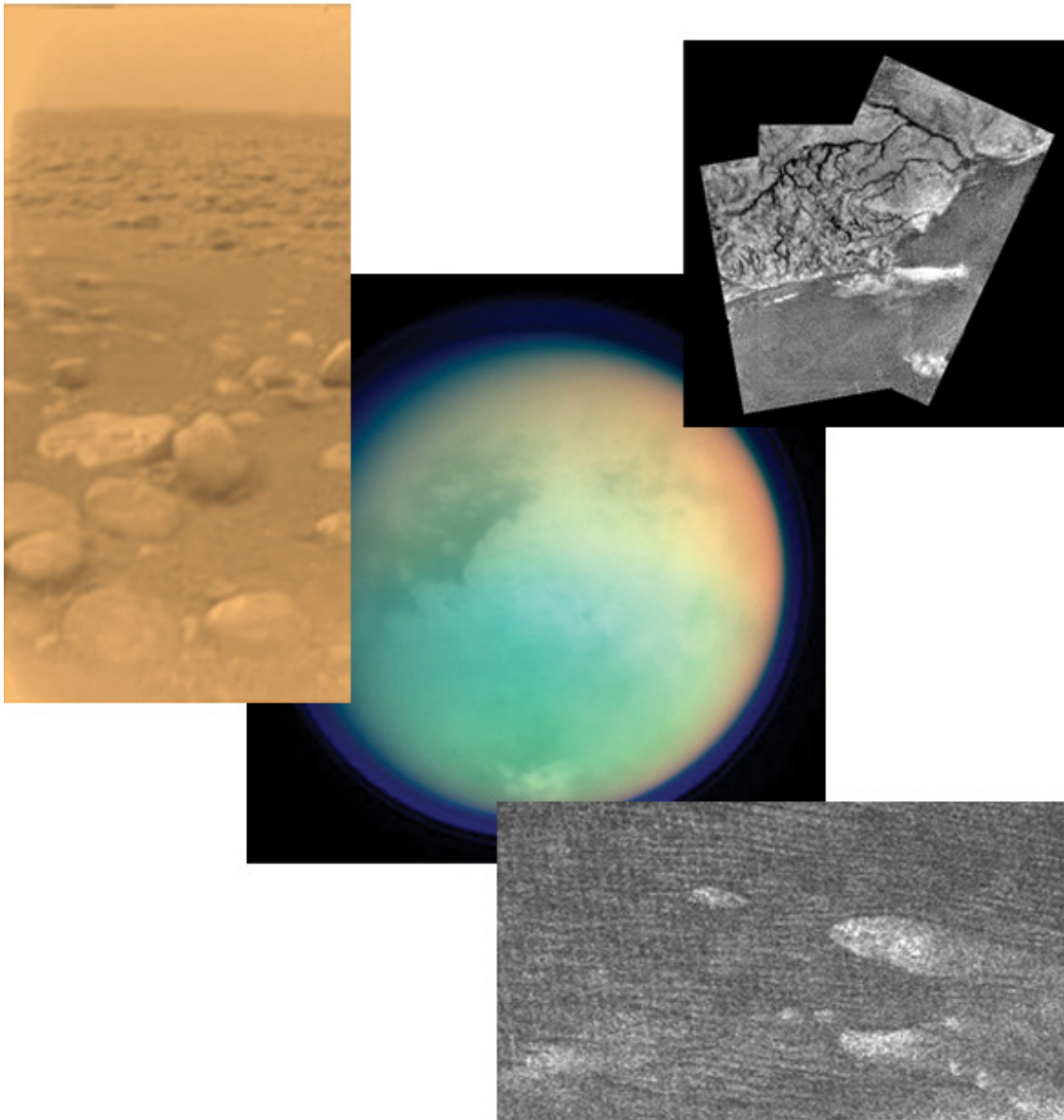


Figure 2-1. Montage of Cassini's Titan results. Counterclockwise from upper left: PIA07232, the surface of Titan from Huygens; PIA06139, Imaging Science Subsystem (ISS) false-color image of Titan; PIA03567, Cassini RADAR image of dunes; and PIA07236, surface channels in Huygens descent image.

## 2.1 The Cassini Orbiter

The Cassini Orbiter had twelve science instruments to study the Saturn system, in addition to the Huygens probe. It stored science data and relayed data back to Earth. The design of the Orbiter was driven by a number of factors, including the great distances from Saturn to the Sun and Earth, the length of the mission, the complexity and volume of the science observations, and the spacecraft's path to Saturn.

The Orbiter consisted of a four-part stack: the high-gain antenna (HGA), provided by ASI; the upper and lower equipment modules; and the propulsion module (Figure 2-2). Attached to this stack were the remote-sensing and fields and particles instruments. The magnetometer was mounted on an 11-m boom. The height of the spacecraft was 6.8 m; it was the largest planetary spacecraft ever launched.

Power was provided by three radioisotope thermoelectric generators (RTGs), which used heat from the decay of plutonium to produce direct-current electricity. The Cassini RTGs were similar to those used on the Galileo and Ulysses missions, and were mounted on the lower equipment module. Cassini's distance from Earth, between 8.2 and 10.2 astronomical units (AU), also made communication with the spacecraft a challenge. Signals between Earth and the spacecraft had a travel time of 68–84 minutes, meaning that the spacecraft team could not give the spacecraft “real-time” commands. This necessitated robust spacecraft-system fault-protection to ensure that, in the event of onboard problems, spacecraft health could be maintained long enough to permit engineers back on Earth to analyze and correct the problems.

Communications on the spacecraft were handled by the Radio Frequency Subsystem (RFS) and the Antenna Subsystem. The Antenna Subsystem was made up of the 4-m-diameter HGA and two low-gain antennas (LGA1 and LGA2). The HGA also housed redundant X-band receivers and transmitters; feeds for a Ka-band receiver, a Ka-band transmitter, and an S-band transmitter, all for radio science; and feeds for the RADAR instrument's Ku-band transmitters and receivers. The RFS produced an X-band carrier (frequency 8.4 GHz), modulated it with data received from the Command and Data Subsystem (CDS), amplified the carrier, and delivered the signal stream to the Antenna Subsystem for transmission to Earth. The RFS received X-band (frequency 7.2 GHz) ground commands and data signals from the Antenna Subsystem, demodulated them, and sent the telemetry to the CDS for storage and/or execution. For the first two and a half years, the spacecraft used the HGA for sun-shading and communicated via the LGAs. When it was no longer needed for shading, the HGA became (and remained) the primary communications antenna. Commands and data from Earth were received at 1000 bps by the HGA, and transmitted to Earth at rates from 14,220 to 165,900 bps. During operations, data were recorded on the solid-state recorders for about 15 hours each day, while the HGA was not pointed at Earth. The data from the solid-state recorders were then played back for nine hours (generally during Goldstone, California, tracking station coverage), while data collection from the fields and particles investigations continued. About one gigabit of data could be returned each day via a 34-m Deep Space Network (DSN) antenna; approximately 4 gigabits of data could be returned in 9 hours via a 70-m ground antenna.



Figure 2-2. The Cassini spacecraft, including the Huygens (Titan) probe.

The CDS on the spacecraft conducted command, control, fault protection, and data handling. The CDS executed sequences of stored commands for normal preplanned flight activities and processed, issued real-time commands sent from Earth, controlled and selected data modes, and collected and formatted science and engineering data for transmission to Earth. Bus interface units (BIUs) in each instrument controlled data flow and allowable power states for the instrument, handled commands and data from the CDS to the instrument, and conveyed data from the instrument to the solid-state recorders. The CDS could handle combined data rates in excess of 430,000 bps from the instruments while still carrying out its command and control functions.

Cassini used solid-state recorders to store data. Two redundant solid-state recorders had a capacity guaranteed to be at least 1.8 gigabits 15 years after launch. The recorders could record and read out data simultaneously, record the same data simultaneously in two different locations on the same recorder, and record simultaneously on both recorders. So that Cassini was not restricted to instantaneous data collection rates, the recorders buffered essentially all data that were collected, permitting data transmission to Earth to occur at the highest available rates. They could be partitioned by command from the CDS, store backup versions of memory loads for almost all computers on the spacecraft, and store a running record of recent engineering activities to assist in fault analysis.

The Attitude and Articulation Control Subsystem (AACS) was primarily responsible for maintaining the orientation of Cassini in space. The AACS consisted of redundant Sun sensors mounted to the HGA, redundant stellar reference units on the remote-sensing platform, three mutually perpendicular reaction wheels on the lower equipment module, and a fourth reaction wheel on the upper equipment module, as a backup that could be rotated to be parallel to any one of the three other reaction wheels. Redundant inertial reference units were located on the upper equipment module, along with an accelerometer, to measure changes in the spacecraft's velocity. The AACS pointed the antenna (either the HGA or LGAs) toward Earth when required, pointed the HGA at appropriate RADAR or radio science targets, pointed the instruments on the remote-sensing pallet toward targets that were themselves in motion relative to the spacecraft, turned the spacecraft at a constant rate around the HGA axis for fields and particles measurements during transmission of data to Earth or receipt of commands from Earth, pointed one of the two redundant main propulsion engines in the desired direction during main-engine burns, performed trajectory-correction maneuvers of smaller magnitude using the onboard thrusters, and provided sufficient data in the transmitted engineering data to support science-data interpretation and mission operations. The AACS used a pointing system known as inertial vector propagation that kept track of spacecraft orientation; the direction and distance of the Sun, Earth, Saturn, and other possible remote-sensing targets in the Saturn system; and the spacecraft-relative pointing directions of all the science instruments, pointing any instrument at its selected target.

The Propulsion Module Subsystem (PMS) was the largest and most massive subsystem on Cassini, consisting of a bipropellant element for trajectory and orbit changes and a hydrazine element for attitude control, small maneuvers, and reaction wheel desaturation or unloading. The RTGs were a part of the Power and Pyrotechnics Subsystem (PPS). The power conditioning equipment converted the RTG power output to provide a regulated 30-V direct-current power bus and provided

the capability to turn power on and off to the various spacecraft power users in response to commands from the CDS. The power conditioning equipment could detect overcurrent conditions. If overcurrent exceeded a predetermined level, the power to the affected user was switched off. The pyro switching unit also provided redundant power conditioning and energy storage, and controlled the firing of pyro devices on 32 commandable circuits, most of which opened or shut valves to control the pressures and flows within the propulsion module plumbing.

The Temperature Control Subsystem (TCS) kept spacecraft units within their specified temperature limits. It monitored temperatures using electrical temperature sensors on all critical parts of the spacecraft. The TCS controlled the temperature of the various units by several means: turning electrical heaters on or off, opening or shutting thermal louvers in one of the bays of the upper equipment module, using small radioisotope heater units to raise the temperatures of selected portions of the spacecraft that would otherwise cool to unacceptably low temperatures, and the use of thermal blankets and shields. Several instruments also had radiator plates to cool their detectors. Even at the distance of Saturn from the Sun, spacecraft orientations that point those radiator plates in the same half of the sky as the Sun could severely degrade the data collected by some of the science instruments. In at least one case, it was even necessary to avoid having Saturn illuminate the radiator plate(s) simultaneously.

New technology incorporated into Cassini-Huygens included the solid-state data recorder, the main onboard computer that incorporated new families of electronic chips, including very-high-speed integrated circuit (VHSIC) chips, and new application-specific integrated circuit (ASIC) parts. The Orbiter power system used an innovative solid-state power switch that eliminated the rapid fluctuations or “transients” that can occur with conventional power switches. In addition, Cassini used hemispherical resonator gyroscopes that had no moving parts.

## 2.2 Mission Operations

Several teams carried out mission planning for Cassini, including the Titan Orbiter Science Team (TOST), Satellites Orbiter Science Team (SOST), and the Rings, Saturn, and Cross-Disciplinary Target Working Teams (TWTs). These teams were responsible for integrating segments of Saturnian orbits (referred to as “revs”). RADAR observations had been included in the integration done by all these teams. The Orbiter Science Teams (OSTs) and TWTs delivered an integrated, conflict-free timeline based on science agreements. Project science working groups on surfaces, atmospheres, rings, and magnetospheres also helped resolve conflicts that could not be resolved in the OSTs and TWTs.

The science planning process consisted of two steps: first, production of a Science Operation Plan (SOP), and then development of a process to allow changes in the plan, called the “Aftermarket” process. The SOP was an integrated, conflict-free plan that included all science and engineering events. The Aftermarket process allowed limited reintegration and/or renegotiations of Tour segments in the Tour SOP (including trades among tour sequences) prior to final sequence command generation. The scope of the Aftermarket process was to allow changes due to (1) liens resulting from the SOP implementation, (2) changed instrument or spacecraft performance, (3) new science discoveries, and (4) rebalance of the science plan to include required

observations that were not integrated. The top priority was solving liens. The renegotiations and reintegration were made through the TWT and OST. Changes that involve multiple tour segments were treated in a joint meeting of all the TWTs and OSTs involved.

The SOP was then updated to reflect changes and trades made in the Aftermarket process. The SOP was updated using the actual DSN station allocations, new ephemeris files, and the latest version of the Mission Sequencing Software (MSS). The final process before uplink was called the Science and Sequence Update Process (SSUP).

Changes to pointing (e.g., to observe new targets identified due to ongoing discoveries) had to be made prior to the start of the SSUP for a particular sequence. The SSUP was started approximately 10 weeks before the sequence start date. Instrument commands, ephemeris changes, and changes due to revised DSN allocations were done during the SSUP.

### 2.3 Mission Phases

The Cassini-Huygens Mission consisted of three phases: the Prime Mission (2004–2008), the Equinox Mission (2008–2010, also known informally as the Extended Mission, XM), and the Solstice Mission (2010–2017, also known as XXM) (Figure 2-3). The Solstice Mission, which ended in September 2017, was named for the Saturnian summer solstice that occurred in May 2017. The northern summer solstice



Figure 2-3. Cassini mission phases.

marked the beginning of summer in the northern hemisphere and winter in the southern hemisphere. As Cassini arrived at Saturn just after the planet's northern winter solstice, the Solstice phase of the Mission permitted the first study of a complete seasonal period. The Grand Finale, a part of the Solstice phase, allowed closer observation of Saturn and its rings before the spacecraft was destroyed by plunging into Saturn on September 15, 2017.

### 3 The Cassini RADAR Experiment

#### 3.1 Cassini RADAR Overview

The Cassini RADAR instrument transmitted and received Ku-band microwave radiation. It operated in both passive (radiometer) and active modes.

In active mode, the RADAR measured the energy returned by the target surface from the transmitted signal. Transmitted energy was linearly polarized, with the electric field vector parallel to the spacecraft X-axis, which was in (or opposite to) the direction of motion during the flyby. Received energy was similarly polarized. Therefore the polarization characteristic in the SAR images is “like” and close to what is generally called “HH” for horizontal transmitting, horizontal receiving (see, e.g., [Elachi and VanZyl 2006](#)). Strictly speaking, it was exactly HH only at closest approach, where the spacecraft X-axis was truly along/against the velocity vector. Moving away from closest approach, pointing deviated from precise side-looking, so the polarization became a mixture of HH and VV (for vertical transmitting, vertical receiving), although the deviation from HH is small, in the -10-min to +10-min time range around closest approach. Figure 3-1 shows examples of the incidence and polarization angle variation taken from T83 and T92 (note that T83 targets SAR imaging only after closest approach). In the outer parts of the targeted SAR swath, a technique called “pushbroom” ([Stiles et al. 2006](#)) was used to extend the swath, and thus the polarization departs rapidly from 0 degrees and the polarization also becomes a mixture of VV and HH. Ride-along SAR ([Section 3.3](#)) and HiSAR ([Section 3.2.2.a](#)) images also have significant departures from HH polarization. Note also that in some observation modes the spacecraft was rotated about the Z axis to accommodate other instruments’ pointing needs. Users should refer to the polarization angle reported in the Short-Burst Data Record (SBDR) (see [Section 4.1.2](#)).

Ground processing of SAR data separated the received energy by round-trip time and Doppler shift. The return energy was used to determine the normalized radar cross

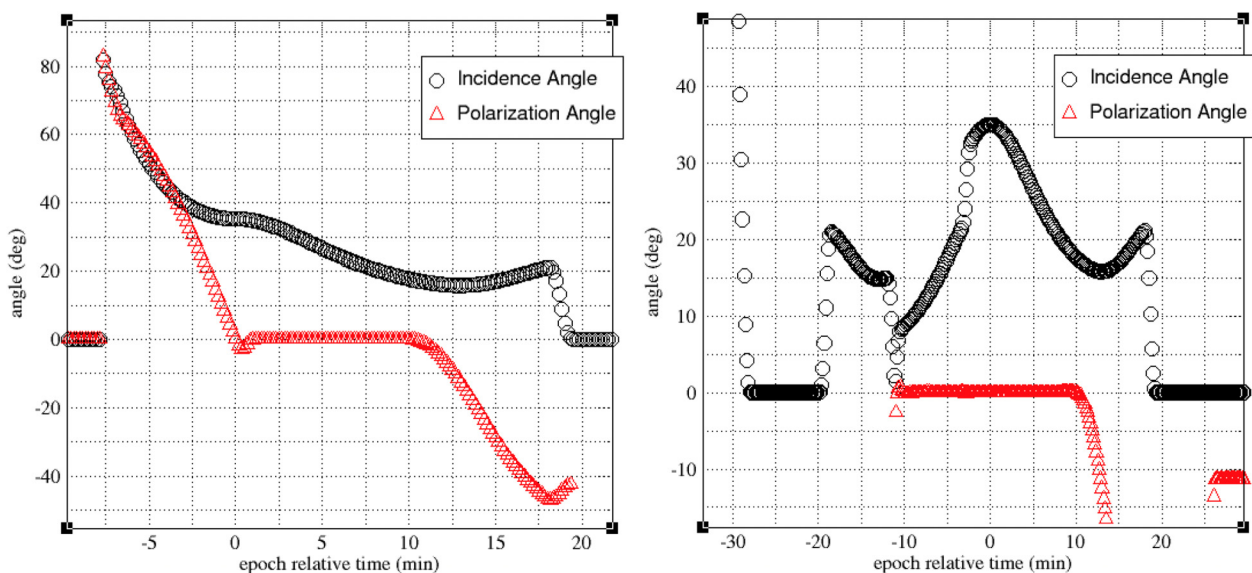


Figure 3-1. Examples of the incidence and polarization angle variation taken from T83 (left) and T92 (right). Note that T83 targets SAR imaging only after closest approach.

section (NRCS, often written as “ $\sigma_0$ ” or “ $\sigma^0$ ”) of the surface. NRCS is the ratio of the energy received to that which one would expect from a uniform scatterer ([Ulaby et al. 1982](#)). This quantity is related to the roughness at the scale of the wavelength of the transmitted signal (2.2 cm, Ku-band; see [Elachi et al. 2004](#)) and the dielectric constant of the surface. It is also affected by the angle at which the radar beam impinges the surface and thus is modulated by the larger-scale shape of the surface. Such effects can depend upon both the incidence and azimuth of the observation, yielding variation in NRCSs that are correlated with topographical features in RADAR imagery (e.g., lakes, mountains, rivers, dunes, etc.). Because return energy can be binned by delay and Doppler shift, one can produce geolocated SAR imagery and/or estimates of surface height depending upon the viewing geometry. As shown in Table 3-1, different signal bandwidths could be used to optimize the measurement of (1) precise NRCS quantities in scatterometer mode, (2) surface heights in altimetry mode, and (3) geolocated high-resolution imagery in SAR mode. Depending upon the accuracy of spacecraft attitude information (among other error sources), obtaining SAR imagery and surface height information simultaneously was also possible in some cases.

Table 3-1. Instrument description.

RADAR MODES	CENTER FREQUENCY AND BANDWIDTH(S)
Imaging	13.78, GHz, with 0.425 MHz, 0.85 MHz bandwidth
Altimetry	13.78, GHz, with 4.25 MHz bandwidth
Scatterometry	13.78, GHz, with 0.10625 MHz bandwidth
Radiometry	13.78, GHz, with 125 MHz bandwidth
DURATION OPERATIONS	300 minutes +/- closest approach
PEAK OPERATING POWER	86 W
DATA RATES	1 kbps (radiometer only) 30 kbps (altimeter, scatterometer/radiometer) 365 kbps (SAR +/- radiometer) (usually limited to ~250 kbps)

In passive mode, the Cassini RADAR instrument measured the linearly polarized radiant power received through the antenna in a bandpass coincident with but much wider than the radar signal receiver (see Table 3-1). Passive measurements were acquired in all operational modes of the RADAR instrument. All radiant power observed in the Saturn system is thermal in origin. In the microwave region, the power radiated by a thermal blackbody emitter is very nearly proportional to its physical temperature, and it is common usage to describe this power, whatever the source, in terms of the temperature of a blackbody that emits the equivalent power. Hence passive microwave measurements were reported in kelvins. In particular, the power collected by the antenna is called the “antenna temperature.” For an ideal antenna with a pencil beam and no sidelobes, the antenna temperature is the same as the “brightness temperature,” or equivalent blackbody temperature, of the source observed in the beam of the antenna. In practice, and particularly for Cassini, the process of obtaining calibrated brightness temperatures from antenna temperature measurements is not straightforward, and caution must be exercised in the interpretation of all antenna temperature data reported from the Cassini RADAR radiometer. A summary of the calibration of the radiometer to obtain brightness temperatures is given in [Section 5](#).

Active- and passive-mode RADAR observations made during the Cassini Mission are archived in the PDS. In addition to archiving the determined geophysical parameters such as NRCS, antenna temperature, and surface height, the raw radar returns and ancillary information needed to process them are also archived.

## 3.2 Experiment Description

### 3.2.1 RADAR Modes

*3.2.1.a. SAR.* SAR was used primarily to characterize Titan's surface morphology. The images returned have brightness variations that in some ways resemble traditional camera images; but in the case of SAR, image brightness represents NRCS, which is a function of surface slope, dielectric properties, roughness, and the amount of volume scattering (e.g., [Ulaby et al. 1982](#)). Typical geomorphological investigations might include the identification and classification of landforms. SAR resolution varies from 350 m at closest approach distances of ~950 km to over 1 km at the maximum range for standard SAR imaging. Thus, SAR image strips typically have high resolution in the center and lower resolution at both ends. The HiSAR data have larger and widely varying resolution (see [Section 3.2.2.a](#)).

[Ford et al. \(1993\)](#) provide a guide to the interpretation of Magellan SAR data that also serves as a useful basis for understanding SAR in general and Cassini SAR data in particular. A more detailed explanation of SAR and microwave interaction with surfaces can be found in [Elachi \(1987\)](#) or [Ulaby et al. \(1982\)](#). Users should keep in mind that SAR images are inherently “grainy” due to a phenomenon called speckle, and they have varying noise and varying resolution along each strip. Radar images contain geometric distortions due to topography, which enable stereomapping, but can in severe (high-slope) cases, cause surfaces to appear to overlap themselves ([Ford et al. 1993](#); this is not generally a problem on Titan where slopes are low).

In places on Titan, multiple SAR images were obtained. But these multiple views of the surface took place with differing geometries, and therefore caution should be used in interpreting apparent surface differences. When two images from different geometries are compared, there will be not only geometric parallax but also illumination differences, so it can be extremely difficult to determine if there is any evidence for actual surface changes ([Hayes et al. 2011](#)).

*3.2.1.b. Altimetry.* There are two broad applications for the altimetry data. One is to use the aggregate of all datatakes to define a geoid for Titan and identify whether there is a frozen-in rotational or tidal bulge. The second application is to generate topographic profiles that characterize landforms (e.g., impact craters, mountains), an important constraint on geophysical models. With further analysis, the strength and form of the returned energy can also be used to derive surface properties, measure liquid depths, etc. (e.g., [Mastrogiuseppe et al. 2014](#)). Altimetry was obtained when the RADAR was pointed within a fraction of a beamwidth (0.35 deg) of nadir. The 4.25-MHz bandwidth resulted in a range resolution of approximately 30 m.

*3.2.1.c. Scatterometry.* Scatterometry data have near-global coverage. They can be used as a “basemap” for SAR, and as a broad characterization of global terrains. The data indicate the backscatter efficiency at various incidence angles at relatively low resolution (real aperture resolution depends on range to surface). As an independent

constraint on surface roughness, scatterometry data are an important complement to radiometry data in order to constrain surface composition.

*3.2.1.d. Radiometry.* Polarized brightness temperatures of the observed scene are obtained from the antenna temperature measurements (see [Section 5](#)). The microwave brightness temperature of a solid surface depends on many properties besides physical temperature; e.g., emission angle, polarization, dielectric constant, porosity, surface and subsurface roughness, etc. The interpretation of brightness temperature generally depends on available ancillary information such as visible and IR imaging and the RADAR active return; in conjunction with such observations it can provide uniquely valuable information about surface properties of Titan, the icy satellites, and the rings. Such information might include bulk dielectric constant and likely composition (e.g., organics with low dielectric constant or water ice with high dielectric constant), surface or subsurface roughness or physical state, or physical temperature. For Saturn's atmosphere, the only significant source of opacity is ammonia vapor, and the thermal radiation at the RADAR wavelength of 2.2 cm comes from the ammonia cloud-forming region around 1–2 bar pressure. The measured brightness temperature reflects the mean atmospheric temperature in the region of absorption, and is generally indicative of the cloud-level ammonia humidity. Maps of the brightness temperature uniquely show the variability of ammonia concentration in and below the clouds and address dynamical properties of the atmosphere from the cloud tops around 1 bar to pressure depths well below the cloud base around 1.4 bar.

### 3.2.2 Secondary RADAR Data Types

*3.2.2.a. HiSAR.* SAR imagery was sometimes obtained at altitudes greater than 10000 km above the target body. In these circumstances, nominal SAR-mode data suffers from excessive noise due to poor signal-to-noise ratio (SNR). In such cases, we used a lower-resolution (1–5 km) version of SAR imaging with resolution between nominal SAR (~500 m) and scatterometry (>10 km). To maintain adequate SNR, only the central, high-gain, beam was used. At higher altitudes, the central beam spanned a wider area, so useful swath widths in the range of 70 km to 150 km were still obtained. Instead of relying on spacecraft motion to sweep the beam across the surface, these imaging segments panned the central beam across the surface by turning the spacecraft. These images extend the area covered by imaging and are useful for mapping the extent of moderate resolution features such as mountains and lakes that are not apparent in lower-resolution scatterometer data.

*3.2.2.b. SARTopo.* Because multiple antenna beams (feeds) are employed in SAR imaging, we can use an amplitude monopulse technique to compare overlapping regions between the beams and thereby estimate surface heights ([Stiles et al. 2009](#)). This technique depends upon accurate knowledge of spacecraft attitude and the antenna gain pattern. It enables two or more surface-height profiles to be obtained along the long dimension of each SAR image. These profiles have approximately 10 km spatial resolution and 100 m height accuracy. By providing coincident surface heights with SAR imagery, the SARTopo technique greatly improves the interpretability of the imagery. Although SARTopo data were not required deliverables (as they were not in the original team commitment), they have been archived in PDS as a voluntary contribution. SARTopo data were produced at NASA's Jet Propulsion Laboratory (JPL).

*3.2.2.c. SAR Stereo.* When overlapping SAR images are obtained at different times, it is often possible to determine surface heights using stereo techniques closely related to those employed for optical images. The stereo mapping process can be divided broadly into two steps: identifying corresponding points (or features) in two different images and using the pixel coordinates of those points to solve for the ground coordinates of the feature. The first step is essentially an image-processing problem and is the same for optical or radar images, though the latter might have greater problems due to noise. The geometric calculations of radargrammetry differ from those of photogrammetry in that they are based on the principles by which SAR images are formed, i.e., a pixel corresponds to a circle of constant range from the spacecraft at the time of imaging, rather than to a ray emanating from the camera in a constant direction. The Cassini RADAR Science Team (CRST) produces Digital Topographic Models (DTMs) from stereo data by using a commercial system that includes flexible image-matching capabilities and that allows the user to write “sensor model” code describing the geometry of the images ([Kirk and Howington-Kraus 2008a](#), [Kirk et al. in prep](#)).

### 3.3 Nominal RADAR Observation of Titan

An encounter that fully utilized the RADAR instrument would start as the spacecraft approached Titan, obtaining only radiometer measurements for up to 3 hours (Figure 3-2). Next, when the spacecraft was within about 30,000 km, the transmitter was turned on, and scatterometer measurements were taken. Altimetry followed when Titan was close enough (~10000 km) for useful data to be taken at the wider bandwidth. Then, about 15 minutes before closest approach at a range of about 5000 km, SAR observation began. On the outbound portion of the pass, these transitions occurred in reverse. HiSAR observations (see [Section 3.2.2.a](#)) were obtained during nominal scatterometer or altimeter periods when data volume and viewing geometry constraints allowed. In practice, observation time during Titan (and other target) passes was mostly shared with other instruments, varied in altitude, and was otherwise constrained; in addition, observations further from Titan than shown were added in various modes. So actual Titan passes assigned fully or partially to RADAR generally used only parts of this scheme, and the combination of observations varied.

Further, because of the extreme competition for observing time when passing close to Titan, and because the two instruments’ preferred observation geometry (spacecraft attitude profile) matched exactly at closest approach to Titan, many passes were shared. In particular, an operating scheme was devised where some Titan passes were shared by RADAR and the Ion and Neutral Mass Spectrometer (INMS). One instrument would observe and control attitude prior to closest approach, the other afterward, and both could obtain useful (though not optimal) data during part of the other’s half-pass. These were called “ride-along” passes, and (for example) RADAR’s observations when in INMS-preferred orientation were referred to as “ride-alongs.” When near closest approach, ride-along RADAR data could be very good, but it degraded rapidly as distance from closest approach increased.

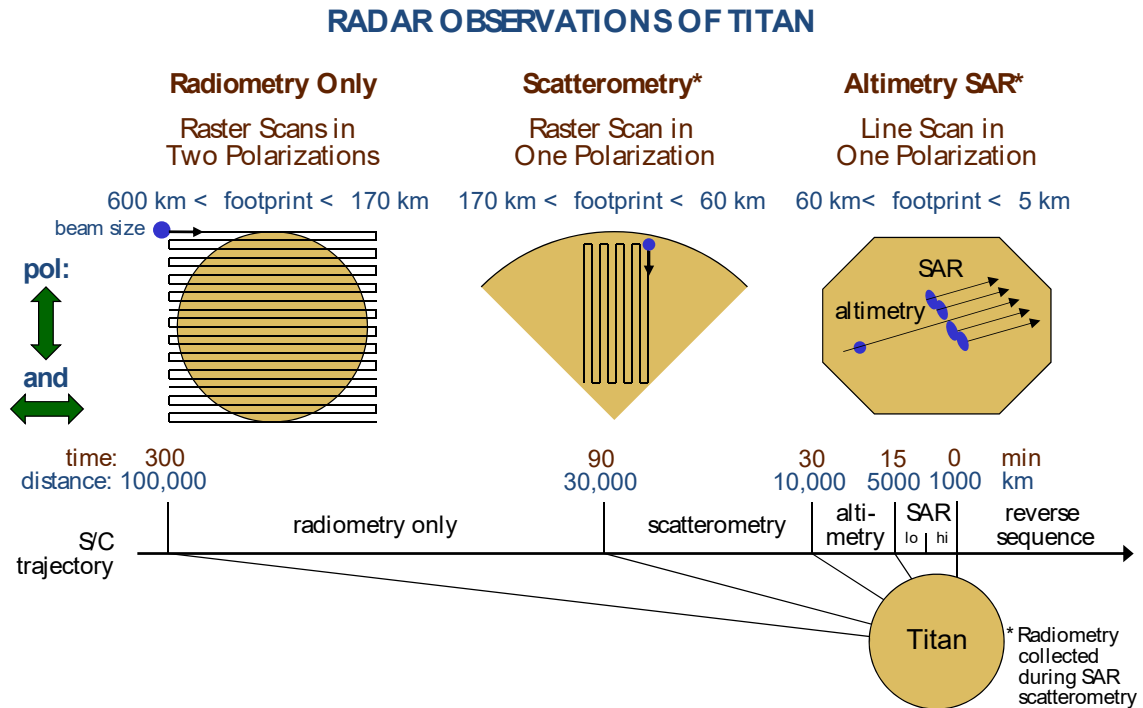


Figure 3-2. Nominal SAR data pass at Titan.

### 3.4 RADAR Operation

RADAR received instructions from the spacecraft's CDS computer in two ways: through direct commands and through instrument execution blocks (IEBs), which were preloaded from the CDS. For detailed operation descriptions, see [Elachi et al. \(2004\)](#) and [Renick \(1997\)](#), but in brief the RADAR operated as follows. Direct commands initiated an observation at the appropriate start time by triggering a previously loaded IEB. The IEB then issued instructions to the instrument relative to that start time, including those instrument parameters that control all of the details of the observation, including (but not limited to) RADAR mode, receiver bandwidth, data compression mode (block-adaptive quantizer [BAQ]—see [Section 4.1.3](#) and [Kwok and Johnson \[1989\]](#)), signal attenuation levels, pulse-repetition frequency, and other details describing the bursts. Some, but not all, of the IEB parameters are recorded in the headers of the various data products (see [Section 4](#)). IEBs were generated during the planning process by the RADAR Mapping Sequencing Software (RMSS, [West et al. 2009](#))

### 3.5 Titan Coverage

On a typical flyby, RADAR was capable of generating a SAR strip of ~1% of Titan's surface. The flyby geometry was determined by the orbital tour around Saturn, driven by a diverse range of scientific objectives and the use of Titan's gravity to modify Cassini's trajectory. Thus, the ground tracks (and possible radar footprints) are not evenly distributed over Titan, and some coverage gaps exist. Further, Titan flybys were dedicated to a range of scientific observations, many of which were incompatible with RADAR observations due to altitude or attitude constraints, or spacecraft operating mode restrictions (e.g., data volume or power). Thus, SAR observations

occurred on only about a quarter of Titan flybys. In many instances those observing opportunities were chosen to address particular objectives (e.g., viewing specific terrain types or latitudes or filling prominent coverage gaps), but in some cases the opportunity drove the geometry. For example, the T113 flyby, which had been originally allocated to the CAPS instrument, was reallocated to RADAR due to the failure of CAPS. Further, while some flyby allocations were made (often years in advance) on the assumption of executing SAR observations throughout, other constraints (e.g., solar heating limits on other instruments) became apparent only during detailed—minute-by-minute—sequencing of observations. This issue was a particular factor in the planning of flybys (T95 and after) in the Solstice Mission: In some instances this necessitated substitution of altimetry observations near closest approach instead of SAR (since altimetry allowed freedom to rotate the spacecraft about the  $-Z$  axis and thereby mitigate heating).

Broadly, the objective driving the observations in the Prime Mission was to obtain a diversity of coverage: infrared bright and dark terrains, such as Xanadu (T13) and Belet (T8), respectively; low (T8, T13), high southern (T7, T39) and high northern (T25, T28, 29, 30) latitudes; and the Huygens landing site (T41). Because the Prime Mission concentrated coverage on the northern hemisphere, the Equinox Mission had more coverage in the south, and swaths T55–T60 in particular provided RADAR coverage there.

The Solstice Mission science planning process addressed a set of designated objectives resulting from the Prime and Equinox findings (extending geographic coverage was explicitly not one of these goals, although some extended coverage inevitably resulted as a collateral benefit of addressing the objectives). These objectives included observation of seasonal changes, notably in Titan's lakes and seas (demanding repeat coverage of the polar regions), measurement of Titan's shape (demanding topographic data—including some long altimetry swaths—distributed in latitude and longitude) and measuring Titan's rotation rate (demanding overlaps with prior coverage to provide tiepoint matching). Thus, while the coverage maps might have a rather random appearance, they are the result of thousands of hours of planning and negotiation.

Figures 3-3 through 3-6 provide a global overview of SAR coverage of Titan from the Cassini missions. Figures 3-3 through 3-5 show outlines of coverage separated by Prime, Equinox, and Solstice missions, and Figure 3-6 shows all coverage combined. Swath colors and labels indicate Titan pass numbers, with colors coded according to the keys at the right of each figure. Note that these figures show both normal SAR and HiSAR (see Section 3.2.2.a). Various calculations of SAR coverage at the end of the Cassini Mission are shown in Table 3-2. Appendix 3 provides detailed information for SAR passes in all three phases. For detailed parameters describing SAR swaths, see Appendix 4.

Altimetry coverage is shown in Figure 3-7. Figure 3-8 shows locations of all surface heights obtained, including altimetry, SARTopo (see Section 4.3) and stereo reduction (see Section 4.4). Scatterometer coverage of Titan is near 100%; radiometer coverage is complete.

Table 3-2. SAR coverage of Titan at the end of the Cassini Mission  
(by Areal Percentage, Ta–T126).

COVERAGE TYPE	PERCENTAGE
Global SAR	46.0%
Global SAR + HiSAR	74.0%
NP (>60N) SAR	57.6%
NP (>60N) SAR + HiSAR	85.0%
SP (<60S) SAR	64.2%
SP (<60S) SAR + HiSAR	79.0%
Repeat (n >1) SAR	14.2%
Repeat (n > 1) SAR + HiSAR	38.8%
Repeat (n >2) SAR	3.1%
Repeat (n >2) SAR + HiSAR	15.5%
Repeat (n >3) SAR	0.5%
Repeat (n >3) SAR + HiSAR	5.1%
Repeat (n >4) SAR	0.1%
Repeat (n >4) SAR + HiSAR	1.5%

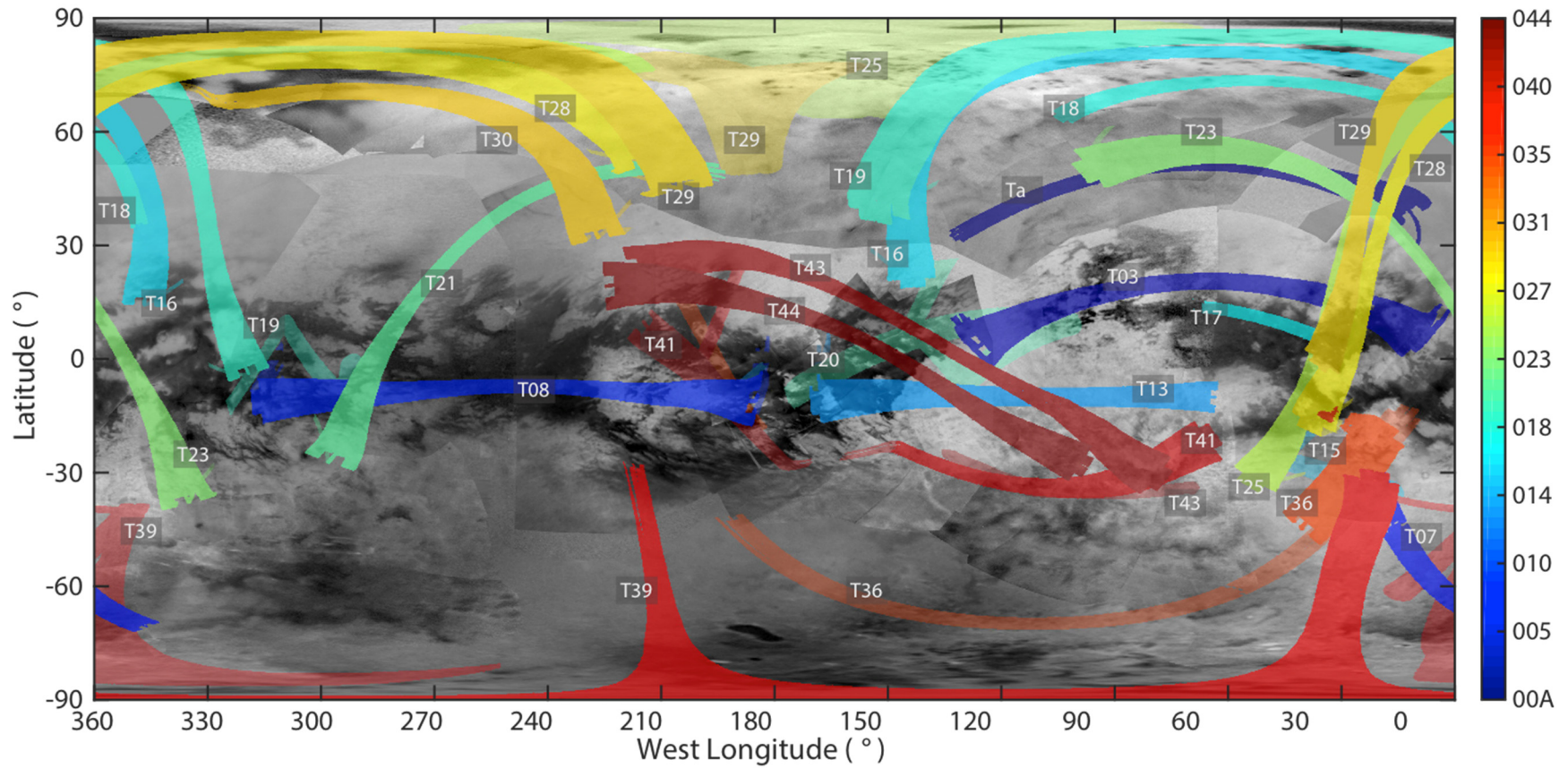


Figure 3-3. Titan SAR coverage from the Prime Mission. The swaths are shown on an ISS basemap. The red dot at  $\sim 190^\circ\text{W}$ ,  $10^\circ\text{S}$  is the Huygens landing site.

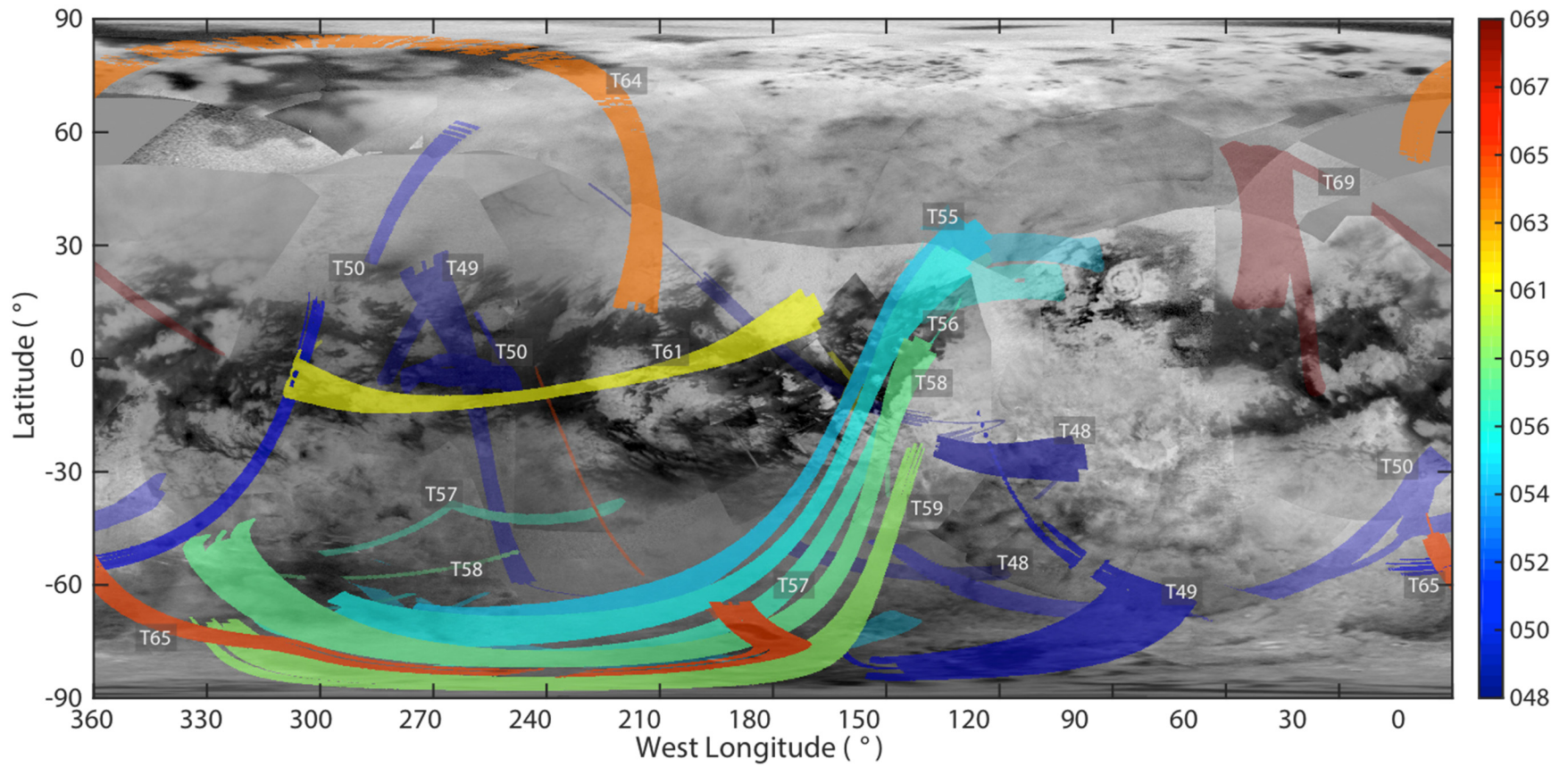


Figure 3-4. Titan SAR coverage from the Equinox (XM) Mission. The swaths are shown on an ISS basemap.

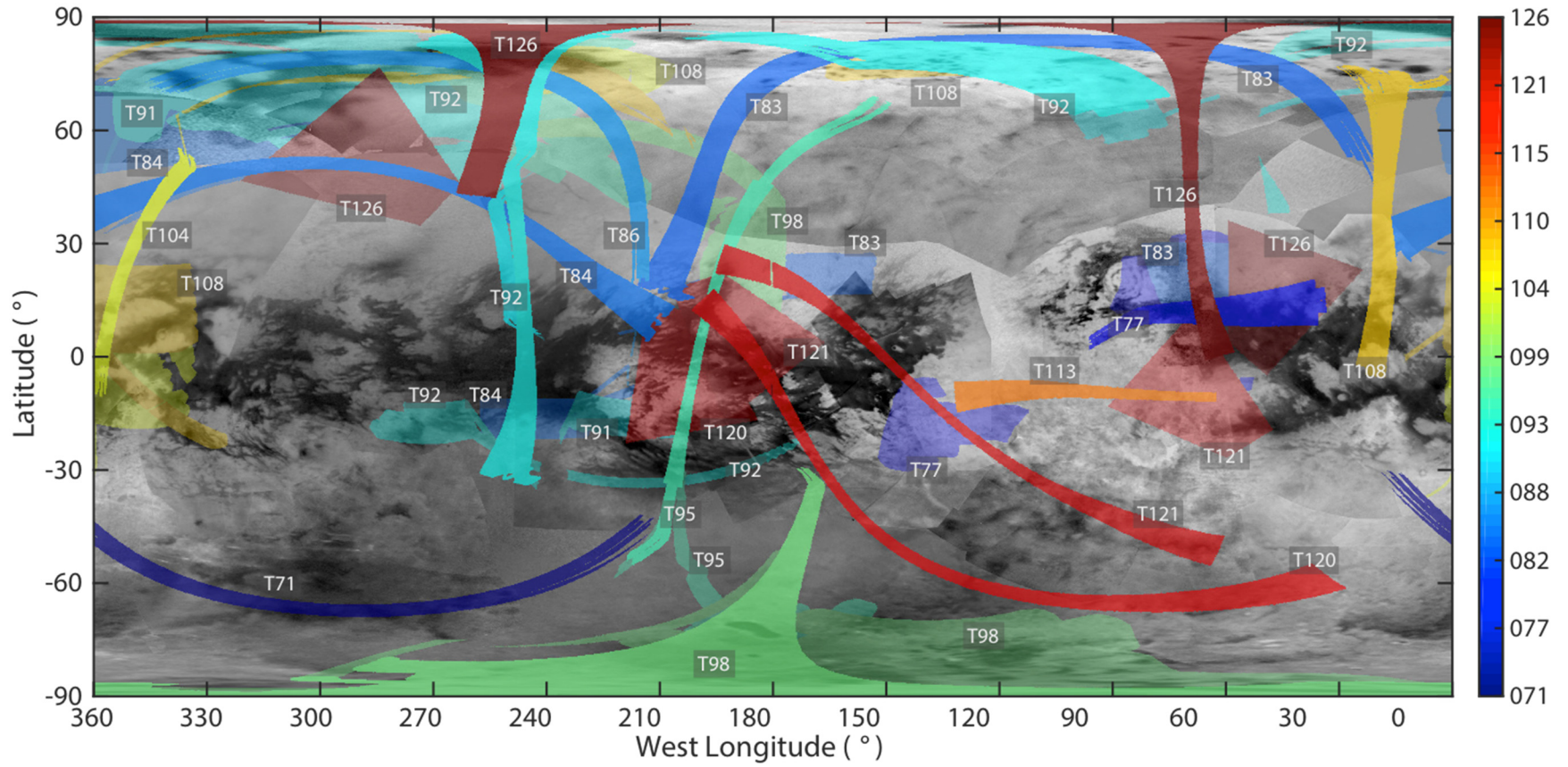


Figure 3-5. Titan SAR coverage from the Solstice (XXM) Mission. The swaths are shown on an ISS basemap.

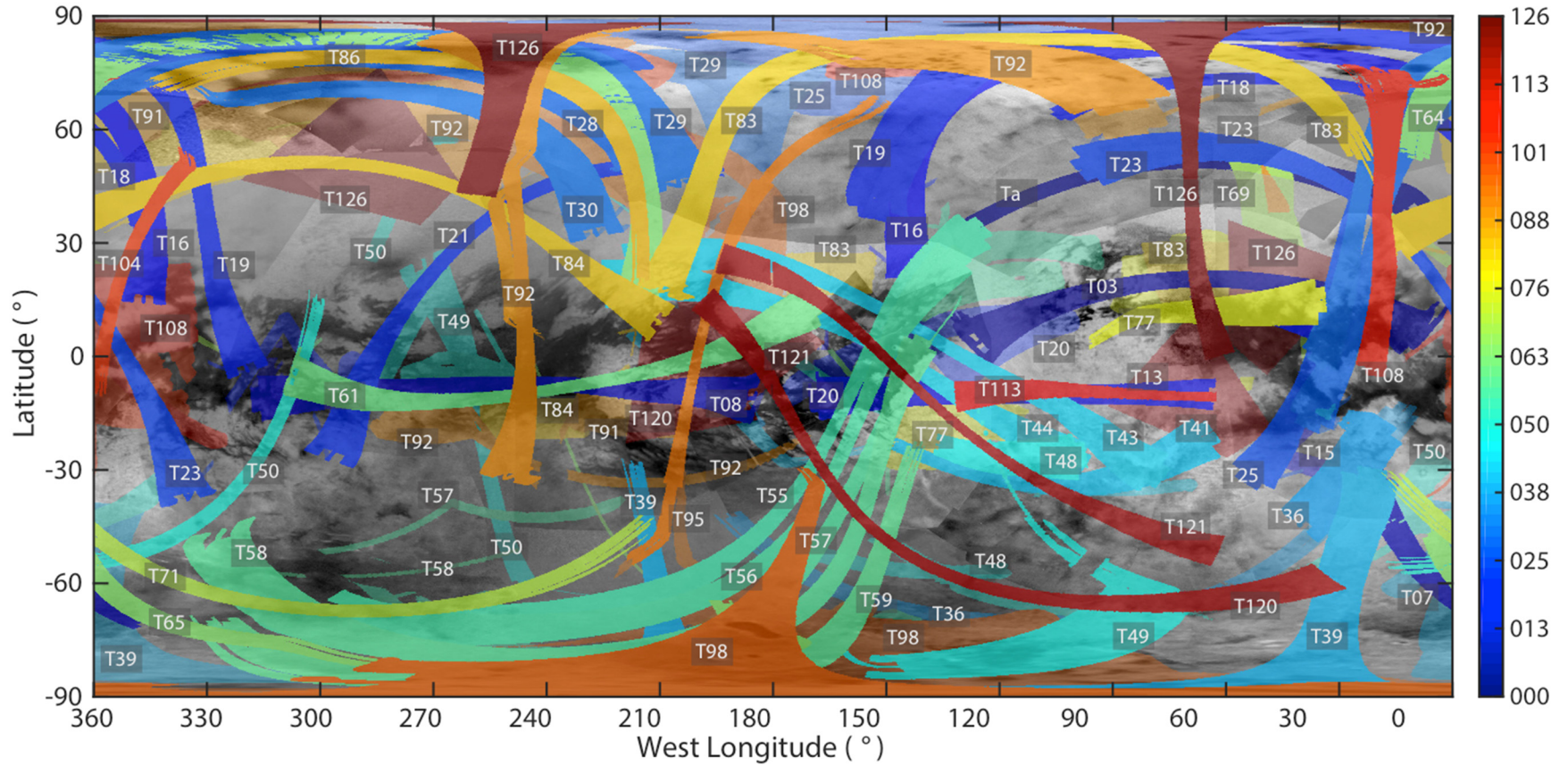


Figure 3-6. Combined Titan SAR coverage from the entire Cassini Mission. The swaths are shown on an ISS basemap.

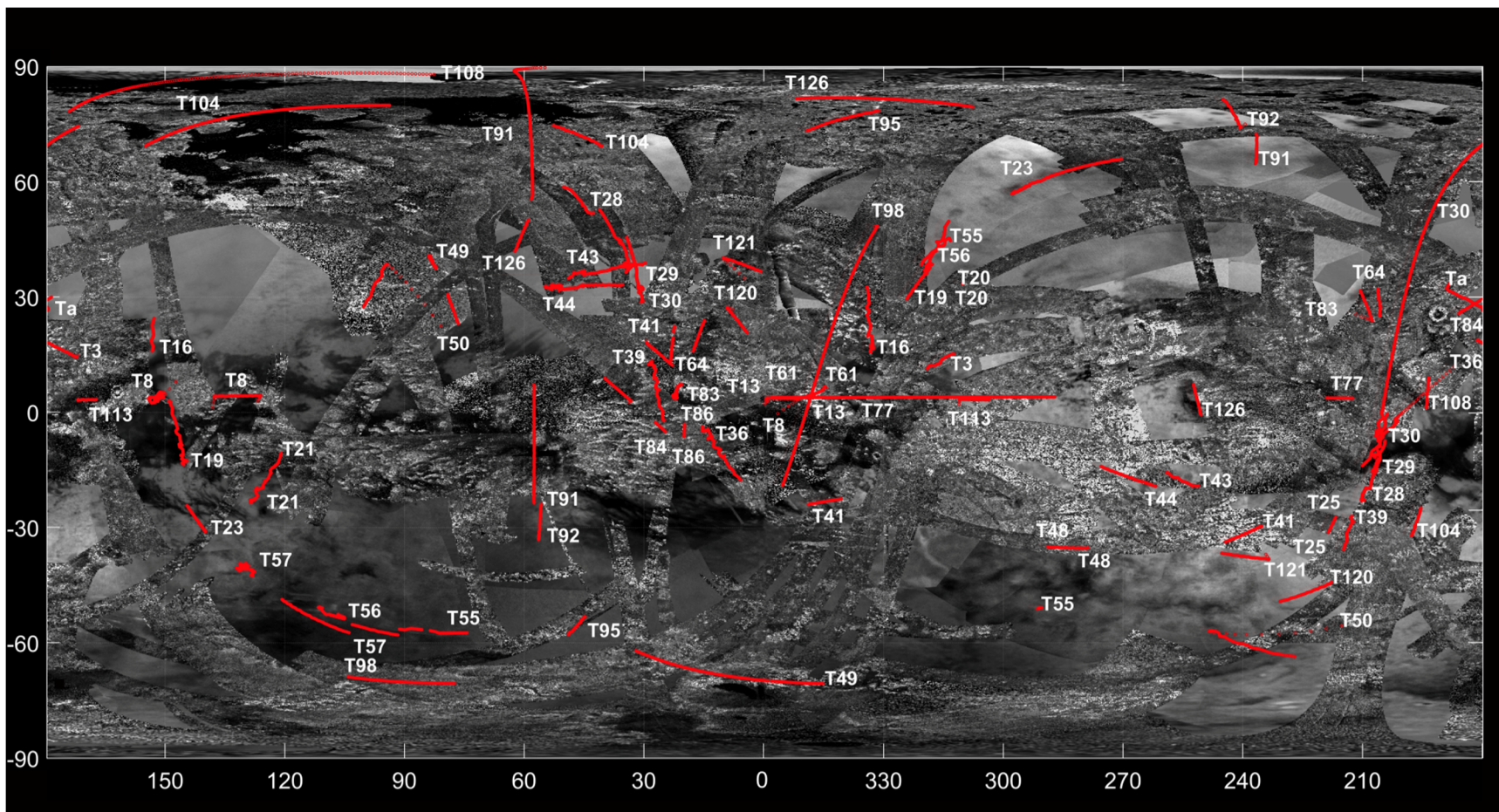


Figure 3-7. Cassini altimetry coverage of Titan.

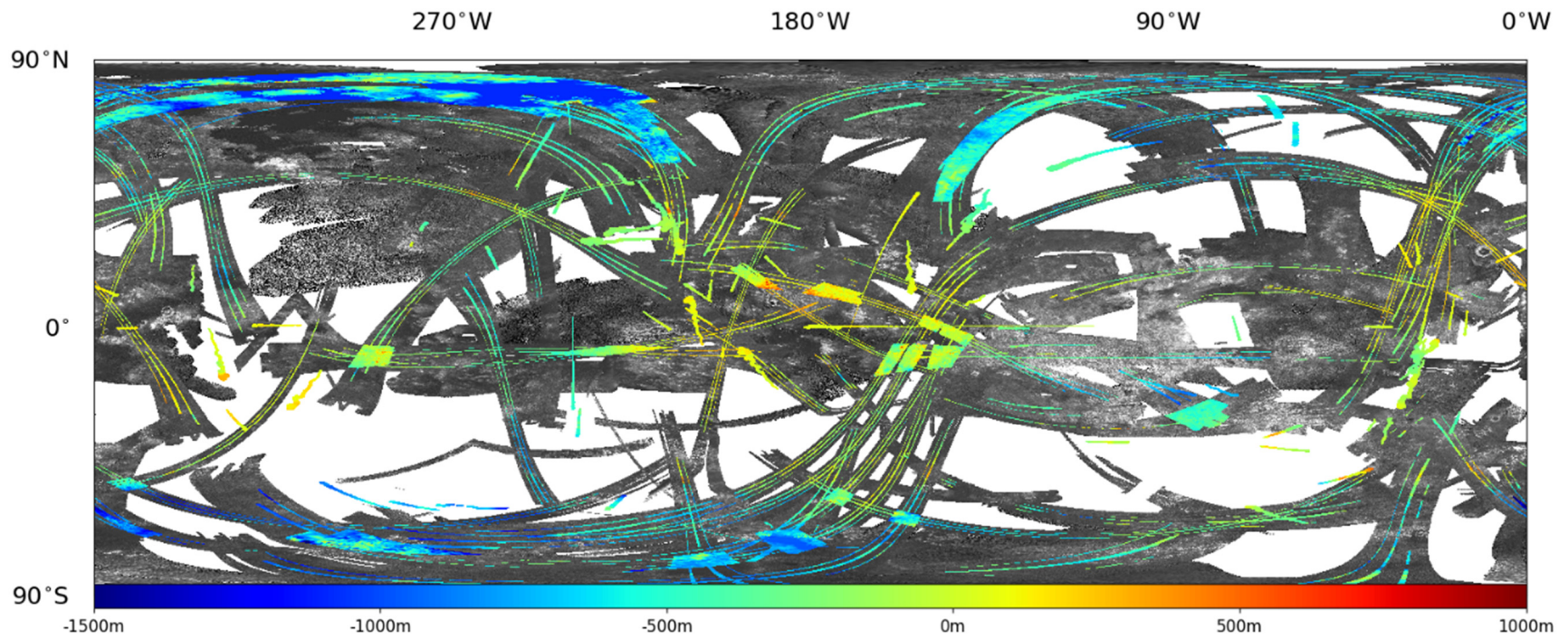


Figure 3-8. All Titan surface heights obtained by the Cassini RADAR. Color swaths were obtained using stereo reduction; color lines within black-and-white SAR swaths are from SARTopo; color lines not parallel to SAR swaths are from altimetry (see [text](#)).

## 3.6 Other RADAR Coverage

### 3.6.1 Rings

Radiometry at 2-cm wavelength provides a unique window on the physical and compositional properties of Saturn's rings. The dominant emission from the rings at this wavelength is scattered disk thermal emission. Pure ice is basically transparent, so that the measurements are sensitive to trace amounts of contaminants. The microwave approach uniquely samples bulk rather than surface properties of particles. The RADAR team's objectives at Saturn were therefore to investigate the structural and compositional properties of the rings by determining their scattering properties from passive observations at different aspects in relation to the disk, and by searching for thermal properties in evidence of intrinsic thermal emission. Sets of prioritized observations were developed and are shown in Table 3-3.

Table 3-3. Ring objectives and observations.

REV	REQUEST	DATE	DATA RECEIVED (KB)
S10	RADAR_006RI_PO8RINGS001_PRIME	12-Apr-05	31942.8
S14	RADAR_014RI_PO8RINGS001_PRIME	3-Sep-05	21987
S23	RADAR_028RI_PO1RINGS002_PRIME	10-Sep-06	152038
S23	RADAR_028RI_045MATCH001_PRIME	11-Sep-06	18065.2
S27	RADAR_038RI_038MATCH1001_PRIME	27-Jan-07	35910
S27	RADAR_038RI_038MATCH2001_PRIME	4-Feb-07	32991.6
S28	RADAR_039RI_39R1MATCH001_PRIME	23-Feb-07	28302.4
S34	RADAR_050RI_PO8RINGS001_PRIME	28-Sep-07	88403.2
S34	RADAR_051RI_PO2RINGS002_PRIME	23-Oct-07	8831.2
S35	RADAR_052RI_PO8RINGS001_PRIME	14-Nov-07	3576565
S35	RADAR_052RI_PO2RINGS002_PRIME	16-Nov-07	8626
S40	RADAR_066RI_046MATCH001_PRIME	4-May-08	46420.8

### 3.6.2 Icy Satellites

RADAR obtained scatterometry and radiometry observations of Saturn's icy satellites (Mimas, Dione, Enceladus, Tethys, Phoebe, Hyperion, Iapetus, Rhea). RADAR scatterometry observations measured the object's radar reflectivity and aided in constraining composition and structure of the top decimeter of the surface of the icy satellites ([Ostro et al. 2006, 2010](#)). Radiometric observations help to constrain the thermal properties of the surfaces. A list of RADAR icy satellites observations is given in Table 3-4.

During most of the icy satellite observations, the RADAR operated at very high ranges of 50,000 to 420,000 km, where SAR and altimetry observations were not possible due to low signal levels. Some HiSAR data is available for three icy satellites, including one observation each for Iapetus, Rhea, and Enceladus. Additionally, a single close-up, high-resolution SAR imaging flyby was performed for Enceladus. For all the other icy satellite observations, only disk-integrated scatterometry and radiometry data were collected.

Table 3-4. Icy satellites observations.

REV	REQUEST	DATE	DATA RECEIVED (KB)
S01	RADAR_000PH_SCATTRAD001_PRIME	11-Jun-04	2705.6
S01	RADAR_000PH_2SCATTRAD001_PRIME	11-Jun-04	285030.4
S06	RADAR_00BDI_SCATTRADL002_PRIME	15-Dec-04	S/C Commanding Error*
S07	RADAR_00BIA_SCATTRADL001_PRIME	31-Dec-04	318295.6
S07	RADAR_00CIA_SCATTRADL001_PRIME	1-Jan-05	1259213.6
S08	RADAR_003EN_SCATTRAD001_PRIME	17-Feb-05	495953.2
S09	RADAR_004EN_SCATTRAD001_PRIME	9-Mar-05	397586.4
S12	RADAR_011RH_SCATTRADL001_PRIME	14-Jul-05	212123.6
S14	RADAR_015TE_SCATTRAD003_PRIME	24-Sep-05	248960.8
S14	RADAR_015HY_SCATTRAD001_PRIME	26-Sep-05	392669.2
S15	RADAR_016DI_SCATTRAD001_PRIME	11-Oct-05	314343.6
S16	RADAR_017IA_SCATTRAD001_PRIME	12-Nov-05	321898
S16	RADAR_018RH_SCATTRAD001_PRIME	27-Nov-05	698675.6
S18	RADAR_021TE_SCATTRADL001_PRIME	25-Feb-06	290570.8
S19	RADAR_022RH_SCATTRAD001_PRIME	21-Mar-06	738347.6
S22	RADAR_027DI_SCATTRADL001_PRIME	16-Aug-06	147956.8
S22	RADAR_027RH_SCATTRADL001_PRIME	17_aug-06	157783.6
S23	RADAR_028EN_SCATTRAD003_PRIME	10-Sep-06	152038
S25	RADAR_032EN_SCATTRADL001_PRIME	9-Nov-06	144567.2
S25	RADAR_033DI_SCATTRAD002_PRIME	21-Nov-06	163826
S27	RADAR_039HY_SCATTRADL001_PRIME	15-Feb-07	246278
S30	RADAR_045RH_SCATTRADL001_PRIME	27-May-07	259500
S30	RADAR_045RH_SCATTRADL002_PRIME	27-May-07	
S31	RADAR_047MI_SCATTRAD001_PRIME	28-Jun-07	264.3
S31	RADAR_047RH_SCATTRADL001_PRIME	28-Jun-07	224
S32	RADAR_048TE_SCATTRADL001_PRIME	20-Jul-07	206172.8
S33	RADAR_049RH_SCATTRAD001_PRIME	29_aug-07	225157.6
S33	RADAR_049IA_SCATTRAD003_PRIME	9-Sep-07	561237.2
S33	RADAR_049IA_SCATTRAD004_PRIME	9-Sep-07	291482.8
S33	RADAR_049IA_SCATTRAD001_PRIME	10-Sep-07	330888.8
S33	RADAR_049IA_SCATTRAD002_PRIME	11-Sep-07	155397.2
S33	RADAR_049IA_SCATTRAD005_PRIME	12-Sep-07	S/C Safing Incident**
S34	RADAR_050DI_SCATTRAD001_PRIME	30-Sep-07	274975.6
S34	RADAR_050EN_SCATTRAD001_PRIME	30-Sep-07	115178
S35	RADAR_053MI_SCATTRAD001_PRIME	3-Dec-07	297965.6
S38	RADAR_061EN_SCATTRAD001_PRIME	12-Mar-08	243815.6
S38	RADAR_061EN_SCATTRAD002_PRIME	12-Mar-08	199644.4
S39	RADAR_064MI_SCATTRAD001_PRIME	11-Apr-08	222700
S44	RADAR_088EN_SCATTRAD001_PRIME	9-Oct-08	402131
S54	RADAR_120EN_SCATTRAD001_PRIME	2-Nov-09	444828
S57	RADAR_126MI_SCATTRAD001_PRIME	13-Feb-10	190402.8
S58	RADAR_127RH_SCATTRAD001_PRIME	2-Mar-10	428822.4

\* This activity did not get downlinked.

\*\* Instrument execution block did not execute.

Radiometry data were collected during the scatterometer integrations and also during a small raster scan centered on the target body. The raster scan provided on- and off-target measurements to help calibrate the radiometer. Scatterometer integrations usually involve transmitting a single-frequency carrier and then recording the Doppler-shifted and spread echoes from the target for five to twenty minutes. Even though the transmitted pulses were very narrow-bandwidth tones, the received echo power was spread out in the frequency domain by Doppler variation, which arises from a combination of the relative motion of a spacecraft and the rotation of a target body. For the icy satellites, the Doppler variation ranged from a few hundred hertz up to about 4 kHz. The pulsed nature of the transmit events also introduced grating lobes spaced at the pulse-repetition frequency (PRF) ([Ostro et al. 2006](#)). This caused the echo power spectrum to be repeated at intervals of the PRF. To make processing easier, the PRF was set to a frequency higher than the predicted Doppler spread of the target body so that the central spectral peak was separated from the grating lobes, showing the natural variation of the echo power over the target body. The measured echoes were processed in the frequency domain to provide an echo power spectrum and a low-noise, disk-integrated radar cross-section measurement. In some cases a chirped pulse was transmitted to allow for range processing. Range processing was limited by the range spread within the antenna-beam footprint projected on the surface of the icy satellite. If a range spread is large enough to cover the pulse-repetition interval, then different ranges within the beam footprint will be ambiguous, making interpretation of range-Doppler images difficult. Low SNR at the typical ranges of RADAR icy-satellite observations can also compromise the usefulness of range-Doppler results. For these reasons, chirped pulses were used only when there was sufficient predicted SNR and some ambiguity-free illuminated area.

### 3.6.3 *Saturn*

Well calibrated, high resolution maps of Saturn's microwave emission were obtained over an approximately 10-year period following Saturn orbit insertion. This emission is thermal in origin and originates in the ammonia cloud region, ammonia vapor being the dominant microwave absorber. Data collected are listed in Table 3-5. Of these, six global maps were obtained by continuously scanning Saturn from pole to pole for periods of approximately 14 hours each around periapsis during close equatorial orbits, using the combination of spacecraft motion and Saturn rotation to sweep out a full sampling in longitude. The first five of these maps were published as cylindrical projections covering  $360^\circ$  in longitude and nearly  $\pm 60^\circ$  in latitude, with sensitivities approaching 0.1 K and resolutions approaching  $1^\circ$  at the equator ([Janssen et al. 2013](#), [Laraia et al. 2013](#)). These maps demonstrated unique features of the dynamics of Saturn's atmosphere in the vicinity of the ammonia cloud region above approximately the 3-bar pressure level, and successfully charted the progress of the 2010–2011 Great Storm.

### 3.6.4 *Venus, Earth, and Jupiter*

Although there was little scientific application of RADAR prior to the first Titan encounter, the instrument was tested during the second flyby of Venus and the Earth flyby (both in 1999). In the inner solar system, Cassini's thermal management required that the HGA shade the spacecraft from solar heating. Thus these flybys were in a sun-pointed orientation, but Venus and Earth "got in the way." No radar echo from

Table 3-5. Saturn observations.

REV	REQUEST	DATE
S14	RADAR_015SA_GLOBALMAP001_PRIME	23-Sep-05
S14	RADAR_015SA_GLOBALMAP002_PRIME	23-Sep-05
S14	RADAR_015SA_GLOBALMAP003_PRIME	24-Sep-05
S37	RADAR_058SA_2POLAR001_PRIME	8-Feb-08
S38	RADAR_059SA_1POLAR001_PRIME	20-Feb-08
S46	RADAR_095SA_NORTHPOL001_PRIME	1-Dec-08
S46	RADAR_095SA_SOUTHPOL001_PRIME	3-Dec-08
S46	RADAR_097SA_NORTHPOL001_PRIME	17-Dec-08
S46	RADAR_097SA_SOUTHPOL001_PRIME	18-Dec-08
S54	RADAR_119SA_GLOBALMAP001_PRIME	13-Oct-09
S55	RADAR_122SA_GLOBALMAP002_PRIME	9-Dec-09
S61	RADAR_135SA_GLOBALMAP001_PRIME	24-Jul-10
S64	DATA LOST	
S67	RADAR_146SA_GLOBALMAP001_PIE	20-Mar-11
S89	RADAR_216SA_GLOBALMAP001_PIE	14-Aug-15

Venus was obtained ([Lorenz et al. 2000](#)) as the thick CO<sub>2</sub> atmosphere is opaque to Ku-band radiation, although the planet's warmth was detectable in radiometry data. During the Earth flyby, the antenna footprint passed from the eastern Pacific across the Andes and Brazil, and both scatterometry and radiometry were obtained. The scatterometry included some near-nadir glints from a lake in Brazil.

The Jupiter flyby was too distant to permit useful observations of the Galilean satellites, but did provide an opportunity to map the Jovian synchrotron radiation emission in two polarizations in order to identify the high-energy electron spectrum in the radiation belts ([Bolton et al. 2002](#)).

## 4 RADAR Data Product Overview

The RADAR instrument collected, returned, digitized, and delivered digital data to the spacecraft. Together with other instruments' data, they were stored on the spacecraft solid-state recorder (SSR) and downlinked, generally at the next scheduled communication opportunity with a DSN complex ([Imbriale 2003](#)), where digital data were extracted and returned to the Cassini operations center at JPL. There, individual instrument data were separated and stored on the Cassini Distributed Object Manager (DOM).

RADAR telemetry was extracted from the Cassini DOM and processed at JPL to produce time-ordered RADAR frames (“Level 0”<sup>3</sup>). For routine processing, the data extraction occurred after the project produced the best possible filled and cleaned telemetry files, approximately 2 days after downlink. These Level-0 data were then further processed to produce three types of Cassini RADAR data products: Burst-Ordered Data Products (BODPs) (Level 1), Basic Image Data Records (BIDRs) (Level 2), and Digital Map Products (DMPs) (Levels 3 and above). BODPs and BIDRs were produced at JPL; DMPs were produced at the United States Geological Survey (USGS) in Flagstaff, Arizona. The DMP archive also includes text files with calibrated radiometry data produced at JPL as an “extra” (non-PDS) product.

BODPs are data sets at various stages of processing that are organized as time-ordered records for each burst. The BIDR and DMP data sets are downstream from production of BODPs. Production of the DMPs also makes use of several types of auxiliary data files (altimeter summary files [see [Section 4.1](#)] and SARTopo files) produced at JPL that are described in corresponding sections below. Each type of product is described briefly here and more fully in the Software Interface Specification (SIS) documents contained in each archived PDS volume. RADAR SISs are available at the following links:

- SIS (DORA-001) “Cassini RADAR Burst-Ordered Data Products SIS”:  
[https://pds-imaging.jpl.nasa.gov/data/cassini/cassini\\_orbiter/CORADR\\_0045/DOCUMENT/BODPSIS.PDF](https://pds-imaging.jpl.nasa.gov/data/cassini/cassini_orbiter/CORADR_0045/DOCUMENT/BODPSIS.PDF)
- SIS (DORA-002) “Volume SIS for Cassini RADAR Instrument Team Data Products”:  
[https://pds-imaging.jpl.nasa.gov/data/cassini/cassini\\_orbiter/CORADR\\_0271/DOCUMENT/VOLSIS.PDF](https://pds-imaging.jpl.nasa.gov/data/cassini/cassini_orbiter/CORADR_0271/DOCUMENT/VOLSIS.PDF)
- SIS (DORA-003) “Cassini RADAR Basic Image Data Records SIS”:  
[https://pds-imaging.jpl.nasa.gov/data/cassini/cassini\\_orbiter/CORADR\\_0271/DOCUMENT/BIDRSIS.PDF](https://pds-imaging.jpl.nasa.gov/data/cassini/cassini_orbiter/CORADR_0271/DOCUMENT/BIDRSIS.PDF)

Like all planetary data, Cassini RADAR data are archived in NASA’s PDS (see [Section 9](#)). PDS is organized by nodes, each of which archives a separate science discipline: Atmospheres, Geosciences, Planetary Plasma Interactions, Rings and Small Bodies, Engineering, Cartography and Imaging Sciences (hereafter “Imaging”), and Navigation and Ancillary Data. Cassini RADAR data are archived in the Imaging Node (<https://pds-imaging.jpl.nasa.gov/>), physically located at both the USGS facility in Flagstaff and at JPL. RADAR data can be accessed directly at the index page (<https://pds-imaging.jpl.nasa.gov/volumes/radar.html>). The CRST delivered data

---

<sup>3</sup> The Planetary Data System (PDS) defines data product levels at [https://pds.nasa.gov/datastandards/pds3/standards/sr/StdRef\\_20090227\\_v3.8.pdf](https://pds.nasa.gov/datastandards/pds3/standards/sr/StdRef_20090227_v3.8.pdf). The present document refers to NASA levels as described therein. Note that this numbering scheme applies to PDS Version 3 (PDS3), which is used for Cassini data. This numbering scheme is not used in PDS4, which future missions will use. In the future, Cassini data might be transitioned to PDS4.

products to the PDS typically within one year of data acquisition. At the Imaging Node Web sites all data products can be downloaded, and search engines are available to aid in locating those of interest. The governing documents for all RADAR data products are the SISs.

Please note that the products described below are not in any widely-used image format (e.g., JPEG or PDF) and require specialized software to read (see Table 4-1). Users interested in common image formats can find JPEG images in PDS in the EXTRAS directory for each Titan pass. For example, a JPEG of Titan pass TA can be found at [https://pds-imaging.jpl.nasa.gov/data/cassini/cassini\\_orbiter/CORADR\\_0035/EXTRAS/](https://pds-imaging.jpl.nasa.gov/data/cassini/cassini_orbiter/CORADR_0035/EXTRAS/). The JPEG images should be used for viewing only and not for any quantitative analysis.

Table 4-1. Software packages that will enable users to make use of RADAR data (some for cost and some free) and their sources (as of 2019).

APPLICATION	NOTES
ArcGIS (a geographic information system [GIS]) ( <a href="http://www.arcgis.com">www.arcgis.com</a> )	Reads Integrated Software for Imagers and Spectrometers (ISIS) .cub files (which are very similar to PDS images), but does not support all projections. Specifically, RADAR's oblique cylindrical projections are not supported unless the plug-in PDS2ISIS is run (images may be loaded, but they must be reprojected to access the cartographic capabilities).
Environment for Visualizing Images (ENVI) ( <a href="http://www.harris.com/solution/envi">www.harris.com/solution/envi</a> )	Tested with 32-bit BIFQ and 8-bit BIBQ RADAR formats (see <a href="#">Section 4.5.1</a> for format definitions).
Fiji/ImageJ ( <a href="http://fiji.sc">fiji.sc</a> )	ImageJ is now called Fiji (for "Fiji is just ImageJ"). It reads PDS, ISIS 2, and ISIS 3 (only BSQ—not tiled—formats) with plug-ins.
ISIS 3 ( <a href="http://isis.astrogeology.usgs.gov">isis.astrogeology.usgs.gov</a> )	ISIS 3 is the standard tool to analyze RADAR data files, and has step-by-step tutorials ( <a href="http://isis.astrogeology.usgs.gov/IsisWorkshop/index.php/Working_with_Cassini_RADAR">http://isis.astrogeology.usgs.gov/IsisWorkshop/index.php/Working_with_Cassini_RADAR</a> ) on how to process RADAR data.
MATLAB ( <a href="http://www.mathworks.com">www.mathworks.com</a> )	Can read the images using any number of readers that have been submitted to the public File Exchange ( <a href="https://www.mathworks.com/matlabcentral/fileexchange/">https://www.mathworks.com/matlabcentral/fileexchange/</a> ).
Photoshop ( <a href="http://www.adobe.com/Photoshop">www.adobe.com/Photoshop</a> )	Photoshop will read the 8-bit BIBQ after the correct dimensions and label length have been input.
QGIS ( <a href="http://www.qgis.org">www.qgis.org</a> )	Reads ISIS .cub files (which are very similar to PDS images), but does not support all projections. Specifically, RADAR's oblique cylindrical projections are not supported unless the plug-in PDS2ISIS is run (images may be loaded, but they must be reprojected to access the cartographic capabilities).
Build your own software	If users wish to write their own software, or need to know details about file formats or contents, they should read the appropriate Software Interface Specification (SIS): <ul style="list-style-type: none"> <li>• General Volume SIS (<a href="https://pds-imaging.jpl.nasa.gov/data/cassini/cassini_orbiter/CORADR_0284/DOCUMENT/VOLSIS.PDF">https://pds-imaging.jpl.nasa.gov/data/cassini/cassini_orbiter/CORADR_0284/DOCUMENT/VOLSIS.PDF</a>)</li> <li>• BIDR SIS (<a href="https://pds-imaging.jpl.nasa.gov/data/cassini/cassini_orbiter/CORADR_0284/DOCUMENT/BIDRSIS.PDF">https://pds-imaging.jpl.nasa.gov/data/cassini/cassini_orbiter/CORADR_0284/DOCUMENT/BIDRSIS.PDF</a>)</li> <li>• BODP SIS (SBDR and LBDR) (<a href="https://pds-imaging.jpl.nasa.gov/data/cassini/cassini_orbiter/CORADR_0284/DOCUMENT/BODPSIS.PDF">https://pds-imaging.jpl.nasa.gov/data/cassini/cassini_orbiter/CORADR_0284/DOCUMENT/BODPSIS.PDF</a>)</li> </ul>

#### 4.1 Burst-Ordered Data Products (BODPs)

BODPs are data files with data set IDs of CO-SSA-RADAR-3-?BDR-V1.0, where the "?" can be S, L, or A, as described below. They include engineering telemetry, RADAR operational parameters, raw echo data, instrument viewing geometry, and calibrated

science data. BODP files contain time-ordered fixed-length records. BODPs come in three different record formats:

- Short-Burst Data Record (SBDR)
- Long-Burst Data Record (LBDR)
- Altimeter-Burst Data Record (ABDR), plus the ABDR Summary File (ASUM)

The Cassini RADAR is operated in “burst mode,” where it transmits a number of pulses, then waits to receive the return signals. All of the data products are in tables, with rows corresponding to a single time period referred to as a burst. Each record corresponds to the full set of relevant data for an individual radar burst. For the BODP, “burst” refers to an entire measurement cycle, including transmit, receipt of echo, and radiometric (passive) measurements of the naturally occurring radiation emitted from the surface. Even when the transmitter is turned off and only passive measurements are made, the measurement cycle is still referred to as a burst.

For each data pass, the ground processing occurs in the following manner: An SBDR record is produced for every burst throughout the pass; an LBDR file (or up to two files, depending on data volume) is produced that contains only records for the middle portion of the pass during which the transmitter was on; and an ABDR file is produced that contains records for only the periods in which the RADAR is in altimeter mode. One data field in each record is a burst identifier, which uniquely distinguishes a burst from all other bursts in the mission; records in different files that correspond to the same burst have the same burst ID.

#### 4.1.1 *Product Overview*

BODPs are fixed header length, fixed record length files. The header is an attached PDS label. All of the BODPs contain binary data. RADAR values have all been decoded and are stored in 32-bit floating point format; other ancillary data is stored as 32-bit integers, 32-bit floating point or 64-bit IEEE floating point as appropriate (see the BODP SIS, cited at the beginning of [Section 4](#)), or fixed length character strings for text variables such as time tags.

To read a particular data value from a particular data field, the header length, the record size, and the byte offset of the data field within the record must be known. As a UTC<sup>4</sup> time tag is included in each record, the data one reads can be restricted to a particular time interval. To further facilitate temporal segmentation of the data, a Cassini RADAR Transition (CRT) file is provided for each Titan pass. This file maintains a temporally ordered list of the times and transition types for all RADAR mode transitions, such as radiometry to scatterometry mode switches. The Volume SIS contains more information about CRT file formats.

#### 4.1.2 *Short-Burst Data Record (SBDR)*

The SBDR includes instrument telemetry and calibrated science data in burst order. It excludes raw echo data and altimeter profiles. For every Titan RADAR pass, an SBDR record is produced for every burst throughout the pass (e.g., for 43200 bursts, record size is 1273 bytes, and file size is 55 MB). The SBDR data record is divided into three consecutive segments from three different levels of processing: (1) the engineering

<sup>4</sup> UTC is an abbreviation for Coordinated Universal Time; it is similar to Greenwich Mean Time (GMT), but see [https://en.wikipedia.org/wiki/Universal\\_Time](https://en.wikipedia.org/wiki/Universal_Time) and references contained therein.

data segment, (2) the intermediate-level data segment (mostly spacecraft geometry), and (3) the science data segment (antenna temperature, backscatter, surface height, measurement geometry, etc.). Three geophysical quantities are in the science data segment: the NRCS obtained from the scatterometer measurement; the antenna temperature determined from the radiometer measurement; and the measured distance from the gravitational center of the body (local radius). The antenna temperature is computed for every burst; the NRCS is computed for all bursts with active-mode data with the exception of distant observations for which a single burst is insufficient to obtain a useful measurement. For every burst in altimeter mode, the local radius is estimated. In addition, ancillary parameters including intermediate values (e.g., receiver temperature, total echo energy, system gain, etc.), analytical estimates of the standard deviation of the residual error in each of the three primary measurements, and measurement geometry are computed. In order to ease the identification of surface features from NRCS maps, the effects of incidence angle are removed by a global average model to compute a “corrected” version of NRCS. For Titan passes, the raw backscatter values have been multiplied by the function  $f(I)$ ,

where

$I$  is the incidence angle,

and

$$f(I) = 0.2907 / (f_1(I) + f_2(I) + f_3(I)),$$

for

$$f_1(I) = 2.8126 * (\cos(I)^4 + 893.9677 * \sin(I)^2)^{-1.5},$$

$$f_2(I) = 0.5824 * (\cos(I)^4 + 34.1366 * \sin(I)^2)^{-1.5},$$

and

$$f_3(I) = 0.3767 * \cos(I)^{1.9782}.$$

For targets other than Titan, incidence angle corrections have only been computed for observations in which we have SAR data. In those cases the specific equation for the correction is documented in the PDS label for the incidence angle corrected BIDR files (filename prefix = BIF). In addition, SAR ancillary data are included in the science data segment when available. The SAR images themselves are stored in the BIDR files.

For active- and passive-mode measurements, measurement geometry information is included. Separate data fields for each are reported, as differences in passive- and active-mode measurement times can cause the two cases to differ, although some active- and passive-mode quantities are likely to be identical (e.g., polarization orientation angle). Active-mode geometry is calculated for the time halfway between the midpoint of the transmission and the midpoint of the active-mode receiver window. Passive geometry is calculated for the time at the midpoint of the passive receiver window (summed radiometer windows). For each case, the full set of measurement geometry includes the polarization orientation angle, emission/incidence angle, azimuth angle, measurement location, and four points on the 3-dB gain contour of the measurement. The location corresponds to the nominal center of the antenna pattern along the spacecraft negative Z axis. This location differs from the peak of the antenna pattern by about 1/10 of the measurement resolution. For investigators interested in location accuracy better than the measurement resolution itself, it is necessary to make use of the archived antenna patterns and also to estimate and account for errors in spacecraft attitude knowledge. SAR geolocations are independently determined and do not depend on attitude. Each SAR pixel corresponds to a known range (delay) and azimuth (Doppler shift). Given this information and reference shape and ephemeris for the target body, SAR pixel locations can be determined precisely. The largest residual

error in SAR geolocation is reference shape error (2- to 3-km errors for Titan passes), but can be as large as 10 km for unusual viewing geometry and locations more than 1 km removed from the reference sphere ([Corlies 2017](#), [Zhang et al. 2017](#)). The centroid and contour points are in latitude and longitude, using the west longitude positive planetodetic coordinate system. Since Titan is treated as a sphere, these coordinates are identical to the standard planetographic coordinates used in the SAR imagery (BIDR) data set. The rectangular coordinates (X, Y, and Z) of this system are defined such that the positive Z-axis is north (in the direction of the spin axis +83.4279 degrees declination, +39.4827 degrees right ascension); the positive X-axis is in the equatorial plane and directed toward the prime meridian; and the Y-axis completes the orthogonal right-hand-rule system. The latitude and longitude are defined by

$$\text{Lon} = 360 - \text{atan2}(Y, X);$$

$$\text{Lat} = \text{asin}(Z/R).$$

The function `atan2` takes the x and y coordinates of a point in 2-D space and returns the counterclockwise angle from the positive x-axis to the vector from (0,0) to (x,y). Unlike the standard `atan` function it preserves information about the quadrant of the angle. For more details see the BIDR SIS (see Sections [4](#) and [4.2](#)).

For nonspherical bodies, the BODP latitudes and longitudes differ from those used in the BIDR. For image projection convenience and convention, the relatively small number of non-Titan SAR images are projected onto a reference sphere whose radius is documented in the labels of the BIDR files. (Other than Titan, only Rhea, Iapetus, and Enceladus have SAR imagery available.) However, the latitudes and longitudes in the BODP data files for these nonspherical bodies are triaxial coordinates. The BODP coordinate system is defined by

$$X' = x/\text{radx}, Y' = y/\text{rady}, Z' = z/\text{radz};$$

$$\text{Lon} = 360 - \text{atan2}(Y', X');$$

$$\text{Lat} = \text{asin}(Z')—$$

where x, y, z are the rectangular coordinates (coordinate system defined the same as above) of a point on the triaxial body with radii = (radx,rady,radz). For the nonspherical bodies this definition is nonstandard. As mentioned in the ERRATA, the SAR coordinates for the same bodies are produced in the more conventional manner. Although the triaxial shape was used for geolocation and calibration, the SAR latitude and longitude backplanes report the equivalent planetographic coordinates with respect to the reference sphere, not the triaxial coordinates. The science data segment is usually not computed for non-Titan bodies with the exception of radiometric observations of Saturn and its rings, so these fields are flagged as invalid for those observations. The exceptional cases are those in which SAR observations of the non-Titan bodies were obtained. For most non-Titan icy satellite observations, only a single antenna temperature or backscatter measurement is computable, rather than values for each burst. This limitation is due to SNR effects caused by the long distance from which the RADAR observations are obtained in order to avoid impacting observations from the other Cassini instruments.

#### 4.1.3 Long-Burst Data Record (LBDR)

The LBDR is the same as the SBDR but includes a raw echo data array as well. The array comprises 32,768 32-bit IEEE floating-point values, and contains the active-mode time-sampled data obtained during the receive window. The data are encoded before downlink from the spacecraft to minimize the data transfer rate, and is then decoded during ground processing. The length of the array corresponds to the maximum amount of echo data that can ever be obtained from a single burst. In the array, only the first  $N$  elements, floating point values typically in the range  $[-127.5, 127.5]$  sampled consecutively at a rate of  $B=2*\text{Bandwidth}$  (in Hz), are valid data. The decompression algorithm occasionally produces values outside the nominal range to account for situations in which saturation occurs due to exceeding the dynamic range of the digital to analog converter.  $N$  is stored in the `raw_active_mode_length` data field and  $B$  is in the `adc_rate` field in the engineering data segment. The `raw_active_mode_rms` field in the engineering data segment contains the root mean square of the  $N$  sampled echo data values. The `BAQ_mode` field identifies the specific compression algorithm used. See the BODP SIS (cited at the beginning of [Section 4](#)) for a full description of this field. For a description of the block-adaptive quantizer (BAQ) compression algorithm, see [Kwok and Johnson \(1989\)](#).

When the `BAQ_mode` field is set to 3, it signifies the compressed scatterometer mode, where all data samples are not downlinked from the spacecraft. In this mode, absolute values of the samples are summed across all corresponding sample positions in each pulse repetition interval (PRI) and downlinked. To track any dc bias, a summation of signed values over the entire receive window is also downlinked. These data are stored in the LBDR raw echo data array as one PRI worth of summed magnitudes, plus one summed value at the end. Thus, if there are 50 PRI in the receive window with 250 samples in one PRI, then the LBDR raw echo data array will contain 250 floating point values, each a sum of 50 magnitudes, followed by one floating value containing the sum over all  $50*250$  samples. The value of  $N$  is set to 50, so the user needs to separately load the dc bias value at the end. The one PRI worth of summed magnitudes are intended to provide a profile of the echo while still reducing the downlinked data volume by a factor equal to the number of PRI in the receive window. These values can be further summed to a single value that is proportional to the average power assuming that the radar echo power is normally distributed. This assumption is expected to hold for radar echoes from natural distributed targets that contain many scattering centers. Since it is a summation, the values might be outside the nominal range.

#### 4.1.4 Altimeter-Burst Data Record (ABDR)

The ABDR is the same as the SBDR but includes altimeter profiles that are range-compressed active-mode data obtained while the RADAR is in altimeter mode and the beam is pointed within less than one-half beamwidth of nadir. The profile is an array of floating point values with the number of values stored in the `altimeter_profile_length` data field in the science data segment. The active-mode data is segmented by pulse during range compression, and each pulse is correlated with a real-valued replica of the chirped transmit waveform to distribute the energy within each returned pulse into range bins. The replica waveform used is a digital-step chirp with identical starting frequency, step duration, step frequency, and number of steps to the

transmitted signal. The modulation of the analog dealiasing filter on the return signal is treated as an ideal filter. Any inaccuracy in the chirp-generator used to produce the transmitted signal is also ignored. It is possible to use rerouted-chirp measurements obtained during each observation to correct for these errors, but this has not been done for the archived data set. The number of pulses, the range for the first sample of the altimeter profile, and the range step are data fields that can be found in the science data segment. The number of range bins can be obtained by dividing the profile length by the number of pulses; the array is arranged so that the range bins for each pulse are contiguous.

A simple altimeter product containing basic location and surface-height information is included as an ASCII comma-separated-value (csv) file called the ABDR Summary File, or ASUM. In this file are presented several estimates of the distance from the spacecraft to the intercept of the antenna boresight and the target surface. The different estimation methods, and the locations of the estimates, are described in the BODP SIS (cited at the beginning of [Section 4](#)). The ASUM file for Titan pass TA (for example) can be found at [https://pds-imaging.jpl.nasa.gov/data/cassini/cassini\\_orbiter/CORADR\\_0035/DATA/ASUM/ABDR\\_SUMMARY\\_04\\_D035\\_V03.CSV](https://pds-imaging.jpl.nasa.gov/data/cassini/cassini_orbiter/CORADR_0035/DATA/ASUM/ABDR_SUMMARY_04_D035_V03.CSV) and a description of its content at [https://pds-imaging.jpl.nasa.gov/data/cassini/cassini\\_orbiter/CORADR\\_0035/DATA/ASUM/ABDR\\_SUMMARY.FMT](https://pds-imaging.jpl.nasa.gov/data/cassini/cassini_orbiter/CORADR_0035/DATA/ASUM/ABDR_SUMMARY.FMT). Files for other passes can be found via corresponding URLs on the index page (<https://pds-imaging.jpl.nasa.gov/volumes/radar.html>).

#### 4.1.5 *Data Validation and Archiving*

All of the BODPs have attached PDS labels, and the data products conform to PDS standards for file formats and labels. PDS labels are stored as ASCII character strings. A sample PDS label can be found in the BODP SIS (cited at the beginning of [Section 4](#)). Validating or ensuring the quality of the products and their readiness for release was the responsibility of the CRST.

## 4.2 **Basic Image Data Records (BIDRs)**

BIDR data files are single-pass, calibrated and gridded SAR image data, with a data set ID of CO-SSA-RADAR-5-BIDR-VX.X, where X.X is the volume version number. The BIDR products are all gridded (raster) maps of Titan derived from SAR data and stored as PDS image files, and are generated at more than one word type (e.g., byte vs. floating point) and resolution. The BIDR is produced in an oblique cylindrical coordinate system, where the great circle corresponding to the ground track of the spacecraft around closest approach is defined to be 0 degrees latitude. The prime meridian of the oblique cylindrical coordinate intersects this great circle at the point of closest approach to the reference sphere. The extent of each BIDR product is the minimum bounding rectangle of the area of coverage in this projection for nominal SAR. This projection was chosen to minimize the amount of “dead space” (pixels not containing data) in the minimum bounding rectangle around image strips that are oriented essentially randomly on Titan. For distant HiSAR observations the oblique cylindrical projection can be much less optimal, but it is retained for the sake of simplicity.

#### 4.2.1 *Data Format and Description*

BIDRs were produced at the JPL by the CRST in full-resolution floating-point format. Several different files containing different steps in the processing of the backscatter images and supplementary maps of key variables (sometimes known informally as “backplanes,” though each map is contained in a separate data file) were produced for each SAR observation. One of these backplanes is the beam mask backplane, which denotes which of the five RADAR beams (antenna feeds) was used to produce each SAR pixel. The values contained in the beam mask image are 16-bit integers. The five least significant bits are used to indicate the beams, and the other 11 bits are always zero. Integer values of 1, 2, 4, 8, and 16 denote beams 1, 2, 3, 4, and 5, respectively. This format allows us to represent the case in which pixels are averaged from multiple beams, but multiple-beam averaging was never used in the SAR processing. Each SAR pixel value comes from a single beam. For more information about the beam mask backplane, see the BIDR SIS<sup>5</sup>.

Different image versions and supplementary backplane files are identified by the third letter in the BIDR filenames. The first two letters in all BIDRs filenames are “BI.” The primary images are the BIF files that contain floating point NRCS data from which systematic biases due to thermal and quantization noise, and systematic variation due to incidence angle have been removed. The quantization noise results from the BAQ scheme that is used to compress the data on the spacecraft before downlink to Earth. This compression induces an offset and a scaling term to the SAR data, which can then be accounted for in the noise subtraction approach. Thermal noise is caused mainly by system noise in the RADAR with a minor contribution due to emission from Titan’s surface. The latter effect is estimated based on Titan’s observed gross radiometric characteristics; the former is dealt with by using estimates made from engineering test data. The incidence angle correction algorithm used for Titan is the sum of three component models: two Hagfors components and a diffuse component (see the BIDR SIS V2.0, April 2008, for details). BIDRs from non-Titan observations use different incidence angle models appropriate to the specific body observed. In all cases the labels of the BIF files contain the precise equations and associated parameters used to perform the incidence angle correction.

There are two other NRCS images produced at JPL: BIU files, which have no corrections for incidence angle or noise, and BIS files, which are noise-corrected but not incidence-angle-corrected. Coregistered images of ancillary data are also produced by JPL including latitude (BIT), longitude (BIN), incidence angle (BIE), beam mask (BIM), noise-equivalent NRCS (BIX), uncorrected NRCS standard deviation (BID), and number of looks (BIL) backplane images. The BIX and BID files are the pixel-by-pixel bias and standard deviation, respectively, of the BIU files due to noise. The BIS and BIF files are both nominally unbiased, but residual errors due to under- or overestimation of the noise floor might remain. The standard deviation of the BIS data is the same as for the BIU data. The standard deviation of the BIF data is scaled by the same incidence-angle-dependent quantity that is multiplied by the BIS data to obtain the BIF data. BIM and BIL backplanes are 8-bit images. All others are 32-bit floating-point-format images. The values in the BIF, BIU, and BIS NRCS backplanes are linear-scale, unitless quantities. BIF files are converted to 8-bit (BIB)-format log-scale

---

<sup>5</sup> [https://pds-imaging.jpl.nasa.gov/data/cassini/cassini\\_orbiter/CORADR\\_0003/DOCUMENT/](https://pds-imaging.jpl.nasa.gov/data/cassini/cassini_orbiter/CORADR_0003/DOCUMENT/)

images at various resolutions by the USGS Flagstaff Astrogeology Team; both the USGS and JPL files are archived. The 8-bit images from the USGS are returned to JPL and archived together with the full-resolution floating-point images. See the BIDR SIS for more information.

BIDRs are generated from BODPs (see [Section 4.1](#)); the encoded raw active-mode data in the BODP (LBDR) files are decoded and processed into SAR images by the CRST. Geometric data used as inputs include a description of the shape and orientation of the RADAR beams derived from in-flight geometric calibration (stored as antenna-gain-pattern files in the CALIB directory of each archived PDS volume); mission-provided spacecraft pointing histories; and Titan and spacecraft ephemerides provided by the Cassini project. Each BIDR file contains data from all the antenna beams (up to five) used in each observation. For the NRCS images, each pixel contains information from the beam with the highest data quality for that pixel. The planetographic latitude/west longitude system is used to produce the latitude and longitude BIDR backplanes. Each BIDR is projected onto the oblique cylindrical map projection described at the beginning of [Section 4.2](#).

Multiple imaging segments can be obtained per spacecraft pass. Each of these segments contains all BIDR file types at each resolution. The “SXX” tag in their filenames distinguishes files from different segments such that “XX” is the 2-digit segment identifier. Typically, segment S01 is the primary SAR imaging segment. Other segments contain HiSAR data or turns at the beginning and end of the SAR observation. Occasionally the nominal SAR imaging period is split into multiple segments due to an unusual spacecraft pointing profile. See the BIDR SIS for a complete specification of the file names.

#### 4.2.2 *Non-Titan BIDRs*

In addition to Titan, SAR imagery is also available for three icy satellites: Rhea, Iapetus, and Enceladus. In order to produce these images the SAR processor needed to run in a special purpose mode. There are two special considerations for non-Titan data that need to be handled appropriately. First, the shapes of the non-Titan satellites are not sufficiently well approximated by a sphere. A spherical approximation in Titan SAR processing was deemed to be good enough, and no better shape information was available until after the acquisition of a sufficient number of SARTopo and altimeter height profiles was acquired. (In theory, the newly determined Titan shape could be used to redo Titan SAR processing with better location accuracy, but no such reprocessing has been performed.) Unlike Titan, triaxial body shape estimates for Iapetus, Rhea, and Enceladus were available from optical measurements. Because Rhea and Enceladus are not sufficiently approximated by a sphere, the SAR processor had to account for body shape in performing SAR pixel geolocation and calibration. Iapetus was treated as a sphere, although it perhaps should not have been. In addition to geolocation differences, with the exception of the closest Enceladus flyby, icy satellite calibration needed to be done in the HiSAR rather than nominal SAR manner. For nominal Titan (and close-up Enceladus) SAR processing, we make use of the fact that antenna gains and range to target do not change significantly within a SAR pixel. For HiSAR this approximation does not hold and instead one must integrate the product of antenna gain and signal attenuation due to range within each pixel in order to accurately calibrate the normalized radar cross-section quantities (primary backplane pixel values) in each SAR image. Table 4-2 lists relevant details for each of the icy-

satellite SAR image segments. Figure 4-1 depicts the Rhea image obtained in HiSAR mode. Figure 4-2 shows a portion of the close-up Enceladus flyby.

Table 4-2. Icy satellite SAR imaging passes.

	RHEA	IAPETUS	DISTANT ENCELADUS	CLOSE-UP ENCELADUS
Volume Number	214	143	207	232
Date	March 2, 2010	Sept. 10, 2007	Nov. 2, 2009	Nov. 6, 2011
Min S/C Altitude	25,000 km	17000 km	30,000 km	700 km
Max S/C Altitude	50,000 km	24000 km	58,000 km	760 km
Min Latitude	-90.0	-75.6	-76.9	-84.3
Max Latitude	90.0	90.0	35.1	-26.7
Easternmost Longitude	0	0	254.1	0
Westernmost Longitude	360	360	54.6	360
Finest Resolution	2 km by 6 km	2 km by 6 km	3 km by 3 km	50 m by 300 m

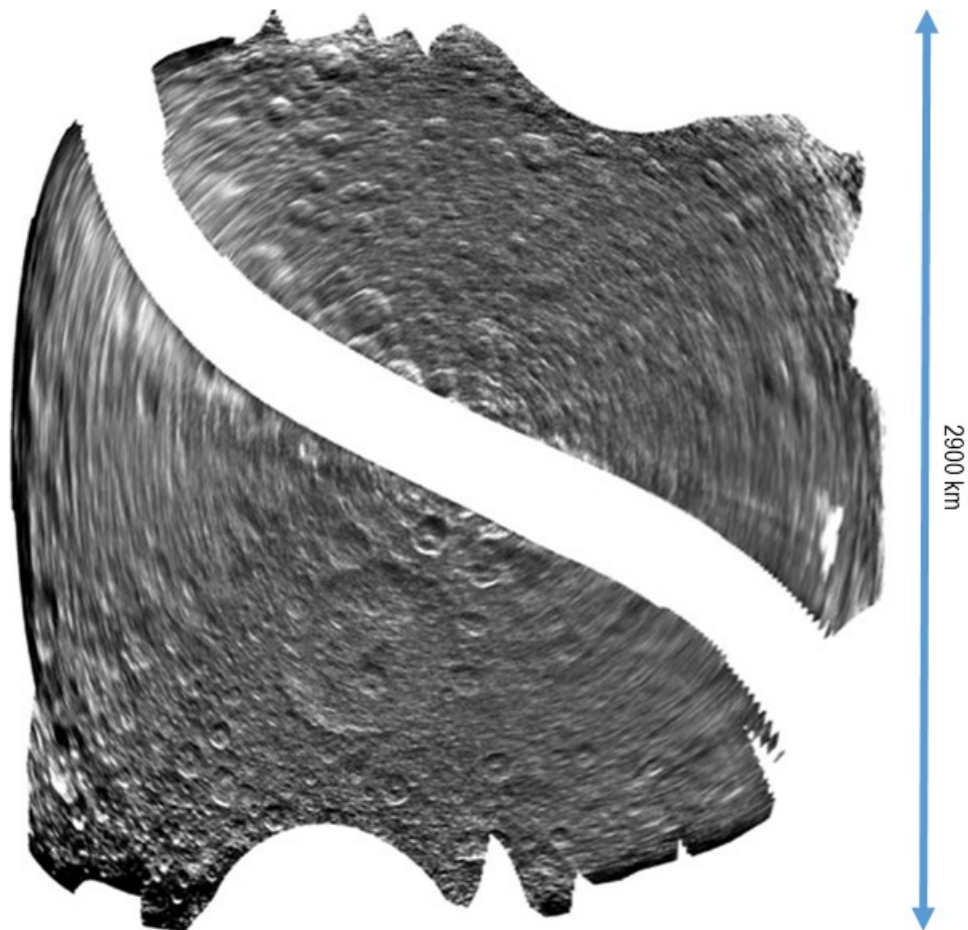


Figure 4-1. Close-up Enceladus SAR image acquired November 6, 2011.

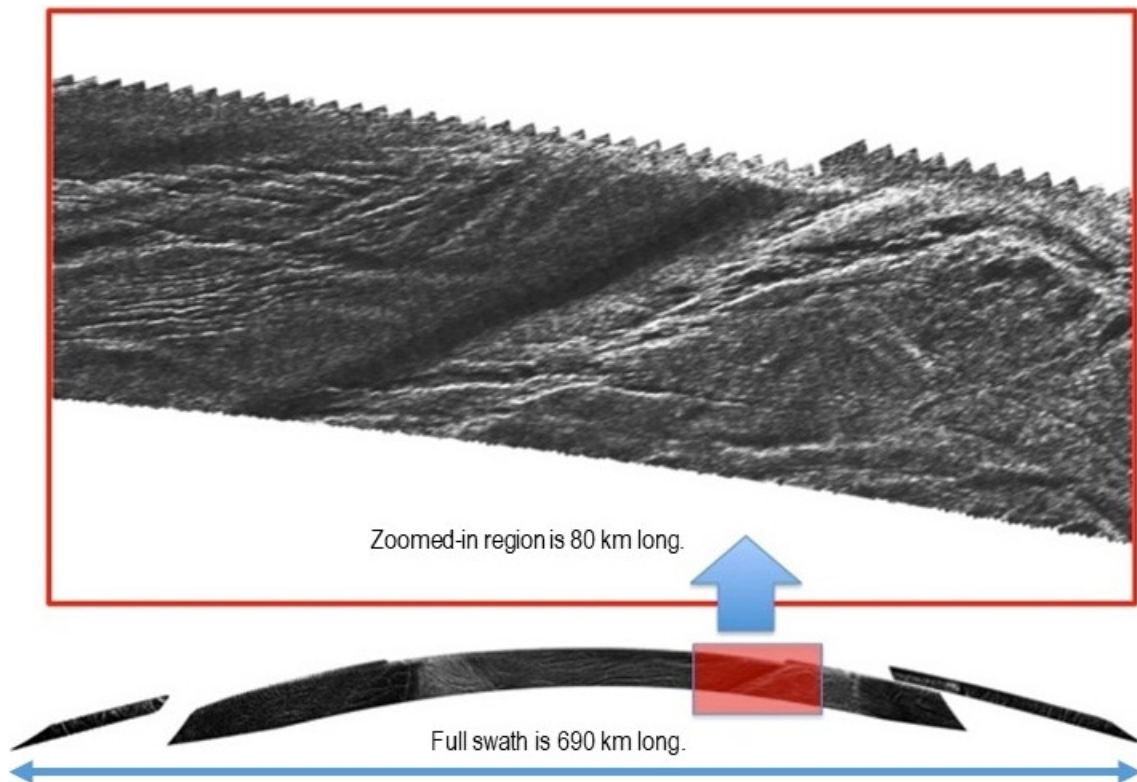


Figure 4-2. Distant Rhea SAR image acquired March 2, 2010.

#### 4.2.3 Data Validation and Archiving

The CRST validated the BIDs for scientific integrity as well as compliance with PDS standards. BIDs are archived as binary files, with the initial records containing a PDS label. Each BID is assigned a string that uniquely identifies the type of data product, bit type, resolution, and location of the data on Titan. This string is used both as the value of the PRODUCT\_ID keyword in the PDS labels and, with extension “.IMG” as the filename for that product. For more information about BID filename conventions see the BIDR SIS, and in [Appendix 6](#).

### 4.3 SARTopo Products

In Stiles et al. 2009 a technique called SARTopo is described that estimates Titan surface heights using SAR mode data. The primary benefit of the technique is the production of height profiles along the long dimension of each Cassini SAR image of Titan. These products are archived in PDS, for example Ta is at [https://pds-imaging.jpl.nasa.gov/data/cassini/cassini\\_orbiter/CORADR\\_0035/DATA/STDR/SARTOPO\\_T00AS01\\_B12\\_V03\\_150730.CSV](https://pds-imaging.jpl.nasa.gov/data/cassini/cassini_orbiter/CORADR_0035/DATA/STDR/SARTOPO_T00AS01_B12_V03_150730.CSV). Their format is described in detail, for example, in [https://pds-imaging.jpl.nasa.gov/data/cassini/cassini\\_orbiter/CORADR\\_0035/DATA/STDR/SARTDR.FMT](https://pds-imaging.jpl.nasa.gov/data/cassini/cassini_orbiter/CORADR_0035/DATA/STDR/SARTDR.FMT) for Ta.

To produce these height profiles, the authors took advantage of the fact that Cassini obtains overlapping SAR imagery from multiple beams (antenna feeds). The overlap between beams is small and is not included in the BIDR image records themselves. Instead, an algorithm is used to select the beam with the highest quality imagery and

only those data are used. To produce the SARTopo heights, it was necessary to reprocess individual beam images from the raw echo returns. The technique depends on the precise manner in which the location and magnitude of each SAR pixel are affected by variation in surface height. Understanding the relationship between surface height and SAR imagery is important not only to estimate surface heights, but also to understand how surface-height variation can impact other quantitative studies of SAR imagery. (See [Section 8.1](#) for an example of such effects.)

Unlike in optical imagery, SAR image pixels can be located on the target body without precise knowledge of the observer's orientation (e.g., spacecraft attitude). Instead, all that is required is knowledge of the shape of the target body and the location and velocity of the observer with respect to that body. SAR processing produces pixels by breaking up the return energy of the radar signal into round trip time and Doppler frequency bins. One can compute the distance (range) from the spacecraft to the ground location of each pixel from its round-trip time. Similarly, one can compute the relative velocity with respect to the spacecraft of each pixel from its Doppler. At that point, one has three critical pieces of information about the location of the pixel: (1) the pixel is on the surface of a sphere whose radius is the range and whose center is the spacecraft location; (2) it is on a cone centered on the spacecraft velocity vector, whose circumscribed angle is determined by the relative velocity of the ground location, and thus by the Doppler; and (3) it is on the surface of the target body. By intersecting the range sphere and the Doppler cone with a model of the surface of the target body, we obtain the locus of possible locations of the pixel. For typical SAR geometry and a spherical target body, there are only two points that intersect all three surfaces. The two points are far enough apart that a very coarse knowledge of spacecraft attitude (tens of degrees) is sufficient to select the correct pixel location. Once pixel locations are determined, they are used to project the SAR image onto the target body and to calibrate the image. Errors in the presumed shape of the target body lead to both mislocation (incorrect placement on the target body) and miscalibration (applying incorrect correction factors to pixel values due to poor knowledge of where the pixel falls in the antenna gain pattern).

Of course, "errors in the presumed shape" are just another name for surface heights. Because the surface of Titan is typically within 1 km of the reference sphere, the resultant mislocation error is usually small. Miscalibration is also small except in regions near the edge of beams. The SARTopo technique estimates surface heights from observed SAR miscalibrations near the beam edges. Cassini's antenna has multiple beams (feeds), so that some points on the ground are observed from two different beams. For different beams, the mislocation error due to surface height is the same, but the miscalibration error is different and of opposite sign. Nonzero surface heights, therefore, result in apparent differences in pixel values between overlapping single beam SAR images. The SARTopo technique first processes single beam SAR images for all five Cassini beams and 17 candidate surface heights (-2 km to +2 km from the 2575-km-radius Titan reference sphere in steps of 250 m). It then determines the surface height profiles that minimize the difference between the overlapping SAR images. Sources of error that affect SAR pixel calibration also affect SARTopo height estimation. The three largest sources of error are (1) thermal and speckle noise variance, (2) misestimation of the noise floor, and (3) spacecraft attitude knowledge error. Errors due to speckle and thermal noise variance are random and can thus be

eliminated by averaging together a sufficiently large number of measurements along the swath (a 10-km averaging length is used). The other two error sources can lead to systematic errors and thus must be handled differently. Errors in the noise-floor estimation cause error in noise subtraction that are only important for low SNR areas. The sensitivity of height to noise floor estimation error is reported in the data and used for quality control. Although, SAR location accuracy is insensitive to spacecraft attitude error, calibration accuracy is not. The gain of the antenna varies with the angle between the antenna beam boresight and the observation vector. If the beam boresight points directly at a pixel location, the antenna gain of the pixel is high. As the boresight moves away from the pixel, its gain quickly decreases. For this reason, a precise knowledge of the orientation of the beam (and thus the spacecraft attitude) is needed for calibration. A network of overlapping SARTopo and nadir altimetry profiles from different Titan flybys is used to correct systematic height errors due to spacecraft attitude. The sensitivity of heights to attitude error is reported in the data set and used for quality control. The data are broken up into different categories for which lower category numbers are better-quality data, as shown in Table 4-3. In addition to assigning categories, expected random and systematic height errors for each height measurement are also reported and can be employed to tailor a user-defined quality-control mechanism.

Table 4-3. Definition of SARTopo quality categories.

CATEGORY NUMBER	HEIGHT SENSITIVITY TO ATTITUDE M/DEG	HEIGHT SENSITIVITY TO NOISE FLOOR ERROR M/UNIT_ERROR (UNIT_ERROR=1 IS A 100% ERROR IN THE NOISE-FLOOR ESTIMATE)	RANDOM HEIGHT ERROR (M)
1	<500	<700	<75
2	≤500 × <750	≤700 × <900	<75
3	≤750 × <1000	≤900 × <1200	<75
4	>1000	>1200	<75

Figure 4-3 shows locations of SARTopo data for the entire Cassini Mission (compare to Figures 3-7 and 3-8). Because the SARTopo technique involves reprocessing SAR

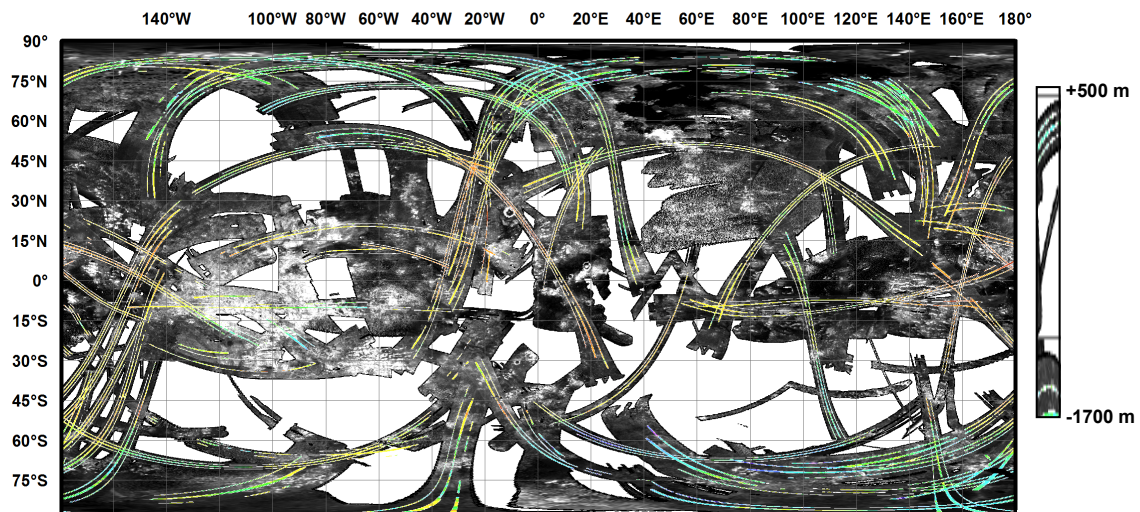


Figure 4-3. Global map of all SARTopo data, shown over SAR swaths.

images, it requires raw radar echo data, instrument transmit and receive parameters, antenna gain patterns, calibration constants, spacecraft ephemeris, and spacecraft attitude data as input. All of these are available in the Long-Burst Data Record files, instrument configuration files, or other files archived in PDS. The processing of the SAR images from the raw data involves three steps: (1) Synthetic-aperture processing: Energy in the raw echoes is broken up into 2-D image bins corresponding to range and Doppler (azimuth); (2) Calibration: Raw counts are converted to a geophysical quantity (NRCS) that corresponds to the ratio of the returned energy to what one would expect from a uniform scatterer; (3) Geolocation: The location on Titan from which the energy in each image pixel was scattered is determined. Because SARTopo has to do a full reprocessing of the images, it requires input data to do all three of these tasks. Tables [8-1](#) through [8-3](#) in [Section 8](#) list the full set of parameters needed for each step and how to find them in the PDS volume. [Section 8](#) provides examples of quantitative SAR data analyses. The parameters in the LBDR files are reported for each radar measurement cycle (burst). The configuration file parameters are contained in the single configuration file archived with each PDS volume. At most four to five instances of each a parameter (organized as keyword/value pairs) are contained in the configuration file. The multiple instances correspond to different RADAR modes (SAR high-resolution, SAR low-resolution, and altimeter low-resolution [scatterometer]) or different antenna beam numbers (1–5). SARTopo is only computed from data in the two SAR modes. For each RADAR measurement cycle, the beam number is available and so are the radar\_mode and receiver\_bandwidth (rc\_bw) parameters that can be used to determine the mode.

Special calibration modes are indicated by flag bits in the calibration source (csr) parameter in the LBDR files. Locations and descriptions of all parameters in the LBDR files are detailed in the DOCUMENTS/BODPSIS.PDF file included in each PDS volume (see [Sections 4](#) and [4.1](#)).

#### 4.4 Digital Map Products (DMPs)

The DMPs are high-level, gridded (raster) maps of Titan produced by the USGS, Flagstaff from the lower-level JPL products just described (SBDR, BIDR, and supplement files). The USGS cartographic system Integrated Software for Imagers and Spectrometers (ISIS) is used for this processing, augmented by the commercial stereoanalysis package Softcopy Exploitation Toolkit (SOCET SET) for production of stereo topographic maps. A total of eight DMP data sets are produced, as shown in [Table 4-4](#). The Global Radiometry Data Record (GRDR), Global Scatterometry Data Record (GSDR), Global Topography Data Record (GTDR), and Mosaicked Image Data Record (MIDR) products are mosaics of data from multiple observation segments. The Pass Radiometry Data Record (PRDR), Pass Scatterometry Data Record (PSDR), and Repeat Image Data Record (RIDR) products have a separate set of files for each segment. Stereo DTM products are derived from pairs of such segments. These are indicated by flyby number TXXX and segment number SXX in the PRODUCT\_ID and file name. Segments during which SAR or HiSAR data were obtained are numbered identically to the BIDRs ([Section 4.2](#)); non-SAR/HiSAR segments are assigned higher numbers. Note that the DMP SIS uses the term “sequence” to denote observation segments. These sequences should not be confused with the sequences for commanding the instrument ([Section 2](#)).

Table 4-4. Cassini RADAR Digital Map Products.

DATA SET ID	CODMAC LEVEL	DESCRIPTION
CO-SSA-RADAR-5-GRDR-V1.0	5	Mosaicked or modeled multipass radiometer data
CO-SSA-RADAR-5-GSDR-V1.0	5	Mosaicked multipass scatterometer data
CO-SSA-RADAR-5-GTDR-V1.0	5	Mosaicked altimetric and SAR topographic data
CO-SSA-RADAR-5-MDIR-V1.0	5	Mosaicked multipass SAR image data
CO-SSA-RADAR-5-PRDR-V1.0	5	Calibrated and gridded single-pass radiometer data
CO-SSA-RADAR-5-PSDR-V1.0	5	Calibrated and gridded single-pass scatterometer data
CO-SSA-RADAR-5-RIDR-V1.0	5	Coregistered multilook SAR image sets
CO-SSA-RADAR-5-DTM-V1.0	5	Digital Topographic Models

The majority of the DMP data sets include, in addition to a primary product (e.g., for the PSDR and GSDR a map of NRCS measured by the scatterometer), associated data products showing the variation of related parameters (e.g., incidence angle, resolution, and so on). The purpose of these products is to make as much of the information in the BIDs and especially the BODPs accessible to the research community in a simple and straightforward map format, obviating the need to understand and process the lower-level products.

The contents of the eight DMP data sets are summarized below.

#### 4.4.1 *Pass Radiometry Data Records (PRDRs)*

Each PRDR is a global map of Titan in equirectangular (cylindrical) projection containing in gridded form the brightness temperature of the surface (or associated information) based on each Titan flyby. PRDRs are provided for the scatterometry, altimetry, and SAR data, as well as for radiometry-only scans. Each PRDR brightness temperature map is produced in three forms (calibrated antenna temperature, antenna temperature with sidelobe contributions subtracted, and sidelobe-corrected temperature normalized to standard viewing geometry of normal incidence and corrected for the variation of physical temperature with latitude and season [see [Section 5](#)]) and is accompanied by companion files in identical map projection, indicating respectively the resolution (beam footprint diameter at 3 dB power contour), emission angle, polarization angle, and ground azimuth angle at which each observation in the map was obtained. See Figure 4-4 for examples.

*4.4.1.a. Radiometry Summary Files.* The calibrated antenna temperatures represented in the “PRU” files of the PRDR data set (first row in Table 4-7) are taken from the BODP, along with the geometric information needed to rasterize them. The sidelobe-subtracted temperatures used for the “PRS” files (second row) and the temperatures corrected for observation geometry and physical temperature used for the “PRF” files (third row) are computed in the calibration and modeling process described in [Section 5](#) ([Janssen et al. 2016](#)). These quantities are documented in “radiometry summary files” produced by the calibration software. Because these files were defined too late to be included in the archive as formal PDS products, they have been included under the EXTRAS directory of the DMP archive.

The format of the radiometry summary files is simple. A text file (file extension .txt) is supplied for each Titan flyby in which radiometry data were collected. The file names vary slightly in format but always begin with the character “t” followed by the number

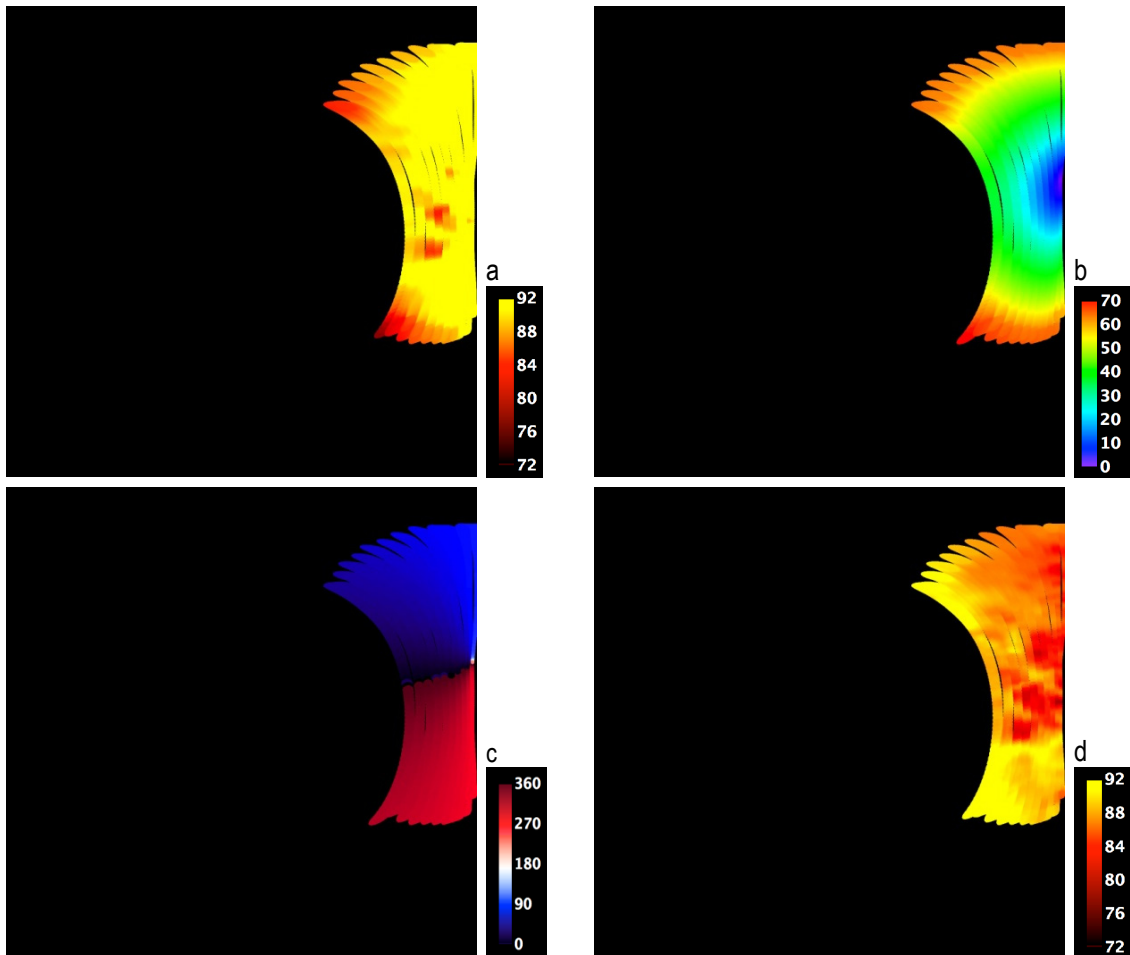


Figure 4-4. Examples of PRDR products: (a) sidelobe-corrected brightness temperature, (b) emission angle, (c) polarization angle, and (d) brightness temperature, corrected to normal incidence, based on emission and polarization angles. All products contain data from Ta segment S04 and show the Saturn western hemisphere (latitude  $-90^{\circ}$  to  $90^{\circ}$ , longitude  $0^{\circ}$  to  $90^{\circ}$ W) in equirectangular projection with north at top. Note that these color figures and those below are derived from the DMPs for illustrative purposes. The actual DMPs are raster maps of floating-point or integer data, not color images.

(or letter, for TA) of the flyby, with no leading zeroes. The first line of the file contains an integer indicating the number of bursts with radiometry data, which is the number of lines in the remainder of the file. The remaining lines each contain four comma-separated values: the burst ID (corresponding to that in the BODPs, thus allowing the files to be joined to the BODP data burst by burst), the calibrated temperature, the sidelobe-subtracted temperature, and the temperature corrected for angular, latitudinal, and seasonal effects. The first value is an integer, and the remainder are floating-point decimal numbers expressed as text.

Where temperature values cannot be calculated, the flag value -999 is used. In particular, the sidelobe calibration of bursts in SAR observations was performed

separately from the software that created the summary files, so the sidelobe-subtracted temperatures are not given for these bursts. However, the fully corrected temperatures (in the final column of the file) are present for SAR segments. A text file, `RADIOMETRIC_DATA_ADDENDUM.txt`, which summarizes the generation and content of the files, is included in the same directory.

#### 4.4.2 *Pass Scatterometry Data Records (PSDRs)*

The PSDR resembles the PRDR in format and also contains gridded data for a single segment of one Titan flyby. The primary mapped quantity in the PSDR, however, is NRCS, which is provided in three forms analogous to those used for BIDR products (calibrated data, data normalized to standard viewing geometry, and normalized data converted to 8-bit integer form with a logarithmic scaling). Real-aperture cross-section values are measured during altimetry and SAR as well as scatterometry mode operation of the RADAR, and PSDRs are provided for all three active modes. As for the PRDR, the PSDR includes maps of resolution and the emission, polarization, and azimuth angles (see Figure 4-5).

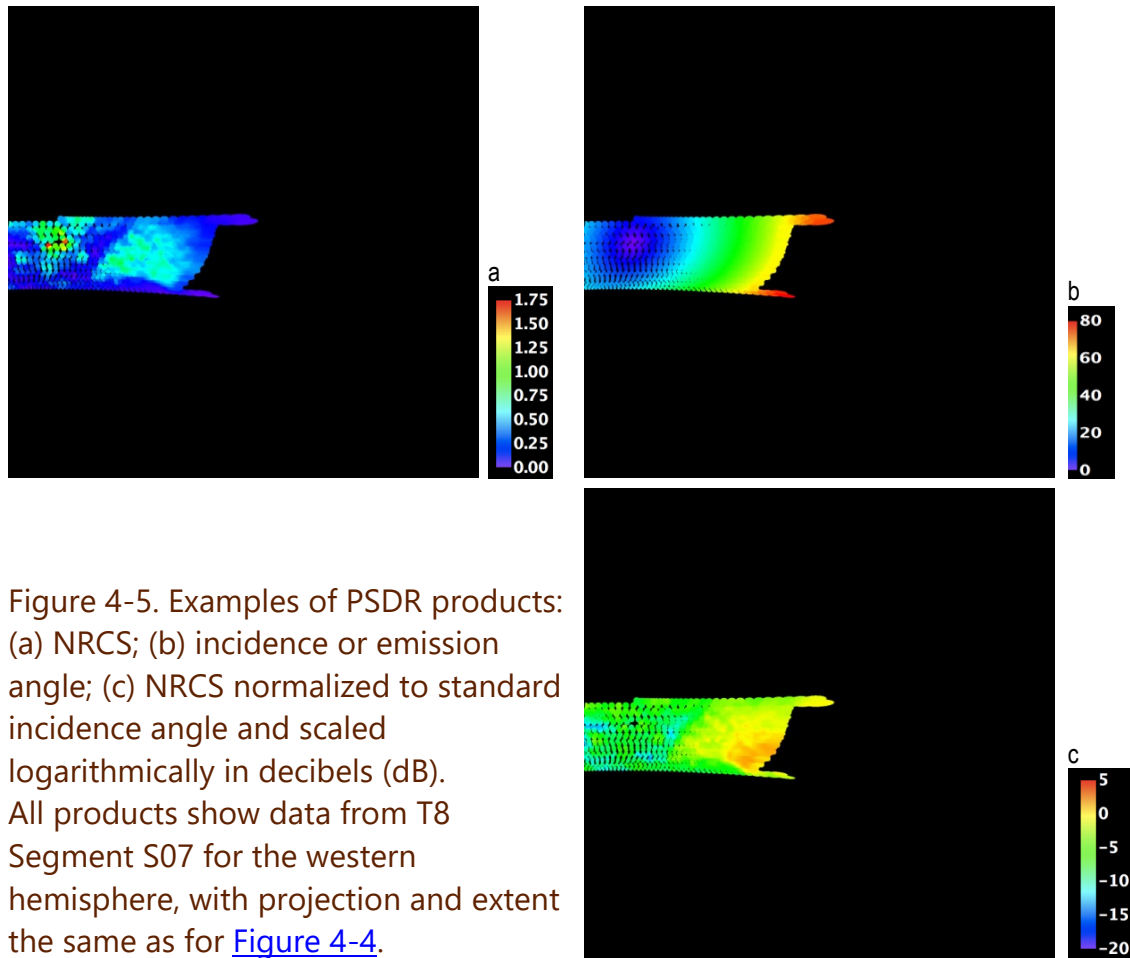


Figure 4-5. Examples of PSDR products: (a) NRCS; (b) incidence or emission angle; (c) NRCS normalized to standard incidence angle and scaled logarithmically in decibels (dB). All products show data from T8 Segment S07 for the western hemisphere, with projection and extent the same as for [Figure 4-4](#).

#### 4.4.3 *Global Radiometry Data Records (GRDRs)*

The GRDR is a mosaic of gridded radiometric brightness temperature data (corrected to normal emission) assembled from the complete set of individual PRDR products. Where data from multiple PRDRs are available at a given grid location, that with the

highest corresponding resolution (smallest footprint diameter) is selected. The GRDR includes maps of the resolution and emission, polarization, and azimuth angles for data used in the brightness temperature mosaic, as well as an index map from which it is possible to determine the PRDR from which any given pixel in the GRDR derives. Perhaps the most useful products in the GRDR data set are four additional maps produced by more sophisticated modeling of all available radiometry observations at each grid point, performed by CRST members at JPL ([Janssen et al. 2016](#)). These include a more accurate and detailed brightness temperature map than that obtained by mosaicking the PRDRs, maps of inferred dielectric constant and emissivity, and a map of volume scattering fraction. See Figures 4-6 and 4-7 for examples.

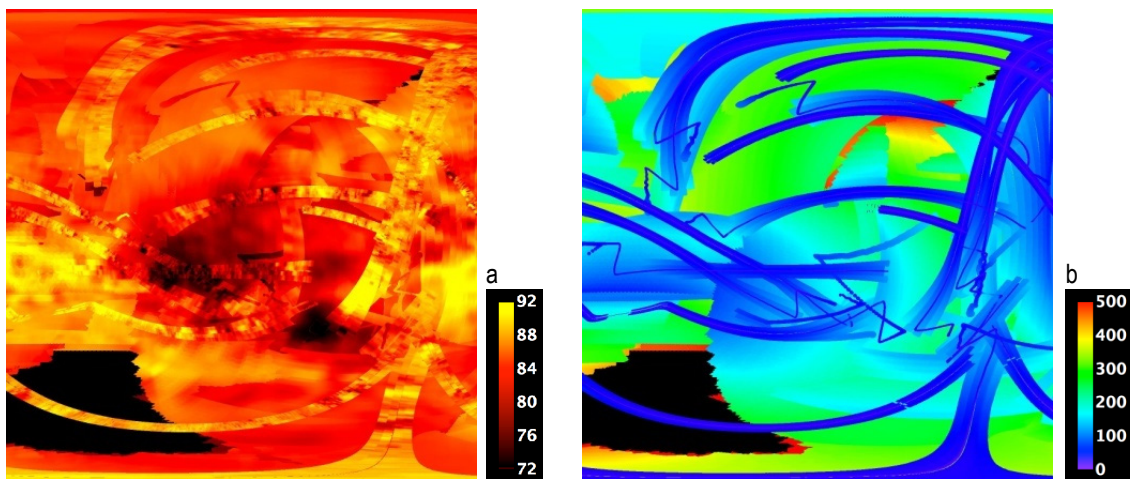


Figure 4-6. Examples of GRDR products produced by mosaicking: (a) normalized brightness temperature, produced as a mosaic of PRDR normalized temperature files with highest-resolution observations on top; (b) resolution (footprint diameter in km). Projection and extent as for [Figure 4-4](#).

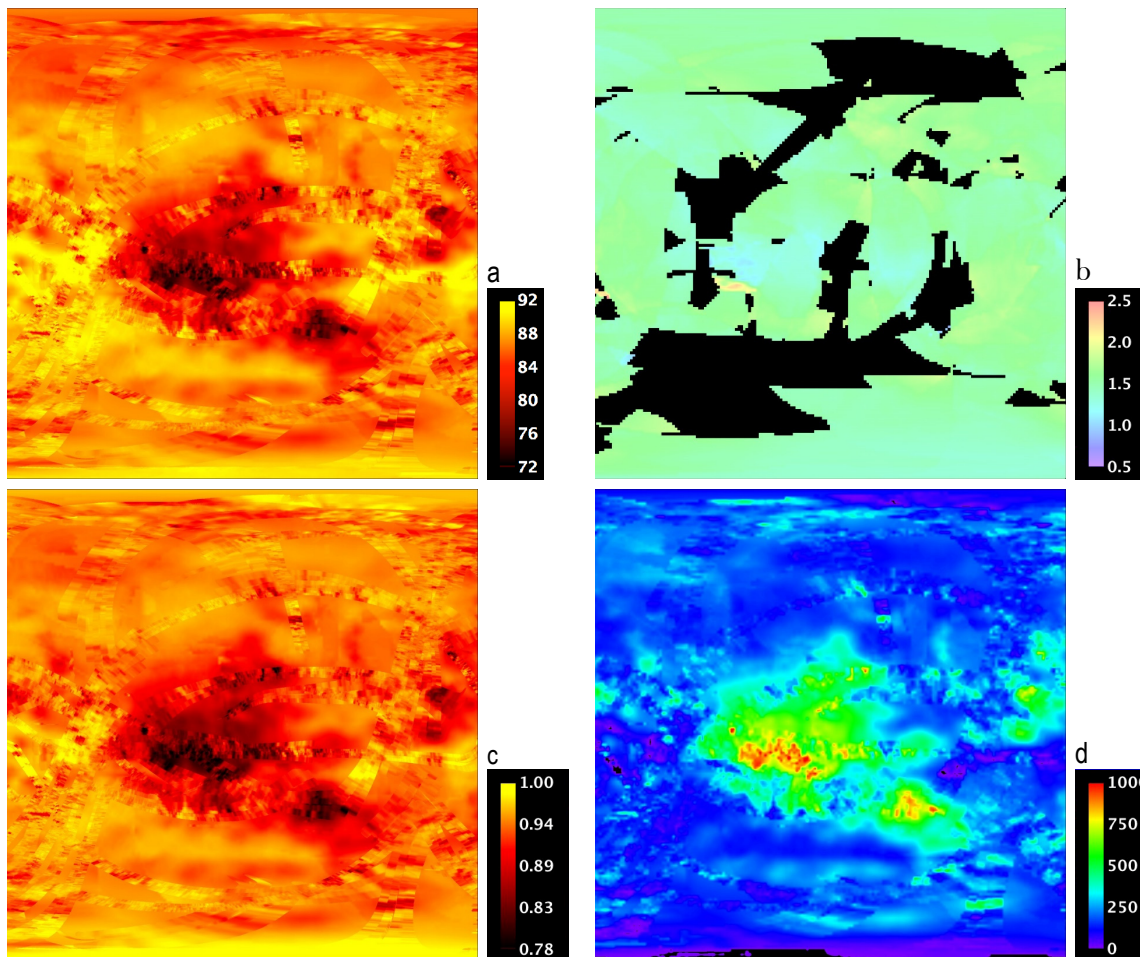


Figure 4-7. Examples of GRDR products produced by analysis of overlapping radiometry observations ([Janssen et al. 2016](#)): (a) normalized brightness temperature, (b) dielectric constant, (c) thermal emissivity, and (d) volume scattering fraction. Projection and extent as for [Figure 4-4](#).

#### 4.4.4 *Global Scatterometry Data Records (GSDRs)*

The GSDR is a mosaic of backscatter cross-section data (corrected to a reference incidence angle) assembled from the PSDRs by the same process used to generate the GRDR from PRDRs. It also includes maps of the resolution and the incidence, emission, and polarization angles of the included data and an index map showing the source PSDR for each pixel (see [Figure 4-8](#)).

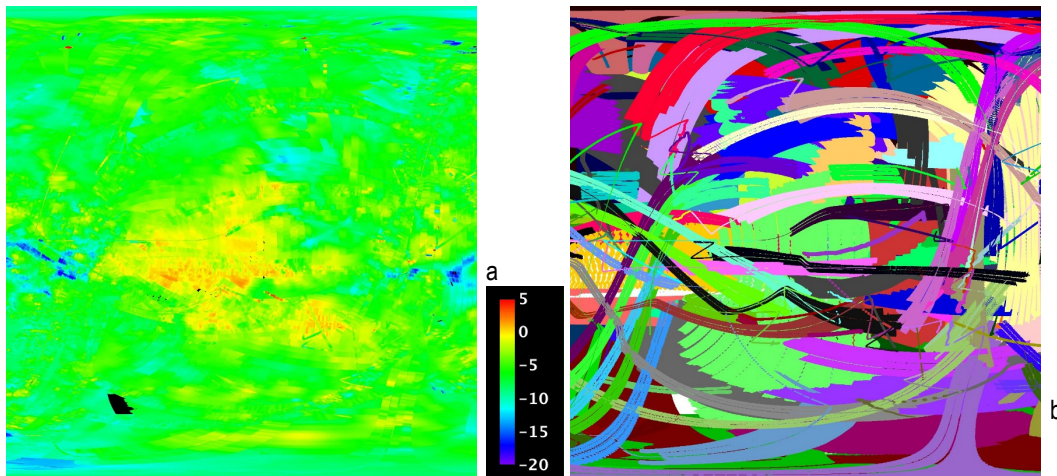


Figure 4-8. Examples of GSDR products: (a) NRCS scaled logarithmically to dB; (b) index map indicating the PSDR from which each pixel derives data by a unique numerical code value. Projection and extent as for [Figure 4-4](#).

#### 4.4.5 *Global Topography Data Records (GTDRs)*

The GTDR is a mosaic of absolute elevation values obtained on multiple Titan flybys. Pass-by-pass Pass Topography Data Records (PTDRs, equivalent to PRDRs and PSDRs) are not archived because the overlap between topographic observations from different flybys is extremely small. The GTDR contains both altimetric data and “SARTopo” elevations derived by monopulse analysis of overlapping beams in the SAR images. These data are contained respectively in an altimeter summary file and a SARTopo file produced by the RADAR engineering team at JPL. The altimeter summary files are part of the BODP archive and the SARTopo files are archived with the BIDs. See [Figure 4-9](#).

The primary GTDR file contains elevation values where altimeter or SARTopo measurements were made, and a special pixel value (“null” or “no data”) in all other pixels. The archive also includes files in which elevation values have been filled in at every pixel. These files are based on a variety of models: spherical and ellipsoidal shapes adjusted to fit the observed data, spherical harmonic fits of various orders to the data, and interpolation of the data. Only the interpolated version preserves the observed elevation values in those pixels where data were available. Finally, a file with values indicating the distance from each pixel to the nearest point with uninterpolated data is provided.

#### 4.4.6 *Mosaicked Image Data Records (MIDRs)*

Each MIDR is a mosaic of SAR image data assembled from the BIDs obtained on multiple Titan passes. MIDRs are archived at full resolution (in multiple quadrangles) and reduced resolutions (multiple quadrangles and a global map divided into files for the eastern and western hemispheres) as described in [Tables 4-2](#) and [4-3](#). Three complete sets of mosaics are produced: one containing data from the main full-resolution SAR swaths, one containing all other SAR segments (both start and end turns adjacent to main swaths and high-altitude SAR) and one containing all data. See [Figure 4-10](#).

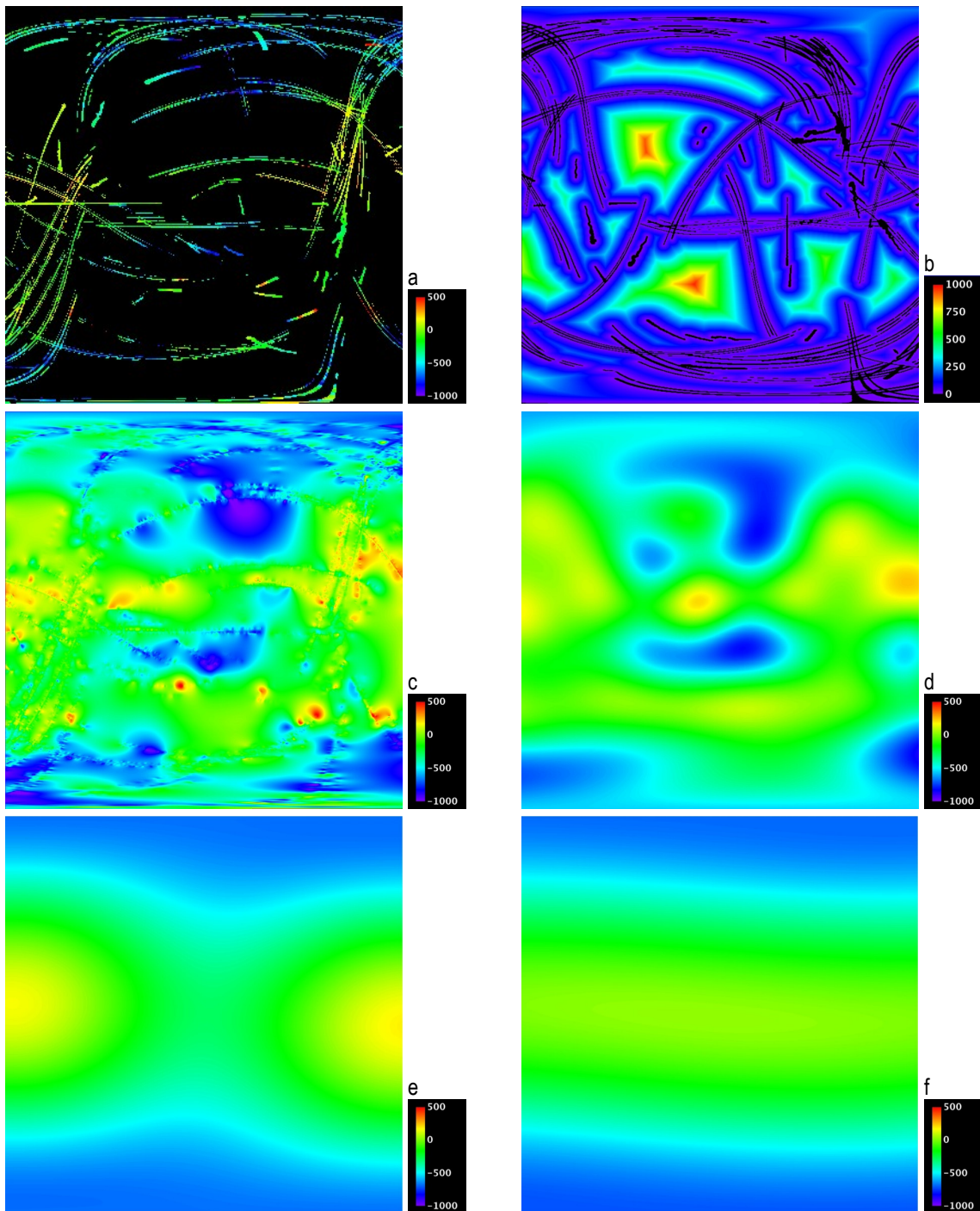


Figure 4-9. Examples of GTDR products: (a) gridded elevation (in m relative to 2575-km-radius reference sphere) as observed by altimetry & SARTopo; (b) distance to nearest uninterpolated observation in km; (c) interpolation from data ([Corlies et al. 2018](#)); (d) spherical harmonic fit to data with maximum degree & order 9; (e) best-fit triaxial ellipsoid with translation from center of mass & rotation; (f) best-fit biaxial ellipsoid (spheroid) with translation & rotation. Profiles in (a) have been broadened to at least  $0.5^\circ$  to ensure their visibility in this figure. GTDR products include a version at 32 pixels per degree, which resolves the actual width. Projection and extent as for [Figure 4-4](#).

4.4.7 Repeat Image Data Records (RIDRs)

The RIDR product is designed to facilitate comparison of overlapping (repeat) SAR image coverage. An RIDR set is produced for each of the 15 map quadrangles (Table 4-5, [Figure 4-10](#)). Every quadrangle contains coverage from two or more separate image files, each containing the SAR data from one of the overlapping BIDs, resampled to a common map projection and common extent. Files showing the emission (incidence) and spacecraft (hence viewing) azimuth angle for each BID are also provided. These can be used to model the stereo geometry and compute the expected vertical precision at each pixel, as discussed in [Section 8.2](#). Files showing the polarization angle are also included, enabling scatterometric modeling. RIDRs are produced in equirectangular and polar stereographic projections, with the same quadrangle divisions as for MIDRs (Table 4-5). Table 4-6 shows data types of Cassini DMPs at various scales.

Table 4-5. Extents of Cassini RADAR Digital Map Product quadrangles.

QUADRANGLE	CENTER LON	CENTER LAT	LON RANGE	LAT RANGE
00N090	90°	0°	0° to 180°	-90° to 90°
00N270	270°	0°	180° to 360°	-90° to 90°
78N180	0°	77.75°	0° to 360°	65.5° to 90°
43N045	45°	43.5°	0° to 90°	21.5° to 65.5°
43N135	135°	43.5°	90° to 180°	21.5° to 65.5°
43N225	225°	43.5°	180° to 270°	21.5° to 65.5°
43N315	315°	43.5°	270° to 360°	21.5° to 65.5°
00N036	36°	0°	0° to 72°	-21.5° to 21.5°
00N108	108°	0°	72° to 144°	-21.5° to 21.5°
00N180	180°	0°	144° to 216°	-21.5° to 21.5°
00N252	252°	0°	216° to 288°	-21.5° to 21.5°
00N324	324°	0°	288° to 360°	-21.5° to 21.5°
43S045	45°	-43.5°	0° to 90°	-65.5° to 21.5°
43S135	135°	-43.5°	90° to 180°	-65.5° to 21.5°
43S225	225°	-43.5°	180° to 270°	-65.5° to 21.5°
43S315	315°	-43.5°	270° to 360°	-65.5° to 21.5°
78S180	0°	-77.75°	0° to 360°	-90° to -65.5°
90N000	0°	90°	0° to 360°	56° to 90°
90S000	0°	-90°	0° to 360°	-90° to -56°

Table 4-6. Data types<sup>1</sup> of Cassini Digital Map Products at various scales.

PRODUCT	PIXELS/DEGREE				
	2	8	32	128	256
PSDR, PRDR, GSDR, GRDR, GTDR <sup>2,3</sup>	8	8, 32			
Emission, polarization, azimuth, and resolution maps for above <sup>2</sup>		32			
Index maps for GSDR, GRDR <sup>2</sup>		16			
MIDR, global format in 2 hemispheres	8	8	8, 32		
MIDR, 15 quad format <sup>3</sup>		8	8	8, 32	
Products including "main swath" SAR data (TjijS01 BIDRs)					
RIDR <sup>2</sup>			8	8, 32	8, 32
DTM, radar-stereogrammetric			8, 32		
DTM, radarclinometric				8, 32	
Products including only non-main-swath BIDRs					
RIDR <sup>2</sup>			8	8, 32	

<sup>1</sup> 8 = 8-bit (byte) unsigned integer; 16 = 16-bit LSB integer; 32 = 32-bit PC real.

<sup>2</sup> Uninterpolated GTDR data are also provided at 32 pixels/degree to resolve the width of elevation profiles.

<sup>3</sup> Including polar regions in polar stereographic projection.

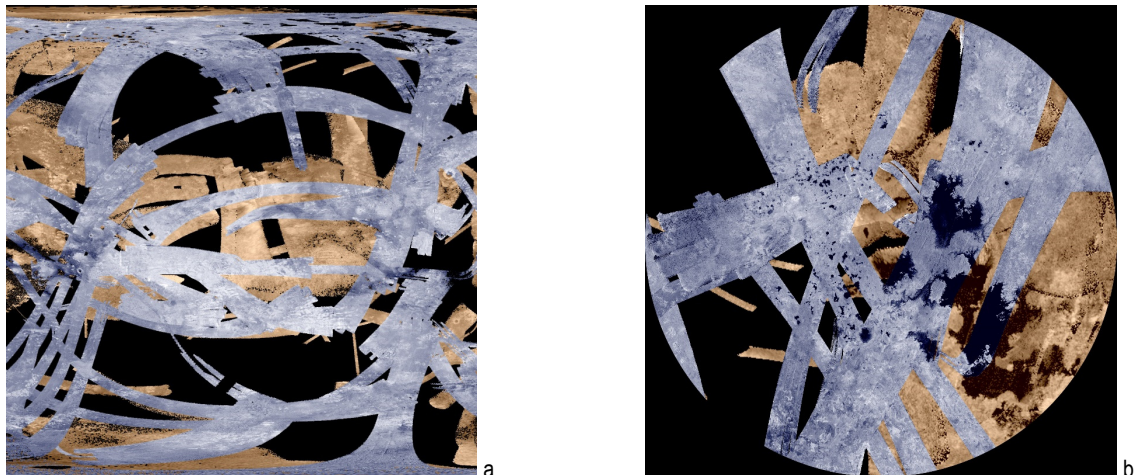


Figure 4-10. Examples of MIDR products: (a) "global" (western hemisphere) map, with projection and extent as for [Figure 4-4](#); (b) north-polar quadrangle of higher-resolution regional map set in polar stereographic projection. Latitude range 60'–90°N, 0° W longitude is at bottom. Data from SAR main swaths are shown here in blue tint; data from other, generally lower-resolution swaths are shown in brown tint to distinguish them. The actual MIDR products consist of separate mosaics of these two types of data plus a combined mosaic, all presented without color.

#### 4.4.8 Digital Topographic Models (DTMs)

DTMs can be generated wherever suitable data are available (Figure 4-11; [Kirk and Howington-Kraus 2008a](#), [Kirk et al. in prep](#), as well as other Kirk et al. publications in [Appendix 1](#)). Some DTMs are produced by radar-stereogrammetric analysis of overlapping SAR image pairs. Production of other DTMs by radarclinometric (shape-

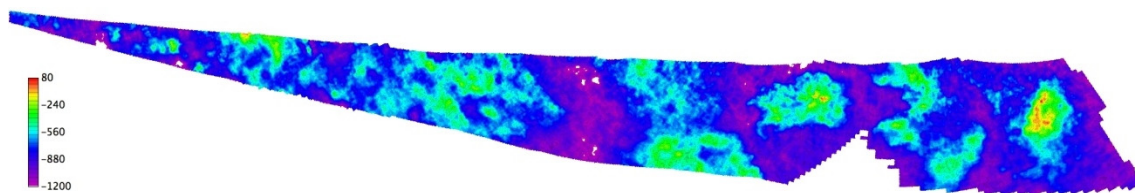


Figure 4-11. Example of a DTM. Color-coded elevation values are shown for the overlap between the northern ends of the T25 and T28 SAR strips, covering the area adjacent to and partly overlapping Kraken Mare. Polar stereographic projection is used, with north approximately at top (the figure has been rotated to fit conveniently on the page).

from-shading) analysis of portions of individual images was planned, but in practice no DTMs were made this way because Titan's surface was not sufficiently uniform in its radar properties for the method to be used. Each DTM is a gridded data product containing absolute or relative elevation values. Stereo DTMs are produced in equirectangular or polar stereographic projection, depending on latitude. Radarclinometric DTMs are archived both in the oblique cylindrical projection of the source BIDR and in either equirectangular or polar stereographic projection.

#### 4.4.9 PDS Label Format for DMPs

All RADAR DMPs are archived as binary files, the initial record of which is a PDS label. Each DMP will be assigned a string that uniquely identifies the type of data product, bit type, resolution, location of the data on Titan, and (where applicable) input data set. This string will be used both as the value of the `PRODUCT_ID` keyword in the PDS labels and, with extension ".IMG" as the filename for that product. Table 4-7 lists the primary and supplementary products for each type of DMP, along with the first three letters of the file name, which uniquely identify them, the data set variable (listed in the catalog files in the DMP archive volume) and data type. The data type descriptors (third character) were assigned with the intent to make them mnemonic and to avoid using the same character for different variables in different DMPs, but as the list of products was expanded the two criteria could not always be met simultaneously. For a full description of the DMP file-naming convention, see [Appendix 8](#). File information in the label includes image dimensions, bits/pixel and precise pixel type, and location of image in the file. Map projection information includes planet name and radii, projection, scale, parameters (e.g., rotations for oblique projection), latitude-longitude extent, and offset of projection center relative to file boundaries. Source data information includes spacecraft, instrument names, input data time/clock range, input product names, data set name, physical units, scaling to data number, processing institution and processing date.

#### 4.4.10 Validation and Archiving of DMPs

DMPs will be validated for both scientific integrity and compliance with PDS standards. Validation is the responsibility of the Cassini Science Archive Working Group Data Validation Team and the CRST. Further details of the labels and processing conducted on these data can be found in the DMP SIS.

Table 4-7. Primary and supplementary mapped quantities for Cassini DMPs.

DATA SET	PRODUCT ID BEGINS WITH	DATA SET VARIABLE <sup>1</sup>	DATA TYPE <sup>2</sup>	DESCRIPTION AND SOURCE
PRDR	PRU	T_B	32	Calibrated antenna temperature, K (BODP antenna_temp)
	PRS	T_B	32	PRU values with antenna sidelobe contributions subtracted (Radiometer Summary File antenna_temp_sidelobe_corr)
	PRF	T_B	32	PRS values, corrected to normal emission by Fresnel formula
	PRB	T_B	8	PRF values scaled linearly to 8 bit range
	PRE	EMA	32	Emission angle, degrees (BODP pass_emission_angle)
	PRP	POL	32	Polarization angle, degrees, between electric vector of received signal and plane containing emission direction and local vertical (BODP pass_pol_angle)
	PRZ	AZI	32	Azimuth angle, degrees, between projection of emission direction onto ground and north (BODP pass_azimuth_angle)
	PRR	RES	32	Resolution, km, defined as long axis dimension of beam footprint (BODP pass_major_width)
	PSDR	PSU	S_0	32
PSF		S_0	32	PSU value, normalized to reference emission angle by Titan backscatter model (BODP sigma0_corrected)
PSB		S_0	8	PSF value, scaled logarithmically (as dB) to 8-bit range
PSE		EMA	32	Emission angle, degrees (BODP act_emission_angle)
PSP		POL	32	Polarization angle, degrees, between electric vector of received signal and plane containing emission direction and local vertical (BODP act_pol_angle)
PSZ		AZI	32	Azimuth angle, degrees, between projection of emission direction onto ground and north (BODP act_azimuth_angle)
PSR		RES	32	Resolution, km, defined as long axis dimension of beam footprint (BODP act_major_width)
GRDR	GRF	T_B	32	As PRF
	GRB	T_B	8	As PRB
	GRE	EMA	32	As PRE
	GRP	POL	32	As PRP
	GRZ	AZI	32	As PRZ
	GRR	RES	32	As PRR
	GRI	IDX	16	Index uniquely identifying the observation segment from which values at each pixel are derived (appears as OBSERVATION_SEQUENCE_INDEX in index files)
	GRH	T_B	32	Brightness temperature, K, corrected to normal emission, estimated by modeling all available radiometric observations
	GRG	T_B	8	GRH values scaled linearly to 8-bit range
	GRD	DIE	32	Dielectric constant, estimated by modeling multipolarization radiometric observations, unitless
	GRC	DIE	8	GRD values scaled linearly to 8-bit range
	GRV	VOL	32	Fractional contribution of volume scattering, estimated by modeling all available radiometric observations, unitless
	GRW	VOL	8	GRV values scaled linearly to 8-bit range
GSDR	GSF	S_0	32	As PSF
	GSB	S_0	8	As PSB
	GSE	EMA	32	As PSE
	GSP	POL	32	As PSP
	GSZ	AZI	32	As PSZ

DATA SET	PRODUCT ID BEGINS WITH	DATA SET VARIABLE <sup>1</sup>	DATA TYPE <sup>2</sup>	DESCRIPTION AND SOURCE
	GSR	RES	32	As PSR
	GSI	IDX	16	As GRI
GTDR	GTF	ELE	32	Elevation, m, relative to reference sphere of 2575 km radius (ABDR Summary File MLE surface height or SARTopo File Elevation)
	GTB	ELE	8	GTF value scaled linearly to 8-bit range
	GTn	ELE	32	Model fit to data in GTF: spherical harmonic expansion of degree and order n = 0, 1, ..., 9
	GTI	ELE	32	Data in GTF filled by interpolation
	GTJ	ELE	8	GTI value scaled linearly to 8-bit range
	GTD	DST	32	Distance to nearest elevation observation in km
	GTS	ELE	32	Model fit to data in GTF: sphere with 3D translation
	GTT	ELE	32	Model fit to data in GTF: triaxial ellipsoid with 3D translation and rotation
	GTU	ELE	32	Model fit to data in GTF: triaxial ellipsoid with 3D translation
	GTV	ELE	32	Model fit to data in GTF: triaxial ellipsoid, no translation or rotation
	GTX	ELE	32	Model fit to data in GTF: biaxial ellipsoid with 3D translation, 2 rotation angles
	GTY	ELE	32	Model fit to data in GTF: biaxial ellipsoid with 3D translation
	GTZ	ELE	32	Model fit to data in GTF: biaxial ellipsoid, no translation or rotation
MIDR	MIF	S_0	32	Backscatter cross section corrected for additive noise and normalized to reference emission angle by Titan backscatter model, unitless, in physical (linear) scale (BIDR BIF pixel value)
	MIB	S_0	8	MIB value, scaled logarithmically (as dB) to 8-bit range
RIDR	RIS	S_0	32	Backscatter cross section corrected for additive noise, unitless, in physical (linear) scale (BIDR BIS pixel value)
	RIF	S_0	32	As MIF
	RIB	S_0	8	As MIB
	RIE	EMA	32	Emission angle, degrees (BIDR BIE pixel value)
	RIP	POL	32	Polarization angle, degrees (BODP act_pol_angle)
	RIZ	AZI	32	Azimuth angle, degrees (BODP act_azimuth_angle)
DTM	DTF	ELE	32	Elevation, m—might be absolute referenced to 2575-km sphere (stereo) or relative (radarclinometry)
	DTB	ELE	8	DTF values scaled linearly to 8-bit range

<sup>1</sup> Value of DATA\_SET\_VARIABLE field of index files.

<sup>2</sup> Where 8 = 8-bit unsigned integer, 16 = 16-bit LSB integer, 32 = 32-bit PC real.

## 4.5 Versions of Data Products and Summary of Errata

Each volume in the PDS archive has an ERRATA.TXT file associated with it that lists any anomaly in the processing or archiving of that volume. This includes counterintuitive aspects of the nominal processing as well as any special processing that might have been done. This section summarizes the common aspects of the ERRATA.TXT files and describes the version numbers used for the volumes. For information specific to a given volume please see the ERRATA.TXT file archived with that volume.

### 4.5.1 Definition of Volume Versions

The volume version ID can be found in the VOLDESC.CAT file for each volume. It is also evident in the data filenames. For example, three different versions of the primary, uncompressed BIDR image for Titan pass TA have been archived:

- Version 1 is named BIFQI48N071\_D035\_T00A\_V01.IMG.
- Version 2 is named BIFQI49N071\_D035\_T00AS01\_V02.IMG.
- Version 3 is named BIFQI49N071\_D035\_T00AS01\_V03.IMG.

Version 1 was archived very early in the mission when Titan's obliquity was assumed to be zero and we had not yet considered the possibility of multiple imaging segments in a single flyby. The incorrect obliquity led to features being misregistered between passes with location errors greater than 10 km. Version 2 represented an early attempt to fix this problem using a Titan spin model that reduced misregistration error to less than 2 km but was not dynamically feasible and would have resulted in larger errors over a long-time baseline. Version 3 made use of a long-term, accurate spin model for Titan and had other improvements, including extra noise-characteristic backplane BIDR files, and SARTopo data. One easy way to tell if one has the latest version of Titan SAR data is to look for SARTopo files. SARTopo data have been delivered only once for each Titan SAR flyby and can be found in the DATA/STDR directory of each such volume. Older versions do not have this directory. Since SARTopo data are not always computable, especially for HiSAR-only passes, another test is to look for the presence of noise-characteristic BIDR backplane files in the DATA/BIDR directory with filenames that start with BID or BIX. These files were also delivered only once and are present for the latest version of all Titan SAR data volumes. Neither BID/BIX nor SARTopo files were produced for non-Titan flybys. Titan passes from TA up to T25 have all three versions, 1, 2, and 3. From T28 on, Version 1 was never produced. For later files, the distinction between Version 2 and Version 3 is more subtle. The very latest flybys (T108-T126) were archived only once and are labeled Version 2, but this is the latest (and only) version and includes the best Titan spin-model, SARTopo, and BID/BIX files. For all earlier Titan SAR flybys, Version 3 is the latest and preferred version.

For the four flybys of Enceladus (Volumes 207 and 232), Rhea (Volume 214), and Iapetus (Volume 143) for which SAR data were acquired, the only archived version is Version 2. These volumes do not have SARTopo or BID/BIX files, and of course since the target is not Titan, Titan's spin model is irrelevant.

Data Volumes without SAR data are all either Version 1 (very old data with bad Titan spin model) or Version 2 (latest preferred data). For non-Titan data, Version 1 is the only delivery for Volumes 156 and earlier because the spin model of Titan is irrelevant; but after Volume 156, all archived data is Version 2.

#### 4.5.2 *Errata Overview*

Each volume has an ERRATA.TXT file that describes all errors in its processing that were known when it was archived. In this section we describe the common items in ERRATA.TXT for all volumes and for three special categories: (1) distant observations, (2) volumes with Titan SAR data, and (3) non-Titan SAR volumes.

For all data volumes, the following statements apply.

1. The uncompressed data products have attached labels. Normally, a file that has been compressed with ZIP would have been generated without an attached label.
2. In the volume index table (INDEX/INDEX.TAB), double quotes enclose all the date/time values. Normally, PDS date/time values are not quoted, but quoting makes parsing easier for some applications.

3. The HTML documents in the DOCUMENT directory contain HTML character codes that, while all-ASCII, are not easily interpretable by someone who is reading the HTML documents as text documents. For example, “&#945;” represents the lowercase Greek character “alpha” and is rendered as such in a web browser. Equivalent and more legible character codes (e.g., “&#alpha;”) are available as of the HTML 4.0 specification but cannot be used here, as PDS requires HTML documents to comply with the HTML 3.2 specification.
4. The Cassini RADAR transition files (EXTRAS/CRT\_XXX\_Vxx.TAB) contain no information about ScanStart and ScanEnd transitions.
5. The science-data-quality flag specifies only the validity of the active and passive boresight geometry when the corresponding active or passive data valid bit is zero (valid). For example, if Bit 1 is set (invalid) then all the active boresight geometry is invalid even though Bits 7 and 8 might be zeroed.
6. Antenna temperature, brightness temperature, and receiver temperature are defined in [Janssen \(1993\)](#). The archived value in the SBDR and LBDR files gives uncalibrated antenna temperature in units of Kelvin. The best current algorithm for correcting the archived antenna temperatures is  $Ta_{corrected} = Ta_{archive} * (0.920 - 0.0041*(t - 1.90))$  where  $t$  = time in years and fractional years since 2004.0 (0 UTC on 1 Jan 2004) This algorithm is based on the radioastronomical flux scale at 2-cm wavelength by direct comparison of distant (unresolved) Titan measurements by the Cassini radiometer with Very Large Array (VLA) measurements of Titan reported by [Butler and Gurwell \(2004\)](#).
7. Ideally the calibrated antenna temperature is referenced to cold sky at 2.7 K, although no guarantee is made that this zero-level accounting has been correctly made. Also, the antenna temperature is not necessarily the brightness temperature seen in the main beam; e.g., there will be an offset if the sidelobes happen to fall on other than cold sky. The antenna pattern has low but significant gain at large angles from the boresight, which can introduce thermal power from other targets besides the intended target in the main lobe. In particular, there is an offset to be expected and accounted for when an extended source like Titan or Saturn is observed from a close distance. System gain is the quantity that multiplies the raw sky counts to convert to the uncalibrated Kelvin scale. Receiver\_temp is the receiver noise temperature  $T_r$  (comparison made at internal reference switch). The receiver temperature plus the antenna temperature is equal to the total signal (raw counts times system gain).
8. ant\_temp\_std is a measure of the RMS uncertainty of  $T_a$ , and is only an estimation. It is obtained as the standard deviation of  $T_a$  for three points,  $T_a(I-1)$ ,  $T_a(I)$ , and  $T_a(I+1)$ , and is a useful measure that identifies questionable data. For example, it gets large when the beam is sweeping across a brightness discontinuity.
9. Every volume from CORADR\_0144 to CORADR\_0229 has missing CUMINDEX entries for Iapetus\_049\_3.
10. The rot\_velocity\_target\_y field is incorrectly assigned in all Cassini RADAR SBDR, ABDR, and LBDR products, but the angular velocity vector of the spacecraft can be computed independently from the time series of the three spacecraft body frame axes, sc\_X\_target, sc\_Y\_target, and sc\_Z\_target.

11. The AAREADME file that is included as part of each PDS volume has a section addressing the version number of all the data products. The AAREADME file for flybys TA–T30 had erroneously reported that the volumes with `PRODUCT_VERSION_ID 02` for flybys T36–T77 represent products processed with the nonsynchronous pole, instead of reporting them as being processed by the synchronous pole. This comment is corrected in the AAREADME files in later flybys.
12. Active and passive boresight locations in the data correspond to the origin of the antenna pattern frames, not the centroids of the measurements. Using these locations as if they were centroids will mislocate scatterometer measurements by approximately 1/10 the resolution of the measurement. To geolocate the weighted spatial response of each measurement precisely, one must use the antenna patterns. One calibrates SAR latitude and longitude backplanes using the antenna patterns and locates them using the Doppler and range of each pixel.

For distant observations, the following statements apply. To determine if a given volume is “distant,” consult its `ERRATA.TXT` file.

1. The active-mode science-data segment fields in the SBDR and LBDR products are invalid and are flagged accordingly. Distant satellite observations do not generate burst-by-burst active-mode results. Instead, the science results for distant satellite observations are summarized in the `AAREADME.TXT` file in the top-level directory of the volume.
2. The user should be aware that the antenna main beam usually covers all or a significant fraction of the target body during distant satellite observations. The boresight geometry fields are of limited value since they apply only to the center of the antenna beam. In some cases spacecraft pointing-control puts the boresight off of the target, and these fields are then invalid.
3. The instrument is operating in a special mode for these datatakes. Multiple bursts in flight are used to accommodate the very high range to the target. This slightly alters the meaning of the active-mode geometry fields in the science data segment of the SBDR and LBDR files.

For volumes with SAR data, the following statements apply.

1. All BIDRs except for the byte-valued backscatter images (`BIB*.IMG`) were produced by JPL. The byte-valued backscatter images were produced by USGS. The USGS BIDRs have unit strings in their labels that are ALL CAPS. The other BIDRs have lowercase units. According to the PDS dictionary, both are acceptable.
2. Checksums were not computed for floating-point-valued BIDRs. The `CHECKSUM` keyword was assigned a zero value.
3. In the primary BIDR images a technique was used to remove systematic errors due to thermal noise and BAQ compression during downlink. The technique appears to have a slight negative bias for very low SNR, i.e., when the signal power is less than one tenth the thermal-noise power. Without noise subtraction, backscatter values are artificially high and always positive. With noise subtraction, negative values occur, both due to the aforementioned bias and due to residual random error. One produces byte-valued BIDRs by transforming all data to decibels by taking the logarithm and then multiplying

by 10. Data are clipped below a minimum value (typically -20 dB) determined by the OFFSET keyword in the attached label. All negative backscatter values or values below 0.01 (-20 dB) are assigned to the minimum pixel value. Anyone interested in viewing data below this threshold needs to use the REAL-VALUED backplanes.

4. The Beammask and Number of Looks BIDR backplanes have a value for SAMPLE\_TYPE="UNSIGNED INTEGER" instead of "UNSIGNED\_INTEGER." The user needs to fix this field before ISIS software ingests the value.
5. Even though radiometry measurements were made using all five beams during regular SAR segments, only Beam 3 brightness temperature results are archived due to calibration challenges of the other four beams.

For non-Titan volumes with SAR data the following statements apply.

1. For Iapetus, geolocation of the SAR imagery is performed on a sphere of radius 718 km. The actual shape of Iapetus is slightly nonspherical, with deviations up to 35 km from the nominal sphere. Geolocation for each pixel is performed by intersecting the equi-Doppler cone, a sphere of radius equal to the range centered at the spacecraft location, and the spherical surface of Iapetus. Location errors of approximately 40 km can occur due to the nonspherical shape of Iapetus. Spacecraft ephemeris information in the SBDRs and LBDRs, along with the correct shape model of Iapetus, could be used to correct the geolocation.
2. For Iapetus, the incidence-angle-corrected (BIF\*.IMG) BIDR file is not included because no reliable relationship between incidence angle and radar backscatter has been determined for Iapetus.
3. For Iapetus, the resolution of the BIDR files is 16 pixels/degree, unlike files for Titan flybys, which are typically 256 pixels/degree and 128 pixels/degree.
4. For Rhea and distant Enceladus (Volume 207), special calibration processing was required. In order to estimate the normalized backscatter cross section from the returned echo power in each SAR pixel, one must divide by the integral of the two-way antenna gain divided by the range to the fourth power. This integral is performed over the area on the surface for each SAR pixel. For nominal Titan SAR, pixels are small compared to the gain pattern and rectangular so that one can use a simple approximation without resorting to a full numerical integration. For Rhea and distant Enceladus, the full integration was performed for each pixel with a 500-m step size.
5. Geolocation on the surface of Rhea makes use of the nominal triaxial shape of Rhea (radx, rady, radz)=(767.2 762.5 763.1) km, rather than assuming a sphere, as was done for Titan. Nonetheless, in order to simplify the map projection, we projected the images onto a 764.2695-km-radius sphere, as described in the labels for each BIDR file. These coordinates are not the same as the triaxial nonstandard coordinates reported in the LBDR and SBDR files.
6. For Rhea, the correction used to remove incidence-angle variation in the BIF\*.IMG and BIB\*.IMG files was different from that used for Titan. Each pixel was multiplied by a function of incidence angle  $f(I)=1.6930/(2.15*\cos(I)^{1.45})$ .
7. For all observations archived after Dec 1, 2010 (i.e., all SAR data except Iapetus SAR), the geolocation code was modified to account for the effect of special

relativity on Doppler shift. Without this change, the SAR geolocation would have been in error by 1.5 pixels for Enceladus SAR. This error corresponds to three parts in one hundred thousand of the overall Doppler-shift of the echo. Such a high level of fidelity was not needed for previous volumes in which the geolocation error due to relativity was much less than a pixel width. Now that it has been implemented, we employ this correction for all observations even when the error is too small to be significant.

8. For Rhea and distant Enceladus (Volume 207), the `act_incidence_angle` parameter in the SBDR and LBDR was redefined to be consistent with the incidence angle used to compute the incidence-angle-corrected  $\sigma_0$ . The boresight incidence-angle value normally reported does not represent the wide range of incidence angles observed within the antenna footprint. Instead, an effective incidence angle is reported that is a weighted average of the incidence angles observed. It is weighted by the estimated distribution of the return energy over incidence angle.
9. For Rhea, pixels with SAR ambiguity contributions greater than 30% are marked as invalid. This includes pixels with contributions from so-called mirror ambiguities that share the same Doppler and range to target as the primary imaging area but come from opposite sides of the spacecraft velocity vector. Note in particular the invalid strip of data that bisects the image. This omission is similar to what has been done in the past for Titan observations, but differs from what was done for the single previously occurring Enceladus SAR observation (Volume 207).
10. For Enceladus Volume 207, the “noise subtraction” technique applied to remove systematic biases due to thermal noise and other effects differs from that used for Titan SAR observations. Because the geometry of this observation is at extremely long range and Enceladus is much smaller than Titan, the shape of the return echo in range and Doppler space differs dramatically from nominal Titan SAR data. The empirical model of the distortion of the signal due to downlink compression is not valid for this observation. For this reason only thermal noise subtraction was performed. An estimate of the thermal noise in each pixel due to 842 K of system noise temperature was subtracted from the images. The chosen noise temperature included 809 K due to the instrument and 33 K due to emission from Enceladus’s surface. Errors in this approach led to negative backscatter measurements for pixels at extremely large (>60-degree) incidence angles.
11. Geolocation on the surface of Enceladus makes use of the nominal triaxial shape of Enceladus (`radx, rady, radz`) = (256.6, 251.4, 248.3) km rather than assuming a sphere, as was done for Titan. Nonetheless, in order to simplify the map projection the images were projected onto a 252.1233-km-radius sphere as described in the labels for each BIDR file. These coordinates are not the same as the nonstandard triaxial coordinates reported in the LBDR and SBDR files.
12. For Enceladus, the correction used to remove incidence-angle variation in the `BIF*.IMG` and `BIU*.IMG` files was different from that used for Titan. Each pixel was multiplied by a function of incidence angle  $f(I)=2.9165/(3.71*\cos(I)^{1.46})$ .

13. For Enceladus Volume 207, because the nadir point is close to the top of the SAR images, pixels near the top of the images are elongated and might contain significant energy from the mirror (identical range and Doppler) regions on the other side of the nadir point. These pixels have been calibrated to account for their full extent on the surface, including the regions on both sides of nadir. Other pixels with significant ambiguous SAR energy were excluded. Mirror ambiguities were allowed because they are limited to the low-resolution region at the top of the image, and the backscatter values near nadir might be useful for scientific purposes, despite the ambiguity in their locations.
14. For Enceladus Volume 207, the three different imaging segments comprise data taken at slightly different times during Cassini's approach to Enceladus.
15. Altimetry data were acquired for some non-Titan targets, but no ABDR products were generated, and no height data are included in the SBDR and LBDR products. Raw altimeter echo data are available in the LBDR file.

The following statements apply to a few specific data volumes.

1. The last field of a few records in the ABDR SUMMARY file corresponding to Flybys T8 and T91 have unusually large numbers. The user should exclude these data points while using results from the ABDR SUMMARY file.
2. The submitted volume CORADR\_0143 has an erroneous INDEX and CUMINDEX entry for BIFQE10N073\_D143\_I049S01\_V02.
3. Volumes CORADR\_0265 and CORADR\_0266 have missing CUMINDEX entries for COARDR\_0035\_V03.

## 5 Calibration

This section briefly summarizes the techniques used to calibrate the various radar and radiometer data products. For a more complete description of the radar calibration see [West et al. \(2009\)](#). The discussion below is highly condensed from this reference. Also refer to [Wye et al. \(2007d\)](#) for a discussion of scatterometry calibration. Radiometer calibration is discussed thoroughly in [Janssen et al. \(2009, 2017\)](#).

Active-mode radar observations measure the level of backscattering from the target of interest, usually in NRCS (see [Section 3.1](#) and [Ulaby et al. 1982](#)). Normalization in this case means dividing out the projected area on the surface of the pixel or footprint of interest from the backscattering cross section that has units of area. The RADAR instrument measured received power ( $P_s$ ) which is converted to NRCS by the radar equation:  $P_s = X \sigma_0$ . Here, X includes terms such as the antenna gain, the range to the target, etc. The value of  $P_s$  is obtained by applying a receiver gain conversion constant (C) to the raw counts from the echo buffer (or from the SAR processing algorithm) converting them to units of power, and then subtracting an estimate of the noise power that corresponds to the measurement. The noise power ( $P_n$ ) is computed using an estimate of the receiver noise temperature ( $T_r$ ) applied to the measurement bandwidth (B):  $P_n = kT_r B$ .

Calibration of the active-mode radar data then consists of two main tasks. First the value of  $P_s$  is determined using the conversion constant and the receiver noise temperature. These vary with bandwidth and with the attenuator setting used in the observation. SAR processing used fixed values that were determined from post-launch engineering test measurements as described in [West et al. \(2009\)](#). Real aperture (scatterometer) results in the SBDR files are also computed using fixed values, except that the noise level is estimated directly from noise only data that is usually available in scatterometer observations (see [Wye et al. 2007d](#)). Second, the value of X is determined from the measurement geometry and some prelaunch values (peak antenna gain, attenuator setting values). The active-mode calibration is tied to the passive radiometer calibration through the receiver noise temperature which is used to set the conversion constant C when observing known reference sources. The same antenna gain pattern characteristics determined by the radiometer calibration (see [Janssen et al. 2009](#)) are applied to the active-mode calibration ensuring consistent active/passive calibrations.

The calculation of X includes the attenuator setting and any BAQ bias correction. Attenuation is set in the receiver chain to prevent saturation of the digital data, which are restricted to the range -127 to +128. For scatterometer measurements, attenuation is almost always set to 9 dB, which provides a reasonable range for the low-SNR signals commonly encountered in scatterometry. SAR and altimeter-mode data use an onboard algorithm called auto-gain to automatically step the attenuator in 2-dB increments until the digital data are comfortably in range. Auto-gain attenuator steps can occur on each instruction boundary, and this helps the instrument to follow unknown variation of the target reflectivity. In a few cases (e.g., T49), some altimetry data are still saturated because there was insufficient time or too few instructions to allow the attenuation to step quickly enough. A similar algorithm called auto-rad automatically adjusts the radiometer integration window length to avoid saturating the radiometer data. Auto-rad is always used for radiometry, except during SAR

imaging, where it is more important to keep the burst rate high. This requires setting a fixed radiometer integration window length that was selected to be 35 ms based on early analysis of system performance. Both attenuation settings and radiometer integration periods are reported in the downlinked telemetry and need to be included in active and passive calibration. SAR data (including high-altitude imaging scatterometry) usually used 8–2 BAQ to compress each 8-bit sample to 2 bits. The BAQ algorithm was designed for unity gain, but sometimes introduced a bias factor that needs to be corrected, as described in [West et al. \(2009\)](#).

The conversion constant,  $C$ , the receiver temperature,  $T_r$ , and the radar equation factor,  $X$ , are all subject to absolute and relative errors that constrain the error budget for  $\sigma_0$ . The overall 3-sigma absolute uncertainty for  $\sigma_0$  is about 1.3 dB. This uncertainty comes mainly from uncertainty in the transmit power (measured prelaunch at 48.1 W), and statistical uncertainty in the determined values of  $C$ . There are also relative errors, both statistical and systematic, of which the user should be aware. Systematic errors are lowest for scatterometry scans, where the relative error (3-sigma) is about 0.6 dB. In between Titan flybys, the systematic relative error is dominated by the uncertainty in  $C$ , which is 0.9 dB (3-sigma). Statistical uncertainties (denoted  $K_{pc}$ ) are usually lower than systematic uncertainties for real aperture observations. For SAR observations, however,  $K_{pc}$  errors can be much larger. In areas where both backscatter and number of looks are low, the statistical error can be many dB. Averaging pixels together can reduce such statistical errors, albeit at the expense of image resolution.

The absolute calibration of the RADAR radiometer antenna temperature measurements requires (1) an accounting for contributions from outside the main beam (the beam-pattern correction) to obtain brightness temperatures of the observed scene, and (2) a calibration of the radiant power received by the antenna and measured by the radiometer. A definition of terms used in microwave radiometry, along with the fundamentals of calibration, will be found in [Janssen \(1993\)](#). The calibration of the Cassini radiometer is described in [Janssen et al. \(2009\)](#). This was updated as described in [Janssen \(2016\)](#) using all the data acquired through the first ten years of the Cassini Mission. The state of the calibration through this period is summarized here. The PDS archive containing Cassini RADAR radiometer files is accompanied by documentation that includes periodic updates to the radiometric calibration factor.

The radiometer has obtained antenna temperature measurements on Titan, at varying angles of incidence and polarization, and at ranges from 1000 km to 100,000 km, in 280 individual observing segments obtained during 48 Titan flybys. Cassini imaged Titan's polarized emission at low resolution by scanning during that portion of selected Titan flybys where the range varied from about 30,000 to 100,000 km (see [Figure 3-2](#)). Maps of effective dielectric constant (equivalent dielectric constant of a nominal simple dielectric surface) were constructed from these measurements. The polarization allows all brightness measurements obtained from the antenna measurements to be referenced to their nominal values at normal incidence, which allows direct comparison with one another and the construction of an inferred normal-incidence brightness temperature map. Sidelobe contributions were accounted for sequentially from low to high resolution by constructing, at first, a very low-resolution map (range >50,000 km) where the antenna beam was sufficiently well known to correct for the sidelobe contributions, and then using this map as a base onto

which successively higher-resolution data were added. Simultaneously, a one-dimensional sidelobe pattern was iteratively determined. The pattern was used to compute and remove sidelobe contributions and then adjusted to minimize the residuals in fitting higher-resolution segments to the accumulating map. Figure 5-1 shows the resulting beam pattern and residuals.

The intrinsic noise in individual antenna temperature measurements is about 0.1 K, insignificant in the present context. By comparing the variation in normal-incidence brightness temperature among measurements in different segments at the same locations on Titan, we evaluated the final residual systematic errors incurred in the map mosaicking process to be about 1 K. As part of the mosaicking process we also solved for the seasonal variation of physical temperature with latitude, which we found to be smaller by a factor of  $0.87 \pm 0.05$  in relative amplitude compared to that reported

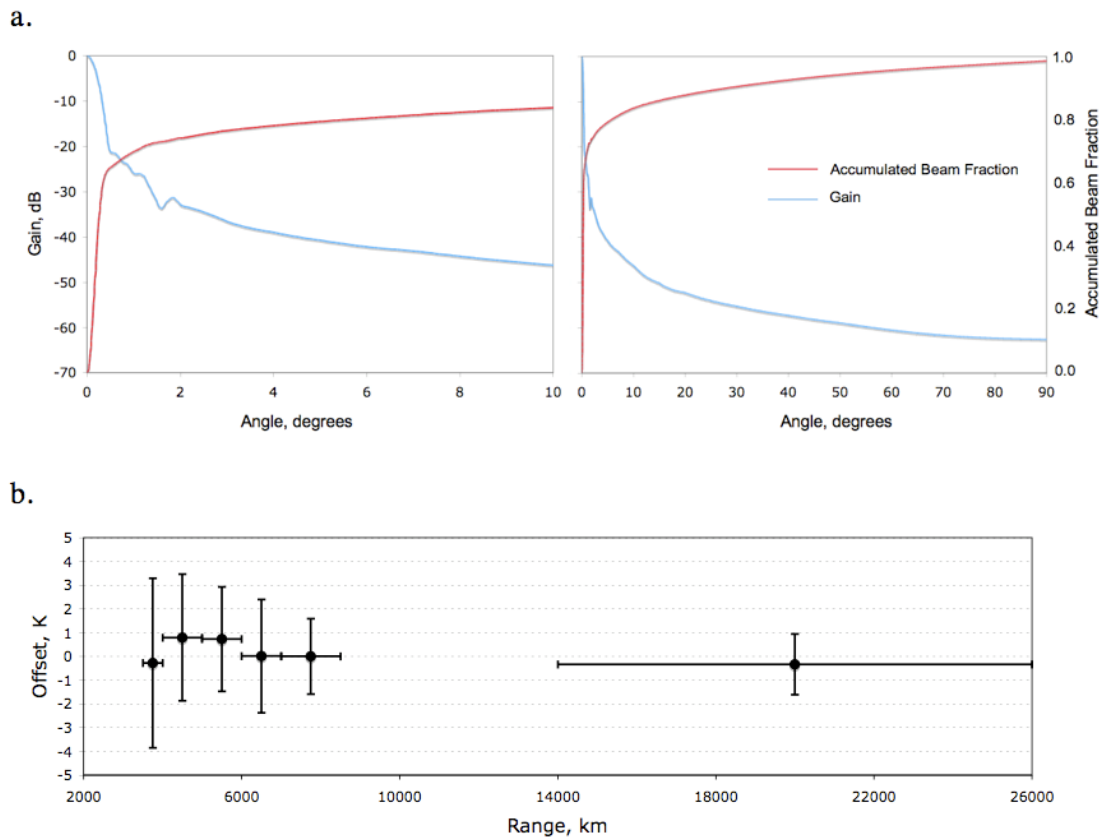


Figure 5-1. (a) The radiometer beam gain determined in the mosaicking process used to obtain the global map shown in [Figure 4-3](#). The full two-dimensional beam shape was determined inside  $2^\circ$  from Sun scans, and the more distant sidelobes were solved for by assuming azimuthal symmetry in the minimization of residuals in the construction of the brightness mosaic. (b) Residuals in the mosaicking process after fitting a one-dimensional far sidelobe pattern. The individual segments were given a final offset adjustment to best fit the accumulating map, so that the residual point-by-point systematic errors are much fewer than those in the figure.

in the thermal infrared by Cassini's Composite Infrared Spectrometer (CIRS). We used the equatorial temperature obtained by the Huygens probe and the seasonal dependence with latitude from CIRS to convert the brightness mosaic to absolute emissivity, from which we could infer global thermophysical properties of the surface in combination with the dielectric mosaic. In the fitting process, we also obtained a small linear gain drift for the ten years of observation.

The absolute calibration is thus obtained using Titan itself. Originally we took the Huygens probe surface-temperature measurement of 93.6 K near the equator as our calibration temperature reference, using a model for the equator-to-pole temperature gradient to extend this temperature to the globe, assuming no day-to-night or other systematic temperature variations. At present we use the CIRS results for surface-temperature distribution ([Jennings et al. 2009](#)), a practice that eliminates many of the uncertainties in this procedure. Knowledge of the surface temperature distribution and its variation with time allows us to establish a seasonally varying absolute brightness map once we establish a time-invariant emissivity reference on Titan's surface. There are in fact two areas on Titan that have well-understood thermoelectric properties and can serve as emissivity references: (1) the dune fields, and (2) Titan's seas, both of which can be argued to have an emissivity of about 0.98 based on a combination of supporting radar, radiometric polarization, and Visible and Infrared Mapping Spectrometer (VIMS) data. As illustrated in Figure 5-2, the observed brightnesses of

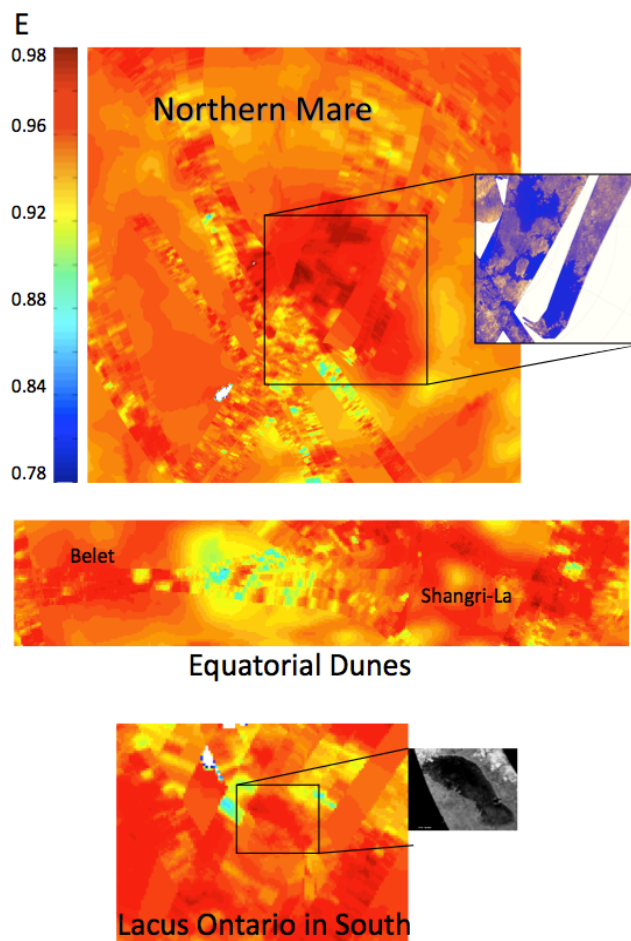


Figure 5-2. Absolute emissivity maps in the vicinity of the equatorial dunes (center panel), seas in the north (top panel), and Ontario in the south (bottom panel). The dielectric constant of both the dunes and the methane seas ( $\sim 1.7$ ) yields an emissivity of 0.98 with a small uncertainty, providing a consistent case for the absolute calibration of the Titan brightness map to about 1 K.

the dunes and the seas in both the north and south yields a consistent story for the absolute calibration.

The highlight of [Jansen 2016](#) was the inference of global features of the surface and subsurface of Titan sampled by the microwave thermal emission. We see strong evidence for subsurface (volume) scattering as a dominant cause of the radar reflectivity in bright regions, and elsewhere a surface composition consistent with the slow deposition and processing of organic compounds from the atmosphere. The presence of water ice in the near subsurface is strongly indicated by the high degree of volume scattering observed in radar-bright regions (e.g., hummocky/mountainous terrains) constituting  $\sim 10\%$  of Titan's surface. A thermal analysis allowed us to infer a mean 2.18-cm emission depth in the range 40–100 cm for the dominant radar-dark terrains (the remainder of Titan's surface) at all latitudes of Titan, consistent with the deposition and possible processing and redistribution of tholin-like atmospheric photochemical products.

A final note on calibration: Cassini RADAR observed the Coastal South Pacific and parts of southern Brazil during the Earth flyby on Aug 18, 1999. These uncalibrated data were delivered to PDS in Volume 3. While it might be tempting to look at these data for calibration purposes, there are a number of issues that make this difficult. The RADAR system was not warmed up for this observation, and the operating temperatures were quite different from the observations in the Saturn system. The spacecraft flew through Earth's shadow during this observation, and temperatures of many components varied significantly. The resistive load and noise diode data channels, which are normally used to normalize out such temperature variations, were completely saturated due to a command error and therefore useless for calibration. The number of pulses transmitted was greater than the receive window length to accommodate range variation; therefore, there are no noise-only intervals available to estimate the noise floor. Finally, all the data were obtained while pointing at the Earth—none were obtained on cold sky, as was normally done in the Saturn system—and this makes it difficult to calibrate the passive radiometry data.

## 6 Titan SAR Swath Summary

[Appendix 4](#) provides a summary of the SAR swaths, including date obtained, longitude and latitude range, incidence-angle range, and range and azimuth resolution. A brief description of the morphologic features within each swath is given below.

### 6.1 Swath Descriptions

*TA.* The TA pass consisted of inbound scatterometry and radiometry, INMS ride-along SAR, SAR imaging, followed by altimetry and outbound scatterometry and radiometry. The TA SAR swath crosses the mid-northern latitudes in an approximately E–W direction, from  $\sim 32^{\circ}\text{N}$ ,  $130^{\circ}\text{W}$  to  $53^{\circ}\text{N}$ ,  $10^{\circ}\text{W}$ . Ganesa Macula, radar-bright lobate features, and two circular features with associated lobate deposits are located in the swath. All of these features are interpreted to be superposed on the surrounding plains units ([Lopes et al. 2010](#)). Channels interpreted to be fluvial in origin also are located throughout the swath, along with small, isolated hills ([Elachi et al. 2005b](#), [Stofan et al. 2006](#)).

*T3.* T3 had inbound and outbound altimetry along with SAR imaging. The T3 SAR swath is located in the low northern latitudes in an  $\sim\text{E–W}$  direction, from  $3^{\circ}\text{S}$ ,  $0.4^{\circ}\text{W}$  to  $22.5^{\circ}\text{N}$ ,  $133^{\circ}\text{W}$  ([Elachi et al. 2006a](#)). Abundant dunes are located throughout the swath, along with two impact craters: Menrva ( $\sim 450$  km diameter,  $19.6^{\circ}\text{N}$ ,  $87.1^{\circ}\text{W}$ ) and Sinlap ( $\sim 70$  km diameter,  $11.3^{\circ}\text{N}$ ,  $16.1^{\circ}\text{W}$ ). The dune fields in T3 are superposed on both intermediate- and low-backscatter plains. Isolated hills are also seen in the swath between  $16$  and  $21^{\circ}\text{N}$  and  $39$  and  $54^{\circ}\text{W}$  and between  $1$  and  $11^{\circ}\text{N}$  and  $10$  and  $23^{\circ}\text{W}$ , with small, circular features of unknown origin near  $15^{\circ}\text{N}$ ,  $33^{\circ}\text{W}$ . Fluvial channels—including the wide anabranching network Elivagar Flunima and a few small features interpreted as cryovolcanic flows ([Lopes et al. 2007a](#))—are also seen. Principal results of T3 were discussed in [Elachi et al. \(2006a\)](#). An early discussion of Titan craters is in [Lorenz et al. \(2007\)](#).

*T7.* The plan for T7 was to collect inbound and outbound radiometry and altimetry, with SAR imaging. T7 SAR is a partial swath extending from  $31^{\circ}\text{S}$ ,  $23^{\circ}\text{W}$  to  $70^{\circ}\text{S}$ ,  $11^{\circ}\text{E}$ . Channels are ubiquitous throughout the swath, but are particularly concentrated in the intermediate to bright unit in the swath center that terminates abruptly into a relatively radar-dark unit. A circular feature in the eastern portion of the swath appears to be an eroded impact crater. Results of T7 and T8 are discussed primarily in [Lunine et al. \(2008\)](#).

*T8.* The T8 pass consisted of inbound radiometry, scatterometry, altimetry, and SAR imaging, and then outbound radiometry, scatterometry, and altimetry. The T8 SAR swath, covering the equatorial region, has closely spaced dunes that cover much of the swath and led to the secure recognition of these features (see, e.g., [Lorenz et al. 2006b](#)). Linear mountain ranges extend from  $13$ – $5^{\circ}\text{S}$  and  $198$ – $225^{\circ}\text{W}$  (see, e.g., [Radebaugh et al. 2008](#)). A few channels interpreted to be fluvial in origin are seen, as well as small, circular features of unknown origin. By design, T8 also imaged the Huygens landing site with RADAR for the first time.

*T13.* The T13 pass included HiSAR and SAR, along with outbound altimetry, scatterometry, and radiometry. The T13 SAR swath includes the central portion of Xanadu (from  $10^{\circ}\text{S}$ ,  $65^{\circ}\text{W}$  to  $12^{\circ}\text{S}$ ,  $170^{\circ}\text{W}$ ), essentially equatorial, like T8. The Xanadu radar-bright terrain has a “crinkled,” hummocky texture and a rugged surface

cut by channels, and is characterized by irregular but not regionally raised topography ([Radebaugh et al. 2010](#)). Some circular features within Xanadu might be eroded impact craters ([Wood et al. 2010](#)). The plains adjacent to Xanadu have abundant dunes. Also to the west of Xanadu is Guabonito, an 80-km-across possibly-eroded impact basin ([Wood et al. 2010](#), [Lopes et al. 2010](#)). A T13 HiSAR observation included the Huygens landing site.

*T15.* The T15 pass consisted of radiometry data collection and HiSAR data only.

*T16.* T16 had inbound radiometry, scatterometry, and altimetry; SAR; then outbound altimetry. The T16 swath, the first obtained in the north-polar region, has scattered lakes north of about 70°N ([Stofan et al. 2006](#), [Hayes et al. 2008a](#)). Some lakes are only partially filled with dark material interpreted to be liquid hydrocarbons ([Stofan et al. 2006](#), [Lopes et al. 2007b](#)), while other basin-shaped features without dark fill are interpreted as empty lakes (e.g., [Hayes et al. 2008a](#)). Channels are seen across the swath, along with some small hills, radar-bright patches. Dunes are located only at the southern end of T16.

*T17.* T17 was a SAR ride-along with INMS. T17 is a partial swath containing the impact crater Ksa (29 km) ([Wood et al. 2010](#)). The swath also covers part of the Fensal sand sea dunes (e.g., [Radebaugh et al. 2008](#)).

*T18.* T18 was an INMS ride-along, SAR only. T18 extends over the north-polar lakes area. The southern portions of the swath have mottled plains, few channels and no dunes.

*T19.* T19 had inbound and outbound radiometry, scatterometry, and altimetry, along with SAR imaging. The SAR swath extends from 2°S, 318°W to 42°N, 160°W, over the northern lake district. Bright, featureless patches occur throughout the swath, as well as dunes in the southernmost extent of the swath. Channels are seen throughout the region, particularly in association with the lakes. Some circular features of unknown origin are seen ([Wood et al. 2010](#)).

*T20.* The T20 pass consisted of HiSAR imagery and radiometry only.

*T21.* T21 was an INMS ride-along, with SAR, and outbound altimetry, scatterometry and radiometry. The T21 swath, 25°S, 290°W to 50°N, 195°W, is mostly characterized by dark, relatively featureless plains, scattered bright patches, dunes, and streaks. Linear mountains with interspersed dunes cover about half the swath. A number of circular features of unknown origin are defined by a faint bright ring ([Wood et al. 2010](#)).

*T23.* T23 SAR was accompanied by inbound and outbound altimetry, scatterometry, and radiometry. T23 contains a region of overlap with the TA swath, including Ganessa. Also in the swath are abundant dunes, channels, and hills, the northern part of a bright flow, and a partial circular feature with morphology similar to that of Guabonito.

*T25.* T25 was a full RADAR pass, with inbound and outbound radiometry, scatterometry, and altimetry, along with SAR imaging. The T25 SAR swath, located in the mid northern latitudes, has a possible cryovolcanic feature at 15°S, 40°W (Sotra Facula), surrounded by lobate deposits ([Lopes et al. 2013](#)). The swath is also characterized by linear hills surrounded by fields of dunes, and some circular features

that might be of impact origin ([Wood et al. 2010](#)). The swath covers part of the northern lakes region, including Mare Ligeia.

*T28.* T28 had inbound radiometry, scatterometry, and altimetry, SAR, then outbound altimetry. The SAR swath covers the northern lakes region, including the large seas. Near the seas, the plains are textured and cut by channels, while to the south the intermediate to dark plains have dune fields and streaks, small hills, and circular to oval bright rim features of unknown origin ([Lopes et al. 2010](#)). Significant overlap exists between T25 and T28, permitting stereo DEM generation ([Kirk and Howington-Kraus 2008a](#), [Kirk et al. in prep](#)). Lake-surface backscatter is discussed in [Notarnicola et al. \(2009\)](#).

*T29.* T29 was a full pass with inbound and outbound radiometry, scatterometry, and altimetry, along with SAR imaging. The T29 SAR swath covers terrain similar to the T25 and T28 swaths. It has dark to intermediate plains, some lakes, circular features of unknown origin, and fields of dunes at low latitudes.

*T30.* T30 was also a full pass, with inbound and outbound radiometry, scatterometry, and altimetry, along with SAR imaging. The inbound half of the pass was devoted to altimetry as it covered the previous SAR swaths T28 and T29. The long pass of altimetry not only provided unique height data, it also allowed diagnosing of some of the features of the altimetry measurement. A detailed discussion of altimetry observations is given in [Zebker et al. \(2009a\)](#). T30 SAR also imaged the north-polar seas (indeed, it was targeted specifically to observe Kraken Mare, initially suggested in ISS imaging). An inventory of lake/sea volume and dune sands was conducted by [Lorenz et al. \(2008b\)](#). In the radar-bright, often hummocky terrain surrounding the seas, channels are common. Radar-bright streaks to the south of the seas have also been identified in ISS images ([Lopes et al. 2010](#), [Perry et al. 2007](#)). T30 featured the first “atmospheric sounding” altimetry/scatterometry observation to detect, or at least establish an upper limit on, rainfall ([Lorenz et al. 2008a](#)). These observations were also done on T36(1), T39(1), T41(1), T43(1), T44(1), T48(1), T49(2), T50(2), T60(2), T61(1), and T64(2). The numbers in parentheses indicate the number of separate atmospheric probe measurements, each of which consisted of two segments—a tone and a chirp measurement using scatterometer mode to give a low noise floor and 4 seconds total of data. Most of these observations had just one pair positioned at the lower-altitude edge of altimetry while the beam was still close to nadir to avoid surface echo return. A few had two pairs positioned at either edge of an altimeter segment.

*T36.* T36 was a ride-along SAR pass with INMS, broken up into SAR imaging segments (S01 and S02), covering a variety of terrains in the mid- to southern latitudes, and partially overlapping T7. The swath has multiple patches of bright to mottled plains and hummocky terrain cut by channels. It has circular features of unknown origin, including some that resemble empty lakes. The pass also had inbound and outbound radiometry, scatterometry, and altimetry.

*T39.* T39 had an imaging segment as well as inbound and outbound scatterometry and altimetry. T39 was a partial ride-along, with regular SAR pointing on the inbound side, and ride-along SAR (with INMS) for the first 5 minutes after closest approach. Like T36, T39 had a sweeping turn across the surface of Titan that began after the INMS ride-along ended, and finished at the start of outbound altimetry. Additional SAR imaging was performed during the turn. The T39 swath over the south-polar

region has patches of hummocky terrain surrounded by plains of intermediate backscatter, labyrinth terrain ([Malaska et al. 2011](#)), apparent sedimentary deposits, a few lakes near the pole, and abundant channels ([Stofan et al. 2008](#)). Some dunes are seen at the northernmost portion of the swath.

*T41.* T41 had three short SAR segments (S01, S02, and S03) due to an unusual pointing design. It was right-looking and switched to left-looking in the middle. It overlapped T13 and swept to the east to connect to the T17 ride-along swath. The inbound imaging was right-looking and covered the Hotei region ([Soderblom et al. 2009](#)). The outbound imaging was left-looking to cover the probe landing site. The inbound swath segment contains lobate flow features in Tui Regio ([Barnes et al. 2006](#)), with channels draining down towards it from mountainous terrain in Xanadu. The closest approach segment is characterized by mottled to featureless plains. The outbound swath has dunes, streaks, and patches of radar-bright hummocky terrain.

*T43.* T43 had a SAR imaging observation as well as inbound and outbound scatterometry, radiometry, and altimetry. At the end of the outbound altimetry, two short observations in scatterometry mode were inserted to look for echo energy coming back from the atmosphere. The SAR pass was left-looking and was adjusted to collect data over the Tortola Facula ([Sotin et al. 2005](#)), and to provide better altimeter track crossings. The T43 SAR swath crosses the equatorial region at Xanadu ([Radebaugh et al. 2010](#)), covering its mountainous and hummocky terrains between the T13 and T41 swaths. The swath also contains featureless to mottled plains, circular features, and dunes. SARTopo and altimetry data through T43 were used to estimate Titan's global shape ([Zebker et al. 2009b](#)).

*T44.* Data volume for the T44 pass was reduced from the nominal value owing to DSN allocation changes to support the Phoenix landing on Mars. No high-altitude imaging was performed, and data rates were reduced from normal values in several places. Most of the main SAR swath was preserved at the nominal rate. At the start of the inbound altimetry, some special nadir-pointed calibration observations were inserted in all four modes to collect data for radiometric cross-calibration. At the end of the outbound altimetry, two short scatterometry observations were done to look for echo energy coming back from Titan's atmosphere. The T44 swath also covers Xanadu, showing channels cutting much of the mountainous terrain. Also in the swath are regions of plains with dunes. [Lorenz and Radebaugh \(2009\)](#) present a map of dunes observed with SAR throughout the Prime Mission, TA–T44.

*T48.* T48 was a ride-along pass, with accompanying HiSAR and inbound radiometry, scatterometry, and altimetry, and outbound radiometry. It covered the margin of Xanadu and the flow-like features of Tui Regio, also seen in T41. Also seen in the swath are channels, and dark, equatorial plains with dunes.

*T49.* T49 consisted of a south-polar SAR pass, a switch to altimetry data collection, a return to SAR, crossing T8 to T21, then to altimetry, with HiSAR data collection and outbound scatterometry and radiometry. The SAR swath contains hummocky and lobate terrains in the first segment, and dark plains with dunes in the second segment. The altimetry observation included coverage of Ontario Lacus: [Wye et al. \(2009b\)](#) present the constraints placed by the echo shape and amplitude on the roughness of Ontario; [Lorenz et al. \(2010b\)](#) compare Ontario with Racetrack Playa in Death Valley.

*T50.* T50 was a ride-along pass, with inbound and outbound scatterometry and radiometry and HiSAR. There was an outbound high-altitude image segment, two sweep-turn image segments, and the ride-along pass that extended from approximately T8 to T7. It covered the area of the VIMS cloud source ([Rodriguez et al. 2009](#)) and mountains to the east of the T7 swath. Dunes, numerous patches of bright, hummocky materials, and some channels characterize the plains in this region.

*T55.* The T55 observation consisted of inbound and outbound HiSAR, with the inbound HiSAR near Ta; altimetry and regular SAR crossing T48 to the south pole; then a switch back to altimetry, scatterometry, and radiometry. The swath overlaps portions of the T39 swath, and contains a great diversity of terrains including lobate deposits, hummocky and labyrinth terrain, and channels in the south-polar regions extending to dune-filled plains close to the equator.

*T56.* T56 was HiSAR, followed by altimetry, regular SAR, altimetry, then outbound radiometry and scatterometry. The swath extends from the equatorial region to the south-polar region, covering plains with dunes and circular features of unknown origin, hummocky and mountainous terrain, and lobate deposits.

*T57.* The T57 observation was a ride-along over Ontario Lacus, followed by altimetry, HiSAR, altimetry, radiometry, and scatterometry. Along with a portion of Ontario, the swath covers plains with dunes, streaks, hummocky and mountainous terrain, and circular features of unknown origin.

*T58.* T58 was a partial pass that consisted of inbound scatterometry calibration and HiSAR. The T58 SAR swath covers Ontario Lacus in the south-polar region, as well as empty lakes, channels, and labyrinthine terrain in that region. Further from Ontario, the swath is characterized by plains with streaks and dunes, as well as hummocky terrains.

*T59.* T59 was a ride-along pass with inbound and outbound radiometry and HiSAR. The T59 swath is adjacent to T58, and cuts across the southern latitudes, with its complex plains regions with dunes, streaks, circular features of unknown origin, channels, and hummocky and mountainous terrains.

*T61.* T61 has an inbound high-altitude SAR imaging division to provide a special dunes observation between  $3^{\circ}\text{S}$ ,  $156^{\circ}\text{W}$  and  $12^{\circ}\text{S}$ ,  $160^{\circ}\text{W}$ , with  $26.5$ -degree slews, to provide incidence and azimuth viewing-angle diversity to study dune geometry and backscatter response. Incidence angles vary between  $11^{\circ}$  and  $23^{\circ}$ ; azimuth angles vary between  $250^{\circ}$  and  $320^{\circ}$ . T61 began with a scatterometry raster, followed by the special dunes observation, followed by an atmospheric probe observation, and then regular altimetry and a SAR imaging pass that overlapped T8 coverage in the equatorial region. The T61 swath covers a portion of Adiri, with its linear hummocky mountains and dunes to the Belet Sand Sea. Atmospheric probe observations (like that on T30) used tone-only transmissions in scatterometer mode to achieve a very low noise floor. They were conducted during low-altitude altimetry passes so that backscatter signals from the atmosphere could be separated from the surface response, and they were intended to look for methane “rain” drops that might be within the beam footprint.

*T64.* T64 was an excursion back to the northern hemisphere, extending from northern mid-latitudes to the lakes region near the north pole. The pass had no radiometry or scatterometry, but did include a dual-polarization experiment crossing the northern part of the T43 pass. This experiment involved two high-altitude imaging scans using

orthogonal polarizations to look for polarization variation of features observed in the T43 swath. To the south of the lakes, the plains are relatively featureless, with patches of hummocky terrain and some bright streaks.

*T65.* T65 had two segments, one veering over a portion of Ontario Lacus, and the other cutting across the diverse terrains of the southern hemisphere.

*T69.* T69 consisted of HiSAR and radiometry only.

*T71.* T71 was a ride-along pass, without inbound and outbound radiometry and SAR, that covered southern mid-latitudes (trailing hemisphere, Northern Mezzoramia).

*T77.* T77 was a SAR pass covering northern Xanadu and northwestern Fensal, including Ksa and Momoy craters. The return of altimetry data over Xanadu has helped with the determination of Titan's global shape. The T77 pass also had accompanying HiSAR of Ksa and Menrva craters, plus radiometry and scatterometry.

*T83.* T83 was a ride-along pass, with outbound SAR, as well as inbound and outbound altimetry, HiSAR, radiometry, and scatterometry. The SAR revisited small lakes first seen in T16 and T19 to search for evidence of change. T83 coverage also overlapped with the later T95 pass.

*T84.* T84 was a ride-along pass, with inbound and outbound SAR, altimetry, HiSAR, scatterometry, and radiometry. The SAR swath covers northern mid-latitudes on the trailing hemisphere, plus HiSAR over western Kraken Mare.

*T91.* T91 was an opportunity to obtain SAR imagery over the Titan north-polar region, in addition to altimetry across Ligeia Mare at closest approach. The altimetry has been used ([Mastrogiuseppe et al. 2014](#)) to determine the depth of Ligeia (~160 m), as well as its complex dielectric constant, which has been used to constrain composition, which was found to be consistent with liquids dominated by methane-nitrogen ([Mitchell et al. 2015](#)). The pass had accompanying HiSAR data of the seas and some lower latitudes, as well as scatterometry and radiometry. The SAR data includes a nondetection (as with T25 and T64) of the "magic island," later observed in T92. Co-analysis of altimetry and radiometry data shows that Ligeia Mare was particularly smooth (<1 mm RMS) at the time of observation, fitting a temperature of  $92 \pm 0.5$  K ([Zebker et al. 2014](#)).

*T92.* T92 was a SAR pass at high latitudes, focused on obtaining stereotopographic images of small lakes, providing repeat coverage of Ligeia Mare, and searching for change relative to previous flybys. The transient "magic island" was first observed in this pass ([Hofgartner et al. 2014](#)) in a part of Ligeia Mare previously observed to be lacking in surface features. T92 had accompanying altimetry, HiSAR, scatterometry, and radiometry.

*T95.* T95 was a ride-along pass showing SAR of predominantly new terrain at near-equatorial latitudes, as well as outbound altimetry, inbound and outbound HiSAR, scatterometry, and radiometry. Lower-resolution HiSAR images revisited Ontario Lacus and Ligeia Mare to look for change and characterize scattering properties.

*T98.* T98 featured SAR imaging of Ontario Lacus, intended to look for changes in the shoreline when compared with T57, T58, and T65. It was accompanied with inbound and outbound altimetry, HiSAR, scatterometry, and radiometry. The HiSAR revealed additional small lakes.

*T104.* T104 was a pass over northern latitudes, and featured altimetry across Kraken Mare, as well as SAR imagery at one end of the pass in an attempt to revisit the “magic island,” previously seen in T92 ([Hofgartner et al. 2014](#)) but absent in other flybys. Analysis of these SAR data provided additional evidence of the transient nature of the phenomenon, and helped to rule out nontransient phenomena. With the exception of a small part of a potential feeder channel, no altimetry signal was received from the sea floor of most of Kraken Mare, suggesting that it is either more absorptive or deeper than other seas ([Mastrogiuseppe et al. 2014](#)). These data are accompanied by inbound scatterometry and radiometry data.

*T108.* T108 was a complex, “contortionist” flyby over northern latitudes, focused on change detection and stereo on dark lakes as well as obtaining altimetry over Punga Mare. The SAR data fill in a gap in coverage between Ligeia Mare and Kraken Mare to explore further the idea that the two seas are connected hydraulically ([Lorenz 2014](#)). These data are accompanied by HiSAR data to fill in high-latitude gaps of coverage, plus scatterometry and radiometry data.

*T113.* T113 included a hand-off to the INMS shortly after closest approach, during which time SAR imagery was obtained as a ride-along, before RADAR became prime again. The SAR imagery features an equatorial traverse (~4000 km long, from 10°S, 0°W to 10°S, 135°W) across much of Titan’s enigmatic Xanadu region, which despite looking mountainous and relatively dune-free does not appear to be consistently elevated above the surrounding lands. The observation is in part intended to generate stereo (3D) views of the complex terrain, when combined with RADAR data from T13, which followed an overlapping path. The east end of the swath extends past Xanadu, covering the sand dunes of Aztlan. These data are accompanied by lower-resolution HiSAR images, to fill in low-latitude gaps in coverage, as well as scatterometry and radiometry.

*T120.* T120 was a partial pass. The observation started with inbound altimetry, followed by the SAR main swath. At closest approach, SAR imaging became a ride-along observation with the INMS. RADAR pointing resumed at 18 minutes past closest approach with outbound altimetry, which included another atmospheric probe event. The observation then concluded with a high-altitude scatterometer imaging set, as well as radiometry. The main SAR imagery significantly enhanced coverage of south-eastern mid-latitudes, of particular value for filling gaps in the shape model, a goal accomplished by combining altimetry with “SARTopo” extracted from the SAR swaths. At the far east end, the SAR imagery starts in the Tsegihi region, crossing west before swinging northwest towards the dune fields of Shangri-La, close to the equator. One of the primary objectives was to image putative lakes observed by the ISS camera ([Griffith et al. 2012](#)).

*T121.* T121 started with inbound high-altitude scatterometer imaging, followed by altimetry. Following this was the SAR main swath, intended in part to reimage two locations of special interest: Hotei Regio and Tui Regio. The pass started in the east in bright terrain, crossing Hotei Regio and heading into mountainous Xanadu. A turn transition from one side to the other was inserted near close approach to allow imaging of Tui Regio, before crossing the sand seas of Shangri-La and ending in the bright Dilmun region. The observation concluded with an outbound altimetry segment followed by a long, high-altitude HiSAR image to improve global coverage that extended into the time normally used for low-resolution scatterometry.

*T126.* T126 was the final targeted (close-range) flyby of the Cassini Mission. It included a partial ride-along with the INMS. The inbound portion crossed high northern latitudes, revealing many lakes as well as reimagining Ligeia Mare in an attempt to provide extra constraints for the “magic island” ([Hofgartner et al. 2014](#)) and to determine if waves have strengthened sufficiently to cause brightening. This was followed soon after by an altimetry segment at closest approach, allowing bathymetry and compositional constraints to be produced across a series of small “cookie-cutter” lakes, before returning to SAR imaging at lower latitudes. Notably, the outbound SAR swath crossed the path of the first targeted flyby, TA, giving the longest high-resolution time differential between images of the mission. These data are accompanied by lower-resolution HiSAR images, to fill in coverage gaps, as well as scatterometry and radiometry.

## 6.2 Ontario Lacus: A Case Study

A series of studies of Ontario Lacus near the south pole of Titan illustrate the benefit of using multiple RADAR data sets to address scientific problems. Ontario is one of the few lakes in the south-polar region, and the largest, with an area over 15,600 km<sup>2</sup> (Figure 6-1). The nature of the lake, the surrounding terrain, and lacustrine processes at Ontario have been determined through the combined use of SAR image, altimetry, and radiometry data ([Wye et al. 2009b](#), [Wall et al. 2010](#), [Hayes et al. 2010](#)).

SAR images of Ontario at 350- to 500-m-resolution cell sizes in the T57 and T58 swaths obtained in 2009 reveal the complex shoreline of Ontario, with a relatively smooth northern shore resembling a terrestrial wave-modified beach (Figure 6-1) ([Wall et al. 2010](#)). Multiple lineations parallel to the lake edge along this shoreline suggest higher lake levels in the past; a higher shoreline for Ontario was observed in

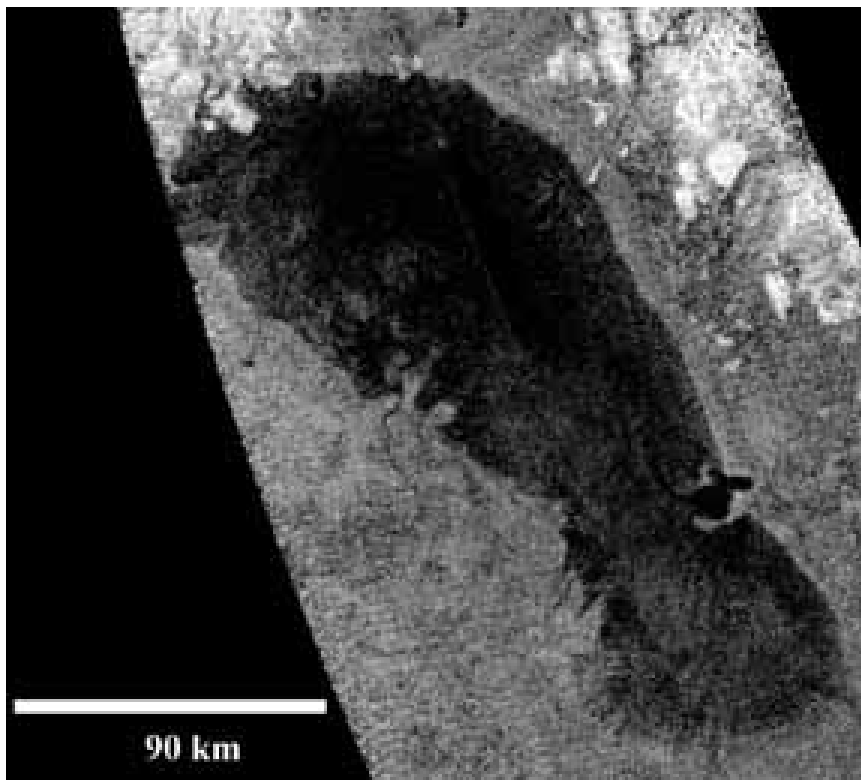


Figure 6-1.  
Cassini RADAR  
image (PIA13172)  
of Ontario Lacus.

ISS images in 2005 ([Turtle et al. 2009](#), [Barnes et al. 2009](#)). The western shoreline of Ontario has more rugged terrain, with lake liquids flooding low-lying areas. To the southwest, a delta has formed in the lake at the terminus of a broad channel  $\sim 1$  km wide. The delta has an area of over 140 km<sup>2</sup>, much smaller than terrestrial deltas fed by similar-size rivers. [Wall et al. \(2010\)](#) interpret this to indicate low sediment supply, slow flow velocity, and a low sediment-transport capability.

Altimetry data indicate the lake lies in a shallow depression, with the mountainous terrain to the west of the lake having elevations of 300–500 m. The region tilts to the west, possibly indicating the lake has formed within a graben ([Wall et al. 2010](#)). At the time the altimetry data were taken, the lake surface was extremely smooth ([Wye et al. 2009b](#)), indicating no wave activity. The apparent wave-modified beach indicates that the lake surface is more dynamic at times, likely relate to seasonal cycling (e.g., [Wall et al. 2010](#)).

The lake is characterized by high emissivity, with a maximum brightness temperature of 88.5 K (with absolute calibration of  $\sim 1$ –1.5 K [[Janssen et al. 2009](#)]) corresponding to a physical temperature of 90.0–90.8 K, allowing for a methane-ethane mixture (e.g., [Paillou et al. 2008b](#), [Wall et al. 2010](#)). This slightly cooler-than-average temperature ( $\sim 92$  K [[Jennings et al. 2009](#)]), if real, could result from evaporative cooling (e.g., [Mitri et al. 2007](#)).

The radar backscatter of the lake surface decreases exponentially away from the shoreline, consistent with attenuation of the radar signal in a deepening liquid ([Hayes et al. 2010a](#)). From this, [Hayes et al. \(2010\)](#) estimated a loss tangent for the liquid consistent with liquid hydrocarbons and calculated a bathymetry map for Ontario. [Hayes et al. \(2011\)](#) used these data and the recession observed between the ISS and RADAR observations to calculate a reduction in the depth of the lake between 2005 and 2009 of  $4 \pm 1.3$  m.

These studies illustrate the importance of using all available data sets to fully characterize processes on Titan. SAR data provides morphologic and surface properties information, altimetry data can constrain the properties of the lake surface as well as help constrain the origin of the surrounding terrain, while the radiometry data provide insight into the lake liquid composition and state. In addition, comparison to other Cassini data sets such as ISS and VIMS data, allow more complete interpretations of lake character and evolution.

### 6.3 Huygens Landing Site: A Case Study

A feature of the Cassini-Huygens Mission for Titan specifically has been combining the Cassini Orbiter's globally-distributed remote-sensing observations with the Huygens probe's in situ observations. This is particularly the case for near-infrared remote sensing, where the hazy atmosphere modifies the radiance sensed by Cassini in both additive and multiplicative ways, frustrating quantitative interpretation of observations as surface albedo. The interpretation of RADAR data also benefits from the much higher spatial resolution afforded by the Huygens descent and surface images ([Tomasko et al. 2005](#)). Moreover, Huygens contributes in situ measurement of the dielectric coefficient of the surface material (e.g., [Hamelin et al. 2016](#)), as well as bistatic reflection of its S-band radio relay link ([Perez-Ayucar et al. 2006](#)) and a terrain elevation profile and Ku-band nadir reflection characteristics from the probe radar altimeters ([Lorenz et al. 2016](#)).

The desire to correlate “ground truth” from Huygens with RADAR observations was a key driver in RADAR observation design (and indeed in the selection of the Cassini orbital tour, which in turn influenced the available observing geometries). When the Prime Mission tour was selected and observing opportunities parsed out among the various instruments (naturally, optical remote sensing [ORS] of the landing site was also desired, but could not be performed simultaneously with RADAR observations of the site, since the ORS instruments are mounted orthogonally to the RADAR boresight), the nominal RADAR SAR imaging view of the Huygens landing site (at Longitude 192.4 degrees W Latitude -10.2 degrees S) was planned (and obtained) for the T41 swath.

Much lower-resolution scatterometer ([Elachi et al. 2005](#), [Wye et al. 2007](#)) and radiometer data of the Huygens landing site were obtained on the first close Titan flyby (TA)—before the Huygens descent—although interpretation was challenged by the evidence in near-IR imaging (e.g., [Porco et al. 2005](#), [Lebreton et al. 2005](#)) that the landing area was heterogeneous on spatial scales smaller than the scatterometer footprint. The TA scat/rad observation rastered a broad region covering the Shangri-La “dark” terrain and the western part of the Xanadu “bright” terrain (these areas being known from pre-Cassini ground-based near-infrared observation) in one linear polarization. The same area was deliberately observed in different polarization on the T8 flyby a year later, with the goal of understanding the scattering and emission characteristics of these two terrains (and the landing site) with the benefit of polarimetric information. These observations are discussed in [Wye et al. \(2007\)](#), [Zebker et al. \(2008\)](#), and [Janssen et al. \(2009, 2011\)](#).

In fact, as the performance of the RADAR instrument and the scattering properties of Titan became understood after the first flybys, it was recognized (e.g., [West et al. 2009](#)) that SAR imaging could be achieved beyond the originally-anticipated inbound and outbound ends of the swath. This augmented coverage in fact allowed the landing site to be covered by the first extended inbound SAR swath on T8 (e.g., [Lunine et al. 2008](#)): As well as correlating (albeit initially ambiguously) the bright highland region in the Huygens descent images ([Tomasko et al 2008](#)), we were able to identify two dark streaks seen by the Huygens Descent Imager/Spectral Radiometer (DISR) about 20 km north of the probe landing site in the RADAR image. These features proved to be the key in linking the Huygens and Cassini data.

The landing site was observed at longer range (and thus slightly poorer resolution) by a high-altitude beam-3 only (HiSAR) observation on T8. Additionally, the landing site was observed (as planned) on T41. Near-infrared observations of the landing site occurred on a number of flybys, but with highest resolution on T47 in November 2008: [Sotin et al. \(2009\)](#) present a detailed analysis of the Cassini VIMS and RADAR data, together with the Huygens DISR mosaic. One notable issue in the design of this observation is that the footprint of VIMS is small enough (when observing near closest approach, when it yields its highest spatial resolution) that the possible uncertainty in Titan’s rotation state and the several years between the descent and the observation could mean that the observation would miss the actual landing site. In the end, the hypothesis of a synchronous rotation rate was adopted (but with the pole obliquity determined by RADAR—[Stiles et al. 2008](#)), and the landing site was captured successfully.

## 7 Data Outages, Anomalies, and Related Data Issues

In all planetary missions, including Cassini, anomalies occur that affect data return in various ways.<sup>6</sup> It is important to note that while this section points out some of the times when various parts of the Cassini systems (which include not only the spacecraft and ground systems but also planners, sequencers, spacecraft engineers, mission operators, DSN station operators, managers, scientists, etc.) in some way didn't work right, to keep a proper perspective, the reader is reminded that most of the time these systems performed flawlessly. In fact, the Cassini systems were remarkable in having had so few of these issues. Most issues have been small, and the amount of data lost has been minimal relative to that of other planetary missions. In this section, we first report anomalies in spacecraft, commanding, or ground system that resulted in known loss or corruption of RADAR data. Second, we report anomalies for which there are no known issues with RADAR data, in the hope that if later researchers should find issues with the related data they might be able to better characterize them with the knowledge of coincident problems. This list is not comprehensive; it includes those anomalies that the authors were able to identify. Errata in data processing are listed separately in [Section 4.5.2](#).

Before we review these events, some introduction to the details of the Cassini and Cassini RADAR ground system terminology is necessary. During the event planning period, each RADAR observation is given a unique identifier of the format `tt_nnn_s`, where `tt` is an abbreviated identification of the target (e.g., `ti` = Titan), `nnn` is the Saturn orbit number, and `s` (if supplied) is a number showing the temporal order of the observation within the pass or Saturn orbit as appropriate. Note that due to the late change of Huygens' deployment, the first three orbits of Saturn were called A, B, and C (shown in this ID as 00a, etc.), followed by the number 3 and so on. Thus `ti_00b_1` is the first observation of Titan in Saturn orbit B.

Some instances of missing data from TA through T77 are indicated in the comprehensive downlink spreadsheet provided in [Appendix 5](#). Unfortunately, this spreadsheet does not include the later Titan passes.

### 7.1 Major Data Outages and Corruption

Anomalies have their most obvious effect when data are lost completely. Data loss can result from failure of the instrument to acquire data, failure of the spacecraft to collect, store, or transmit data, or failure of the ground system to receive and process data properly. Less obvious, and potentially more damaging to subsequent research, are data that are present but corrupted. Processing of SAR-mode data is inherently resistant to errors, since it tends to combine data taken at separate times, but this is not necessarily a good thing, as the resulting compressed image data might appear to be normal but have different quantitative characteristics (e.g., number of looks, SNR, etc.) caused by the corrupted raw data.

#### 7.1.1 *Dione/Mimas 00b (Total Loss)*

On December 16, 2001, substantial gaps in all science data were noticed immediately following that day's downlink. RADAR data were received from the instrument warm-

<sup>6</sup> In this report, we use "errata" for errors in processing, as discussed in [Section 4.5.2](#), and "anomalies" for issues that affect data return, as discussed in this section.

up period but not during actual science data acquisition. Investigation revealed that during data acquisition, a command timing error caused the science data to be not recorded on the SSR. All RADAR science data were lost. RADAR observations di\_00b\_1 and mi\_00b\_1 of Dione and Mimas respectively, were completely lost. For further details see JPL Incident/Surprise/Anomaly Report (ISA) Z85233<sup>7</sup>.

### 7.1.2 The T7 Anomaly

On September 9, 2005, a Cassini downlink to the Goldstone 70-m antenna (DSS-14) failed when the antenna refused to point correctly. The antenna operator investigated and found that the antenna had been instructed to point to the spacecraft location in the year 2023 rather than 2005. After correcting the incorrect date the antenna pointed and the remainder of the downlink was received. Unfortunately, the playback from the spacecraft was also imperfect and revealed a flight software error involving the way that data playbacks from the spacecraft were managed. Following this pass, the flight software was fixed (see ISA Z87618, ECR 104281, P/FR Z87475 for details).

From a data standpoint, the net result is that the T7 SAR data terminate at approximately 170°W, 70°S, as shown by the dashed line in Figure 7-1. Some data degradation might be present at the SE end of the data, just prior to the end.

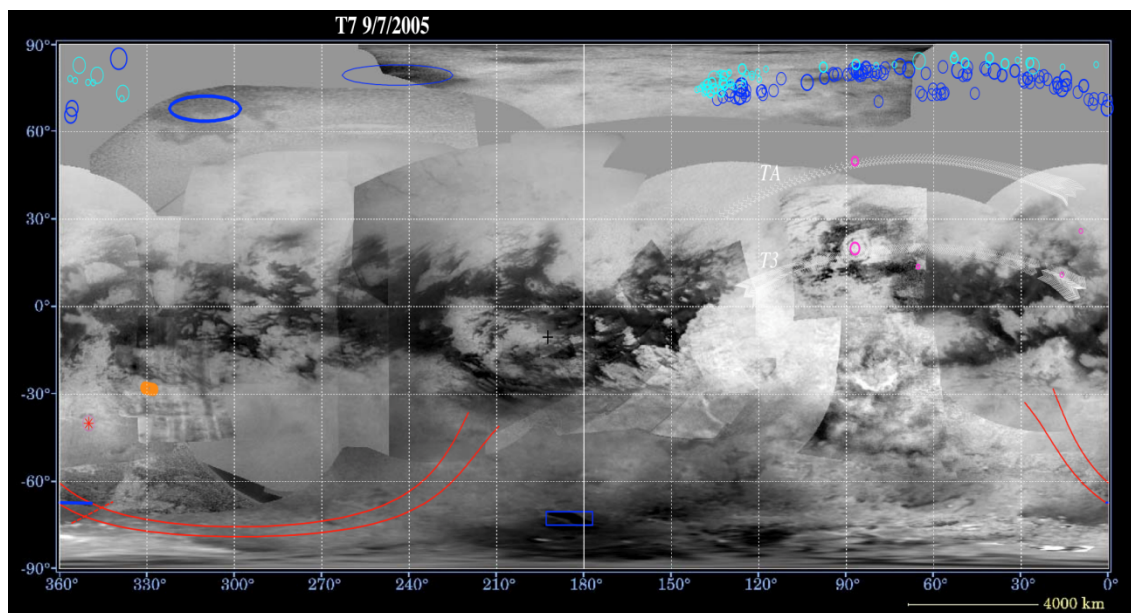


Figure 7-1. T7 planned swath with actual coverage limit marked (red dashed line at lower left). Note that the horizontal scale in this figure does not follow convention.

Following the Titan T13 encounter on May 12, 2006, when the spacecraft was expected to downlink, the ground system did not acquire its signal. A failure in the spacecraft Power Subsystem's solid-state power switches (see [Section 2.1](#)) was diagnosed, but the downlink transmission was lost. A second downlink was performed, and most of the RADAR data were recovered, but minor losses remain. The net effect

<sup>7</sup> JPL ISAs, Engineering Change Requests (ECRs), Problem/Failure Reports (P/FRs), and Discrepancy Reports (DRs) can be obtained from the Jet Propulsion Laboratory, 4800 Oak Grove Drive, Pasadena CA 91109 USA.

is that the T13 swath does not extend as far to the east as planned. (Much of this lost coverage was obtained 100 flybys later, in September 2015 on T113).

### 7.1.3 *The T60 Anomaly*

On August 9, 2009, the spacecraft was to downlink Titan pass T60 to the Goldstone, CA DSN antenna complex, using the 70-m antenna (DSS-14). DSS-14 experienced an azimuth antenna bearing problem when tracking the Mars Reconnaissance Orbiter prior to the start of the Cassini track and could not be moved. A 34-m antenna, DSS-25, was “borrowed” from Kepler and New Horizons; it was able to communicate with Cassini and provided uplink and coherent tracking for navigation. Unfortunately, the downlink telemetry data rate was too high for the smaller antenna, and the entire downlink, including T60, was lost. For further details, see JPL Discrepancy Report DR G109608, “All TLM from T60 lost, ALC problem.” (“TLM” is telemetry; “ALC” is automatic level-control.)

### 7.1.4 *Iapetus Pass 49 Anomaly*

Cassini’s solid-state power switches turned themselves off spontaneously several times during the mission, probably because of cosmic-ray interference. On September 11, 2007, one such event turned off Travelling-Wave Tube Amplifier A, which sent the spacecraft into safing. RADAR Iapetus Pass 49, scheduled for later that same day, did not execute (ISA Z91542).

### 7.1.5 *The T64 Anomaly*

On Dec 29, 2009, a Cassini downlink to the antenna complex in Madrid, Spain, was significantly affected by heavy rain. Seventy-six minutes of telemetry were lost due to both rain and an incorrect set of parameters used for the receiver (downlink controller table). Even though a second, redundant playback of the spacecraft solid-state recorder was planned and executed, the redundant playback was in the same pass and was also affected. As a result, data from Titan Pass T64 were very noisy (see Figure 7-2).

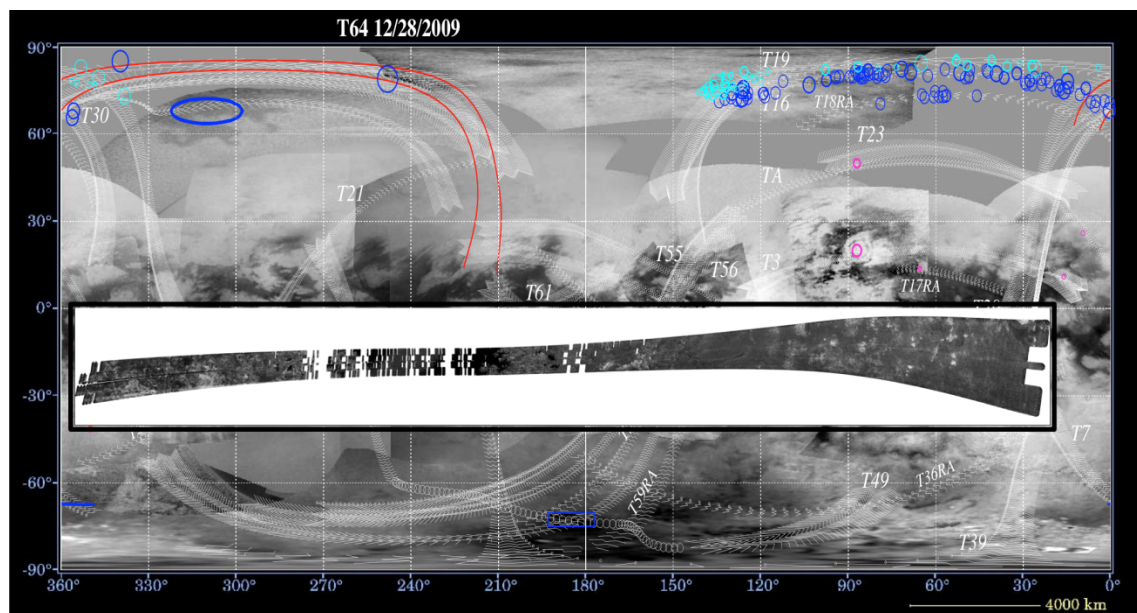


Figure 7-2. T64 planned swath and actual data prior to recovery efforts (inset, in oblique cylindrical projection).

When these noisy data were processed through the Cassini ground-processing software, incorrect bits resulted in lost data packets, which in turn caused the Cassini RADAR data processor to lose entire frames of data. The resulting SAR data contain many gaps, some large (DR M105593).

It is sometimes possible to recover corrupted data, and attempts were made at recovering some of the T64 losses by rerunning the ground software that detects valid data, but there was no significant improvement.

#### *7.1.6 The T69 Anomaly*

Gap in inbound radiometry.

#### *7.1.7 The T71 Anomaly*

SSR pointer error in the dual playback—no effect on data

#### *7.1.8 The T77 Anomaly*

Data gap in the turn to SAR. Also dual playback was cancelled due to conflicts.

#### *7.1.9 The T83 Anomaly*

Gaps in inbound scatterometry, outbound altimetry and radiometry.

#### *7.1.10 The T86 Anomaly*

Gaps in ride-along SAR and HiSAR due to heavy rain at DSN station.

#### *7.1.11 The T92 Anomaly*

Gap in outbound altimetry (outside the dual playback).

#### *7.1.12 The T104 IEB Error*

T104 had an IEB error (see [Section 3.4](#), RADAR Operation). Auto-gain mode should have been turned off and on to reset it before setting the special high-attenuator value needed for the lake crossing, but was forgotten when making the IEB. The high-attenuator setting was specified correctly, but RMSS ignored it and maintained the prior level. The error could have been caught by the Integrated Test Lab (ITL) test, but was missed when looking over the ITL data (so two mistakes). The lake crossing was then too fast for the auto-gain algorithm to get on-scale in time. There is no data loss, but some of the data are saturated and require detailed modeling of the instrument operation to interpret ([Wye et al. 2009b](#)).

#### *7.1.13 Rev 277 RADAR Rings Anomaly*

During the proximal orbits, near the end of the Cassini Solstice Mission, downlink of data from an observation of Saturn's rings was not fully received due to an anomaly at DSS-43 (the Canberra, Australia 70-meter antenna). RADAR lost all data from 2017-155T02:56:31-03:42:00. In total 569.5 Mb out of 1095.9 Mb were received, about 52%. The anomaly is described in DR C112725, available (with access) at <https://cmmaster.jpl.nasa.gov/dr/view.asp?no=C112725>. In brief, the previous use of the antenna was for radio astronomy, which uses a different feedcone in the antenna. The subreflector is rotated to address different feed cones ([Imbriale 2005](#)), but the command to rotate it to the proper feedcone did not actually take effect.

### 7.1.14 *Other Experiment Anomalies*

Numerous minor anomalies have occurred in instrument commanding and in spacecraft and ground systems, some of which have had minor effects on data products. It is common, for example, when telemetry modes are changed for a variety of reasons or receiving antennas are swapped (for example, due to Earth's rotation), to lose a small number of data packets. Miscellaneous "bit hits" occur in all data, including RADAR, for reasons that are often not known. These events can cause much larger losses, as ground processing software often excludes entire packets of data when only a few bits are missing. Such losses generally result in a lower number of looks rather than image gaps and would thus go unnoticed. Some quantitative use of the data will be affected. Missing packets in SAR mode, for example, might reduce the number of looks and thus affect the speckle characteristics (the "grainy" aspects of the images), which could in turn affect data analysis; other modes might be affected differently. Similar effects have resulted at ends of observations when data volume had to be trimmed to fit allocations (see below). For the earlier passes, [Appendix 5](#) might be of help in identifying the latter effect.

## 7.2 **Anomaly Statistics and Review**

The unique and rapidly changing geometry of every Cassini observing opportunity, to say nothing of the diverse operating modes of Cassini's instruments and the variety of scientific questions being addressed, means that every observation was a custom design. This is in stark contrast to astronomical observatory satellites (where instrumentation settings might vary, but the target geometry does not typically change rapidly) or spacecraft in mapping orbits where the geometry tends to be repeatable.

The development of unique instrument sequences provided ample opportunities for errors to be introduced: Occasions where spacecraft attitude limits would be violated were usually detectable in the observation planning software (which included a kinematic model of the spacecraft and its attitude control system), and occasions where instrument errors would occur were identified and eliminated by sequences run on a ground testbed. Most of the errors described above can be considered as data quality issues (apparent only when the interaction of the instrument with the physical universe had introduced amplitude changes and propagation delays into the radar signals that were not always modeled correctly) rather than failures per se. In other instances, data loss occurred through sometimes subtle "operator error" or hardware failures (on the DSN or the spacecraft) unrelated to the instrument.

Despite rigorous efforts, then, a few percent of RADAR observations suffered partial loss or data-quality issues. Further, a couple of percent (or so) of Cassini observations were lost entirely. It is not obvious that any reasonable project investment could have prevented most of these (e.g., the 70-m DSN antenna bearing failure), and so observation loss of a few percent should perhaps be assumed in the planning of future missions with similar custom designs and operation. Such a loss can be acute where specific scientific objectives of a mission rely on individual observing opportunities that cannot be recovered subsequently.

### 7.3 Complexities to Consider When Interpreting SAR Images

Special care is needed when interpreting SAR images. Synthetic-aperture image construction includes complexities that might be unfamiliar to researchers who are used to optical imagery (for a good tutorial on the interpretation of SAR images, see [Ford et al. 1993](#)). Most notably, the viewing geometry can dramatically affect the appearance of the surface. This occurs for at least two reasons that apply to some extent to optical images but can be more severe for RADAR.

The first is the difference in illumination direction that follows from any change in viewing direction because the spacecraft is also the source of “lighting.” In extreme cases, when two images of the same region have been obtained from opposite sides and the bright-dark shading of topographic slopes is more important than intrinsic variations in radar scattering strength, one image might even look like a photographic negative of the other. Reversals of contrast can also occur between images illuminated from the same side, if intrinsic scattering variations are dominant and the brightness of one type of terrain varies more strongly with incidence angle than that of another terrain. The brighter of two terrains in one image might then appear as the darker in the other image.

Second, features with topographic relief will appear distorted in different ways depending on the incidence angle and viewing direction. This effect, topographic parallax, occurs for optical images as well, but can be especially dramatic for radar. Areas with slopes exceeding the incidence angle will actually appear folded over on top of themselves, potentially rendering them unrecognizable when compared to less distorted images.

Less extreme cases in which the contrast of individual features is reversed or the edges of features appear to move slightly are more common and can pose subtle challenges to interpreting the images. Thus, it is important to keep these effects in mind as alternative explanations for image-to-image differences that might initially suggest that the surface is undergoing active changes.

A further complication for SAR interpretation occurs in dark regions. There is often a strong temptation to assign meaning to fuzzy features near the noise floor. Often such features are purely due to noise. A good indicator for this is the presence of negative backscatter values in the floating-point (BIF\*.IMG or BIS\*.IMG), noise-subtracted BIDR files. Negative backscatter is physically impossible but statistically meaningful. It means there is insufficient evidence to conclude that any radar energy returned from the surface. It occurs only in regions where the signal level is much less than thermal noise. One should not assign meaning to features in any region with a large number of negative values (~25% or more) unless one can formally show statistical significance using an accurate model of radar noise. An added complication for Cassini SAR in dark regions is that the central narrow antenna beam (Beam 3) has much higher SNR than do the wider beams on either side of it. When analysts contrast-stretch dark regions, they commonly observe seams along the edge of the center beam where the noise variance drops off rapidly. In this event there might be useful information in the Beam 3 portion of the data even if the other beams detect no signal, but only if the Beam 3 region contains few negative values. The (BIM\*.IMG) beam-mask BIDR files can be used to determine which beam contributes to each pixel in the image.

Linear artifacts are a third important feature of SAR imagery. Artifacts that look like bright or dark lines running along the long dimension of the SAR swath between beams or at the edges of the swath are common. These artifacts are primarily caused by residual errors in calibration due to surface topography. This effect is utilized by the SARTopo technique to estimate surface heights along the beam seams. A repeated pattern of lines in the orthogonal direction (perpendicular to the long axis of the SAR strips) can also occur. This effect is most pronounced when the number of independent looks for each pixel is less than 4. The number of looks for each pixel is contained in the BIL\*.IMG BIDR files. A common rule of thumb for artifacts is that if it looks artificial it probably is.

## 8 Studies in Quantitative Use of Cassini RADAR Data

Most scientific analyses of Cassini RADAR data performed to date have used SAR imagery, altimeter surface heights, scatterometer backscatter values (NRCS), or radiometer temperatures. These are the primary scientific measurements in the data set. The SAR imagery is contained in the BIDR files. The other values are in the SBDR files. Both of these data sets are archived by PDS. A handful of more data-intensive studies have used intermediate or ancillary data and/or used different data types in combination in a manner in which the relationship between the various data elements is crucial to the investigations. These studies have sometimes even involved reprocessing data from raw radar returns. In this section, we describe two recent studies and briefly describe what a user would need to know to replicate these studies. The goal of this section is to provide interested users with enough background to get them started on similar data-intensive analyses of their own.

Tables 8-1 and 8-2 provide general data types required to process or calibrate RADAR data. Table 8-3 shows data required for SAR geolocation.

Table 8-1. Data needed to perform synthetic-aperture processing.

PARAMETER DESCRIPTOR	SYMBOL	FILE IN PDS VOLUME	PARAMETER NAME(S)
Raw radar echo counts	s(t)	DATA/LBDR/LBDR*.ZIP	Sampled Echo Data (See Section 2.3.4 of BODPSIS.PDF)
Spacecraft velocity	v	DATA/LBDR/LBDR*.ZIP	sc_vel_target_x, sc_vel_target_y, sc_vel_target_z
Spacecraft position	U <sub>sc</sub>	DATA/LBDR/LBDR*.ZIP	sc_pos_target_x, sc_pos_target_y, sc_pos_target_z
Beam boresight orientation	U <sub>bore</sub>	DATA/LBDR/LBDR*.ZIP	act_centroid_lat, act_centroid_lon (Boresight location on reference sphere can be used to compute the boresight orientation)
Pulse repetition interval	t <sub>p</sub>	DATA/LBDR/LBDR*.ZIP	PRI
Number of pulses transmitted	N <sub>p</sub>	DATA/LBDR/LBDR*.ZIP	num_pulses
Chirp start frequency	f <sub>c</sub>	DATA/LBDR/LBDR*.ZIP	chirp_start_freq
Chirp step frequency	Δf <sub>c</sub>	DATA/LBDR/LBDR*.ZIP	chirp_freq_step
Chirp length	Δt <sub>c</sub>	DATA/LBDR/LBDR*.ZIP	chirp_length
Number of chirp steps	N <sub>c</sub>	DATA/LBDR/LBDR*.ZIP	num_chirp_steps
Transmit frequency	f	CALIB/CONFIG	Keyword = carrier_frequency
Beam number	b	DATA/LBDR/LBDR*.ZIP	beam_number
Radar mode	m	DATA/LBDR/LBDR*.ZIP	radar_mode
Sampling frequency	f <sub>adc</sub>	DATA/LBDR/LBDR*.ZIP	adc_rate
Receive window delay	t <sub>rx</sub>	DATA/LBDR/LBDR*.ZIP	rx_window_delay
Receive window length	Δt <sub>rx</sub>	DATA/LBDR/LBDR*.ZIP	rx_window_pri (units are PRI)
Measurement start time	t <sub>0</sub>	DATA/LBDR/LBDR*.ZIP	t_ephem_time
Transmit delay	t <sub>tx</sub>	DATA/LBDR/LBDR*.ZIP	transmit_time_offset
Receiver bandwidth	B	DATA/LBDR/LBDR*.ZIP	rc_bw

Table 8-2. Data needed to calibrate SAR imagery.

PARAMETER DESCRIPTOR	SYMBOL	FILE IN PDS VOLUME	PARAMETER NAME(S)
Antenna gain pattern	G	CALIB/BEAMPAT/BEAM*_V01.PAT	See DOCUMENT/VOLSIS.PDF for description
Spacecraft position	p	DATA/LBDR/LBDR*.ZIP	sc_pos_target_x, sc_pos_target_y, sc_pos_target_z
Beam boresight orientation	U <sub>bore</sub>	DATA/LBDR/LBDR*.ZIP	act_centroid_lat, act_centroid_lon
Attenuator gain	G <sub>a</sub>	DATA/LBDR/LBDR*.ZIP	at1_tot, at3_tot, at4_tot for beams (1,2), (3), and (4,5) respectively.
Transmit frequency	f	CALIB/CONFIG/PCF*.CFG	Keyword=carrier_frequency
Transmit power	P <sub>t</sub>	CALIB/CONFIG/PCF*.CFG	Keyword = Pt
System noise temperature	T <sub>r</sub>	CALIB/CONFIG/PCF*.CFG	Keyword = SYSTEM_TEMPERATURE_XXXX where XXXX is ALTH, ALTL,SARH or SARL depending on radar mode
Echo-count-to-power conversion factor	C	CALIB/CONFIG/PCF*.CFG	Keyword = squared_deviation_of_system_noise_input_at_XXXX where XXXX is ALTH, ALTL, SARH or SARL depending on radar mode.
Beam number	b	DATA/LBDR/LBDR*.ZIP	beam_number
Radar mode	m	DATA/LBDR/LBDR*.ZIP	radar_mode

Table 8-3. Data needed to geolocate SAR imagery.

PARAMETER DESCRIPTOR	SYMBOL	FILE IN PDS VOLUME	PARAMETER NAME(S)
Spacecraft velocity	v	DATA/LBDR/LBDR*.ZIP	sc_vel_target_x, sc_vel_target_y, sc_vel_target_z
Spacecraft position	U <sub>sc</sub>	DATA/LBDR/LBDR*.ZIP	sc_pos_target_x, sc_pos_target_y,sc_pos_target_z
Titan pole location	U <sub>pole</sub>	DATA/LBDR/LBDR*.ZIP	pole_right_ascension, pole_declination
Titan rotation angle	ω	DATA/LBDR/LBDR*.ZIP	target_rotation_angle
Titan spin rate	dω/dt	DATA/LBDR/LBDR*.ZIP	target_rotation_rate
Beam boresight orientation	U <sub>bore</sub>	DATA/LBDR/LBDR*.ZIP	act_centroid_lat, act_centroid_lon
Transmit frequency	f	CALIB/CONFIG/PCF*.CFG	Keyword=carrier_frequency

## 8.1 Study 1: Titan Pole and Spin-Rate Estimation

### 8.1.1 SAR Spin-Model Estimation

The first example study is detailed in [Stiles et al. \(2008\)](#). As [Davies \(1992\)](#) did for Venus using Magellan data, the authors of this study used SAR imagery of the same features taken months and years apart to refine the pole location and spin rate of Titan. For the purposes of this discussion we refer to this technique as SAR Spin-Model Estimation (SARSME). The authors used apparent misregistrations of the observed features to constrain the motion of Titan’s surface about its pole during the time period observed.

To understand how SARSME is performed, we first need some background on geolocation, which is the method whereby the location of pixels in an image is determined. After pixels from an arbitrary image are geolocated, the image can then be interpolated onto a regular geographic grid. For passive imagery such as optical photographs from ambient light, geolocation is performed using a combination of the

known location and orientation of the camera and the known shape and location of the observed body (e.g., planet or moon). Even if the optical photography uses an artificial light source, if the precise waveform and transmit time of that light source is not known, geolocation is performed in the same manner as for the ambient light case. Geolocation is performed very differently for SAR, or for its optical equivalent, synthetic aperture lidar (SAL). For SAR data, the energy in the return signal is broken up into pixels based upon the range to target, and azimuth. Azimuth is the angle with respect to the velocity vector of the sensor. Azimuth is proportional to the Doppler shift in the signal. Range to target is proportional to round-trip delay in the signal return. The primary purpose of SAR is to break the return signal into pixels to provide finer resolution than would otherwise be obtained. SAR works for three reasons: (1) the precise waveform is known; (2) the sensor is moving with respect to the target body; and to a lesser degree (3) the waveform is specifically chosen to optimize its utility for SAR processing.

In addition to improving resolution, SAR also changes how geolocation is performed. Initially, a SAR image is computed in the two-dimensional space of range and azimuth. For each such SAR pixel, one achieves geolocation by intersecting three surfaces: (1) a sphere centered on the sensor with a radius of the range; (2) a cone with the sensor at its apex, its axis along the direction of movement of the sensor and its interior angle twice the azimuth angle; and (3) the target body itself.

SARSME is a three-step procedure. First, one selects a set of recognizable landmarks that have each been observed in two different SAR images obtained at different times. Second, one geolocates the landmarks in the inertial frame as described above. Finally, one estimates the spin-state parameters by minimizing the misregistration error, that is, the apparent movement in Titan body fixed coordinates of the landmarks between observation times. In this manner, [Stiles et al. 2008](#) fit a 6-parameter spin model, including the right ascension and declination of Titan's pole, and Titan spin rate, at 19:16:25 UTC on Aug 1, 2006, and the first derivatives of these three parameters with respect to time. The strongest conclusion of the study was that the obliquity (angle between Titan's pole and the normal vector to its orbit) was 0.3 degrees, not 0 degrees, as had been assumed previously ([Davies et al. 1989](#)). When this obliquity was accounted for, the RMS misregistration of the observed features dropped from 20 km to 2 km. This initial misregistration number was determined for a relatively small portion of the Cassini Mission period. For this reason, there was not yet enough data to constrain longer-term variation in the pole (e.g., precession) and the rotation rate (e.g., forced libration). So the spin model used to archive the data was a constant-spin-rate, constant-pole-simplification of the model in [Stiles et al \(2008\)](#). When more data became available, it was found that the misregistration of the spin model increased slightly with time, leading to an overall misregistration error of 3.1 km. Table 8-4 shows the misregistration error for 2,427 tiepoints over the entire Cassini Mission. Three cases are shown: (1) the original pre-Cassini spin model, (2) the spin model used to produce the archived Cassini SAR data, and (3) a new spin model, described below, developed from the full mission data. The first two cases used a spherical model of Titan with a 2575-km radius to geolocate the SAR pixels. The last case uses SARTopo to determine the distance between each tiepoint and the center of Titan.

Table 8-4. Misregistration error over 2,447 features for three geolocation methods.

CASES	DESCRIPTION	ROOT MEAN SQUARE (KM)	95TH PERCENTILE (KM)
First datatake method.	Pre-Cassini Titan spin model, geolocated on reference sphere	17.1	29.3
Currently archived method	Archived Titan spin model, geolocated on reference sphere	3.1	5.8
Proposed method	New Titan spin model, geolocated using SARTopo	1.6	3.4

SARSME is complementary to SARTopo. SARTopo estimates heights from SAR calibration error and is insensitive to pixel misregistration error due to inaccuracy in our knowledge of Titan's spin. Both single-beam images used in SARTopo have the same horizontal location error due to spin-model error, so one can use the differences in their pixel values to determine a height estimate without concern for misregistration error. SARSME estimates the location of Titan's pole and its spin rate using SAR geolocation error and is insensitive to calibration error. Because calibration accuracy depends strongly upon attitude knowledge, SARTopo's largest error source is attitude knowledge error. Because SAR geolocation does not depend on spacecraft attitude, SARSME is insensitive to attitude error. Because of the relationship between the two techniques, each can be used to refine the results of the other.

The primary error source in SARSME involves human error in the matching up of landmarks between SAR images. Differences in resolution and observation geometry between SAR passes can make it hard to match up features, thereby compounding the risk of this error. One can reasonably assume that feature-matching error is random, so that one can beat down the errors by acquiring a large number of landmarks. The second largest error source is errors in locating the features due to errors in the presumed shape of Titan. This error source is not random, because Titan's shape diverges from a sphere in a systematic (nonrandom) manner that is primarily due to its observed oblateness. SARTopo heights or a shape model derived from those heights (e.g., [Zebker et al. 2009a](#)) can reduce systematic errors in the SARSME fits. Figure 8-1 illustrates the improvement in tiepoint misregistration error when SARTopo is used in geolocation, so that the data is orthorectified. Orthorectification, using an accurate model of Titan's shape in geolocation, improves the accuracy of the SAR pixel locations in an absolute sense and more importantly reduces the relative location errors between SAR images acquired at different times. Figure 8-1 is a scatter plot of misregistration error for all 2,427 features observed with and without orthorectification. Without orthorectification there were 144 features with apparent movement between observations greater than 5 km. With orthorectification, that number dropped to 21. We expect many of the remaining outliers to be regions where the expected errors in the SARTopo heights were large or where no nearby SARTopo heights were available. Orthorectification appears to help most in the northern-hemisphere lakes regions, where the surface heights were most different from the reference sphere.

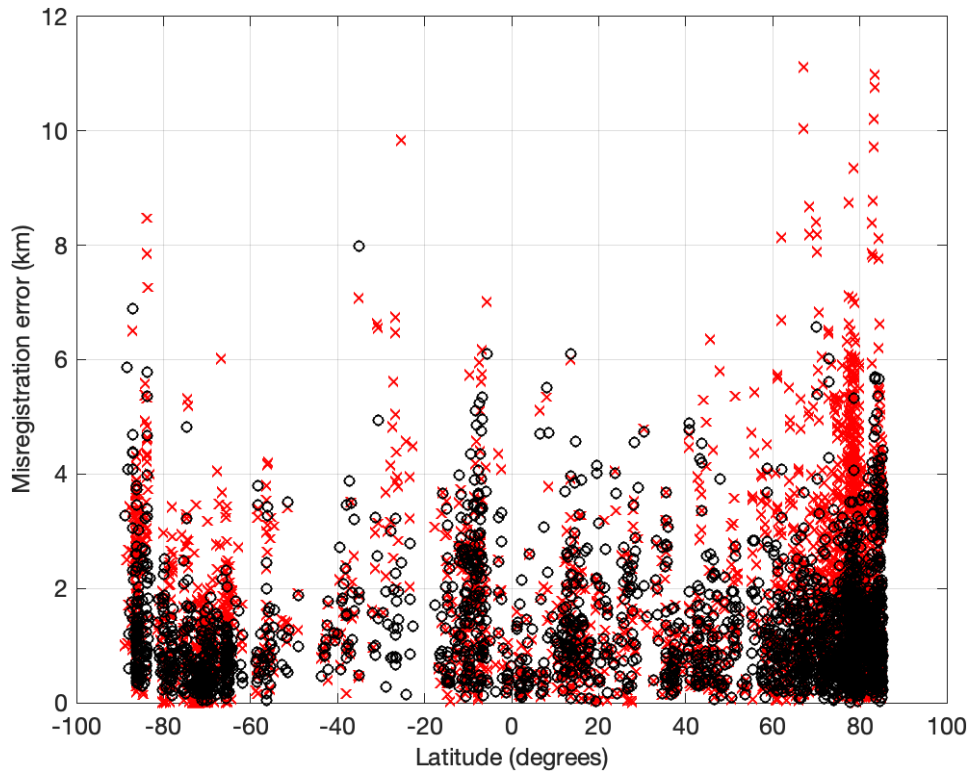


Figure 8-1. Misregistration error for all 2427 tiepoints vs. latitude. Improved spin model was used. Red "x" symbols are without orthorectification. Black circles are with orthorectification. Note the predominance of large misregistration errors in the high northern latitudes without orthorectification.

The data needed to perform SARSME are the same as needed to do SAR geolocation ([Table 8-3](#)) with the additions of the primary BIDR images (DATA/BIDR/BIF\*.IMG) and the latitude (DATA/BIDR/BIT\*.IMG), longitude (DATA/BIDR/BIN.IMG), and beam number mask (DATA/BIDR/BIM\*.IMG) backplanes. Landmarks are found in the SAR images and located by their line and sample numbers in each image. Analysts use the line and sample numbers to look up the apparent longitude and latitude in the backplanes. They can then determine the inertial coordinates of each feature by inverting the SAR geolocation process to recover the Doppler and range estimates from the latitudes and longitudes. To do this inversion one needs the Titan pole, rotation angle, and rotation rate and spacecraft velocity and position originally used to do the geolocation. Even though pixels in the SAR image are averaged from multiple single-look (single measurement cycle) SAR images, it is sufficient to pick the measurement cycle (burst) with the correct beam number mask that has a boresight ( $u_{\text{bore}}$ ) closest to the landmark. One can then look up all the relevant parameters for the selected measurement in the SBDR file.

After the publication of [Stiles et al \(2008\)](#), 9 more years of Cassini data were acquired. Dr. Stiles and his JPL colleague Dr. Bruce Bills used this data to obtain a new, longer-term model of Titan's spin that is both more accurate than the currently archived model and more physically reasonable, and thus more likely to predict the location of Titan surface features decades from now.

### 8.1.2 Titan Spin-Model Improvements

To geolocate SAR data, one needs to know the shape of the target body. One also needs to know how that body is oriented in space—that is, one needs to know how the body is rotating. The types of errors that result if that knowledge is missing can be broken up into (1) rotation-rate errors and (2) pole-location errors. Rotation-rate errors result in differences in the apparent longitude of features over time. Pole-location errors lead to differences in both latitude and longitude. The spin model used to geolocate the current Cassini SAR archive (henceforth referred to as simply *the current model*) has both types of errors. We know that rotational error dominates because misregistration error is primarily longitudinal (Figure 8-2). However, because the current model makes the nonphysical assumption that the pole does not precess, there is undoubtedly pole-location error as well. To reduce these known errors and to develop a more physically reasonable spin model, Dr. Bruce Bills developed a two-parameter model of the rotation rate that accounts for forced libration due to observed variations in Titan’s orbit. The two free parameters of this model are the free libration period and the long-term damping period. Values of these two parameters were chosen that minimized the RMS misregistration error of the 2427 tiepoints. For a more detailed description see [Section 8.1.2.a](#) below. A pole precession was determined from (1) the mean pole location during the Cassini observation of Titan that best minimized RMS misregistration on the same tiepoints, and (2) the dynamical relationship

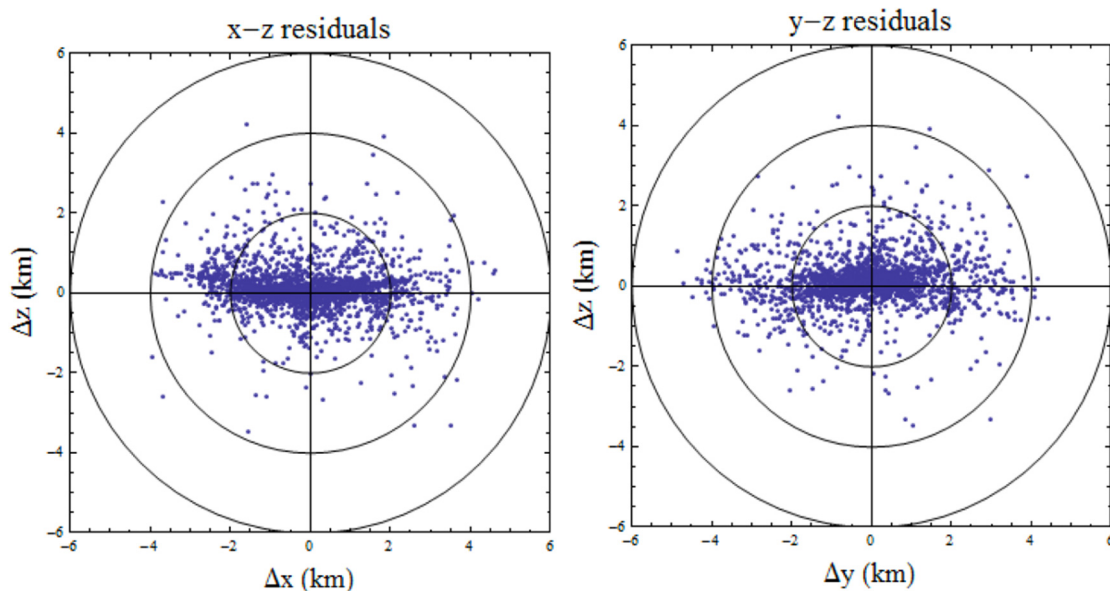


Figure 8-2. Longitudinal error dominates tiepoint error due to spin model. Left: The vertical axis shows the z-component (latitudinal) difference in tiepoint location between the two observations for the current spin model with orthorectification. The horizontal axis is the x-component. Note that the latitudinal (north/south) misregistration error is much smaller than the error in the x-component depicted for most tiepoints. Right: The equivalent plot comparing the z- and y-components has the same narrower spread in the z-component error.

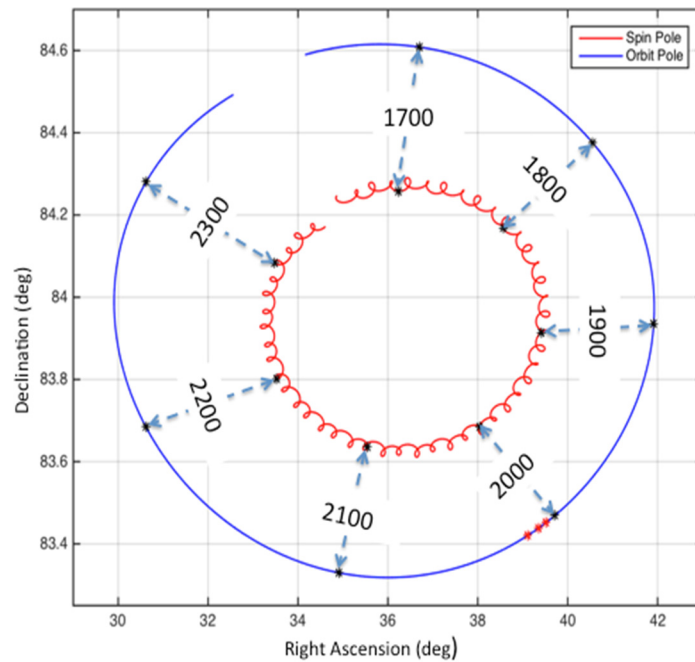


Figure 8-3. Spin- and orbit-pole precession. The red curve is the normal vector to Titan's orbit plane. The blue curve is our estimate of the spin axis of Titan.

between the spin pole and the orbit pole (normal vector to Titan's orbit plane) (Figure 8-3). Although the mean pole location was fit, the precession of the pole was determined solely from physical considerations without resorting to any fitting. Despite this fact, RMS misregistration errors were smaller for the precessing pole than for the best-fit nonprecessing pole.

*8.1.2.a. Rotation-Rate Variation Model.* We now describe a dynamic model for Titan's rotation-rate variations, in which a gravitational torque acts upon the triaxial body, attempting to keep its axis of least inertia oriented toward Saturn. That is the rotational configuration of lowest potential energy, and any deviation from that state will produce a restoring torque. We also include a dissipative torque, which attempts to keep the angular rates of orbital and rotational motion aligned. This is a simplified representation of tidal torques, which drive the body initially into synchronous rotation ([Goldreich and Peale 1966](#), [Efroimsky 2012](#)).

There are short-period librational torques, and associated rotational responses, in a fixed elliptical orbit ([Goldreich and Peale 1966](#), [Eckhardt 1981](#), [Comstock and Bills 2003](#)); but for Titan these are very small and will be ignored in this analysis. Instead, our interest is in longer-period forced librations, which are mainly due to long-period variations in the orbital mean longitude. Somewhat similar behavior is seen in librational motions of Mercury ([Peale et al. 2007](#), [Yseboodt et al. 2011](#)).

A primary theme of our approach to constructing dynamical models is that we use accurately computed variations in the orbital elements of Titan, along with appropriate control parameters, to produce our Titan rotation models. The orbital inclination and longitude of the ascending node determine the orientation of the orbit pole. The spin pole precesses about the orbit pole. For a synchronous rotator, the rotational azimuth angle (angle rotated in inertial space for a point on Titan's equator)

should closely track the orbital mean longitude. For both applications, we use orbital elements obtained from the JPL HORIZONS Web site, <https://ssd.jpl.nasa.gov/horizons.cgi>. We obtained values of the orbital elements at 5-day time steps for 1000 years. The first time is 1 January 1600, and the last time is 29 December 2599.

Figure 8-4 shows the variation in orbital mean longitude over that period.

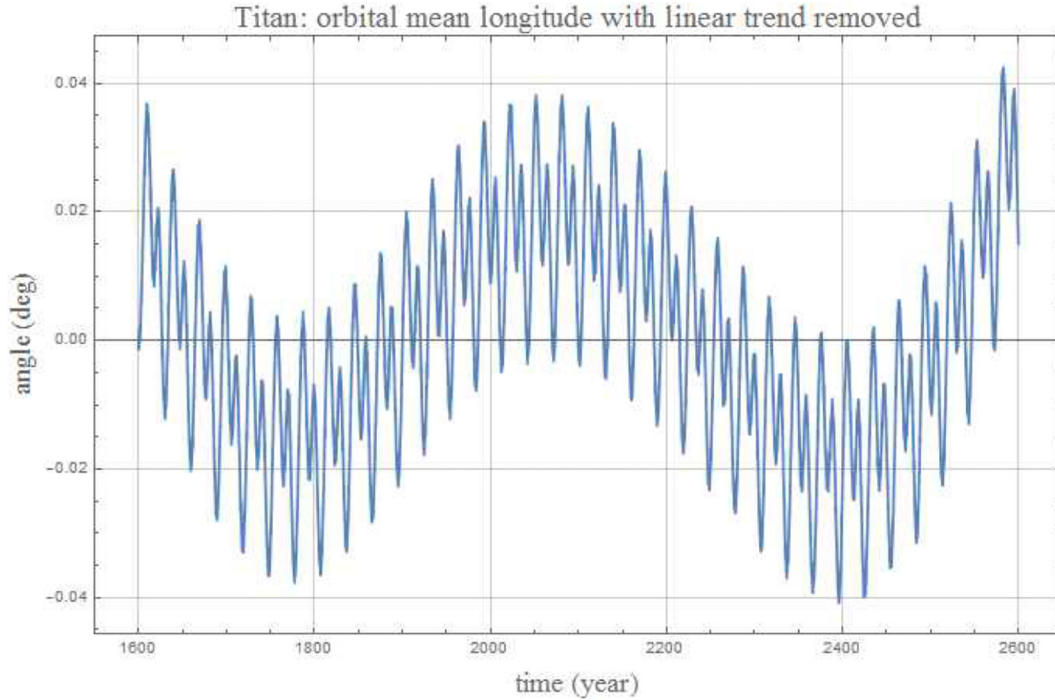


Figure 8-4. Titan orbital mean longitude variations for 1000 years, with linear trend removed.

The angular rates for orbital mean longitude,  $L$ , and rotation,  $\phi$ , are denoted  $dL/dt=\lambda$ , and  $d\phi/dt=\mu$ , respectively. In this notation, the torque balance can be written as

$$\frac{d\mu}{dt} = -\sigma^2(\phi - L) - \gamma(\mu - \lambda) \quad (1),$$

where  $\sigma$  is the free libration rate, and  $\gamma$  is a viscous damping rate. The damping term is motivated by the observation that the libration amplitude must remain finite, even if the forcing period is close to resonance with the free libration period. This form of the torque balance assures that both the angles ( $L$ ,  $\phi$ ) and rates ( $\lambda$ ,  $\mu$ ) of the orbital and rotational motions stay close together.

We express the mean longitude time variation  $L[t]$  (see Figure 8-4) as a linear term  $L_0+\lambda_0t$  plus a sum of periodic terms, each of the form  $\alpha_j e^{its_j}$ , where  $\alpha_j$  is a complex constant containing amplitude and phase information and  $s_j$  is a real frequency. It follows from Equation (1) that the rotation angle  $\phi(t)$  can be expressed similarly as  $L_0+\lambda_0t$  plus a sum periodic terms of the form  $\beta_j e^{its_j}$ , where each  $\beta_j$  coefficient is computed from each  $\alpha_j$  coefficient by  $\beta_j=\alpha_j F(\sigma,\gamma,s_j)$ . The amplitude of  $F$  for various ratios of  $\gamma/\sigma$  is shown in Figure 8-5 as a function of  $s/\sigma$ .

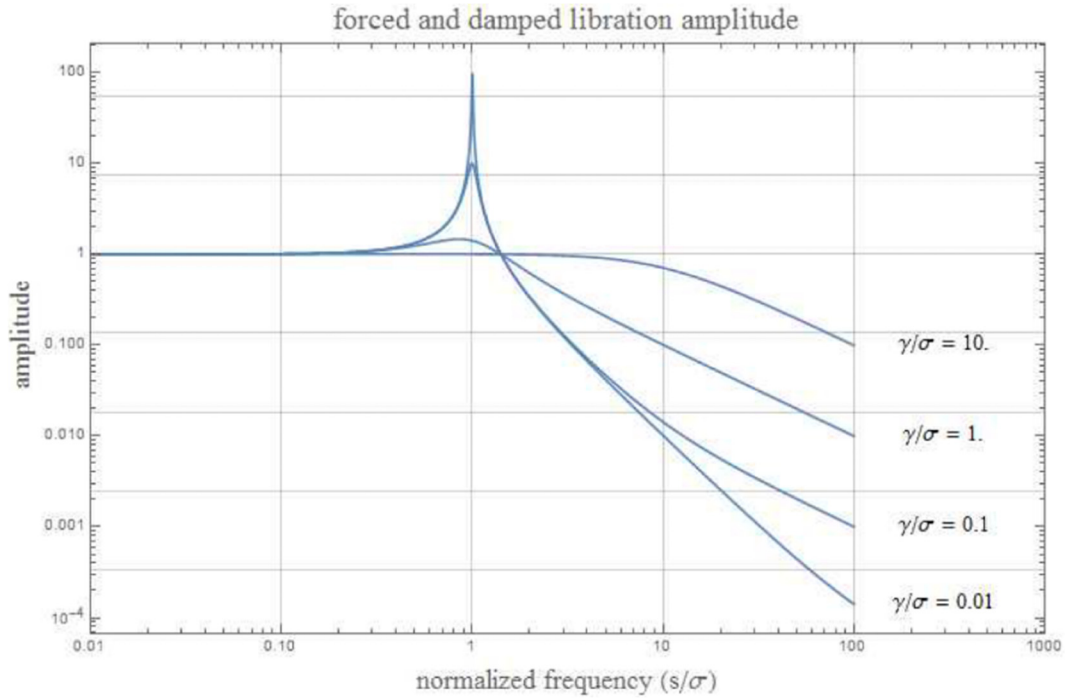


Figure 8-5. Amplitude of librational admittance  $F$ .

Given  $\sigma$  and  $\gamma$ , and time  $t$ , the rotation azimuth angle is given by:

$$\phi[\sigma, \gamma, t] = L_0 + \lambda_0 t + \sum_{j=1}^N F[\sigma, \gamma, s_j] \alpha_j e^{i s_j t} \quad (2)$$

Using the pole precession model described in [Section 8.1.2.b](#) below, and Equation (2), we determine a rotation matrix  $M[t, \sigma, \gamma]$  from inertial space to Titan body fixed coordinates for each time  $t$ , free libration rate  $\sigma$ , and damping rate  $\gamma$ . Using the known Cassini spacecraft position and velocity in inertial space with respect to the center of Titan, the measured radar azimuth (Doppler) and range, and the Titan surface heights from SARTopo, we determine the Titan-centered inertial coordinates of each tiepoint at each observation time, as described in [Section 8.1.1](#). We then compute the Titan body fixed coordinates for the  $k^{\text{th}}$  tiepoint at both observation times as follows:

$$p_{1k} = M[t_{1k}, \sigma, \gamma] P_{1k} \quad (3)$$

$$p_{2k} = M[t_{2k}, \sigma, \gamma] P_{2k} \quad (4)$$

Here  $t_{1k}$  and  $t_{2k}$  are the first and second observation times of the  $k^{\text{th}}$  tiepoint,  $P_{1k}$  and  $P_{2k}$  are its Titan-centered inertial coordinates, and  $p_{1k}$  and  $p_{2k}$  are its Titan body fixed coordinates.

We compute the RMS misregistration error  $\varepsilon(\sigma, \gamma)$  as follows:

$$\varepsilon(\sigma, \gamma) = \sum_{k=1}^{2427} \|p_{1k} - p_{2k}\| \quad (5)$$

We vary  $\sigma$  and  $\gamma$  until we find a minimal  $\varepsilon$ . Figure 8-6 depicts how  $\varepsilon$  varies with free libration rate  $\sigma$  for a constant damping rate. For ease of understanding, we henceforth refer to free libration period and damping period, which are the inverses of  $\sigma$  and  $\gamma$ , respectively. Figure 8-7 shows a contour plot of  $\varepsilon(\sigma, \gamma)^2$  in the near vicinity of the absolute minima, with free libration period of 1340.1 days and damping period of 9000 years.

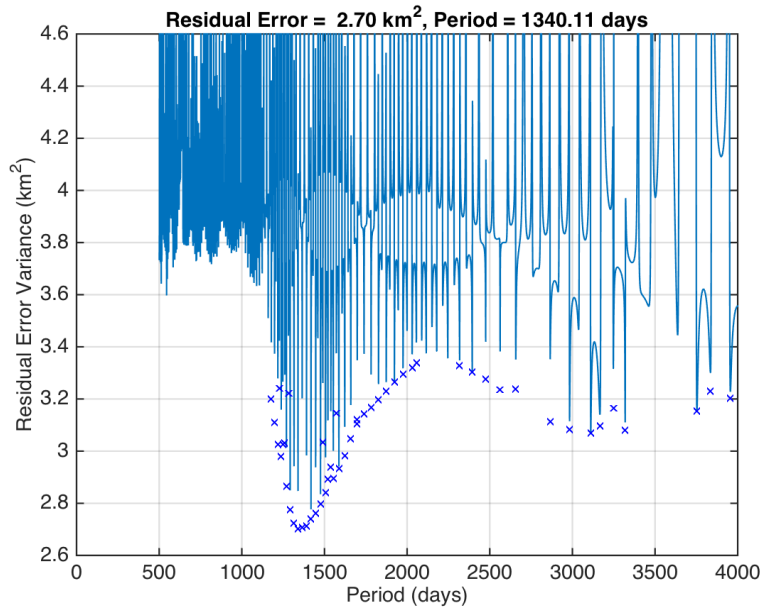


Figure 8-6. Mean square misregistration error versus free libration period. The y-axis is  $\epsilon(\sigma, \gamma)^2$  for a 10,000-year damping period. The curve is sampled every 0.5 days in free libration period. The blue "x" symbols denote the precise minima in both free libration and damping period for the lowest 50 minima. Note that the absolute minima is  $\epsilon^2=2.7 \text{ km}^2$ , that is  $\epsilon=1.6 \text{ km}$ .

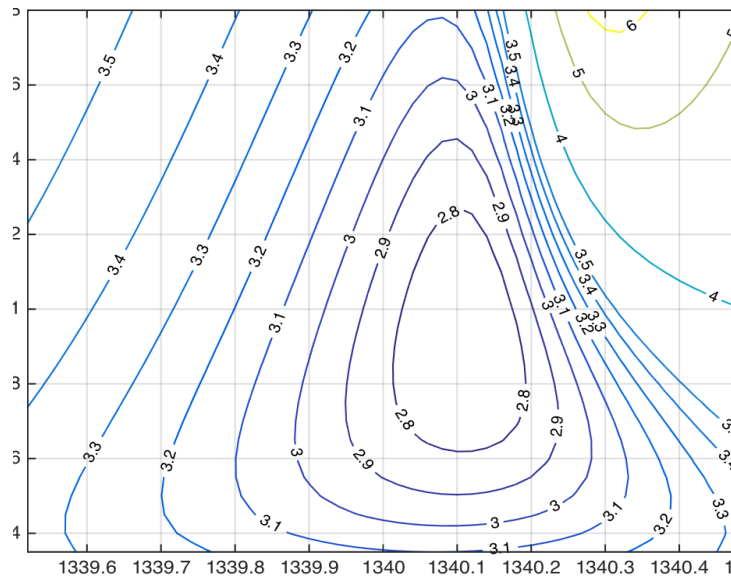


Figure 8-7. Contour plot of mean square misregistration error near the absolute minima. Y-axis is damping period in years, X-axis is free libration period in days.

*8.1.2.b. Pole Precession Model.* In this section, we briefly describe the precessional motions of the orbit and spin poles of Titan. The spin pole precession is slow enough that the  $\sim 10$  year time span of Cassini RADAR data mainly sees motion of the spin pole which is well approximated by a linear trend in right ascension and declination; nonetheless, we develop a longer term model so we can accurately predict Titan's

orientation further into the future. One reason we know our model is consistent is that the sub-Saturn point on Titan, while varying within each orbit, does not have longer-term variation, so that Titan remains tidally locked over the entire 1000-year period for which we have orbit data.

We use the RADAR data to provide an initial condition and use a dynamical model of spin pole precession to give us the rates of motion. Titan's orbit plane has a small inclination to Saturn's equatorial plane but a relatively large inclination to Saturn's heliocentric orbit plane. Solar torques attempt to make Titan's orbit pole precess about Saturn's orbit pole, and torques from the oblate figure of Saturn attempt to make it precess about Saturn's spin pole. Motion in such cases, where two competing torques act about different axes, are often best referred to an intermediate axis, perpendicular to the local Laplace surface [Tremaine et al. 2009]. A principal advantage of that perspective is that the precession about the axis perpendicular to the Laplace surface is very nearly uniform in rate. The combination of gravitational and dissipative torques, acting upon the triaxial figure of Titan, causes the spin pole to precess about the orbit pole. If the orbit pole were inertially fixed, the obliquity damping would eventually lead to perfect alignment of the spin and orbit poles. However, in a case like Titan, where the orbit pole is also precessing, the fully damped spin state has the obliquity adjusted to a value in which the spin and orbit poles remain coplanar with the invariable pole. This is known as a Cassini state [Peale 1969]. By assuming a dynamic equilibrium and thus a Cassini state, and by fitting the best pole location for the time at the midpoint of the Cassini Mission, we derive the spin pole shown in [Figure 8-3](#).

Table 8-5 lists the top ten minima for precessing- and fixed-pole fits. Even though the parameters of the precession are not determined by fitting data, using the precessing-pole results in better fits with an absolute minima of  $\epsilon=1.6$  km as compared to 1.8 km for the best fixed-pole solution. The duration of the Cassini Mission was insufficiently long to distinguish among the best nine minima. This is true because the rotation azimuth angle  $\phi(t, \sigma, \gamma)$  does not differ significantly over the time span of the Cassini Mission among these minima. If we assume that random errors in the tiepoints are 1 km on each axis, Gaussian, and uncorrelated, a perfect spin model yields an error

Table 8-5. Ten best fits for fixed- and precessing-pole dynamic rotation models.

RANK	FIXED POLE			PRECESSING POLE		
	$\epsilon^2$ (KM <sup>2</sup> )	$1/\sigma$ (DAYS)	$1/\gamma$ (YEARS)	$\epsilon^2$ (KM <sup>2</sup> )	$1/\sigma$ (DAYS)	$1/\gamma$ (YEARS)
1	3.221	1315.88	11600	2.702	1340.11	9300
2	3.224	1340.09	9300	2.706	1365.23	9300
3	3.247	1292.52	18200	2.712	1391.34	7500
4	3.253	1365.21	9300	2.724	1315.9	11600
5	3.283	1391.3	7500	2.74	1418.48	7500
6	3.323	1418.46	7500	2.761	1446.64	9300
7	3.34	1269.96	44000	2.775	1292.54	14600
8	3.376	1446.64	7500	2.796	1476.01	14600
9	3.376	1238.36	28000	2.84	1506.55	36000
10	3.411	1217.65	14600	2.864	1269.99	36000

variance for the 2427 tiepoints in the range  $[2.92, 3.08]$  km<sup>2</sup> with 95% probability. So  $3.08-2.92=0.16$  km<sup>2</sup> is the amount of decrease in the residual that we can be 95% sure is not due to random chance. We can thus confidently exclude minima that have variance 0.16 km<sup>2</sup> more than the best fit. By this reasoning we can exclude the tenth-lowest minima and all minima with residuals greater than that, but we cannot exclude any of the lowest nine minima. While this ambiguity is important to scientists who wish to know the free libration and damping periods of Titan in order to better understand its internal structure, it does not matter much for the purpose of improving the alignment of Cassini SAR imagery. We use the absolute best fit—but if we had used any of the top nine it would make an insignificant difference in SAR pixel-location accuracy.

The MATLAB code snippet shown below implements the first-rank spin model from Table 8-5. The code uses an approximate periodic model to avoid the need to incorporate the entire 1000-year HORIZONS Titan orbital mean longitude data set ([Figure 8-4](#)). The differences from tiepoint positions obtained using the full model described above are on the order of 1 m. Given a time  $t$ , the MATLAB model yields the rotation matrix  $M$ .

```
function [M]=getM_final(t)
    %%% This routine computes the rotation matrix M to go from inertial to body
        fixed coordinates
    %%% given a time t in seconds since Jan 1, 2000, 12:00 PM UTC.
        (Note that 12:00 PM is noon, not midnight.)

    %%% Rotation model parameters
    model.ra=36.31167338; % J2000 Pole Right ascension in degrees
    model.dec=83.97814793; % J2000 Pole declination
    model.pm=189.6462471; % J2000 Prime meridian orientation
    model.N_pole_period=3; % Number of periodic terms in pole
    model.pole_period=[2.4252 7.2756 3.6378 ]; %Pole periods in Julian centuries

    % pole periodic term coefficients
    model.ra_acos=[-0.04111 3.2251 0.21872 ];
    model.ra_asin=[-0.067951 -4.9209 0.31223 ];
    model.dec_acos=[-0.0057535 -0.53258 0.02932 ];
    model.dec_asin=[0.0022929 -0.34822 -0.034548 ];

    % Long term spin rate
    model.w=22.57697476;

    % Number of periodic terms in prime meridian
    model.N_spin_period=19;
```

```

% Prime meridian periods in days
model.spin_period=[1340.1 21518 32278 43037 53796 ...
64555 75314 86074 10759 5379.6 ...
3586.4 2689.8 2151.8 1793.2 1537 ...
1344.9 88581 2.6574e+05 1.3287e+05 ];

% Prime meridian periodic term coefficients
model.spin_acos=[0.044238 -0.00027595 0.00015837 -0.00066762 0.002548 ...
-0.0048052 0.0023819 0.0042475 0.0077164 -0.0089309 ...
-0.0013046 -2.1249e-05 -6.4822e-06 8.7773e-06 4.2238e-05 ...
0.00176 0.03813 -3.2075 -0.21714 ];
model.spin_asin=[0.030685 6.8923e-05 -8.2119e-05 0.00021903 -0.00038963 ...
0.0016994 -0.005073 0.0049381 -0.0085448 0.0037722 ...
-0.00059496 -0.00012837 -3.9979e-05 8.6978e-06 -1.9703e-05 ...
-0.0023689 0.066716 4.8901 -0.31163 ];

% constants for converting to/from degrees/radians
dtr= pi/180;
rtd= 1/dtr;

% time unit conversions
second_to_day=1/(24*3600);
second_to_cent=1/(100*365.25*24*3600);

% Copy model fields into variables for convenience
ra0=model.ra;
dec0=model.dec;
theta0=model.pm;
w0=model.w;

% Get times in other units
cent=t/(365.25*100*24*3600); % time in centuries
d=t*second_to_day; % time in days

% Convert J2000 Right ascension and declination into Euler angles in radians
alpha=pi/2-dec0*dtr;

```

```

beta=pi/2+ra0*dtr;

% Compute third Euler angle as a function of time
theta=theta0*dtr + w0*d*dtr;
for c=1:model.N_spin_period
cw=cos(2*pi*d/model.spin_period(c));
sw=sin(2*pi*d/model.spin_period(c));
theta=theta+dtr*model.spin_acos(c)*cw+dtr*model.spin_asin(c)*sw;
end

% Compute other two Euler angles as a function of time
for c=1:model.N_pole_period
cp=cos(2*pi*cent/model.pole_period(c));
sp=sin(2*pi*cent/model.pole_period(c));
alpha=alpha-dtr*model.dec_acos(c)*cp-dtr*model.dec_asin(c)*sp;
beta=beta+dtr*model.ra_acos(c)*cp+dtr*model.ra_asin(c)*sp;
end

%% Compute rotation Matrix from Euler angles
%rotate desired pole location to prime meridian
M3=[cos(beta),sin(beta),0;-sin(beta),cos(beta),0;0,0,1];

%rotate pole to z
M2=[1,0,0;0,cos(alpha),sin(alpha);0,-sin(alpha),cos(alpha)];

%rotate prime meridian to its correct location
M1=[cos(theta),sin(theta),0;-sin(theta),cos(theta),0;0,0,1];
M=M1*M2*M3;

```

## 8.2 Study 2: SAR Stereo

Three developments have been crucial in bringing us to the current state in which detailed stereo DTMs can be derived for a large and growing collection of areas of Titan. The first is the acquisition of the overlapping SAR images required as inputs. Prior to T18 on September 23, 2006, RADAR had acquired seven SAR images, none of which overlapped. Beginning with T18 and continuing throughout the mission, nearly every new image overlapped at least one and sometimes several prior images. Not only were voids in the map of Titan gradually filled, making incidental overlaps more likely, but mission designers also became aware of the value of stereo imaging for understanding the satellite and deliberately searched for stereo opportunities. Because of these effects, stereo pairs accumulated at a rate that accelerated over time. The

second step has been the identification and elimination of major errors in Titan cartography and geodesy resulting from the lack of an accurate model of Titan's rotation prior to the mission. The rotation modeling SARSME technique described above has led to the production of reprocessed images that coregister much more accurately, facilitating stereo comparison efforts. The final key ingredient for extensive stereo mapping has been the development of the needed software tools. Useful "spot" measurements of relative elevations were obtained in a few cases shortly after the acquisition of the stereo pairs by making manual measurements of the parallax between features in two images and then using a simplified version of the imaging geometry to convert parallaxes to height differences ([Kirk et al. 2007a, c](#)). The formulae for converting parallax to height are given below. To go beyond point measurements and collect DTMs of extensive areas requires more sophisticated software that combines automated and manual image-measurement capabilities, and the ability to derive reliable absolute as well as relative heights, which requires a full model of the geometry of image formation, known as a "sensor model."

The approach taken by CRST members at the USGS ([Kirk and Howington-Kraus 2008a](#), [Kirk et al. in prep](#)) has been to adapt a commercial stereo-mapping software system for use with RADAR data by developing the needed sensor model and taking advantage of the other features the system provides. This approach works because radargrammetry is analogous to photogrammetry as commonly carried out with images from optical cameras ([Slama 1980](#)), though it is based on a slightly different geometrical construction. In either discipline, an image represents a two-dimensional projection of a three-dimensional world, and a given pixel could correspond to one or more points along a given curve in space. In the more familiar case of optical images this curve is a straight line through the detector pixel and the optical center of the camera (hence the term "colinearity equations" for the fundamental principle of photogrammetry), but for a SAR image it is a circle of constant range and Doppler frequency centered on the flight path. Note that while uncertainties in the location and velocity of the spacecraft will affect the range and Doppler measurements, the pointing of the spacecraft does not enter into the measurements. This insensitivity of the image-formation process to pointing simplifies the analysis of the images and leads to greater accuracy because an error source that is important in photogrammetry can be ignored. If the same point can be identified in two images, the location of the point can be determined as the intersection of the two corresponding curves (or, in the presence of measurement errors, midway between the closest approach of two curves that do not precisely intersect). The precision of an elevation estimate from stereo then depends on three factors: the error  $\rho$  (in pixels) with which corresponding points in two images can be measured; the resolutions of the images; and the geometry of intersection of the circular loci for the two images, which determines the ratio of parallax to height. The dimensionless matching error  $\rho$  is often taken to be 0.2 pixel for optical images, but can be expected to be larger for radar images both because of the influence of speckle noise and because the pixel separation is chosen to deliberately oversample the true resolution. The CRST generally produces DTMs of Titan from the "full-resolution" 256-pixel/degree images. The ground-sample distance (GSD) of these images is 175 m, roughly a factor of two smaller than the best resolution obtained near closest approach, which is on the order of 300 m ([Elachi et al. 2004](#)).

Empirical comparisons of stereo and SARTopo data suggest that a matching precision of  $\rho = 1.4$  pixels can be obtained ([Kirk et al. in prep](#)).

It is simplest to begin by considering pairs of images with parallel flight tracks, in which case the circular loci are coplanar, and the geometry is fully characterized by the incidence angles of the images. Because the illumination in radar images comes from the spacecraft, there are conflicting requirements on the incidence angles. Image matching is most successful when the resemblance between the images is maximized, requiring same-side illumination and viewing with incidence angles as similar as possible. Unfortunately, this also minimizes the strength of stereo and increases the vertical errors. Conversely, opposite-side viewing provides very strong stereo convergence but can make the identification of matching points in the images much more difficult. More complex imaging geometries, in which the image strips cross at an angle  $\alpha$ , are intermediate between the same-side and opposite-side cases in both ease of matching and stereo strength, but are generally closer to the opposite-side case. The limits of acceptable imaging depend critically on the terrain, however. [Leberl et al. \(1992a\)](#) found that Magellan stereo pairs with  $\alpha > 30^\circ$  were not useful, but this was for rugged terrain near the north pole of Venus in which the images dominantly showed slope shading. [Howington-Kraus et al. \(2006\)](#) found that, in the Venusian lowlands, where relief is subtle and most of the information in the image comes from intrinsic backscatter variations (which do not change appearance with the illumination) rather than shading, opposite-side imaging is preferred in practice. The situation for most of Titan is similar, with low slopes and strong intrinsic variations in radar brightness, so that opposite-side or high-angle stereo pairs are useful except perhaps in some mountainous areas ([Kirk et al. in prep](#)). For two images with incidence angles  $i_1$  and  $i_2$ , matching uncertainty  $\rho$  in pixels, and ground-sample distance  $GSD$  between pixels in meters, the expected vertical precision (EP) is:

$$EP = \frac{\rho GSD}{p/h}, \quad (6)$$

where  $p/h$  is the parallax-to-height ratio set by the imaging geometry. For the simple case of parallel image tracks, this is ([Leberl et al. 1992b](#))

$$\epsilon \quad p/h = |\cot(i_1) \mp \cot(i_2)|, \quad (7)$$

where the minus sign applies to same-side imaging and the plus sign to opposite-side imaging. For a nominal pair of Cassini RADAR high-resolution SAR images with  $i_1 = 10^\circ$ ,  $i_2 = 20^\circ$ , Equations 6 and 7 give  $EP = 80$  m for same-side imaging but 30 m for opposite-side. For the case of images that cross at an angle  $\alpha$ , the expression for the parallax-height ratio generalizes to

$$p/h = \sqrt{\cot^2(i_1) + \cot^2(i_2) - 2\cot(i_1)\cot(i_2)\cos(\alpha)}. \quad (8)$$

Because of the need to compare finite image areas (e.g., matching patches no smaller than 3–5 pixels across), the minimum spacing for independent height estimates or “posts” is normally given as 3–5 pixels, but the case of radar is more likely limited to several times the actual resolution. The CRST typically produced Titan DTMs with a post spacing of 8 pixels or 32 posts/degree ( $\sim 1.4$  km/post). This spacing might oversample the achievable resolution for DTMs made with images of lower resolution (i.e., the ends of the image strips, obtained at distances greater than closest approach).

The data required to do SAR stereo are the same as those required for SARSME. The 8-bit/pixel logarithmically scaled BDRs are used as the images for feature-matching, and information about the beam, burst, and time of observation of a given pixel and the spacecraft position and velocity at this time are derived from the corresponding SBDR. To speed the sensor-model calculation, the appropriate burst identifier for each pixel is precomputed from the SBDR information and stored in a burst ID map file in the same projection as the image.

## 9 Obtaining Cassini RADAR Data Products

Under the direction of NASA's Science Mission Directorate, the PDS archives and distributes scientific data from NASA planetary missions, astronomical observations, and laboratory measurements. The intent of the PDS is to ensure the long-term usability of NASA data and to stimulate research. It is a worldwide resource for scientists, as well as the public. PDS products must be peer-reviewed, well documented, and easily accessible through an online catalog system. The PDS works with project teams to help them design products that can be released quickly and used easily.

The PDS is made up of eight nodes: Atmospheres, Geosciences, Planetary Plasma Interactions, Ring-Moon System, Small Bodies, Engineering, Cartography and Imaging Sciences, and Navigation and Ancillary data. The nodes are geographically distributed around the U.S., and several have "subnodes" to support a specific aspect of the node's discipline. An expert in the subject discipline leads each node, and each node has an advisory group.

Cassini data were due to the PDS 9–12 months after acquisition, delivered every 3 months. PDS must still validate those data before they are considered archived. This requirement might have resulted in a delay between the time when Cassini delivered data and the time when PDS made the data available. Alternately, PDS might have chosen to put data online while they were being validated. PDS urges caution when using any data that have been released to PDS for less than three months.

RADAR data sets are archived by the PDS Cartography and Imaging Sciences Node at the Jet Propulsion Laboratory and at USGS's Astrogeology Science Center. To download Cassini RADAR data from the PDS Imaging Node site, the user can find a complete set of links at <https://pds-imaging.jpl.nasa.gov/volumes/radar.html> (see Figure 9-1).

In addition, a number of Cassini data products (RADAR and others) are publicly available through the NASA Planetary Photojournal (<http://photojournal.jpl.nasa.gov/target/Titan>) (Figure 9-2).

The International Astronomical Union's (IAU's) Gazetteer of Planetary Nomenclature (<http://planetarynames.wr.usgs.gov/>) contains labeled images of features on Titan, as well as all of the other bodies in the solar system. The IAU Working Group for Planetary System Nomenclature (WGPSN) is responsible for identifying types of features to be named and for providing names for individual features so that they can be referenced easily. Many features on Titan have been named, with feature types including Albedo Feature, Arcus, Crater, Facula, Fluctus, Flumen, Insula, Labyrinthus, Lacuna, Lacus, Large Ringed Feature, Macula, Mare, Planitia, Regio, and Virga. The Gazetteer contains the locations and labeled images for each feature, as well as definitions of feature types.

## Cassini Radar Volumes

Online data volumes may be found at one or more sites. To access a volume, click on the icon(s) shown by the volume name. (IN - Imaging Node; DN - Data Node)										
Online Data Volumes for ISS, Radar, VIMS and Cartographic Map products can be found by clicking on the links to the right	<a href="#">ISS Raw Ground Calibration</a>	<a href="#">ISS Earth/Venus/Jupiter</a>	<a href="#">ISS Saturn</a>	<a href="#">ISS Cartographic Maps</a>	<a href="#">Radar</a>	<a href="#">VIMS</a>				
Cassini RADAR Users Guide - (May 3, 2017)										
Cassini Radar Instrument										
<a href="#">Volume 3 Documentation</a>			Contains a set of scatterometer and radiometer data that were obtained during the Earth Flyby, Aug 18, 1999. The radar observed portions of the South Pacific and South America							
<a href="#">Volume 6 Documentation</a>			Seq C23, Jan 3, 2001; contains radiometer only data acquired during a set of Jupiter scans. These data were used to analyze synchrotron emission from Jupiter's radiation belts							
<a href="#">Volume 9 Documentation</a>			Seq C26, Jul 5, 2001; contains radiometer only data acquired during a Sun scan. It is intended for calibration of the beam 3 antenna pattern. Beam 3 is the central beam used for radiometry, scatterometry, and altimetry							
<a href="#">Volume 11 Documentation</a>			Seq C27, Aug 28, 2001; contains radiometer data acquired during a Sun scan. These data were used to produce the 5 beam patterns							
<a href="#">Volume 32 Documentation</a>			Seq S01, Jun 11, 2004; contains a distant scatterometer/radiometer observation of Phoebe. In this observation, the target is smaller than the antenna beam main lobe							
<a href="#">Volume 34 Documentation</a>			Seq S05, Oct 26, 2004; contains a distant scatterometer/radiometer observation of Titan. In this observation, the target is larger than the antenna beam main lobe							
<a href="#">Volume 35 Documentation</a>			Oct 27 2004; contains Cassini Radar Burst Ordered Data Record and Basic Image Data Record products including SAR Imagery from Titan Flyby TA							
<a href="#">Volume 36 Documentation</a>			Seq S05; contains a distant radiometer observation of Titan obtained on Nov 6, 2004							
<a href="#">Volume 40 Documentation</a>			Seq S07, Dec 31, 2004; contains a distant scatterometer/radiometer observation of Iapetus. In this observation, the target is larger than the antenna beam main lobe							
<a href="#">Volume 42 Documentation</a>			Seq S08; contains a distant radiometer observation of Titan obtained on Jan 26, 2005							
<a href="#">Volume 43 Documentation</a>			Seq S08; contains a distant radiometer observation of Titan obtained on Jan 28, 2005							
<a href="#">Volume 45 Documentation</a>			Titan Flyby T3, Feb 15, 2005; contains Cassini Radar Burst Ordered Data Record and Basic Image Data Record products including SAR Imagery							
<a href="#">Volume 46 Documentation</a>			Seq S08, Feb 17, 2005; contains a distant scatterometer/radiometer observation of Enceladus. In this observation the target is smaller than the antenna beam main lobe							
<a href="#">Volume 47 Documentation</a>			Seq S09, Mar 9, 2005; contains a distant scatterometer/radiometer observation of Enceladus. In this observation the target is slightly smaller than the antenna beam main lobe							
<a href="#">Volume 48 Documentation</a>			Contains Burst Ordered (LBDR and SBDR) data products for the T4 flyby of Titan on Mar 31, 2005. Scatterometer and radiometer data are contained on this volume							
<a href="#">Volume 50 Documentation</a>			Seq S10, Apr 12, 2005; contains radiometry scans of Saturn and its rings							

Figure 9-1. Upper portion of the web page at <https://pds-imaging.jpl.nasa.gov/volumes/radar.html> (retrieved June 3, 2019). Titan pass numbers are shown in the notes in the fourth column. Note that the two links in Column 2 should produce identical results.

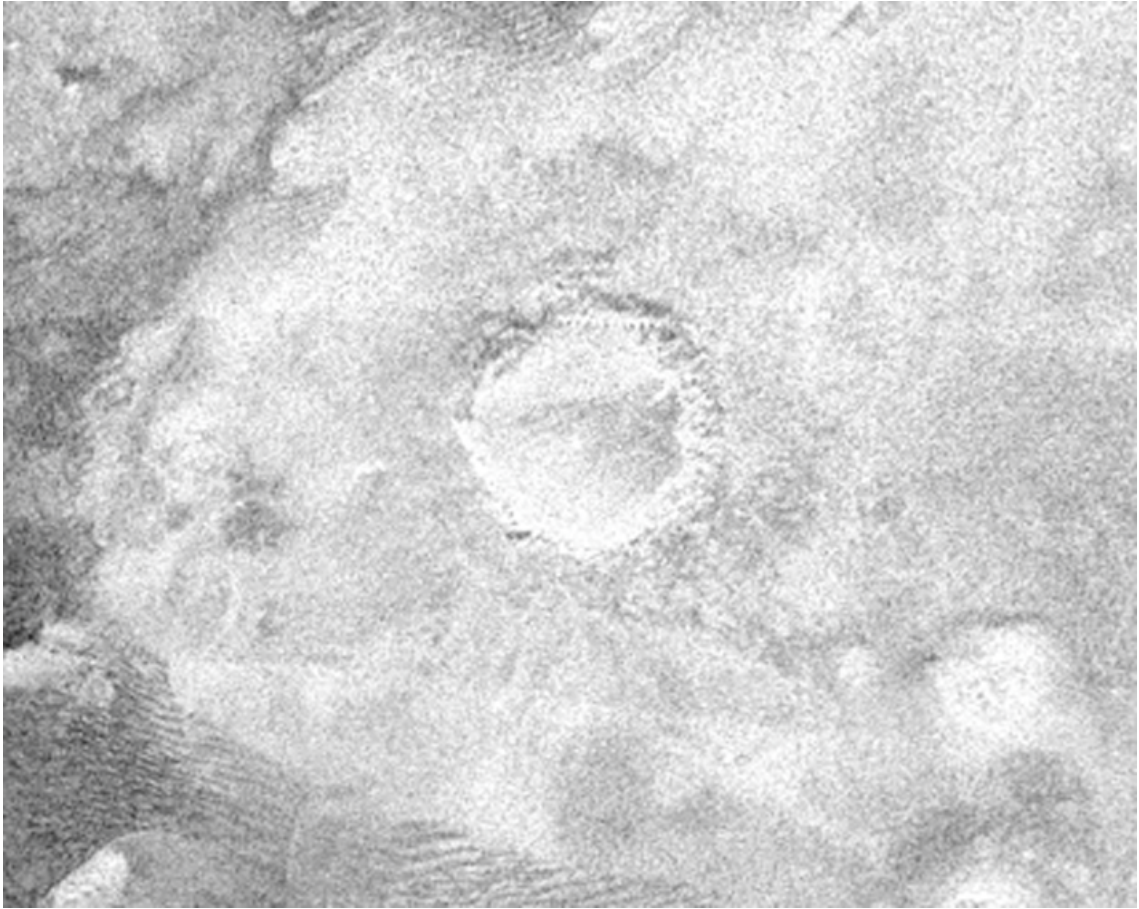


Figure 9-2. PIA07368. Cassini RADAR image of an impact crater on Titan.

## 10 Appendix 1: References and Selected Bibliography

- Aharonson, O., et al., 2008: Titan's global asymmetry in lake distribution and implications. *Amer. Geophys. Union Fall Mtg.*, Abstract P11D-08.
- Aharonson, O., A. G. Hayes, J. I. Lunine, R. D. Lorenz, M. D. Allison, and C. Elachi, 2009: An asymmetric distribution of lakes on Titan as a possible consequence of orbital forcing. *Nature Geosci.*, **2**, doi:10.1038/NCEO698.
- Alberti, G., Catallo, C., Festa, L., Flamini, E., Orosei, R., Papa, C., ... and Vingione, G. (2007). The processing of altimetric data (PAD) system for Cassini RADAR. *Memorie della Societa Astronomica Italiana Suppl.*, **11**, 68.
- Allison, M. D., 2000: A similarity model for the windy jovian thermocline. *Planet. Space Sci.*, **48**, 753–774.
- Allison, M. D., D. A. Godfrey, and R. F. Beebe, 1990: A wave dynamical interpretation of Saturn's polar hexagon. *Science*, **247**, 1061–1063, doi:10.1126/science.247.4946.10611990.
- Artemieva, N., and J. I. Lunine, 2005: Impact cratering on Titan II. Global melt, escaping ejecta and surface organics. *Icarus*, **175**, 522–533.
- Barnes, J. W., R. H. Brown, E. P. Turtle, A. S. McEwen, R. D. Lorenz, M. Janssen, E. L. Schaller, M. E. Brown, B. J. Buratti, C. Sotin, C. Griffith, R. Clark, J. Perry, S. Fussner, J. Barbara, R. West, C. Elachi, A. H. Bouchez, H. G. Roe, K. H. Baines, G. Bellucci, J.-P. Bibring, F. Capaccioni, P. Cerroni, M. Combes, A. Coradini, D. P. Cruikshank, P. Drossart, V. Formisano, R. Jaumann, Y. Langevin, D. L. Matson, T. B. McCord, P. D. Nicholson, and B. Sicardy, 2005: A 5-micron-bright spot on Titan: Evidence for surface diversity. *Science*, **310**, 92–95.
- Barnes, J. W., R. H. Brown, J. Radebaugh, B. J. Buratti, C. Sotin, S. Le Mouélic, S. Rodriguez, E. P. Turtle, J. Perry, R. Clark, K. H. Baines, and P. D. Nicholson, 2006: Cassini observations of flow-like features in western Tui Regio, Titan. *Geophys. Res. Lett.*, **33**, L16204, doi:10.1029/2006GL026843.
- Barnes, J. W., J. Radebaugh, R. H. Brown, S. Wall, L. Soderblom, J. Lunine, D. Burr, C. Sotin, S. Le Mouélic, B. J. Buratti, R. Clark, K. H. Baines, R. Jaumann, P. D. Nicholson, R. L. Kirk, R. Lopes, R. Lorenz, K. Mitchell, C. A. Wood, and the Cassini RADAR Science Team, 2007: Near-infrared spectral mapping of Titan's mountains and channels. *J. Geophys. Res.*, **112**, E11006, doi:10.1029/2007JE002932.
- Barnes, J. W., R. H. Brown, J. M. Soderblom, L. A. Soderblom, R. Jaumann, B. Jackson, S. Le Mouélic, C. Sotin, B. J. Buratti, K. M. Pitman, K. H. Baines, R. N. Clark, P. D. Nicholson, E. P. Turtle, and J. Perry, 2009: Shoreline features of Titan's Ontario Lacus from Cassini/VIMS observations. *Icarus*, **201**, 217–225.
- Birch, S. P. D., A. G. Hayes, A. D. Howard, J. M. Moore, and J. Radebaugh, 2016: Alluvial fan morphology, distribution and formation on Titan. *Icarus*, **270**, 238–247.
- Bolton, S. J., M. Janssen, R. Thorne, S. Levin, M. Klein, S. Gulkis, T. Bastian, R. Sault, C. Elachi, M. Hofstadter, A. Bunker, G. Dulk, E. Gudim, M. Hamilton, W. Johnston, Y. Leblanc, O. Liepack, R. McLeod, J. Roller, L. Roth, and R. West, 2002: Ultra-relativistic electrons in Jupiter's radiation belts. *Nature*, **415**, 987–991.

- Bonnefoy, I. E., A. G. Hayes, P. O. Hayne, M. J. Malaska, A. Le Gall, A. Solomonidou, and A. Lucas, 2016: Compositional and spatial variations in Titan dune and interdune regions from Cassini VIMS and RADAR. *Icarus*, **270**.
- Boubin, G. M., E. G. Reffet, J. Lunine, J. Radebaugh, R. M. Lopes, and the Cassini RADAR Science Team, 2005: Mapping and characterization of “cat scratches” on Titan. *Amer. Astron. Soc. Div. Planet. Sci. Mtg.*, Cambridge, England, September.
- Butler, B. J., and M. A. Gurwell, 2004: Radio wavelength observations of Titan with the VLA. *Bulletin of the American Astronomical Society*, **36**, 1075.
- Casarano, D., B. Ventura, C. Notarnicola, and F. Posa, 2007: Cassini RADAR: Observations of Titan’s surface features. *Proc. 5th Intl. Symposium on Retrieval of Bio and Geophys. Parameters from SAR Data for Land Applications*, ESA, Bari, Italy, September 25–28.
- Comstock, R. L., and Bills, B. G., 2003: A solar system survey of forced librations in longitude. *J. Geophys. Res.: Planets*, **108**(E9).
- Cordier, D., T. Cornet, J. W. Barnes, S. M. MacKenzie, T. Le Bahers, D. Nna-Mvondo, P. Rannou, and A. G. Ferreira, 2016: Structure of Titan’s evaporites. *Icarus*, **270**.
- Corlies, P., A. G. Hayes, S. P. D. Birch, R. Lorenz, B. W. Stiles, R. Kirk, V. Poggiali, H. Zebker, and L. Iess, 2017: Titan’s topography and shape at the end of the Cassini Mission. *Geophysical Res. Lett.*, **44**(23).
- Crapeau, M., S. Rodriguez, S. Le Mouélic, P. Paillou, C. Sotin, P. Encrenaz, and S. D. Wall, 2006a: Benefits of combining RADAR altimeter and VIMS data: Example using Ta and T13 flybys. *First Eur. Planet. Sci. Congress*, Berlin, Germany, September.
- Crapeau, M., S. Rodriguez, S. Le Mouélic, P. Paillou, C. Sotin, and S.D. Wall, 2006b: Cassini altimeter and VIMS complementarity: Example using observations over the same area from Ta and T13 Titan flybys. *38th Amer. Astron. Soc. Div. Planet. Sci. Mtg.*, Pasadena, CA, October.
- Cumming, I. G., and F. H. Wong, 2005: *Digital Processing of Synthetic Aperture Radar Data: Algorithms and Implementation*. Artech House, 660 pp.
- Curlander, J. C., and R. N. McDonough, 1991: *Synthetic Aperture Radar: Systems and Signal Processing*. Wiley, 672 pp.
- Davies, M. E., V. K. Abalakin, M. Bursa, G. E. Hunt, J. H. Lieske, B. Morando, R. H. Rapp, P. K. Seidelmann, A. T. Sinclair, and Y. S. Tjuflin, 1989: Report of the IAU/IAG/COSPAR working group on cartographic coordinates and rotational elements of the planets and satellites. *Celest. Mech. Dyn. Astron.*, **46**, 187–204.
- Davies, M. E., T. R. Colvin, P. G. Rogers, P. W. Chodas, W. L. Sjogren, E. L. Akim, V. A. Stepanyantz, Z. P. Vlasova, and A. I. Zakharov, 1992: The rotational period, direction of the north-pole, and geodetic control network of Venus. *J. Geophys. Res., Planets*, **97**, 13141–13151.
- Eckhardt, D. H., 1981: Theory of the libration of the moon. *The Moon and the Planets*, **25**(1), 3–49.
- Efroimsky, M., 2012: Bodily tides near spin–orbit resonances. *Celestial Mechanics and Dynamical Astronomy*, **112**(3), 283–330.
- Elachi, C., 1987: *Spaceborne Radar Remote Sensing: Applications and Techniques*. IEEE Press, 255 pp.

- Elachi, C., and J. J. Van Zyl, 2006: *Introduction to the Physics and Techniques of Remote Sensing* (Vol. 28). John Wiley & Sons.
- Elachi, C., M. D. Allison, L. Borgarelli, E. Encrenaz, E. Im, M. A. Janssen, W. T. K. Johnson, R. L. Kirk, R. D. Lorenz, J. I. Lunine, D. O. Muhleman, S. J. Ostro, G. Picardi, F. Posa, C. G. Rapley, L. E. Roth, R. Seu, L. A. Soderblom, S. Vetrell, S. D. Wall, C. A. Wood, and H. A. Zebker, 2004: RADAR: The Cassini Titan radar mapper. *Space Sci. Rev.*, **115**, 71–110, doi:10.1007/s11214-004-1438-9.
- Elachi, C., S. D. Wall, M. D. Allison, Y. Anderson, R. Boehmer, P. Callahan, P. Encrenaz, E. Flamini, G. Francescetti, Y. Gim, G. Hamilton, S. Hensley, M. A. Janssen, W. T. K. Johnson, K. Kelleher, R. L. Kirk, R. M. Lopes, R. D. Lorenz, J. I. Lunine, D. O. Muhleman, S. J. Ostro, F. Paganelli, G. Picardi, F. Posa, L. E. Roth, R. Seu, S. Shaffer, L. A. Soderblom, B. Stiles, E. R. Stofan, S. Vetrella, R. A. West, C. A. Wood, L. Wye, and H. A. Zebker, 2005a: Cassini RADAR's first look at Titan. *Lunar Planet. Sci. Conf.*, League City, TX, March 14–18.
- Elachi, C., S. D. Wall, M. D. Allison, Y. Anderson, R. Boehmer, P. Callahan, P. Encrenaz, E. Flamini, G. Francescetti, Y. Gim, G. Hamilton, S. Hensley, M. A. Janssen, W. T. K. Johnson, K. Kelleher, R. Kirk, R. Lopes, R. Lorenz, J. Lunine, D. Muhleman, S. Ostro, F. Paganelli, G. Picardi, F. Posa, L. Roth, R. Seu, S. Shaffer, L. Soderblom, B. Stiles, E. Stofan, S. Vetrella, R. West, C. Wood, L. Wye, and H. Zebker, 2005b: First views of the surface of Titan from the Cassini RADAR. *Science*, **308**, 970–974.
- Elachi, C., S. Wall, M. Janssen, E. Stofan, R. Lopes, R. Kirk, R. Lorenz, J. Lunine, F. Paganelli, L. Soderblom, C. Wood, L. Wye, H. Zebker, Y. Anderson, S. Ostro, M. Allison, R. Boehmer, P. Callahan, P. Encrenaz, E. Flamini, G. Francescetti, Y. Gim, G. Hamilton, S. Hensley, W. Johnson, K. Kelleher, D. Muhleman, G. Picardi, F. Posa, L. Roth, R. Seu, S. Shaffer, B. Stiles, S. Vetrella, and R. West, 2006a: Titan Radar Mapper observations from Cassini's Ta and T3 flybys. *Nature*, **441**, 709–713, doi:10.1038/nature0486.
- Elachi, C., S. D. Wall, M. D. Allison, Y. Anderson, R. Boehmer, P. Callahan, P. Encrenaz, E. Flamini, G. Francescetti, Y. Gim, G. Hamilton, S. Hensley, M. A. Janssen, W. T. K. Johnson, K. Kelleher, R. L. Kirk, R. M. Lopes, J. I. Lunine, K. Mitchell, D. O. Muhleman, G. Ori, R. Orosei, S. J. Ostro, F. Paganelli, G. Picardi, F. Posa, L. E. Roth, R. Seu, S. Shaffer, L. A. Soderblom, B. Stiles, E. Stofan, S. Vetrella, R. West, C. A. Wood, L. Wye, and H. A. Zebker, 2006b: Cassini RADAR's third and fourth looks at Titan. *37<sup>th</sup> Lunar Planet. Sci. Conf.*, Abstract 1249.
- English, M. A., L. M. Lara, R. D. Lorenz, P. R. Ratcliff, and R. Rodrigo, 1996: Ablation and chemistry of meteoric materials on Titan. *Advances in Space Research*, **12**, 157–160.
- Ford, J. P., J. J. Plaut, C. M. Weitz, T. G. Farr, D. A. Senske, E. R. Stofan, G. Michaels, and T. J. Parker, 1993: *Guide to Magellan Image Interpretation*, JPL Publication 93-24, Jet Propulsion Laboratory. [Available online at [http://history.nasa.gov/JPL-93-24/jpl\\_93-24.htm](http://history.nasa.gov/JPL-93-24/jpl_93-24.htm).]
- Franceschetti, G., and R. Lanari, 1999: *Synthetic Aperture Radar Processing*. CRC, 328 pp.
- Franceschetti, G., P. S. Callahan, A. Iodice, D. Riccio, and S. D. Wall, 2006: Titan, fractals, and filtering of Cassini altimeter data. *IEEE Trans. Geosci. and Remote Sensing*, **44**(8), August.

- Furfaro, R., J. S. Kargel, J. I. Lunine, W. Fink, and M. P. Bishop, 2010: Identification of cryovolcanism on Titan using fuzzy cognitive maps. *Planet. Space Sci.*, **58**, 761–779, doi:10.1016/j.pss.2009.12.003.
- Giuseppe, M., R. Merriggiola, A. Hayes, A. Lefevre, G. Tobie, A. Genova, J. Lunine and H. Zebker 2014: Shape, topography, gravity anomalies and tidal deformation of Titan. *Icarus*, **236**, 169–177.
- Goldreich, P., and S. Peale, 1966: Spin-orbit coupling in the solar system. *The Astronomical Journal*, **71**, 425.
- Griffith, C. A., J. M. Lora, J. Turner, R. H. Brown, M. G. Tomasko, L. Doose, and C. See, 2012: Possible tropical lakes on Titan from observations of dark terrain. *Nature*, **486**, 237–239, doi:10.1038/nature11165.
- Hamelin, M., A. Lethuillier; A. Le Gall, R. Grard, C. Beghin, K. Schwingenschuh, I. Jernej; J.-J. Lopez-Moreno, V. Brown; R. D. Lorenz, F. Ferri, V. Ciarletti, 2016: The electrical properties of Titan’s surface at the Huygens landing site measured with the PWA/HASI Mutual Impedance Probe. New approach and new findings. *Icarus*, **270**, 272–290.
- Hayes, A. G., 2010: Exploring lakes on Titan. *Astronomy Beat*, *Astron. Soc. Pacific*, **56**, September 20.
- Hayes, A. G., O. Aharonson, K. Lewis, K. Mitchell, R. Lorenz, P. Callahan, J. Lunine, R. Lopes, S. Wall, C. Elachi, G. Mitri, R. Kirk, Y. Gim, E. Stofan, and the Cassini RADAR Science Team, 2008a: Hydrocarbon lakes on Titan: Distribution and interaction with a porous regolith. *Geophys. Res. Lett.*, **35**, L09204, doi:10.1029/2008GL033409.
- Hayes, A. G., O. Aharonson, D. Stevenson, J. Lunine, R. Lorenz, K. Mitchell, R. Lopes, B. Stiles, R. Kirk, S. Wall, and the Cassini RADAR Science Team, 2008b: Titan’s global lake distribution and implied hydrocarbon hydrology from Cassini SAR. *Amer. Geophys. Union*, P11D-07.
- Hayes, A. G., O. Aharonson, S. Wall, C. Sotin, A. Le Gall, R. Lopes, M. Janssen, and the Cassini RADAR Science Team, 2008c: Joint analysis of Titan’s surface using the Cassini VIMS and RADAR instruments. *Bull. Amer. Astron. Soc.*, **40**, 457, DPS2008 P3406.
- Hayes, A. G., A. S. Wolf, O. Aharonson, H. Zebker, R. Lorenz, P., Paillou, S. Wall, and C. Elachi, 2010: Bathymetry and absorptivity of Titan’s Ontario Lacus. *J. Geophys. Res., Planets*, **115**, September, E09009, doi:10.1029/2009JE003557.
- Hayes, A. G., O. Aharonson, J. I. Lunine, R. L. Kirk, H. A. Zebker, L. C. Wye, R. D. Lorenz, E. P. Turtle, P. Paillou, G. Mitri, S. D. Wall, E. R. Stofan, K. L. Mitchell, C. Elachi, and the Cassini RADAR Science Team, 2011: Transient surface liquid in Titan’s polar regions from Cassini. *Icarus*, **211**(1), 655–671, doi:10.1016/j.icarus.2010.08.017.
- Hofgartner, J. D., A. G. Hayes, J. I. Lunine, H. Zebker, B. W. Stiles, C. Sotin, J. W. Barnes, E. P. Turtle, K. H. Baines, R. H. Brown, and B. J. Buratti, 2014: Transient features in a Titan sea. *Nature Geoscience*, **7**(7), 493.
- Howington-Krause, E., R. L. Kirk, D. Galuszka, and B. Redding, 2006: USGS Magellan stereomapping of Venus. *Eur. Planet. Sci. Congr.*, Berlin, September 18–22.
- Iess, L., N. J. Rappaport, R. A. Jacobson, P. Racioppa, D. J. Stevenson, P. Tortora, J. W. Armstrong, and S. W. Asmar, 2010: Gravity field, shape, and moment of inertia of Titan. *Science*, **327**, 1367, doi:10.1126/science.1182583.

- Imbriale, W. A., 2003: *Large Antennas of the Deep Space Network*. JPL Deep-Space Communications and Navigation Series, John Wiley and Sons, 302 pp. [Available online at <http://onlinelibrary.wiley.com/book/10.1002/0471728497>.]
- Jacobsen, R. E., D. L. Roth, D. M. Burr, C. Phillips, and K. L. Mitchell, 2008: Identification, mapping, and measurement of Titan fluvial features. *Amer. Geophys. Union*.
- Janssen, M. A., 1993: An introduction to the passive microwave remote sensing of atmospheres. Chapter 1 of *Atmospheric Remote Sensing by Microwave Radiometry*, M. Janssen, Ed. Wiley & Sons, 1–35.
- Janssen, M. A., R. Lorenz, C. Elachi, Y. Z. Anderson, R. A. Boehmer, Y. Gim, W. T. K. Johnson, K. D. Kelleher, R. M. Lopes, L. E. Roth, S. D. Wall, and R. D. West, 2005a: First mapping of Titan with the Cassini RADAR radiometer. *Bull. Amer. Astron. Soc.*, **36**, 1075.
- Janssen, M. A., F. Paganelli, R. Kirk, R. D. Lorenz, R. M. Lopes, and the Cassini RADAR Science Team, 2005b: Titan's surface properties from the Cassini RADAR radiometer. *Bull. Amer. Astron. Soc.*, **37**, 739.
- Janssen, M. A., R. D. Lorenz, F. Paganelli, R. L. Kirk, R. M. Lopes, and the Cassini RADAR Science Team, 2007: Absolutely calibrated 2-cm radiometry of Titan and implications. *38<sup>th</sup> Amer. Astron. Soc. Div. Planet. Sci. Mtg.*, Orlando, FL, October 7–12.
- Janssen, M. A., M. Allison, S. Gulkis, R. D. Lorenz, and K. D. Kelleher, 2008: Saturn's thermal emission at 2-cm wavelength and implications for atmospheric composition and dynamics. *Amer. Geophys. Union Fall Mtg.*, Abstract P11B-1278.
- Janssen, M. A., R. D. Lorenz, R. West, F. Paganelli, R. M. Lopes, R. L. Kirk, C. Elachi, S. D. Wall, W. T. K. Johnson, Y. Anderson, R. A. Boehmer, P. Callahan, Y. Gim, G. A. Hamilton, K. D. Kelleher, L. Roth, B. Stiles, A. Le Gall, and the Cassini RADAR Science Team, 2009: Titan's surface at 2.2-cm wavelength imaged by the Cassini RADAR radiometer: Calibration and first results. *Icarus*, **200**, 222–239, doi:10.1016/j.icarus.2008.10.017.
- Janssen, M. A., A. Le Gall, and L. C. Wye, 2011: Anomalous radar backscatter from Titan's surface. *Icarus*, **212**, 321–328.
- Janssen, M. A., A. Ingersoll, M. D. Allison, S. Gulkis, A. Laraia, K. Baines, S. Edgington, Y. Anderson, and K. Kelleher, 2013: Saturn's thermal emission at 2.2-cm wavelength as imaged by the Cassini RADAR radiometer. *Icarus*, **226**, 522–535.
- Janssen, M. A., A. Le Gall, R. M. Lopes, R. D. Lorenz, M. J. Malaska, A. G. Hayes, C. D. Neish, et al., 2016: Titan's surface at 2.18-cm wavelength imaged by the Cassini RADAR radiometer: Results and interpretations through the first ten years of observation. *Icarus*, **270**.
- Jaumann, R., R. H. Brown, K. Stephan, J. W. Barnes, L. A. Soderblom, C. Sotin, S. Le Mouélic, R. N. Clark, J. Soderblom, B. J. Buratti, R. Wagner, T. B. McCord, S. Rodriguez, K. H. Baines, D. P. Cruikshank, P. D. Nicholson, C. A. Griffith, M. Langhans, and R. D. Lorenz, 2008: Fluvial erosion post-erosional processes on Titan. *Icarus*, **197**(2), 526–538.

- Jennings, D. E., F. M. Flasar, V. G. Kunde, R. E. Samuelson, J. C. Pearl, C. A. Nixon, R. C. Carlson, A. A. Mamoutkine, J. C. Brasunas, E. Guandique, R. K. Achterberg, G. L. Bjoraker, P. N. Romani, M. E. Segura, S. A. Albright, M. H. Elliott, J. S. Tingley, S. Calcut, A. Coustenis, and R. Courtin, 2009: Titan's surface brightness temperatures. *Astrophys. J. Lett.*, **691**, L103–L105.
- Johnson, W. T. K., 2008: The Cassini mission to Saturn: Innovative design of the Ku-band Titan radar mapper, *PIERS*.
- Kirk, R. L., 2010: Mapping Titan from global geodesy to Huygens hydrology with RADAR...and a Dash of DISR. *Cassini-Huygens Legacy and Future Titan Exploration*, Barcelona, 13–15 January.
- Kirk, R. L., 2012: Titan's topography as a clue to geologic processes and landscape evolution. *Amer. Geophys. Union Fall Mtg. Suppl.*, Abstract P22B-02.
- Kirk, R. L., and E. Howington-Kraus, 2008a: Radargrammetry on three planets. *International Archives of Photogrammetry, Remote Sensing, and Spatial Information Sciences*, XXXVII, Part 4, "A Silk Road for Information from Imagery," Beijing, 3–11 July, 973–980 (DVD-ROM).
- Kirk, R. L., and E. Howington-Kraus, 2008b: Topography of Titan from stereoanalysis of Cassini RADAR images with a rigorous sensor model. *Titan after Cassini-Huygens Symposium*, Corpus Christi, TX, 7–11 July.
- Kirk, R. L., and E. Howington-Kraus, 2010: Radargrammetry on three planets: Mapping the Solar System's hidden corners. *Eos Trans. Amer. Geophys. Union Fall Mtg. Suppl.*, **91**(52), Abstract P33E-01.
- Kirk, R. L., P. Callahan, R. Seu, R. D. Lorenz, F. Paganelli, R. M. Lopes, C. Elachi, and the Cassini RADAR Science Team, 2005: RADAR reveals Titan topography. *Lunar Planet. Sci. Conf.*, XXXVI, Abstract 2227, Lunar and Planetary Institute, Houston, TX (CD-ROM).
- Kirk, R. L., E. Howington-Kraus, K. L. Mitchell, S. Hensley, B. W. Stiles, and the Cassini RADAR Science Team, 2007a: First stereoscopic radar images of Titan. *Lunar Planet. Sci.*, XXXVIII, Abstract 1427, Lunar and Planetary Institute, Houston (CD-ROM).
- Kirk, R. L., E. Howington-Kraus, K. L. Mitchell, S. Hensley, B. W. Stiles, and the Cassini RADAR Science Team, 2007b: First stereoscopic radar images of Titan. *XXIII International Cartographic Congress*, 6411 (DVD-ROM).
- Kirk, R. L., E. Howington-Kraus, B. W. Stiles, S. Hensley, K. L. Mitchell, and the Cassini RADAR Science Team, 2007c: Topography of Titan from Cassini RADAR stereo data. *Eos Trans. Amer. Geophys. Union Fall Mtg. Suppl.*, **88**(52), Abstract P22B-01.
- Kirk, R. L., E. Howington-Kraus, B. W. Stiles, S. Hensley, K. L. Mitchell, and the Cassini RADAR Science Team, 2007d: Titan's topography from stereoscopic radar images. *Amer. Astron. Soc. Bull.*, **39**(3), 57.04.
- Kirk, R. L., E. Howington-Kraus, B. L. Redding, T. L. Becker, E. M. Lee, B. W. Stiles, S. Hensley, A. G. Hayes, R. M. C. Lopes, R. D. Lorenz, K. L. Mitchell, J. Radebaugh, F. Paganelli, L. A. Soderblom, E. R. Stofan, C. A. Wood, S. D. Wall, and the Cassini RADAR Science Team, 2008a: A three-dimensional view of Titan's surface features from Cassini RADAR Stereogrammetry. *Eos Trans. Amer. Geophys. Union*, **89**(53), *Fall Meet. Suppl.*, Abstract P11D-09.

- Kirk, R. L., E. Howington-Kraus, B. W. Stiles, S. Hensley, and the Cassini RADAR Science Team, 2008b: Digital topographic models of Titan produced by radar stereogrammetry with a rigorous sensor model. *Lunar Planet. Sci.*, XXXIX, Abstract 2320, Lunar and Planetary Institute, Houston (CD-ROM).
- Kirk, R. L., E. Howington-Kraus, B. L. Redding, T. L. Becker, E. M. Lee, B. W. Stiles, S. Hensley, and the Cassini RADAR Science Team, 2009a: Three-dimensional views of Titan's surface from Cassini RADAR stereogrammetry. *Geophys. Res. Abstracts*, **11**, EGU2000-10296.
- Kirk, R. L., E. Howington-Kraus, B. L. Redding, T. L. Becker, E. M. Lee, B. W. Stiles, S. Hensley, A. G. Hayes, R. M. C. Lopes, R. D. Lorenz, K. L. Mitchell, J. Radebaugh, F. Paganelli, L. A. Soderblom, E. R. Stofan, C. A. Wood, S. D. Wall, and the Cassini RADAR Science Team, 2009b: Three-dimensional views of Titan's diverse surface features from Cassini RADAR stereogrammetry. *Lunar Planet. Sci.*, XL, Abstract 1413.
- Kirk, R. L., E. Howington-Kraus, A. G. Hayes, R. M. C. Lopes, R. D. Lorenz, J. I. Lunine, K. L. Mitchell, E. R. Stofan, and S. D. Wall, 2010a: La Sotra y los otros: Topographic evidence for (and against) cryovolcanism on Titan. *Eos Trans. Amer. Geophys. Union*, **91**(52), *Fall Meet. Suppl.*, Abstract P22A-03.
- Kirk, R. L., E. Howington-Kraus, B. L. Redding, E. M. Lee, J. M. Barrett, and A. G. Hayes, 2010b: Radargrammetric mapping of Titan with multi-image bundle adjustment. *ISPRS TC IV/Autocarto/ASPRS/CaGIS Conference*, Orlando, FL, 15–19 November.
- Kirk, R. L., C. A. Wood, C. Neish, A. Lucas, and A. G. Hayes, 2011: Morphometry and morphology of fresh craters on Titan. *Eos Trans. Amer. Geophys. Union Fall Mtg. Suppl.*, **92**(52), Abstract P32C-08.
- Kirk, R. L., E. Howington-Kraus, B. Redding, P. S. Callahan, A. G. Hayes, A. Le Gall, R. M. C. Lopes, R. D. Lorenz, A. Lucas, K. L. Mitchell, C. D. Neish, O. Aharonson, J. Radebaugh, B. W. Stiles, E. R. Stofan, S. D. Wall, C. A. Wood, and the Cassini RADAR Science Team, 2012a: Topographic mapping of Titan: Latest results. *Lunar Planet. Sci.*, XLIII, Abstract 2759.
- Kirk, R. L., E. Howington-Kraus, B. Redding, P. S. Callahan, A. G. Hayes, A. Le Gall, R. M. C. Lopes, R. D. Lorenz, A. Lucas, K. L. Mitchell, C. D. Neish, O. Aharonson, J. Radebaugh, B. W. Stiles, E. R. Stofan, S. D. Wall, and C. A. Wood, 2012b: Topographic mapping of Titan: Latest results. *Geophys. Res. Abstracts*, **14**, EGU2012-13507.
- Kirk, R. L., E. Howington-Kraus, B. Redding, O. Aharonson, B. Bills, A. G. Hayes, L. Iess, R. D. Lorenz, A. Lucas, J. I. Lunine, R. Merigiolla, K. L. Mitchell, C. D. Neish, J. Radebaugh, B. W. Stiles, E. R. Stofan, S. D. Wall, and C. A. Wood, 2013: Topographic mapping of Titan: Completion of a global radargrammetric control network opens the floodgates for stereo DTM production. *Lunar Planet. Sci.*, XLIV, Abstract 2898.
- Kirk, R. L., E. Howington-Kraus, B. L. Redding, T. L. Becker, E. M. Lee, B. W. Stiles, S. Hensley, A. G. Hayes, R. M. Lopes, K. L. Lorenz, K. L. Mitchell, J. Radebaugh, F. Paganelli, L. A. Soderblom, E. R. Stofan, C. A. Wood, S. D. Wall, C. Elachi, and the Cassini RADAR Science Team, in preparation: High-resolution topographic models of Titan's surface derived by radar stereogrammetry with a rigorous sensor model. *Icarus*.

- Kossacki, K. J., and R. D. Lorenz, 1996: Hiding Titan's ocean: Densification and hydrocarbon storage in an icy regolith. *Planet. Space Sci.*, **44**, 1029–1037/
- Kwok, R., and W. T. K. Johnson, 1989: Block adaptive quantization of Magellan SAR data. *IEEE Trans. Geosci. Remote Sensing*, **27**, 375–383.
- Lara, L. M., R. D. Lorenz, and R. Rodrigo, 1994: Liquids and solids on the surface of Titan: Results of a new photochemical model. *Planet. Space Sci.*, **42**, 5–14.
- Laraia, A. L., A. P. Ingersoll, M. A. Janssen, S. Gulkis, F. A. Oyafuso, and M. D. Allison, 2013: Analysis of Saturn's thermal emission at 2.2-cm wavelength: Spatial distribution of ammonia vapor. *Icarus*, **226**, 641–654.
- Laurence, A., R. H. Soderblom, R. H. Brown, J. M. Soderblom, J. W. Barnes, R. L. Kirk, C. Sotin, R. Jaumann, D. J. Mackinnon, D. W. Mackowski, K. H. Baines, B. J. Buratti, R. N. Clark, and P. D. Nicholson, 2009: The geology of Hotei Regio, Titan: Correlation of Cassini VIMS and RADAR. *Icarus*, **204**, 610–618, doi:10.1016/j.icarus.2009.07.033.
- Le Gall, A. A., M. A. Janssen, R. D. Lorenz, L. Wye, P. S. Callahan, A. G. Hayes, F. Paganelli, and H. A. Zebker, 2008: Titan's dunes and interdunes: New insights from Cassini RADAR observations. *Amer. Geophys. Union Fall Mtg.*, December, Abstract #P21A-1310.
- Le Gall, A. A., M. A. Janssen, P. Paillou, R. D. Lorenz, S. D. Wall, and the Cassini RADAR Science Team, 2010: Radar-bright channels on Titan. *Icarus*, **207**, 948–958, doi:10.1016/j.icarus.2009.12.027.
- Le Gall, A. A., M. A. Janssen, R. L. Kirk, and R. D. Lorenz, 2014: Modeling microwave backscatter and thermal emission from linear dune fields: Application to Titan. *Icarus*, **230**, 198–207.
- Le Mouélic, S., P. Paillou, C. Sotin, S. Rodriguez, M. Crapeau, M. Hirtzig, M. H. Brown, and S. D. Wall, 2006: Comparison between VIMS and RADAR data on Sinlap crater on Titan. *First European Planetary Science Congress*, Berlin, Germany, September.
- Le Mouélic, S., P. Paillou, M. Janssen, J. Barnes, S. Rodriguez, C. Sotin, R. H. Brown, K. Baines, B. Buratti, R. Clark, M. Crapeau, P. Encrenaz, R. Jaumann, D. Geutner, F. Paganelli, L. Soderblom, G. Tobie, and S. Wall, 2008: Joint analysis of Cassini VIMS and RADAR data: Application to the mapping of Sinlap crater on Titan, *J. Geophys. Res.*, **113**, E04003, doi:10.1029/2007JE002965.
- Leberl, F. W., K. E. Maurice, J. K. Thomas, C. E. Leff, and S. D. Wall, 1992a: Images and topographic relief at the north pole of Venus. *J. Geophys. Res.*, **97**(E8), 13,667–13,674.
- Leberl, F. W., J. K. Thomas, and K. E. Maurice, 1992b: Initial results from the Magellan stereo experiment. *J. Geophys. Res.*, **97**(E8), 13,675–13,689.
- Liu, Z. Y.-C., J. Radebaugh, R. A. Harris, E. H. Christiansen, C. D. Neish, Randolph L. Kirk, Ralph D. Lorenz, and Cassini RADAR Science Team, 2016a: The tectonics of Titan: Global structural mapping from Cassini RADAR. *Icarus*, **270**.
- Liu, Z. Y.-C., J. Radebaugh, R. A. Harris, E. H. Christiansen, and S. Rupper, 2016b: Role of fluids in the tectonic evolution of Titan. *Icarus*, **270**, 2–13.
- Lopes, R. M. C., 2006: Titan: Cassini reveals a new world. *Space Exploration 2007*, B. Harvey, Ed., Praxis-Springer.

- Lopes, R. M. C., and the Cassini RADAR Science Team, 2013: Cryovolcanism on Titan: New results from Cassini RADAR and VIMS, *J. Geophys. Res., Planets*, **118**, 1–20, doi:10.1029/2012JE004239, 2013.
- Lopes, R. M. C., C. Elachi, F. Paganelli, K. Mitchell, E. Stofan, C. Wood, R. Kirk, R. Lorenz, J. Lunine, S. Wall, and the Cassini RADAR Science Team, 2005a: Flows on the surface of Titan as revealed by the Cassini RADAR. *Amer. Astron. Soc. Planet. Sci. Mtg.*, Cambridge, England, September.
- Lopes, R. M. C., C. Elachi, E. Stofan, F. Paganelli, C. Wood, R. Kirk, R. Lorenz, A. D. Fortes, J. Lunine, L. A. Soderblom, S. D. Wall, and the Cassini RADAR Science Team, 2005b: Cryovolcanic features on Titan's surface as revealed by the Cassini RADAR, solicited talk, *Eur. Geosci. Union Mtg.*, April.
- Lopes, R. M. C., C. Elachi, E. Stofan, F. Paganelli, C. Wood, R. Kirk, R. Lorenz, A. D. Fortes, J. I. Lunine, S. D. Wall, and the Cassini RADAR Science Team, 2005c: Cryovolcanic features on Titan's surface as revealed by the Cassini RADAR. *36<sup>th</sup> Lunar Planet. Sci. Conf.*, Abstract 1885.
- Lopes, R. M. C., E. R. Stofan, C. Elachi, R. L. Kirk, R. Lorenz, J. I. Lunine, K. L. Mitchell, G. G. Ori, F. Paganelli, L. Soderblom, S. D. Wall, C. A. Wood, and the Cassini RADAR Science Team, 2005d: Geologic features on Titan's surface as revealed by the Cassini RADAR Mapper. *Eos Trans. Amer. Geophys. Union Fall Mtg. Suppl.*, **85**(52), Abstract P44A-02.
- Lopes, R. M. C., E. R. Stofan, F. Paganelli, K. L. Mitchell, C. Wood, R. Kirk, R. Lorenz, J. Lunine, S. Wall, and C. Elachi, 2005e: Geologic features on Titan's surface as revealed by the Cassini RADAR. *Geological Soc. Amer. Ann. Mtg.*, Abstract 102-6.
- Lopes, R. M. C., K. L. Mitchell, E. Stofan, J. Lunine, and Cassini RADAR Science Team, 2006a: Cryovolcanic features on Titan's surface as revealed by the Cassini RADAR. Invited talk, *AOGS Mtg.*, Singapore, July.
- Lopes, R. M. C., E. R. Stofan, F. Paganelli, K. L. Mitchell, R. Kirk, R. Lorenz, J. Lunine, L. A. Soderblom, S. D. Wall, C. Wood, J. Radebaugh, L. E. Robshaw, C. Elachi, and the Cassini RADAR Science Team, 2006b: Geologic features on Titan's surface as revealed by the Cassini Titan Radar Mapper. *37<sup>th</sup> Lunar Planet. Sci. Conf.*, Abstract 1347, League City, TX, March 13–17.
- Lopes, R. M. C., K. L. Mitchell, E. R. Stofan, J. I. Lunine, R. Lorenz, F. Paganelli, R. L. Kirk, C. A. Wood, S. D. Wall, L. E. Robshaw, A. D. Fortes, C. D. Neish, J. Radebaugh, E. Reffet, S. J. Ostro, C. Elachi, M. D. Allison, Y. Z. Anderson, R. A. Boehmer, G. Boubin, P. S. Callahan, P. Encrenaz, E. Flamini, G. Franceschetti, Y. G. Gim, G. A. Hamilton, S. Hensley, M. A. Janssen, W. T. K. Johnson, K. Kelleher, D. O. Muhleman, G. Ori, R. Orosei, G. Picardi, F. Posa, L. E. Roth, R. Seu, S. Shaffer, L. A. Soderblom, B. Stiles, S. Vetrella, R. D. West, L. Wye, and H. A. Zebker, 2007a: Cryovolcanic features on Titan's surface as revealed by the Cassini Titan RADAR Mapper, *Icarus*, **186**(2).
- Lopes, R. M. C., K. L. Mitchell, S. D. Wall, G. Mitri, M. Janssen, S. Ostro, R. L. Kirk, A. G. Hayes, E. R. Stofan, J. I. Lunine, R. D. Lorenz, C. Wood, J. Radebaugh, P. Paillou, H. Zebker, F. Paganelli, and the Cassini RADAR Science Team, 2007b: The lakes and seas of Titan. *Eos*, **88**(51), 569–576.

- Lopes, R. M. C., R. Peckyno, A. Le Gall, and M. A. Janssen, 2008a: Surface parameters of Titan feature classes from Cassini RADAR backscatter measurements. *Amer. Geophys. Union Fall Mtg.*, P21A-1318.
- Lopes, R. M. C., E. R. Stofan, C. Wood, J. Radebaugh, R. Kirk, R. Lorenz, J. Lunine, S. D. Wall, K. L. Mitchell, and G. Mitri, 2008b: New views of Titan's surface geology from the Cassini RADAR. Invited talk, *Eur. Geosci. Union*, Vienna, Austria, April 13–18.
- Lopes, R. M. C., S. D. Wall, E. R. Stofan, C. A. Wood, R. M. Nelson, K. L. Mitchell, J. Radebaugh, B. W. Stiles, L. W. Kamp, R. D. Lorenz, J. I. Lunine, M. A. Janssen, T. G. Farr, G. Mitri, R. Kirk, and F. Paganelli, 2008c: Cryovolcanism on Titan: Interpretations from Cassini RADAR data. *Amer. Geophys. Union Fall Mtg.*, P52A-03.
- Lopes, R. M. C., S. D. Wall, E. R. Stofan, C. A. Wood, J. R. Radebaugh, K. L. Mitchell, B. W. Stiles, R. M. Nelson, L. W. Kamp, M. A. Janssen, R. D. Lorenz, J. I. Lunine, T. Farr, G. Mitri, and P. Paillou, 2008d: Hotei Arcus and western Xanadu, Titan: Evidence for cryovolcanic activity. *Amer. Astron. Soc. Div. Planet. Sci.*
- Lopes, R. M. C., E. R. Stofan, R. Peckyno, J. Radebaugh, K. L. Mitchell, G. Mitri, C. A. Wood, R. L. Kirk, S. D. Wall, J. I. Lunine, A. Hayes, R. Lorenz, T. Farr, L. Wye, J. Craig, R. J. Ollerenshaw, M. Janssen, A. Le Gall, F. Paganelli, R. West, B. Stiles, P. Callahan, Y. Anderson, P. Valora, L. Soderblom, and the Cassini RADAR Science Team, 2010: Distribution and interplay of geologic processes on Titan from Cassini RADAR data. *Icarus*, **205**, 540–558, doi:10.1016/j.icarus.2009.08.010.
- Lopes, R. M. C., M. J. Malaska, Anezina Solomonidou, Alice Le Gall, Michael A. Janssen, C. D. Neish, Elizabeth P. Turtle et al., 2016: Nature, distribution, and origin of Titan's undifferentiated plains. *Icarus* **270**.
- Lorenz, R. D., 1993a: The life, death and afterlife of a raindrop on Titan. *Planet. Space Sci.*, **41**(9), 647–655.
- Lorenz, R. D., 1993b: Wake-induced dust cloud formation following impact of planetary landers. *Icarus*, **101**, 165–167.
- Lorenz, R. D., 1994a: Crater lakes on Titan: Rings, horseshoes and bullseyes. *Planet. Space Sci.*, **42**, 1–4.
- Lorenz, R. D., 1994b: Huygens Probe impact dynamics. *ESA J.*, **18**, 93–117.
- Lorenz, R. D., 1995: Raindrops on Titan. *Adv. Space Res.*, **15**, 317–320.
- Lorenz, R. D., 1996: Pillow lava on Titan: Expectations and constraints on cryovolcanic processes. *Planet. Space Sci.*, **44**, 1021–1028.
- Lorenz, R. D., 1999: Calorimetric radar absorptivity measurement using a microwave oven, *Meas. Sci. Tech.*, **10**(6), June, L29–L32.
- Lorenz, R. D., 2002: Thermodynamics of geysers: Application to Titan. *Icarus*, **156**, 176–183.
- Lorenz, R. D., 2005: Lifting Titan's veil, invited talk, *Amer. Inst. Physics, Industrial Physics Forum*, Gaithersburg, MD, 7 November.
- Lorenz, R. D., 2006a: The exploration of Titan. *JHU-APL Technical Digest*, **27**, 133–144.
- Lorenz, R. D., 2006b: Surface modification processes on Titan. *Astrobiology Conf. (AbSciCon)*, Washington, DC, March.
- Lorenz, R. D., 2006c: Titan's dynamic surface revealed by Cassini RADAR, *Royal Astron. Soc.*, London, February.

- Lorenz, R. D., 2007: Comments on “In situ atmospheric turbulence measurement using the terrestrial magnetic field—a compass for a radiosonde.” *J. Atmos. Oceanic Tech.*, **24**, 1520–1521.
- Lorenz, R. D., 2008a: Atmospheric electricity hazards. *Space Sci. Rev.*, **137**, 287–294.
- Lorenz, R. D., 2008b: Effects of atmospheric electricity on chemistry. *Space Sci. Rev.*, **137**, 295–299.
- Lorenz, R. D., 2010: Titan and Enceladus: Icy cauldrons of organic synthesis, invited talk, *Pardee Symposium, GSA An. Mtg.*, Denver, CO, Oct. 31–Nov. 3.
- Lorenz, R. D., 2014. Physics of saltation and sand transport on Titan: A brief review. *Icarus*, **230**, 162–167.
- Lorenz, R. D., and J. I. Lunine, 1996: Erosion on Titan: Past and present, *Icarus*, **122**, 79–91.
- Lorenz, R. D., and S. E. Shandera, 2001: Physical properties of ammonia-rich ice: Application to Titan. *Geophys. Res. Lett.*, **28**, 215–218.
- Lorenz, R. D., and J. I. Lunine, 2005: The surface of Titan before Cassini. *Planet. Space Sci.*, **53**, 557–576.
- Lorenz, R. D., and J. Radebaugh, 2009: Global pattern of Titan’s dunes: Radar survey from the Cassini Prime Mission. *Geophys. Res. Lett.*, **36**, L03202, doi:10.1029/2008GL036850.
- Lorenz, R. D., and J. Zimbelman, 2014: *Dune Worlds: How Wind-Blown Sand Shapes Planetary Landscapes*, Praxis-Springer, ISBN 978-3-540-89724-8.
- Lorenz, R. D., M. Bannister, P. M. Daniell, Z. Krysinski, M. R. Leese, R. J. Miller, G. Newton, P. Rabbetts, D. M. Willett, and J. C. Zarnecki, 1994: An impact penetrometer for a landing spacecraft. *Meas. Sci. Tech.*, **5**, 1033–1041.
- Lorenz, R. D., J. I. Lunine, J. A. Grier, and M. A. Fisher, 1995: Prediction of aeolian features on planets: Application to Titan paleoclimatology. *J. Geophys. Res., Planets*, **88**, 26,377–26,386.
- Lorenz, R. D., C. P. McKay, and J. I. Lunine, 1997: Photochemically-driven collapse of Titan's atmosphere. *Science*, **275**, 642–644.
- Lorenz, R. D., C. P. McKay, and J. I. Lunine, 1999: Analytic stability of Titan’s climate: Sensitivity to volatile inventory. *Planet. Space Sci.*, **47**, 1503–1515.
- Lorenz, R. D., J. I. Lunine, C. P. McKay, and P. G. Withers, 2001: Entropy production by latitudinal heat flow on Titan, Mars and Earth. *Geophys. Res. Lett.*, **28**, 415–418.
- Lorenz, R. D., C. Elachi, B. Stiles, R. A. West, M. A. Janssen, R. M. Lopes, E. R. Stofan, F. Paganelli, C. A. Wood, R. L. Kirk, J. Lunine, and S. D. Wall, 2005a: Titan’s elusive lakes? Properties and context of dark spots in Cassini Ta radar data. *36<sup>th</sup> Lunar Planet. Sci. Conf.*, Abstract 1682, League City, TX, Mar. 14–18.
- Lorenz, R. D., E. Kraal, E. Eddlemon, J. Cheney, and R. Greeley, 2005b: Sea-surface wave growth under extraterrestrial atmospheres: Preliminary wind tunnel experiments with application to Mars and Titan. *Icarus*, **175**, 556–560.
- Lorenz, R. D., J. I. Lunine, and W. Zimmerman, 2005c: Post-Cassini exploration of Titan: Science goals, instrumentation and mission concepts. *Adv. in Space Res.*, **36**, 281–285.
- Lorenz, R. D., and the Cassini RADAR Science Team, 2006a: Dunes on Titan (poster). *European Geophys. Soc.*, Vienna, Austria, April.

- Lorenz, R. D., S. Wall, J. Radebaugh, G. Boubin, E. Reffet, M. Janssen, E. Stofan, R. Lopes, R. Kirk, C. Elachi, J. Lunine, F. Paganelli, L. Soderblom, C. Wood, L. Wye, H. Zebker, Y. Anderson, S. Ostro, M. Allison, R. Boehmer, P. Callahan, P. Encrenaz, G. G. Ori, G. Francescetti, Y. Gim, G. Hamilton, S. Hensley, W. Johnson, K. Kelleher, K. Mitchell, D. Muhleman, G. Picardi, F. Posa, L. Roth, R. Seu, S. Shaffer, B. Stiles, S. Vetrella, E. Flamini, and R. West, 2006b: The sand seas of Titan: Cassini RADAR observations of longitudinal dunes. *Science*, **312**, 724–727.
- Lorenz, R. D., S. D. Wall, E. Reffet, G. Boubin, J. Radebaugh, C. Elachi, M. D. Allison, Y. Anderson, R. Boehmer, P. Callahan, P. Encrenaz, E. Flamini, G. Francescetti, Y. Gim, G. Hamilton, S. Hensley, M. A. Janssen, W. T. K. Johnson, K. Kelleher, R. L. Kirk, R. M. Lopes, J. I. Lunine, K. Mitchell, D. O. Muhleman, G. Ori, R. Orosei, S. J. Ostro, F. Paganelli, G. Picardi, F. Posa, L. E. Roth, R. Seu, S. Shaffer, L. A. Soderblom, B. Stiles, E. Stofan, S. Vetrella, R. West, C. A. Wood, L. Wye, and H. A. Zebker, 2006c: Radar imaging of giant longitudinal dunes: Namib Desert (Earth) and the Belet Sand Sea (Titan). *Lunar Planet. Sci. Conf.*, **37**, Abstract 1249.
- Lorenz, R. D., C. A. Wood, J. I. Lunine, S. D. Wall, R. M. Lopes, K. L. Mitchell, F. Paganelli, Y. Z. Anderson, L. Wye, C. Tsai, H. Zebker, and E. R. Stofan, 2007: Titan's young surface: Initial impact crater survey by Cassini RADAR and model comparison. *Geophys. Res. Lett.*, **34**, L07204, doi:10.1029/2006GL028971.
- Lorenz, R. D., K. L. Mitchell, R. L. Kirk, A. G. Hayes, O. Aharonson, H. A. Zebker, P. Paillou, J. Radebaugh, J. I. Lunine, M. A. Janssen, S. D. Wall, R. M. Lopes, B. Stiles, S. Ostro, G. Mitri, and E. R. Stofan, 2008a: Titan's inventory of organic surface materials. *Geophys. Res. Lett.*, **35**, L02206, doi:10.1029/2007GL032118.
- Lorenz, R. D., R. D. West, and W. T. K. Johnson, 2008b: Cassini RADAR constraint on Titan's winter polar precipitation. *Icarus*, **195**, 812–816, doi:10.1016/j.icarus.2007.12.025.
- Lorenz, R. D., J. Radebaugh, S. D. Wall, R. Kirk, A. Le Gall, M. A. Janssen, H. Zebker, F. Paganelli, L. Wye, and J. Lunine, 2009: The dunes of Shangri-La: New Cassini RADAR results on patterns of aeolian features and the influence of topography. *Amer. Geophys. Union Fall Mtg.*, Abstract P21A-1309.
- Lorenz, R. D., P. Claudin, B. Andreotti, J. Radebaugh, and T. Tokano, 2010a: A 3-km atmospheric boundary layer on Titan indicated by dune spacing and Huygens data. *Icarus*, **205**(2), 719–721, doi:10.1016/j.icarus.2009.08.002.
- Lorenz, R. D., B. Jackson, and A. Hayes, 2010b: Racetrack and Bonnie Claire: Southwestern US playa lakes as analogs for Ontario Lacus, Titan. *Planet. Space Sci.*, **58**(4), 724–731.
- Lorenz, R. D., C. Newman, and J. I. Lunine, 2010c: Threshold of wave generation on Titan's lakes and seas: Effect of viscosity and implications for Cassini observations. *Icarus*, **207**(2), 932–937, doi:10.1016/j.icarus.2009.12.004.
- Lorenz, R. D., E. P. Turtle, B. Stiles, A. Le Gall, A. Hayes, O. Aharonson, C. A. Wood, E. Stofan, and R. Kirk, 2011: Hypsometry of Titan. *Icarus*, **211**, 699–706.
- Lorenz, R. D., et al., 2014a: The flushing of Ligeia: Compositional variations across Titan's seas in a simple hydrological model. *Geophys. Res. Lett.* **41**, 5764–5770.
- Lorenz, R. D., M. R. Leese, J. C. Zarnecki, A. Hagermann, P. Rosenberg, M. Towner, J. Garry, and H. Svedhem, 2014b: Silence on Shangri-La: Detection of Titan surface volatiles by acoustic absorption. *Planet. Space Sci.*, **90**, 72–80.

- Lorenz, R. D., A. A. Le Gall, and M. A. Janssen, 2016: Detecting volcanism on Titan and Venus with microwave radiometry. *Icarus*, **270**.
- Lorenz R. D., H. Svedhem, R. Trautner, W. Kofman, A. Herique, D. Plettemeier, J.-P. Lebreton, O. Witasse, P. Falkner, N. Floury, and F. Ferri, 2016: Observations of the surface of Titan by the radar altimeters on the Huygens probe. *Icarus*, **270**, 248–259.
- Lucas, A. R., O. Aharonson, C. Deledalle, A. G. Hayes, R. Kirk, E. Howington-Kraus, and the Cassini RADAR Science Team, 2014a: Insights into Titan’s geology and hydrology based on enhanced image processing of Cassini RADAR data. *J. Geophys. Res., Planets*, **119**(10), 2149–2166.
- Lucas, A., S. Rodriguez, C. Narteau, B. Charnay, S. C. Pont, T. Tokano ..., and O. Aharonson, 2014b: Growth mechanisms and dune orientation on Titan. *Geophys. Res. Lett.*, **41**(17), 6093–6100.
- Lunine, J. I., 2005: Numerical modeling of impact cratering on Titan with implications for the age of Titan’s surface. *Lunar Planet. Sci. Conf.* 36, Abstract 1504.
- Lunine, J. I., and D. J. Stevenson 1987: Clathrate and ammonia hydrates at high pressure—application to the origin of methane on Titan. *Icarus*, **70**, 61–77.
- Lunine, J. I., and S. K. Atreya, 2008: The methane cycle on Titan. *Nature Geosci.*, **1**, 160–164.
- Lunine, J. I., D. J. Stevenson, and Y. L. Yung, 1983: Ethane ocean on Titan. *Science*, **222**, 1229–1230.
- Lunine, J. I., C. Elachi, , S. D. Wall, M. D. Allison, Y. Anderson, R. Boehmer, P. Callahan, P. Encrenaz, E. Flamini, G. Franceschetti, Y. Gim, G. Hamilton, S. Hensley, M. A. Janssen, W. T. K. Johnson, K. Kelleher, R. L. Kirk, R. M. Lopes, R. Lorenz, D. O. Muhleman, R. Orosei, S. J. Ostro, F. Paganelli, P. Paillou, G. Picardi, F. Posa, J. Radebaugh, L. E. Roth, R. Seu, S. Shaffer, L. A. Soderblom, B. Stiles, E. R. Stofan, S. Vetrella, R. West, C. A. Wood, L. Wye, H. Zebker, G. Alberti, E. Karkoschka, B. Rizk, E. McFarlane, C. See, and B. Kazeminejad, 2008: Titan diverse landscapes as evidenced by Cassini RADAR’s third and fourth looks at Titan. *Icarus*, **195**, 414–433, doi:10.1016/j.icarus.2007.12.022.
- Malaska, M. J., J. Radebaugh, A. Le Gall, K. Mitchell, R. Lopes, and S. Wall, 2011: Evidence for an eroded upwarp near Sikun Labyrinthus, Titan. *42<sup>nd</sup> Lunar Planet. Sci. Conf.*, Abstract 1568, The Woodlands, TX, Mar7–11.
- Malaska, M. J., R. M. C. Lopes, A. G. Hayes, J. Radebaugh, R. D. Lorenz, and E. P. Turtle, 2016a: Material transport map of Titan: The fate of dunes. *Icarus*, **270**.
- Malaska, M. J., R. M. C. Lopes, D. A. Williams, Catherine D. Neish, Anezina Solomonidou, Jason M. Soderblom, Ashley M. Schoenfeld et al., 2016b: Geomorphological map of the Afekan Crater region, Titan: Terrain relationships in the equatorial and mid-latitude regions. *Icarus*, **270**, 130–161.
- Mastrogiuseppe, M., V. Poggiali, A. Hayes, R. Lorenz, J. Lunine, G. Picardi, R. Seu, E. Flamini, G. Mitri, C. Notarnicola, P. Paillou, and H. Zebker, 2014: The bathymetry of a Titan sea, *Geophys. Res. Lett.* **41**, 1432–1437, doi:10.1002/2013GLO58618.
- McDonald, G. D., A. G. Hayes, R. C. Ewing, J. M. Lora, C. E. Newman, T. Tokano, A. Lucas, A. Soto, and G. Chen, 2016: Variations in Titan’s dune orientations as a result of orbital forcing. *Icarus*, **270**.

- Michaelides, R. J., A. G. Hayes, M. Mastrogiuseppe, H. A. Zebker, T. G. Farr, M. J. Malaska, V. Poggiali, and J. P. Mullen, 2016: Constraining the physical properties of Titan's empty lake basins using nadir and off-nadir Cassini RADAR backscatter. *Icarus*, **270**.
- Mitchell, K. L., R. M. Lopes, R. L. Kirk, and the Cassini RADAR Science Team, 2005: Preliminary analysis of the rheological properties of a probable cryovolcanic flow on Titan, by radarclinometric analysis of Cassini RADAR data. *Amer. Astron. Soc. Div. Planet. Sci. Mtg.*, Cambridge, England, September.
- Mitchell, K. L., J. S. Kargel, R. M. Lopes, J. I. Lunine, G. Mitri, R. D. Lorenz, N. Petford, and L. Wilson, 2006a: Eruption of ammonia-water cryomagmas on Titan 1: Crystallisation and cooling during ascent, *37<sup>th</sup> Lunar Planet. Sci. Conf.*, Abstract 2355, Lunar and Planetary Institute, Houston (CD-ROM).
- Mitchell, K. L., R. M. C. Lopes, L. E. Robshaw, Kargel, J. S., J. I. Lunine, R. D. Lorenz, Petford, N., E. R. Stofan, L. Wilson, and the Cassini RADAR Science Team, 2006b: Eruption of ammonia-water cryomagmas on Titan 2: Eruption styles and landforms, *37<sup>th</sup> Lunar Planet. Sci. Conf.*, Abstract 2425, Lunar and Planetary Institute, Houston (CD-ROM).
- Mitchell, K. L., E. R. Stofan, C. Elachi, J. I. Lunine, R. D. Lorenz, B. Stiles, S. Ostro, L. Soderblom, C. Wood, H. Zebker, S. Wall, M. Janssen, R. Kirk, R. Lopes, F. Paganelli, J. Radebaugh, L. Wye, Y. Anderson, M. Allison, R. Boehmer, P. Callahan, P. Encrenaz, E. Flamini, G. Francescetti, Y. Gim, G. Hamilton, S. Hensley, W. T. K. Johnson, K. Kelleher, D. Muhleman, P. Paillou, G. Picardi, F. Posa, L. Roth, R. Seu, S. Shaffer, S. Vetrella, R. West, and the Cassini RADAR Science Team, 2008: The Lakes of Titan, *GSA Ann. Mtg.*, Houston, TX, October 5–9.
- Mitchell, K. L., M. B. Barmatz, C. S. Jamieson, R. D. Lorenz, and J. I. Lunine, 2015: Laboratory measurements of cryogenic liquid alkane microwave absorptivity and implications for the composition of Ligeia Mare, Titan. *Geophys. Res. Lett.* **42**, 1340–1345, doi:10.1002/2014GL059475.
- Mitri, G., and A. P. Showman, 2007: Thermal convection in ice-I shells of Titan and Enceladus. *Icarus*, **193**, 387–396, doi:10.1016/j.icarus.2007.07.016.
- Mitri, G., A. P. Showman, J. I. Lunine, and R.D. Lorenz, 2007: Hydrocarbon lakes on Titan. *Icarus*, **186**, 385–394.
- Mitri, G., M. T. Bland, R. M. C. Lopes, J. R. Radebaugh, A. P. Showman, J. I. Lunine, and the Cassini RADAR Science Team, 2008a: Mountains on Titan. *Amer. Astron. Soc. Div. Planet. Sci.*
- Mitri, G., M. T. Bland, R. M. C. Lopes, and A. P. Showman, 2008b: Mountain building on Titan. *Eur. Geosci. Union*, Vienna, Austria, April 13–18.
- Mitri, G., A. P. Showman, J. I. Lunine, and R. M. Lopes, 2008c: Cryovolcanism on Titan. *Amer. Geophys. Union Fall Mtg.*, P11D-05.
- Mitri, G., A. P. Showman, J. I. Lunine, and R. M. Lopes, 2008d: Resurfacing of Titan by ammonia-water cryomagma, *Icarus*, **196**, 216–224.
- Mitri, G., M. T. Bland, A. P. Showman, J. R. Radebaugh, B. W. Stiles, R. M. C. Lopes, J. I. Lunine, R. Pappalardo, and the Cassini RADAR Science Team, 2010: Mountains on Titan: Modeling and observations. *J. Geophys. Res.*, **115**, E10002, doi:10.1029/2010JE003592.

- Mousis, O., J. I. Lunine, A. G. Hayes, and J. D. Hofgartner, 2016: The fate of ethane in Titan's hydrocarbon lakes and seas. *Icarus*, **270**.
- Neish, C. D., and R. D. Lorenz, 2014: Elevation distribution of Titan's craters suggests extensive wetlands. *Icarus*, **228**, 27–34.
- Neish, C. D.; R. D. Lorenz, and D. P. O'Brien, 2006: The potential for prebiotic chemistry in the possible cryovolcanic dome Ganesa Macula on Titan. *Intl. J. Astrobio.*, **5**(1).
- Neish, C. D., R. D. Lorenz, and R. L. Kirk, 2008: Radar topography of domes on planetary surfaces. *Icarus*, **196**, 552–564, doi:10.1016/j.icarus.2008.03.013.
- Neish, C. D., R. D. Lorenz, R. L. Kirk, and L. C. Wye, 2010: Radarclinometry of the sand seas of Africa's Namibia and Saturn's moon Titan. *Icarus*, **208**, 385–394, doi:10.1016/j.icarus.2010.01.023
- Neish, C. D., J. L. Molaro, J. M. Lora, A. D. Howard, R. L. Kirk, P. Schenk, V. J. Bray, and R. D. Lorenz, 2016: Fluvial erosion as a mechanism for crater modification on Titan. *Icarus*, **270**.
- Nelson, R. M., L. W. Kamp, R. M. C. Lopes, D. L. Matson, R. L. Kirk, B. W. Hapke, M. D. Boryta, F. E. Leader, W. D. Smythe, K. H. Baines, R. Jauman, C. Sotin, R. N. Clark, D. P. Cruikshank, P. Drossart, B. J. Buratti, R. H. Brown, M. Combes, G. Bellucci, J.-P. Bibring, F. Capaccioni, P. Cerroni, A. Coradini, V. Formisano, G. Filacchione, R. Y. Langevin, T. B. McCord, V. Mennella, P. D. Nicholson, and B. Sicardy, 2008a: Saturn's Titan: Reports suggesting surface activity from Cassini VIMS and Radar observations. *39<sup>th</sup> Lunar Planet. Sci. Conf.*, Abstract 1862.
- Nelson, R. M., L. W. Kamp, R. M. C. Lopes, D. L. Matson, R. L. Kirk, B. W. Hapke, S. D. Wall, M. D. Boryta, F. E. Leader, W. D. Smythe, K. L. Mitchell, K. H. Baines, R. Jaumann, C. Sotin, R. N. Clark, D. P. Cruikshank, P. Drossart, J. I. Lunine, M. Combes, G. Bellucci, J.-P. Bibring, F. Capaccioni, P. Cerroni, A. Coradini, V. Formisano, G. Filacchione, Y. Langevin, T. B. McCord, V. Mennella, P. D. Nicholson, B. Sicardy, P. G. J. Irwin, and J. C. Pearl, 2008b: Photometric changes on Saturn's Titan: Evidence for active cryovolcanism. *Geophys. Res. Lett.*, **36**, L04202, doi:10.1029/2008GL036206.
- Nelson, R. M., L. W. Kamp, R. M. C. Lopes, D. L. Matson, S. D. Wall, R. L. Kirk, K. L. Mitchell, G. Mitri, B. W. Hapke, M. D. Boryta, F. E. Leader, W. D. Smythe, K. H. Baines, R. Jauman, C. Sotin, R. N. Clark, D. P. Cruikshank, P. Drossart, B. J. Buratti, R. H. Brown, J. Lunine, M. Combes, G. Bellucci, J.-P. Bibring, F. Capaccioni, P. Cerroni, A. Coradini, V. Formisano, G. Filacchione, R. Y. Langevin, T. B. McCord, V. Mennella, P. D. Nicholson, and B. Sicardy, 2008c: The changing surface of Saturn's Titan: Cassini observations suggest active cryovolcanism, *Amer. Geophys. Union*.
- Nelson, R. M., L. W. Kamp, R. M. C. Lopes, D. L. Matson, S. D. Wall, R. L. Kirk, K. L. Mitchell, G. Mitri, B. W. Hapke, M. D. Boryta, F. E. Leader, W. D. Smythe, K. H. Baines, R. Jauman, C. Sotin, R. N. Clark, D. P. Cruikshank, P. Drossart, B. J. Buratti, R. H. Brown, J. Lunine, M. Combes, G. Bellucci, J.-P. Bibring, F. Capaccioni, P. Cerroni, A. Coradini, V. Formisano, G. Filacchione, R. Y. Langevin, T. B. McCord, V. Mennella, P. D. Nicholson, and B. Sicardy, 2008d: Saturn's Titan: Cassini instruments document surface change suggesting cryovolcanism, *Amer. Astron. Soc. Div. Planet. Sci. Mtg.*

- Nicholson, P. D., R. G. French, D. B. Campbell, J.-L. Margot, M. C. Nolan, G. J. Black, and H. J. Salo, 2005: Radar imaging of Saturn's rings. *Icarus*, **177**, 32–62, doi:10.1016/j.icarus.2005.03.023.
- Notarnicola, C., B. Ventura, D. Casarano, and F. Posa, 2009: Cassini RADAR data: Estimation of Titan's lake features by means of a Bayesian inversion algorithm. *IEEE Trans. Geosci. and Remote Sensing*, **47**(5), 1503–1511.
- Notarnicola, C., B. Ventura, D. Casarano, F. Posa and M. Janssen, 2010: Titan lakes: Characterization of physical properties by combined electromagnetic models of SAR and radiometric data, *Italian J. Remote Sensing*, **42**(1), 37–54.
- O'Brien, D. P., R. D. Lorenz, and J. I. Lunine 2005. Numerical calculations of the longevity of impact oases on Titan. *Icarus*, **173**, 243–253.
- Ostro, S. J., R. D. West, M. A. Janssen, H. A. Zebker, L. C. Wye, J. I. Lunine, R. M. Lopes, K. Kelleher, G. A. Hamilton, Y. Gim, Y. Z. Anderson, R. A. Boehmer, R. D. Lorenz, and the Cassini RADAR Science Team, 2005: Cassini RADAR observations of Phoebe, Iapetus, Enceladus, and Rhea. *Eos Trans. Amer. Geophys. Union Fall Mtg. Suppl.*, **85**(52), Abstract P22A-01.
- Ostro, S. J., R. D. West, M. A. Janssen, R. D. Lorenz, H. A. Zebker, G. J. Black, J. I. Lunine, L. C. Wye, R. M. Lopes-Gautier, S. D. Wall, C. Elachi, L. Roth, S. Hensley, K. Kelleher, G. A. Hamilton, Y. Gim, Y. Z. Anderson, R. A. Boehmer, W. T. K. Johnson, and the Cassini RADAR Science Team, 2006: Cassini RADAR observations of Enceladus, Thethys, Dione, Rhea, Iapetus, Hyperion, and Phoebe. *Icarus*, **183**, 479–490.
- Ostro, S. J., R. D. West, L. C. Wye, C. A. Wood, P. Paillou, M. A. Janssen, B. Stiles, K. Kelleher, Y. Z. Anderson, R. A. Boehmer, P. Callahan, Y. Gim, G. A. Hamilton, W. T. K. Johnson, C. Veeramachaneni, and the Cassini RADAR Science Team, 2007: New Cassini RADAR results for Iapetus and Saturn's other icy satellites. *Amer. Geophys. Union Fall Mtg.*
- Ostro, S. J., R. D. West, L. C. Wye, H. A. Zebker, M. A. Janssen, B. Stiles, K. Kelleher, Y. Z. Anderson, R. A. Boehmer, P. Callahan, Y. Gim, G. A. Hamilton, W. T. K. Johnson, C. Veeramachaneni, R. D. Lorenz, and the Cassini RADAR Science Team, 2010: New Cassini RADAR results for Saturn's icy satellites. *Icarus*, **206**, 498–506, doi:10.1016/j.icarus.2009.07.041.
- Paganelli, F., C. Elachi, R. M. Lopes, R. A. West, B. Stiles, M. A. Janssen, E. R. Stofan, C. A. Wood, R. D. Lorenz, J. I. Lunine, R. L. Kirk, L. E. Roth, S. D. Wall, L. A. Soderblom, and the Cassini RADAR Science Team, 2005a: Channels and fan-like features on Titan surface imaged by the Cassini RADAR. *36<sup>th</sup> Lunar Planet. Sci. Conf.*, League City, TX, March 14–18.
- Paganelli, F., M. A. Janssen, R. M. Lopes, R. L. Kirk, R. D. Lorenz, and the Cassini RADAR Science Team, 2005b. Titan's surface from combined SAR and radiometry using the Cassini RADAR. *Eos Trans. Amer. Geophys. Union Fall Mtg. Suppl.*, **85**(52), Abstract P44A-04.
- Paganelli, F., M. A. Janssen, R. M. Lopes, E. Stofan, B. Stiles, R. West, L. Roth, S. D. Wall, R. D. Lorenz, J. I. Lunine, R. L. Kirk, L. Soderblom, C. Elachi, and the Cassini RADAR Science Team, 2006a: A look at Titan's surface from the Cassini RADAR SAR and radiometry data. *37<sup>th</sup> Lunar Planet. Sci. Conf.*, Abstract 1497.

- Paganelli, F., J. van Zyl, M. A. Janssen, B. Stiles, R. West, R. M. Lopes, E. Stofan, P. Callahan, L. Roth, S. D. Wall, T. G. Farr, C. Elachi, R. D. Lorenz, L. Soderblom, and the Cassini RADAR Science Team, 2006b: Titan electromagnetic response and surface roughness imaged by Cassini RADAR. *37<sup>th</sup> Lunar Planet. Sci. Conf.*, Abstract 1501.
- Paganelli, F., M. A. Janssen, B. Stiles, R. West, R. D. Lorenz, J. I. Lunine, R. M. Lopes, E. R. Stofan, S. D. Wall, R. L. Kirk, L. Roth, C. Elachi, and the Cassini RADAR Science Team, 2007a: Titan's surface from the Cassini RADAR radiometry data during SAR mode. *Planet. Space Sci. Special Issue from EGU 2006*.
- Paganelli, F., M. A. Janssen, B. Stiles, R. West, R. D. Lorenz, J. I. Lunine, S. D. Wall, P. Callahan, R. M. Lopes, E. Stofan, R. L. Kirk, W. T. K Johnson, L. Roth, C. Elachi, and the Cassini RADAR Science Team, 2007b: Titan's surface from the Cassini RADAR SAR and high-resolution radiometry data of the first five flybys. *Icarus*, **191**, 211–222.
- Paganelli, F., P. Callahan, S. Hensley, R. D. Lorenz, J. I. Lunine, R. L. Kirk, B. W. Stiles, Y. Gim, R. West, M. A. Janssen, R. M. Lopes, E. R. Stofan, S. D. Wall, P. Paillou, and the Cassini RADAR Science Team, 2008a: A different look at Titan's dunes. *Amer. Geophys. Union*.
- Paganelli, F., P. Callahan, S. Hensley; R. D. Lorenz; J. I. Lunine; R. L. Kirk; B. W. Stiles, Y. Gim, R. West, M. A. Janssen, R. M. Lopes, E. R. Stofan, S. D. Wall, P. Paillou, J. Radebaugh, and the Cassini RADAR Science Team, 2008b: Different appearance of Titan's dunes. *Amer. Geophys. Union Fall Mtg.*
- Paganelli, F., M. A. Janssen, R. M. Lopes, E. Stofan, S. D. Wall, R. D. Lorenz, J. I. Lunine, R. L. Kirk, L. Roth, C. Elachi, and the Cassini RADAR Science Team, 2008c: Titan's surface from the Cassini RADAR radiometry data during SAR mode. *Planet. Space Sci.*, **56**(1), 100–108.
- Paillou, P., M. Crapeau, C. Elachi, S. D. Wall, and P. Encrenaz, 2006a: Modeling SAR backscattering of bright flows and dark spots on Titan. *37<sup>th</sup> Lunar Planet. Sci. Conf.*, Houston, TX, March.
- Paillou, P., M. Crapeau, C. Elachi, S. D. Wall, and P. Encrenaz, 2006b: Models of synthetic aperture radar backscattering for bright flows and dark spots on Titan. *J. Geophys. Res.*, **111**, E11011, doi:10.1029/2006JE002724.
- Paillou, P., J. I. Lunine, G. Ruffié, P. Encrenaz, S. D. Wall, R. D. Lorenz, and M. A. Janssen, 2008a: Microwave dielectric constant of Titan-relevant materials. *Geophys. Res. Lett.*, **35**, L18202, doi:10.1029/2008GL035216.
- Paillou, P., K. L. Mitchell, S. D. Wall, G. Ruffié, C. A. Wood, R. D. Lorenz, E. R. Stofan, J. I. Lunine, R. M. Lopes, and P. Encrenaz, 2008b: Microwave dielectric constant of liquid hydrocarbons: Application to the depth estimation of Titan's lakes. *Geophys. Res. Lett.*, **35**, L05202, doi:10.1029/2007GL032515.
- Paillou, P., D. Bernard, J. Radebaugh, R. Lorenz, A. Le Gall, and T. Farr, 2014: Modeling the SAR backscatter of linear dunes on Earth and Titan. *Icarus*, **230**, 208–214.
- Paillou, P., B. Seignover, J. Radebaugh, and W. Wall, 2016: Radar scattering of linear dunes and mega-yardangs: Application to Titan. *Icarus*, **270**.
- Pérez-Ayúcar, M., R. Lorenz, N. Floury, R. Prieto-Cerdeira, and J.-P. Lebreton, 2006. Surface properties of Titan from post-landing reflections of the Huygens radio signal. *J. Geophys. Res.: Planets* 111, E07001. doi:10.1029/2005JE002613

- Peale, S. J., 1969: Generalized Cassini's laws. *The Astronomical Journal*, **74**, 483.
- Peale, S. J., Yseboodt, M., and Margot, J. L., 2007: Long-period forcing of Mercury's libration in longitude. *Icarus*, **187**(2), 365–373.
- Perry, J. E., E. P. Turtle, A. S. McEwen, D. D. Dawson, and C. C. Porco, 2007: Cassini ISS observations of Titan's trailing hemisphere. *Ices, Oceans, and Fire: Satellites of the Outer Solar System workshop*, Boulder, Colorado, Abstract 6064.
- Petford, N., K. L. Mitchell, and R. M. C. Lopes, 2006: Flow rheology of congested ammonia-water cyromagmas on Titan. *Royal Astronomical Society Titan Mtg.*, February.
- Radebaugh, J. R., 2008: The Mountains of Titan. *GSA Ann. Mtg.*
- Radebaugh, J. R., 2009: Titan's sticky dunes? *Nature Geosci.*, **2**, 608–609, doi:10.1038/ngeo623.
- Radebaugh, J. R., R. D. Lorenz, R. L. Kirk, J. I. Lunine, and the Cassini RADAR Science Team, 2005: Mountains on Titan observed by Cassini RADAR. *Lunar Planetary Sci. Conf. 37*, Abstract 1007.
- Radebaugh, J. R., R. D. Lorenz, J. I. Lunine, S. D. Wall, G. Boubin, E. Reffet, R. L. Kirk, R. M. C. Lopes, L. Soderblom, and the Cassini RADAR Science Team, 2006a: Orientations of dunes on Titan: Implications for global winds, *Amer. Astronom. Soc. Div. Planet. Sci. Mtg. 38*, Pasadena, CA, October, Abstract 52.07.
- Radebaugh, J. R., R. D. Lorenz, J. I. Lunine, S. D. Wall, G. Boubin, E. Reffet, R. L. Kirk, R. M. C. Lopes, E. Stofan, L. Soderblom, M. Allison, and the Cassini RADAR Science Team, 2006b: Longitudinal dunes on Titan as indicators of regional and local winds. *EOS Trans. Amer. Geophys. Union Fall Mtg. Suppl.*, Abstract P12A-03.
- Radebaugh, J. R., R. D. Lorenz, R. L. Kirk, J. I. Lunine, E. Stofan, R. M. C. Lopes, S. D. Wall, and the Cassini RADAR Science Team, 2007a: Mountains on Titan from Cassini RADAR. *Icarus*, **192**, 77–91, doi:10.1016/j.icarus.2007.06.020.
- Radebaugh, J. R., R. D. Lorenz, J. I. Lunine, and the Cassini RADAR Science Team, 2007b: Longitudinal dunes on Titan: Distributions and indicators of winds. *Spring EGU Mtg.*, Vienna, Austria, Abstract 04702.
- Radebaugh, J. R., R. D. Lorenz, J. I. Lunine, S. D. Wall, G. Boubin, E. Reffet, R. L. Kirk, R. M. C. Lopes, E. R. Stofan, L. Soderblom, M. Allison, P. Callahan, and the Cassini RADAR Science Team, 2007c: Dunes on Titan from Cassini RADAR. *38<sup>th</sup> Lunar Planetary Sci. Conf.*, Abstract 1338.
- Radebaugh, J. R., R. D. Lorenz, J. I. Lunine, S. D. Wall, G. Boubin, E. Reffet, R. L. Kirk, R. M. C. Lopes, E. R. Stofan, L. Soderblom, M. Allison, P. Callahan, and the Cassini RADAR Science Team, 2007c: Longitudinal dunes on Titan as indicators of global climate. *Workshop on Ices, Oceans, and Fire, Satellites of the Outer Solar System*, Boulder, CO, Abstract 6005.
- Radebaugh, J. R., R. D. Lorenz, J. I. Lunine, S. D. Wall, G. Boubin, E. Reffet, R. L. Kirk, R. M. C. Lopes, E. R. Stofan, L. Soderblom, M. Allison, P. Callahan, and the Cassini RADAR Science Team, 2007e: Orientations of longitudinal dunes on Titan: Implications for global wind and climate. *Bull. Amer. Astron. Soc.*, **39**(3), 57.02.

- Radebaugh, J. R., R. D. Lorenz, J. I. Lunine, S. D. Wall, C. Spencer, R. L. Kirk, R. M. Lopes, E. R. Stofan, M. Allison, P. Callahan, and the Cassini RADAR Science Team, 2007f: Titan's sand seas of longitudinal dunes as indicators of winds and sediment transport. *Eos Trans. Amer. Geophys. Union Fall Mtg. Suppl.*, **88**(52), Abstract 10910.
- Radebaugh, J. R., R. D. Lorenz, J. I. Lunine, S. D. Wall, G. Boubin, E. Reffet, R. L. Kirk, R. M. C. Lopes, E. R. Stofan, L. Soderblom, M. Allison, M. Janssen, P. P. Paillou Callahan, C. Spencer, and the Cassini RADAR Science Team, 2008: Dunes on Titan observed by Cassini RADAR. *Icarus*, **194**(2), 690–703, doi:10.1016/j.icarus.2007.10.015.
- Radebaugh, J. R., R. Lorenz, T. Farr, P. Paillou, C. Savage, and C. Spencer, 2010: Linear dunes on Titan and Earth: Initial remote sensing comparisons. *Geomorphology*, **121**, 122–132, doi:10.1016/j.geomorph.2009.02.022.
- Radebaugh, J. R., R. D. Lorenz, S. D. Wall, R. L. Kirk, C. A. Wood, J. I. Lunine, E. R. Stofan, R. M. C. Lopes, P. Valora, T. G. Farr, A. Hayes, B. Stiles, G. Mitri, H. Zebker, M. Janssen, L. Wye, A. Le Gall, K. L. Mitchell, F. Paganelli, R. D. West, E. L. Schaller, and the Cassini RADAR Science Team, 2011: Regional geomorphology and history of Titan's Xanadu province. *Icarus*, **211**, 672–685, doi:10.1016/j.icarus.2010.07.022.
- Raney, K., 1998: The delay/Doppler radar altimeter. *IEEE Trans. Geosci. and Remote Sensing*, **36**(5), September.
- Reffet, E. G., G. M. Boubin, J. Lunine, J. Radebaugh, R. M. Lopes, and the Cassini RADAR Science Team, 2005: Cryovolcanic features on Titan: Interpretation of Cassini RADAR data. *Amer. Astron. Soc. Div. Planet. Sci. Mtg.*, Cambridge, England, September.
- Renick, P., 1997: Cassini RADAR digital assembly (DSS) high level design. JPL D-11201, Revision G. Jet Propulsion Laboratory, California Institute of Technology, Pasadena CA.
- Rodriguez, S., S. Le Mouélic, P. R. G. Tobie, K. H. Baines, J. W. Barnes, C. A. Griffith, M. Hirtzig, K. M. Pitman, C. Sotin, R. H. Brown, B. J. Buratti, R. N. Clark, and P. D. Nicholson, 2009: Global circulation as the main source of cloud activity on Titan. *Nature*, **459**, 678–682, doi:10.1038/nature08014.
- Roth, L., 2005: Planetary radar exploration: The Cassini RADAR. *Joint Conf. Czech and Slovak Phys. Soc.*, Kosice, Slovakia, September 5.
- Rubin, D. M., and P. A. Hesp, 2009: Multiple origins of linear dunes on Earth and Titan. *Nature Geosci.*, **2**, 653–658, doi:10.1038/ngeo610.
- Savage, C., J. Radebaugh, E. Christiansen, and R. D. Lorenz, 2014: Implications of dune pattern analysis for Titan's surface history. *Icarus*, **230**, 180–190.
- Slama, C. C., 1980: *Manual of Photogrammetry*, 4th Ed. American Society of Photogrammetry and Remote Sensing, 1056 pp.
- Soderblom, J. M., B. J. Buratti, R. Wagner, T. B. McCord, S. Rodriguez, K. H. Baines, D. P. Cruikshank, P. D. Nicholson, C. A. Griffith, M. Langhans, and R. D. Lorenz, 2008: Fluvial erosion post-erosional processes on Titan. *Icarus*, **197**(2), 526–538, October.

- Soderblom, L. A., R. Kirk, J. I. Lunine, J. Anderson, K. Baines, J. Barnes, J. Barrett, R. Brown, B. Buratti, R. Clark, D. Cruikshank, C. Elachi, M. A. Janssen, R. Jaumann, E. Karkoschka, S. Le Mouélic, R. M. Lopes., R. D. Lorenz, T. McCord, P. Nicholson, J. R. Radebaugh, B. Rizk, C. Sotin, E. R. Stofan, T. Sucharski, M. Tomasko, and S. D. Wall, 2007a: Correlations between Cassini VIMS spectra and RADAR SAR images: Implications for Titan's surface composition and the character of the Huygens Probe Landing Site. *Planet. Space Sci.*, **55**, 2025–2036, doi:10.1016/j.pss.2007.04.014.
- Soderblom, L. A., M. Tomasko, B. Archinal, T. Becker, M. Bushroë, D. Cook, L. Doose, L. Galuszka, T. Hare, A. Howington-Kraus, E. Karkoschka, R. L. Kirk, J. I. Lunine, E. McFarlane, B. Redding, B. Rizk, M. Rosiek, C. See, and P. Smith, 2007b: Topography and geomorphology of the Huygens landing site on Titan. *Planet. Space Sci.*, **55**, 2015–2024, doi:10.1016/j.pss.2007.04.015.
- Soderblom, L. A., R. H. Brown, J. M. Soderblom, J. W. Barnes, R. L. Kirk, C. Sotin, R. Jaumann, D. J. Mackinnon, D. W. Mackowski, K. H. Baines, B. J. Buratti, R. N. Clark, and P. D. Nicholson, 2009: The geology of Hotei Regio, Titan: Correlation of Cassini VIMS and RADAR. *Icarus*, **204**, 610–618.
- Sohl, F., W. D. Sears, and R. D. Lorenz, 1995: Tidal dissipation on Titan. *Icarus*, **115**, 278–294.
- Solomonidou, A., A. Coustenis, M. Hirtzig, S. Rodriguez, K. Stephan, R. M. C. Lopes, P. Drossart, et al., 2016: Temporal variations of Titan's surface with Cassini/VIMS. *Icarus*, **270**.
- Sotin, C., R. Jaumann, B. J. Buratti, R. H. Brown, R. N. Clark, L.A. Soderblom, K. A. Baines, G. Bellucci, J.-P. Bibring, F. Capaccioni, P. Cerroni, M. Combes, A. Coradini, D. P. Cruikshank, P. Drossart, V. Formisano, Y. Langevin, D. L. Matson, T. B. McCord, R. M. Nelson, P. D. Nicholson, B. Sicardy, S. LeMouelic, S. Rodriguez, K. Stephan, and C. K. Scholz, 2005: Release of volatiles from a possible cryovolcano from near-infrared imaging of Titan. *Nature*, **435**, 786–789.
- Sotin, C., E. Karkoschka, L. Le Corre, S. Le Mouelic, R. H. Brown, R. Jaumann, L. Soderblom, K. Baines, B. Buratti, R. Clark, and P. D. Nicholson, 2009: Comparing VIMS observations of the Huygens landing site with DISR and radar observations: Implications for Titan geology and its spin rate. *European Planetary Science Congress*, 14–18.
- Sromovsky, L. A., H. E. Revercombe, R. J. Kraus, and V. E. Suomi, 1983: Voyager 2 observations of Saturn's northern mid-latitude cloud features: Morphology, motions and evolution. *J. Geophys. Res.*, **88**, 8650–8666.
- Stephan, K., R. Jaumann, R. H. Brown, J. M. Soderblom, L. A. Soderblom, J. W. Barnes, C. Sotin, C. A. Griffith, R. L. Kirk, K. H. Baines, B. J. Buratti, R. N. Clark, D. M. Lytle, R. M. Nelson, and P. D. Nicholson, 2010: Specular reflection on Titan: Liquids in Kraken Mare. *Geophys. Res. Lett.*, **37**, L07104, doi:10.1029/2009GL042312.
- Stiles, B. W., Y. Gim, G Hamilton, S. Hensley, W. T. K. Johnson, J. Shimada, R. D. West, and P. Callahan, 2006: Ground processing of Cassini RADAR imagery of Titan. *Proc. IEEE Radar Conf.*, Verona, NY.

- Stiles, B. W., R. L. Kirk, R. D. Lorenz, S. Hensley, E. Lee, S. J. Ostro, M. D. Allison, P. S. Callahan, Y. Gim, L. Iess, P. Persi del Marmo, G. Hamilton, W. T. K. Johnson, R. D. West, and The Cassini RADAR Science Team, 2008: Determining Titan's spin state from Cassini RADAR images. *Astronom. J.* **135**, 1669–1680, doi:10.1088/0004-6256/135/5/1669.
- Stiles, B. W., S. Hensley, Y. Gim, D. M. Bates, R. L. Kirk, A. Hayes, J. Radebaugh, R. D. Lorenz, K. L. Mitchell, P. S. Callahan, H. Zebker, W. T. K. Johnson, S. D. Wall, J. I. Lunine, C. A. Wood, M. A. Janssen, F. Pelletier, R. D. West, C. Veeramacheni, and the Cassini RADAR Science Team, 2009: Determining Titan surface topography from Cassini SAR data. *Icarus*, **202**, 584–598, doi:10.1016/j.icarus.2009.03.032.
- Stofan, E. R., C. Elachi, R. Lopes, R. Lorenz, R. L. Kirk, F. Paganelli, C. A. Wood, S. D. Wall, J. Lunine, L. Soderblom, and the Cassini RADAR Science Team, 2005: Mapping of Titan: First results from the Cassini RADAR. *36<sup>th</sup> Lunar Planet. Sci. Conf.*, Abstract 1714.
- Stofan, E. R., J. I. Lunine, R. M. Lopes, F. Paganelli, R. D. Lorenz, C. A. Wood, R. L. Kirk, S. D. Wall, C. Elachi, L. A. Soderblom, S. Ostro, M. Janssen, J. Radebaugh, L. Wye, H. Zebker, Y. Anderson, M. Allison, R. Boehmer, P. Callahan, P. Encrenaz, E. Flamini, G. Francescetti, Y. Gim, G. Hamilton, S. Hensley, W. T. K. Johnson, K. Kelleher, D. Muhleman, G. Picardi, F. Posa, L. Roth, R. Seu, S. Shaffer, B. Stiles, S. Vetrella, and R. West, 2006: Mapping of Titan: Results from the first two Titan radar passes. *Icarus*, **185**(2), 443–456, doi:10.1016/j.icarus.2006.07.015.
- Stofan, E. R., C. Elachi, J. I. Lunine, R. D. Lorenz, B. Stiles, K. Mitchell, S. Ostro, L. Soderblom, C. Wood, H. Zebker, S. Wall, M. Janssen, R. Kirk, R. Lopes, F. Paganelli, J. Radebaugh, L. Wye, Y. Anderson, M. Allison, R. Boehmer, P. Callahan, P. Encrenaz, E. Flamini, G. Francescetti, Y. Gim, G. Hamilton, S. Hensley, W. T. K. Johnson, K. Kelleher, D. Muhleman, P. Paillou, G. Picardi, F. Posa, L. Roth, R. Seu, S. Shaffer, S. Vetrella, R. West, 2007: The lakes of Titan. *Nature*, **445**, doi:10.1038/nature05438.
- Stofan, E. R., C. Elachi, J. I. Lunine, R. D. Lorenz, R. L. Kirk, R. M. Lopes, C. A. Wood, J. Radebaugh, S. D. Wall, K. L. Mitchell, L. A. Soderblom, P. Paillou, T. Farr, B. Stiles, P. Callahan, and the Cassini RADAR Science Team, 2008: Varied geologic terrains at Titan's south pole: First results from T39. *39<sup>th</sup> Lunar Planet. Sci. Conf.*, Abstract 1492, Houston, TX.
- Tobie, G., O. Grasset, J. I. Lunine, A. Mocquet, and C. Sotin, 2005: Titan's internal structure inferred from a coupled thermal-orbital model. *Icarus*, **175**, 496–502, doi:10.1016/j.icarus.2004.12.007.
- Tobie, G., J. I. Lunine, and C. Sotin, 2006: Episodic outgassing as the origin of atmospheric methane on Saturn's moon Titan. *Nature*, **440**, 61–64.
- Tokano, T., 2009: Limnological structure of Titan's hydrocarbon lakes and its astrobiological implication. *Astrobio.*, **9**(2), 147–164, doi:10.1089/ast.2007.0220.
- Tokano, T., 2011: Precipitation climatology on Titan, *Science*, **331**, 1393, doi:10.1126/science.1204092.
- Tokano, T., and R. D. Lorenz, 2006: GCM simulation of balloon trajectories on Titan, *Planet. Space Sci.*, **54**, 685–694.

- Tokano, T., and R. D. Lorenz, 2016: Sun-stirred Kraken Mare: Circulation in Titan's seas induced by solar heating and methane precipitation. *Icarus*, **270**.
- Tomasko, M. G., B. Archinal, T. Becker, B. Bézard, M. Bushroë, M. Combes, D. Cook, A. Coustenis, C. de Bergh, L. E. Dafeo, L. Doose, S. Douté, A. Eibl, S. Engel, F. Gliem, B. Grieger, K. Holso, E. Howington-Kraus, E. Karkoschka, H. U. Keller, R. Kirk, R. Kramm, M. Küppers, P. Lanagan, E. Lellouch, M. Lemmon, J. Lunine, E. McFarlane, J. Moores, G. M. Prout, B. Rizk, M. Rosiek, P. Rueffer, S. E. Schröder, B. Schmitt, C. See, P. Smith, L. Soderblom, N. Thomas, and R. West, 2005: Rain, winds and haze during the Huygens probe's descent to Titan's surface. *Nature*, **438**, 765–778, doi:10.1038/nature04126.
- Tosi, F., R. Orosei, R. Seu, A. Coradini, J. I. Lunine, G. Filacchione, A. I. Gavrishin, F. Capaccioni, P. Cerroni, A. Adriani, M. L. Moriconi, A. Negrão, E. Flamini, R. H. Brown, L. C. Wye, M. Janssen, R. D. West, J. W. Barnes, S. D. Wall, R. N. Clark, D. P. Cruikshank, T. B. McCord, P. D. Nicholson, J. M. Soderblom, and the Cassini VIMS and RADAR Teams, 2010: Correlations between VIMS and RADAR data over the surface of Titan: Implications for Titan's surface properties. *Icarus*, **208**, 366–384, doi:10.1016/j.icarus.2010.02.003.
- Towner, M. C., J. R. C. Garry, R. D. Lorenz, A. Hagermann, B. Hathi, H. Svedhem, B. C. Clark, M. R. Leese, and J. C. Zarnecki, 2006: Physical properties of Titan's surface at the Huygens landing site from the Surface Science Package Acoustic Properties sensor (API-S), *Icarus*, **185**, 457–465, doi:10.1016/j.icarus.2006.07.013.
- Tremaine, S., Touma, J. and Namouni, F., 2009. Satellite dynamics on the Laplace surface. *The Astronomical Journal*, **137**(3), p.3706.
- Turtle, E. P., J. Barnes, B. Buratti, G. Collins, S. Fussner, R. M. Lopes, R. D. Lorenz, J. I. Lunine, T. B. McCord, A. S. McEwen, R. M. Nelson, J. Perry, C. C. Porco, L. Soderblom, C. Sotin, and S. D. Wall, 2005: Exploring the surface of Titan with Cassini-Huygens. *Eos Trans. Amer. Geophys. Union Fall Mtg. Suppl.*, **85**(52), Abstract P44A-01.
- Turtle, E. P., J. E. Perry, A. S. McEwen, A. D. DelGenio, J. Barbara, R. A. West, D. D. Dawson, and C. C. Porco, 2009: Cassini imaging of Titan's high-latitude lakes, clouds, and south-polar surface changes. *Geophys. Res. Lett.*, **36**, L02204, doi:10.1029/2008GL036186.
- Turtle, E. P., J. E. Perry, A. G. Hayes, R. D. Lorenz, J. W. Barnes, A. S. McEwen, R. A. West, A. D. Del Genio, J. M. Barbara, J. I. Lunine, E. L. Schaller, T. L. Ray, R. M. C. Lopes, and E. R. Stofan, 2011a: Rapid and extensive surface changes near Titan's equator: Evidence of April showers. *Science*, **331**, 1414, doi:10.1126/science.1201063.
- Turtle, E. P., J. E. Perry, A. G. Hayes, and A. S. McEwen, 2011b: Shoreline retreat at Titan's Ontario Lacus and Arrakis Planitia from Cassini imaging science subsystem observations. *Icarus*, in press, doi:10.1016/j.icarus.2011.02.005.
- Ulaby, F. T., R. K. Moore, and A. K. Fung, 1982: *Radar Remote Sensing and Surface Scattering and Emission Theory*. Vol. 2, *Microwave Remote Sensing: Active and Passive*, Addison-Wesley Publishing Co., 609 pp.
- Ventura, B., D. Casarano, C. Notarnicola., D. Di Rosa, and F. Posa, 2006a: Cassini RADAR data analysis: Inference of physical and morphological properties of selected Titan's surface features. *Proc. IEEE Gold Symposium*, Bari, Italy, December.

- Ventura, B., D. Casarano, C. Notarnicola., D. Di Rosa, and F. Posa, 2006b: Modeling the electromagnetic response of Titan's surface features observed by the Cassini RADAR. *Proc. EUROPTO 2006 SPIE Conf. on SAR Image Analysis, Modeling and Techniques IV*, Stockholm, Sweden, September.
- Ventura, B., D. Casarano, C. Notarnicola., M. A. Janssen, and F. Posa, 2007a: Inferring Titan's surface features by means of Bayesian inversion algorithm applied to radar data. *Proc. Intl. Symposium Remote Sensing*, **6746**, Florence, Italy, September 17–20.
- Ventura, B., D. Casarano, C. Notarnicola, and F. Posa, 2007b: Cassini RADAR: Investigation of Titan's surface parameters by means of Bayesian inversion technique and gravity-capillary waves modelling of liquid hydrocarbons surfaces. *Proc. IEEE Intl. Geosci. and Remote Sensing Symposium*, Barcelona, Spain, July 23–27.
- Ventura, B., D. Casarano, C. Notarnicola, and F. Posa, 2007c: Double-layer backscattering model and Bayesian inversion for retrieval of Titan's surface parameters from Cassini RADAR data. *Proc. 5th Intl. Symposium on Retrieval of Bio and Geophys. Parameters from SAR Data for Land Applications, ESA Conf.*, Bari, Italy, September 25–28.
- Wall, S. D., and E. Flamini, 2008: The Cassini RADAR investigation, *7<sup>th</sup> European Conference on Synthetic Aperture Radar (EUSAR)*, June 2–5, ISBN 978-3-8007-3084-7.
- Wall, S. D., S. L. McConnell, C. E. Leff, R. S. Austin, K. K. Beratan, and Mark J. Rokey, 1995: *User Guide to the Magellan Synthetic Aperture Radar Images*, Jet Propulsion Laboratory.
- Wall, S. D., C. Elachi, and the Cassini RADAR Science Team, 2005: An overview of Cassini RADAR Mapper observations of Titan. *AAS Div. Planet Sci. Mtg.*, Cambridge, England, September.
- Wall, S. D., R. M. C. Lopes, and the Cassini RADAR Science Team, 2008: Evidence for cryovolcanic activity on the surface of Titan, *IAVCEI Conf.*
- Wall, S. D., M. Janssen, A. Le Gall, H. Zebker, L. Wye, and P. Paillou, 2009a: Cassini RADAR: What microwaves tell us about Titan. *PIERS*, Beijing, China, March.
- Wall, S. D., R. M. C. Lopes, E. R. Stofan, C. A. Wood, J. R. Radebaugh, S. M. Hörst, B. W. Stiles, R. M. Nelson, L. W. Kamp, M. A. Janssen, R. D. Lorenz, J. I. Lunine, T. G. Farr, G. Mitri, P. Paillou, F. Paganelli, and K. L. Mitchell, 2009b: Cassini RADAR images at Hotei Arcus and western Xanadu, Titan: Evidence for geologically recent cryovolcanic activity. *Geophys. Res. Lett.*, **36**, L04203, doi:10.1029/2008GL036415.
- Wall, S. D., A. Hayes, C. Bristow, R. Lorenz, E. Stofan, J. Lunine, A. Le Gall, M. Janssen, R. Lopes, L. Wye, P. Soderblom, P. Paillou, O. Aharonson, H. Zebker, T. Farr, G. Mitri, R. Kirk, K. Mitchell, C. Notarnicola, D. Casarano, and B. Ventura, 2010: Active shoreline of Ontario Lacus, Titan: A morphological study of the lake and its surroundings. *Geophys. Res. Lett.*, **37**, L05202, doi:10.1029/2009GL041821.
- West, R. D., Y. Anderson, B. Stiles, K. Kelleher, L. Wye, P. Callahan, A. Le Gall, Y. Gim, G. Hamilton, M. Janssen, R. L. Kirk, W. T. K. Johnson, R. Lorenz, C. Veeramachaneni, H. Zebker, and the Cassini RADAR Science Team, 2008a: Survey of Cassini Prime Mission radar data on Titan. *40<sup>th</sup> Amer. Astron. Soc. Div. Planet. Sci., Bull. Amer. Astron. Soc.*, **40**, 449.

- West, R. D., Y. Anderson, B. Stiles, K. Kelleher, L. Wye, P. Callahan, A. Le Gall, Y. Gim, G. Hamilton, M. Janssen, R. Kirk, W. T. K. Johnson, R. Lorenz, C. Veeramachaneni, H. Zebker, and the Cassini RADAR Science Team, 2008b: Cassini RADAR: Extended Mission Plans and Expected Results. *Amer. Geophys. Union*.
- West, R. D., Y. Anderson, R. Boehmer, L. Borgarelli, P. Callahan, C. Elachi, Y. Gim, G. Hamilton, S. Hensley, M. A. Janssen, W. T. K. Johnson, K. Kelleher, R. Lorenz, S. Ostro, L. Roth, S. Shaffer, B. Stiles, S. Wall, L. C. Wye, and H. A. Zebker, 2009: Cassini RADAR sequence planning and instrument performance. *IEEE Trans. Geosci. and Remote Sensing*, **47**(6), 1777–1795, doi:10.1109/TGRS.2008.2007217.
- Wood, C. A., R. Lorenz, R. Kirk, R. Lopes, K. Mitchell, and E. Stofan, 2010: Impact craters on Titan. *Icarus*, **206**, 334–344, doi:10.1016/j.icarus.2009.08.021.
- Wye, L. C., H. A. Zebker, S. J. Ostro, R. D. West, Y. Gim, M. A. Janssen, R. D. Lorenz, S. Hensley, and the Cassini RADAR Science Team, 2005: Titan’s surface observed with the Cassini RADAR scatterometer. *Amer. Geophys. Union Joint Assembly Mtg.*, New Orleans, LA, May 23–27.
- Wye, L. C., H. A. Zebker, and the Cassini RADAR Science Team, 2006a: A second look at reduction and analysis of low-resolution Cassini RADAR scatterometer Titan data. *Amer. Astron. Soc. Div. Planet. Sci. Mtg.*, Oct 8–13.
- Wye, L. C., H. A. Zebker, R. D. Lorenz, and the Cassini RADAR Science Team, 2006b: Modeling Titan’s surface from Cassini RADAR’s scatterometer and radiometer measurements. *37<sup>th</sup> Lunar Planet. Sci. Conf.*, Abstract 1473, March 15.
- Wye, L. C., H. A. Zebker, M. Janssen, R. Lorenz, R. West, and the Cassini RADAR Science Team, 2007a: Composition of Titan’s surface features constrained through backscatter modeling, *Workshop on Ices, Oceans, and Fires: Satellites of the Outer Solar System*, Boulder, CO, August 13–15.
- Wye, L. C., H. A. Zebker, M. Janssen, R. Lorenz, R. West, Y. Gim, P. Paillou, and the Cassini RADAR Science Team, 2007b: Backscatter modelling of Titan’s surface features using a comprehensive collection of Cassini RADAR data. *39th Amer. Astron. Soc. Div. Planet. Sci. Mtg.*, Orlando, FL, October 7–12.
- Wye, L. C., H. A. Zebker, S. J. Ostro, R. D. West, and the Cassini RADAR Science Team, 2007c: Range-Doppler processing of Saturn’s icy satellites using the Cassini RADAR scatterometer. *Amer. Geophys. Union Fall Mtg.*, San Francisco, CA, December 10–14.
- Wye, L. C., H. A. Zebker, S. J. Ostro, R. D. West, Y. Gim, R. D. Lorenz, and the Cassini RADAR Science Team, 2007d: Electrical properties of Titan’s surface from Cassini RADAR scatterometer measurements. *Icarus*, **188**, 367–385.
- Wye, L. C., H. A. Zebker, R. M. Lopes, R. Peckyno, A. Le Gall, and M. A. Janssen, 2009a: A backscatter analysis of Titan’s surface features and their global distribution using Cassini RADAR data, *Bull. Amer. Astron. Soc.*, **41**, 560.
- Wye, L. C., H. A. Zebker, and R. D. Lorenz, 2009b: Smoothness of Titan’s Ontario Lacus: Constraints from Cassini RADAR specular reflection data. *Geophys. Res. Lett.*, **36**, L16201, doi:10.1029/2009GL039588.
- Yseboodt, M., J. L. Margot, and S. J. Peale, 2010: Analytical model of the long-period forced longitude librations of Mercury. *Icarus*, **207**(2), 536–544.

- Zebker, H. A., 2008: The shape of Saturn's moon Titan from radar scattering properties. *PIERS*, Cambridge, MA, July 2–6.
- Zebker, H. A., and L. Wye, 2006: Electrical properties of Titan surface from Cassini scatterometer and radiometer measurements. *PIERS*, Cambridge, MA, March 27.
- Zebker, H. A., B. Stiles, S. Hensley, P. Callahan, Y. Gim, R. D. Lorenz, and R. L. Kirk, 2008: Titan's shape from Cassini radar altimeter and SAR monopulse observations. *Amer. Geophys. Union Fall Mtg.*
- Zebker, H. A., Y. Gim, P. Callahan, S. Hensley, R. Lorenz, and the Cassini RADAR Science Team, 2009a: Analysis and interpretation of Cassini Titan radar altimeter echoes. *Icarus*, **200**(1), 240–255.
- Zebker, H. A., B. Stiles, S. Hensley, R. D. Lorenz, R. L. Kirk, and J. Lunine, 2009b: Size and shape of Saturn's moon Titan. *Science*, published online. *Science Express Reports*, April 2, doi:10.1126/science.1168905.
- Zebker, H., A. Hayes, M. Janssen A. Le Gall, R. Lorenz, and L. Wye, 2014: Surface of Ligeia Mare, Titan, from Cassini altimeter and radiometer analysis. *Geophys. Res. Lett.*, **41**, 308–313, doi:10.1002/2013GL058877.
- Zhang, Z., A. G. Hayes, M. A. Janssen, P. D. Nicholson, J. N. Cuzzi, I. de Pater, D. E. Dunn, P. R. Estrada, and M. M. Hedman, 2017: Cassini microwave observations provide clues to the origin of Saturn's C ring. *Icarus*, **281**, 297–321.
- Zimbelman, J. R., M. C. Bourke, and R. D. Lorenz, 2013: Recent developments in planetary aeolian studies and their terrestrial analogs. *Aeolian Res.*, **11**, 109–126.

## 11 Appendix 2: Acronyms

AACS	Attitude and Articulation Control Subsystem
ABDR	Altimeter-Burst Data Record
ALC	automatic level-control
ASI	Agenzia Spaziale Italiana (Italian Space Agency)
ASIC	application-specific integrated circuit
ASUM	ABDR Summary File
AU	astronomical unit
BAQ	block-adaptive quantizer
BG	background
BIDR	Basic Image Data Record
BIE	incidence angle data
BIL	number of looks data
BIM	beam mask data
BIN	longitude data
BIS	image file with correction for noise but not incidence angle
BIT	latitude data
BIU	bus interface unit
BIU	image file without correction for incidence angle or noise
BODP	Burst-Ordered Data Product
CCSDS	Consultative Committee for Space Data Systems
CDAP	Cassini Data Analysis Program
CDS	Command and Data Subsystem
CIRS	Composite Infrared Spectrometer
CO	carryover
CODMAC	Committee on Data Management and Computation
CRST	Cassini RADAR Science Team
CRT	Cassini RADAR Transition
csr	calibration source
csv	comma-separated value
DBE	double-bit error
DISR	Descent Imager/Spectral Radiometer
DMP	Digital Map Product
DOM	Distributed Object Manager (Cassini project database)
DR	Discrepancy Report
DSN	Deep Space Network
DSS	Deep Space Station

DTM	Digital Topographic Model
DTN	datatake number
DV	data volume
ECR	Engineering Change Request
ENVI	Environment for Visualizing Images
EP	vertical precision
ESA	European Space Agency
Fiji	Fiji is just ImageJ
FSIV	Final Sequence Integration and Validation
GIS	geographic information system
GRDR	Global Radiometry Data Record
GSA	Geological Society of America
GSD	ground-sample distance
GSDR	Global Scatterometry Data Record
GTDR	Global Topography Data Record
HGA	high-gain antenna
HH	horizontal transmitting, horizontal receiving (polarization)
HiSAR	high-altitude SAR imaging
IDAP	Immediate/Delayed Action Program
IEB	instrument execution block
IEEE	Institute of Electrical and Electronics Engineers
IAU	International Astronomical Union
INMS	Ion and Neutral Mass Spectrometer
ISA	Incident/Surprise/Anomaly Report
ISCT	Inbound Scatterometry
ISIS	Integrated Software for Imagers and Spectrometers
ISS	Imaging Science Subsystem
ITL	Integrated Test Lab
IVP	Inertial Vector Propagator
LBDR	Long-Burst Data Record
LGA	low-gain antenna
LSB	least significant bit
MIDR	Mosaicked Image Data Record
MSS	Mission Sequence Software
NASA	National Aeronautics and Space Administration
ND	not determined
nnn	Saturn orbit number

NP	north pole
NRCS	normalized radar cross section
OALT	Outbound Altimetry
OD	orbit determination
ORAD	Outbound Radiometry
ORS	optical remote sensing
OST	Orbiter Science Team
OTM	Orbit Trim Maneuver
P/FR	Problem/Failure Report
PDS	Planetary Data System
PIA	Planetary Image Archive
PIERS	Progress in Electromagnetics Research Symposium
PMS	Propulsion Module Subsystem
POL	polarization angle
PPS	Power and Pyrotechnics Subsystem
PRDR	Pass Radiometry Data Record
PRF	pulse-repetition frequency
PSDR	Pass Scatterometry Data Record
PSIV	Preliminary Sequence Integration and Validation
PDT	Pacific Daylight Time
PST	Pacific Standard Time
PTDR	Pass Topography Data Record
RADAR	Cassini Radio Detection and Ranging instrument
RFS	Radio Frequency Subsystem
RIDR	Repeat Image Data Record
RL	resistive load
RMSS	RADAR Mapping Sequencing Software
RTG	radioisotope thermoelectric generator
s	temporal order of observation
S/C	spacecraft
SAB	SAR-altimetry burst
SAL	synthetic aperture lidar
SAR	synthetic aperture radar
SARSME	SAR Spin-Model Estimation
SBDR	Short-Burst Data Record
SFDU	Standard Formatted Data Unit
SOCET	Softcopy Exploitation Toolkit (SOCET SET is pronounced “socket set”)

SIS	Software Interface Specification
SNR	signal-to-noise ratio
SOI	Saturn Orbit Insertion
SOP	Science Operation Plan
SOST	Satellites Orbiter Science Team
SP	south pole
SSG	subsequence generation
SSR	solid-state recorder
SSUP	Science and Sequence Update Process
TCS	Temperature Control Subsystem
ti	Titan
TLM	telemetry
TOST	Titan Orbiter Science Team
TWT	Target Working Team
USGS	United States Geological Survey
UTC	Coordinated Universal Time
VHSIC	very-high-speed integrated circuit
VIMS	Visible and Infrared Mapping Spectrometer
VLA	Very Large Array
VV	vertical transmitting, vertical receiving (polarization)
WGPSN	Working Group for Planetary System Nomenclature
WTK	William T. K. Johnson data volume
XM	Equinox Mission (Cassini's first extended mission)
XXM	Solstice Mission (Cassini's second extended mission, the extended extended mission)



# Cassini RADAR Users Guide

TIMING										REFERENCE TRAJECTORY 180628																		Illumination of Titan	I/B or O/B wrt Saturn	Occ	LST	Dual pb?	C/A		Phase @C/A	Flyby						
RANGE (KM)					Angular Diameter (degrees)																		Inbound to c/a (hours)										Outbound from c/a (hours)									Lat
Flyby	REV	SEQ	Date	DOY	C/A Time	gms	Hyd	Alt																			Dec-Hr	(deg)	(deg)	(deg)	Flyby											
T34	S32	48	07/19/07	200	01:11:20	275.8	1332	CIRS ISS CIRS VIMS UVIS ISS RSS VIMS ISS C ISS CIRS DSN Pass																		Out	I/B	18.46	1.4	244.7	34.4	T34										
								T35	S33	49	08/31/07	243	06:32:36	3324	CIRS VIMS ISS C ISS CIRS DSN Pass																		Out	O/B	UV	11.41	63.0	111.0	86.8	T35		
															T36	S34	50	10/02/07	275	04:42:43	299.0	973	CIRS ISS UVIS RADAR VIMS ISS CIRS ISS V CIRS DSN																		Out	O/B
T37	S35	52	11/19/07	323	00:47:25	341.6	999	VIMS CIRS VIMS ISS C ISS CIRS DSN																		Out	O/B	Dual PB	11.29	-21.2	117.3	51.3	T37									
								T38	S35	53	12/05/07	339	00:06:50	1298	CIRS ISS UVIS CIRS VIMS ISS C ISS CIRS ISS V CIRS																		Out	O/B	Dual PB	11.29	-79.1	173.6	69.8	T38		
T39	S36	54	12/20/07	354	22:57:55	334.0	969								VIMS CIRS RADAR CIRS ISS V I Rhea VIMS																		Out	O/B	Dual PB	11.27	-70.3	175.7	61.4	T39		
								T40	S36	55	01/05/08	5	21:30:19	329.9	1014	I Tethys CIRS ISS UVIS ISS C U IN VIMS ISS C VIMS ISS CIRS																		Out	O/B	UV	11.23	-11.5	130.3	37.6	T40	
T41	S38	59	02/22/08	53	17:32:07	850.3	1000									CIRS ISS VIMS RADAR UVIS ISS CIRS ISS V DSN Pass CIRS UVIS																		Out	O/B	U	11.12	-34.8	151.5	30.2	T41	
								T42	S39	62	03/25/08	85	14:27:48	379.2	999	VIMS CIRS VIMS ISS CIRS ISS VIMS																		Out	O/B	Dual PB	11.02	-27.2	156.3	21.4	T42	
T43	S40	67	05/12/08	133	10:01:58	257.5	1001									C ISS VIMS RADAR CIRS DSN Pass CIRS																		Out	O/B	Dual PB	10.89	18.1	137.3	35.8	T43	
								T44	S40	69	05/28/08	149	08:24:32	891.3	1400	CIRS ISS CIRS VIMS UVIS ISS RADAR ISS CIRS ISS VIMS DSN Pass VIMS																		Out	O/B	Dual PB	10.84	10.4	150.3	21.0	T44	
T45	S42	78	07/31/08	213	02:13:11	1614	CIRS ISS RSS CIRS RSS DSN Pass																		IN	O/B	Dual PB	10.64	-43.5	195.2	49.1	T45										
							T46	S45	91	11/03/08	308	17:35:23	404.8	1105	CIRS ISS CIRS RSS UVIS ISS CIRS ISS CIRS DSN Pass																		IN	O/B	R	10.39	-3.4	340.0	171.4	T46		
T47	S45	93	11/19/08	324	15:56:28	184.1									1023	VIMS ISS VIMS U V U CIRS ISS CIRS ISS CIRS OpNav DSN Pass																		IN	O/B	U	10.34	-21.7	177.5	28.1	T47	
							T48	S46	95	12/05/08	340	14:25:45	360.2	961		VIMS CIRS ISS C ISS R IN U C UVIS VIMS ISS CIRS DSN Pass																		IN	O/B	U	10.29	-10.4	178.7	25.0	T48	
T49	S46	97	12/21/08	356	12:59:52	340.4									971	CIRS ISS C VIMS RADAR CIRS VIMS ISS CIRS ISS DSN Pass																		IN	O/B	Dual PB	10.25	-44.2	236.7	82.6	T49	
							T50	S47	102	02/07/09	38	08:50:52	393.2	967		VIMS CIRS RADAR IN RADAR UVIS ISS CIRS ISS CIRS ISS DSN Pass																		IN	O/B	Dual PB	10.14	-33.9	306.4	136.1	T50	
T51	S49	106	03/27/09	86	04:43:36	350.3									963	CIRS ISS CIRS ISS VIMS ISS V R CIRS ISS CIRS ISS CIRS ISS DSN Pass																		IN	O/B	Dual PB	10.03	-30.6	234.8	84.1	T51	
							T52	S49	108	04/04/09	94	01:47:46	957.2	4147		CIRS VIMS RADAR UVIS RSS CIRS ISS CIRS ISS CIRS DSN Pass																		Out	I/B	RU	21.87	-2.7	176.3	151.5	T52	
T53	S49	109	04/20/09	110	00:20:45	3599									CIRS ISS VIMS UV CIRS U C V RADAR VIMS ISS VIMS CIRS DSN Pass																		Out	I/B	UV	21.83	-7.6	177.6	148.5	T53		
							nT109	S49	109	04/27/09	117	04:05:52	694947	ISS ISS Rhea ISS DSN Pass ISS CAPS																		ALL	O/B	8.50	28.3	69.6	64.0	nT109				
T54	S50	110	05/05/09	125	22:54:15	3242								CIRS ISS CIRS ISS UVIS CIRS VIMS DSN																		Out	I/B	Dual PB	21.79	-13.6	177.8	145.9	T54			
							T55	S50	111	05/21/09	141	21:26:41	351.3	966	C VIMS UVIS RADAR CIRS ISS CIRS DSN Pass																		Out	I/B	Dual PB	21.75	-21.9	177.9	141.5	T55		
T56	S50	112	06/06/09	157	20:00:00	366.6									968	CIRS ISS VIMS RADAR UVIS CIRS VIMS DSN																		Out	I/B	U	21.71	-31.9	178.1	135.1	T56	
							T57	S51	113	06/22/09	173	18:32:35	556.7	955		CIRS ISS UVIS C R IN RADAR UVIS VIMS CIRS DSN Pass																		Out	I/B	R	21.67	-42.0	178.4	127.9	T57	
T58	S51	114	07/08/09	189	17:04:03	236.7									966	VIMS UVIS V U R U V CIRS ISS CIRS ISS VIMS DSN																		Out	I/B	UV	21.62	-52.1	178.8	120.2	T58	
							T59	S52	115	07/24/09	205	15:34:03	373.5	956		ISS CIRS ISS CIRS VIMS CAPS IN CIRS DSN Pass																		Out	I/B	Dual PB	21.58	-62.1	179.6	112.2	T59	
T60	S52	116	08/09/09	221	14:03:53	288.0									971	CIRS ISS UVIS RADAR ISS DSN Pass DSN playback pass lost due to station issue																		Out	I/B	Dual PB	21.53	-72.3	180.8	104.1	T60	
							T61	S53	117	08/25/09	237	12:51:37	285.4	961		VIMS CIRS VIMS RADAR VIMS VIMS																		Out	I/B	Dual PB	21.51	-19.2	237.1	85.9	T61	
T62	S54	119	10/12/09	285	08:36:24	270.5									1299	ISS CIRS ISS UVIS C U CIRS UVIS CIRS ISS VIMS DSN Pass																		Out	I/B	UV	21.39	-61.8	68.9	99.4	T62	
							T63	S55	122	12/12/09	346	01:03:14	4847	CIRS ISS CIRS RADAR CAPS C ISS VIMS CIRS																		Out	O/B	Dual PB	16.61	33.4	114.6	124.4	T63			
T64	S56	123	12/28/09	362	00:16:58	439.5								951	CIRS ISS CIRS R VIMS CIRS ISS VIMS																		Out	O/B	Dual PB	16.61	82.1	172.4	85.9	T64		
							T65	S56	124	01/12/10	12	23:10:36	265.6		1074	C VIMS CIRS CAPS CAPS CIRS																		Out	O/B	Dual PB	16.59	-82.2	359.1	95.2	T65	
T66	S57	125	01/28/10	28	22:28:50	7486								CIRS ISS UVIS CIRS ISS UVIS CIRS VIMS																		Out	O/B	V	16.60	-53.0	296.7	68.6	T66			
							T67	S59	129	04/05/10	95	15:50:54	7438	ISS reset CIRS ISS CIRS ISS C ISS VIMS DSN Pass																		Out	I/B	Dual PB	20.89	0.4	240.4	73.0	T67			





13 Appendix 4: SAR Swath Details

SWATH	SEGMENT	DATE			WEST LONGITUDE (DEG)				LATITUDE (DEG)				INCIDENCE (DEG)				POLARIZATION (DEG)				AZIMUTH (DEG)				SAR RANGE RESOLUTION (KM)				SAR AZIMUTH RESOLUTION (KM)				NUMBER OF LOOKS			
		T#	M	D	Y	MEAN	MEDIAN	MIN	MAX	MEAN	MEDIAN	MIN	MAX	MEAN	MEDIAN	MIN	MAX	MEAN	MEDIAN	MIN	MAX	MEAN	MEDIAN	MIN	MAX	MEAN	MEDIAN	MIN	MAX	MEAN	MEDIAN	MIN	MAX	MEAN	MEDIAN	MIN
A	1	10	26	2004	69.53	70.95	-2.10	137.57	41.93	42.27	20.55	56.87	24.37	23.82	1.83	46.26	172.21	177.04	124.98	185.23	93.64	88.26	22.77	181.85	0.78	0.79	0.27	3.83	0.37	0.30	0.24	1.30	6.68	4.00	1.00	91.00
3	1	2	15	2005	67.89	68.14	-1.80	137.06	15.52	15.41	-6.31	32.13	19.08	19.89	0.83	30.30	176.79	178.72	130.09	183.17	275.74	275.57	234.59	346.67	0.49	0.44	0.32	13.60	0.50	0.33	0.25	1.93	8.51	7.00	1.00	30.00
7	1	9	7	2005	8.79	11.73	-30.69	30.83	-50.07	-50.46	-75.24	-24.83	20.36	20.21	7.02	35.59	187.21	358.99	0.00	360.00	213.10	212.99	196.70	231.14	0.46	0.42	0.28	0.97	0.36	0.30	0.25	0.73	6.47	5.00	1.00	17.00
8	1	10	28	2005	250.73	250.74	181.25	320.14	-10.17	-10.17	-18.87	-1.90	21.02	21.53	5.33	30.02	154.36	24.04	0.00	360.00	262.53	262.79	219.07	279.30	0.49	0.43	0.34	2.28	0.45	0.31	0.25	1.63	7.92	6.00	1.00	38.00
8	2	10	28	2005	313.59	313.59	306.94	320.26	-6.78	-6.78	-18.38	4.80	17.02	17.17	3.65	30.51	51.45	46.56	19.32	127.43	224.53	229.73	145.23	253.39	1.15	0.77	0.40	9.17	1.57	1.35	1.07	5.26	3.10	3.00	1.00	9.00
8	3	10	28	2005	184.29	184.29	179.08	189.51	-5.31	-5.31	-16.90	6.27	11.47	10.78	1.95	24.90	30.42	13.03	0.13	179.66	234.18	248.69	88.43	268.10	3.76	2.09	0.83	21.44	0.76	0.62	0.61	3.82	4.97	5.00	1.00	11.00
13	1	4	30	2006	116.36	116.37	60.33	172.35	-11.46	-11.46	-19.23	-3.72	20.51	20.84	9.99	29.29	18.10	5.02	0.01	360.00	263.43	265.62	224.01	276.03	0.47	0.44	0.33	1.00	0.40	0.31	0.25	1.30	6.71	7.00	1.00	37.00
13	2	4	30	2006	167.83	167.83	163.30	172.36	-5.23	-5.23	-17.74	7.28	12.64	12.25	1.48	27.31	54.71	41.54	2.13	177.84	217.72	230.51	92.04	267.76	2.10	1.16	0.43	18.32	1.51	1.20	0.97	8.01	16.44	15.00	1.00	55.00
13	3	4	30	2006	189.81	189.81	180.31	199.30	-6.69	-6.69	-13.70	0.31	14.88	15.43	3.20	25.04	317.15	316.71	314.18	323.22	221.91	222.35	215.11	225.59	2.12	1.57	1.44	6.87	2.76	2.71	2.47	3.37	50.78	35.00	1.00	225.00
15	2	7	2	2006	30.40	30.39	8.17	52.52	-30.47	-30.47	-42.53	-18.36	36.78	36.82	32.29	42.01	145.29	18.37	0.00	359.97	246.43	243.19	225.69	276.96	2.14	2.15	2.08	2.16	3.04	2.99	2.76	3.45	159.18	163.00	1.00	255.00
15	3	7	2	2006	42.49	42.49	31.39	53.54	-22.52	-22.52	-33.54	-11.49	33.10	33.19	24.78	41.17	21.65	21.41	20.94	23.22	227.64	227.19	225.84	231.05	2.36	2.27	2.11	2.99	2.66	2.67	2.52	2.76	19.14	17.00	1.00	49.00
16	1	7	22	2006	62.71	50.82	-22.06	152.52	50.18	50.92	11.42	88.29	21.78	21.02	8.71	40.27	173.24	48.16	0.00	360.00	252.13	230.30	0.00	359.99	0.46	0.40	0.25	1.91	0.42	0.30	0.25	1.91	6.41	7.00	1.00	13.00
16	2	7	22	2006	147.03	147.03	135.09	158.36	23.73	23.73	16.01	31.44	17.37	17.84	1.70	29.57	47.05	48.12	36.99	51.25	316.56	315.46	314.55	325.30	1.92	0.92	0.59	12.66	1.47	1.51	0.60	1.62	9.69	9.00	1.00	68.00
16	3	7	22	2006	341.12	341.12	332.49	349.91	17.56	17.56	11.53	23.62	12.21	12.20	1.61	22.25	314.33	313.12	312.70	323.30	220.26	220.43	214.94	221.10	1.80	0.85	0.59	11.82	1.35	1.34	1.24	1.43	14.28	11.00	1.00	78.00
17	1	9	7	2006	52.32	52.16	29.93	74.28	9.85	9.96	0.31	17.69	36.00	36.07	29.45	45.03	255.92	332.98	0.00	359.97	268.65	268.35	245.67	292.32	0.28	0.28	0.25	0.32	0.27	0.27	0.25	0.35	2.22	2.00	1.00	3.00
18	1	9	23	2006	30.50	15.18	-20.70	119.66	59.71	63.84	31.29	77.50	31.25	30.70	18.93	45.35	178.60	56.00	0.02	360.00	236.65	235.75	218.19	264.12	0.38	0.37	0.29	0.45	0.32	0.30	0.25	0.48	2.28	2.00	1.00	3.00
19	1	10	9	2006	33.73	-19.14	-180.00	180.00	48.05	51.14	-8.90	90.00	21.76	21.19	8.71	39.33	174.40	178.10	104.86	241.31	92.19	26.09	0.04	359.93	0.53	0.42	0.25	2.60	0.42	0.31	0.25	3.17	6.91	7.00	1.00	20.00
19	2	10	9	2006	143.61	143.61	129.94	155.20	42.76	42.75	33.50	51.72	12.95	12.99	1.63	23.60	124.45	123.43	121.74	129.46	217.65	219.37	210.31	221.03	2.41	1.06	0.57	20.54	2.16	2.20	1.35	5.13	13.77	11.00	1.00	89.00
19	3	10	9	2006	324.49	324.49	315.81	333.13	-2.70	-2.69	-9.91	4.41	12.76	12.79	2.14	22.37	225.57	225.61	223.45	227.46	329.32	330.53	315.67	335.50	1.61	0.97	0.59	8.96	1.50	1.45	1.23	2.02	20.37	21.00	1.00	87.00
19	4	10	9	2006	317.40	317.35	293.83	340.56	-3.29	-3.21	-25.61	16.86	22.95	23.20	4.29	39.72	125.50	125.76	123.84	125.90	56.88	56.88	56.58	57.10	6.24	2.96	2.14	35.53	1.99	2.00	1.90	2.11	19.63	14.00	1.00	84.00
19	5	10	9	2006	300.74	300.63	282.93	317.71	-1.85	-1.87	-24.91	17.72	35.23	35.27	31.21	39.73	145.40	143.66	125.65	170.89	40.61	41.85	20.34	57.02	2.19	2.19	2.14	2.22	2.13	2.15	1.92	2.32	161.60	177.00	1.00	255.00
19	6	10	9	2006	291.85	291.78	278.62	305.04	-6.73	-6.64	-20.92	5.44	39.89	39.82	33.69	46.19	166.40	167.87	156.49	170.89	24.04	22.87	20.34	31.96	2.05	2.08	1.83	2.15	2.35	2.33	2.29	2.47	22.07	19.00	1.00	61.00
20	2	10	25	2006	147.23	147.98	89.12	206.78	0.44	0.22	-31.13	23.36	35.35	32.83	19.24	61.80	226.81	295.60	0.76	359.92	290.65	307.84	227.28	322.19	2.83	2.80	2.15	3.65	8.67	8.95	6.01	12.01	21.75	15.00	1.00	126.00
20	3	10	25	2006	122.92	122.93	75.79	169.83	0.63	0.59	-31.42	32.37	34.49	34.87	23.18	43.56	258.97	318.51	0.05	359.89	285.68	287.85	245.71	322.14	2.56	2.24	2.10	3.94	5.21	4.61	3.38	10.35	176.75	255.00	1.00	255.00
20	4	10	25	2006	138.46	138.33	105.03	178.40	18.35	18.34	-15.27	50.37	17.09	17.20	3.94	29.39	28.00	28.25	25.90	28.46	244.58	244.76	243.08	245.73	10.55	5.45	3.78	64.29	4.14	4.14	3.52	6.49	34.88	31.00	1.00	92.00
21	1	12	12	2006	258.54	266.47	185.58	305.65	21.21	25.41	-32.19	59.16	26.48	23.46	8.66	56.70	177.34	178.30	119.10	251.96	325.10	325.72	267.27	349.32	0.46	0.34	0.24	2.28	0.42	0.31	0.25	2.60	5.98	5.00	1.00	52.00
21	2	12	12	2006	300.54	300.54	290.17	311.31	-20.54	-20.53	-30.16	-10.86	12.54	12.50	0.89	23.40	224.25	237.30	3.45	349.68	278.55	289.12	131.94	301.95	1.75	0.91	0.56	20.84	1.69	1.71	1.47	2.84	17.57	18.00	1.00	58.00
23	1	1	13	2007	19.76	8.82	-35.32	108.92	19.53	25.63	-42.66	61.03	21.47	20.87	8.86	38.75	181.56	293.81	0.00	360.00	223.99	221.55	187.88	266.36	0.50	0.42	0.26	2.18	0.41	0.31	0.25	1.67	6.66	7.00	1.00	42.00
23	2	1	13	2007	94.43	94.31	81.47	111.07	56.06	56.04	47.03	65.20	12.64	12.68	1.88	22.54	46.12	48.42	31.59	49.51	250.85	251.13	248.17	256.84	2.00	0.84	0.59	15.94	1.43	1.45	1.32	1.68	14.60	11.00	1.00	91.00
23	3	1	13	2007	333.10	332.98	318.83	346.74	-34.14	-34.10	-43.57	-24.32	17.01	17.52	1.44	28.40	305.85	305.42	292.79	322.60	239.99	239.80	229.72	264.11	1.66	1.12	0.64	8.40	1.27	1.33	0.58	1.38	9.36	6.00	1.00	42.00
25	1	2	22	2007	10.52	28.02	-152.07	62.06	30.74	32.96	-39.91	89.01	21.18	20.54	8.45	38.92	177.59	178.54	117.34	244.63	155.65	161.89	0.14	359.84	0.49	0.42	0.25	2.05	0.39	0.29	0.24	1.57	6.34	7.00	1.00	12.00
25	2	2	22	2007	45.63	45.66	34.99	56.81	-31.54	-31.50	-40.14	-23.05	12.39	12.46	1.59	22.13	136.02	133.16	131.53	157.38	192.87	192.77	181.56	196.84	1.65	0.80	0.59	9.15	1.31	1.31	1.21	1.39	3.06	2.00	1.00	18.00
25	3	2	22	2007	36.95	95.47	-180.00	180.00	65.78	65.88	41.17	90.00	39.60	39.48	35.27	45.87	112.75	113.56	94.53	128.19	331.81	333.22	312.57	339.62	2.00	1.99	1.84	2.27	2.30	2.14	1.74	3.46	53.14	57.00	1.00	110.00
25	4	2	22	2007	24.																															

# Cassini RADAR Users Guide

SWATH	SEGMENT	DATE			WEST LONGITUDE (DEG)				LATITUDE (DEG)				INCIDENCE (DEG)				POLARIZATION (DEG)				AZIMUTH (DEG)				SAR RANGE RESOLUTION (KM)				SAR AZIMUTH RESOLUTION (KM)				NUMBER OF LOOKS			
		T#	M	D	Y	MEAN	MEDIAN	MIN	MAX	MEAN	MEDIAN	MIN	MAX	MEAN	MEDIAN	MIN	MAX	MEAN	MEDIAN	MIN	MAX	MEAN	MEDIAN	MIN	MAX	MEAN	MEDIAN	MIN	MAX	MEAN	MEDIAN	MIN	MAX	MEAN	MEDIAN	MIN
36	1	10	2	2007	32.74	32.27	10.21	59.10	-28.91	-28.92	-52.38	-5.68	19.49	19.86	1.49	38.35	175.51	175.43	2.05	244.24	201.81	268.06	0.17	359.81	0.92	0.79	0.23	13.36	0.91	0.76	0.37	6.80	5.45	4.00	1.00	46.00
36	2	10	2	2007	24.94	24.27	5.20	49.61	-29.09	-29.13	-53.24	-4.79	28.68	26.47	9.94	54.93	174.97	174.13	2.05	244.24	200.22	267.77	0.17	359.81	0.92	0.79	0.23	13.36	0.91	0.76	0.37	6.80	1.65	1.00	1.00	10.00
36	3	10	2	2007	107.53	103.88	20.95	198.59	-57.85	-59.11	-77.67	-32.55	43.37	42.31	30.29	61.52	178.02	177.77	115.54	242.07	213.08	226.22	0.00	359.98	0.28	0.28	0.23	0.32	0.31	0.28	0.24	0.55	1.77	2.00	1.00	3.00
36	4	10	2	2007	195.89	195.98	179.32	212.22	1.56	1.48	-22.13	25.38	37.50	38.41	4.06	68.63	292.72	287.28	0.09	359.88	88.80	101.62	30.06	115.26	1.70	1.42	1.24	2.77	2.56	2.56	1.24	4.69	7.10	6.00	1.00	45.00
39	1	12	20	2007	-53.81	-12.47	-180.00	180.00	-57.56	-57.81	-90.00	-23.54	26.56	23.87	8.22	57.89	179.47	178.59	110.10	240.11	209.29	182.88	0.07	359.99	0.42	0.32	0.24	2.20	0.40	0.28	0.23	2.42	5.18	5.00	1.00	11.00
39	7	12	20	2007	28.85	28.86	18.99	40.20	-35.85	-35.85	-43.64	-27.62	12.38	12.36	1.64	23.05	127.80	125.90	125.00	142.44	34.26	37.18	15.19	39.55	2.20	1.02	0.51	13.60	1.62	1.64	1.24	1.69	2.43	2.00	1.00	11.00
39	2	12	20	2007	196.83	196.75	172.24	223.69	8.47	8.50	-20.43	34.16	25.39	24.44	3.75	51.28	276.74	262.07	255.31	351.34	98.89	53.86	0.78	359.47	0.94	0.79	0.47	2.52	1.37	1.35	0.86	2.81	6.26	6.00	1.00	20.00
39	3	12	20	2007	0.02	-0.74	-42.52	45.08	-50.08	-49.65	-72.93	-30.16	42.53	42.46	38.51	48.53	238.42	239.88	216.87	257.32	320.45	319.58	295.10	347.47	1.90	1.92	1.79	1.96	2.24	2.07	1.53	3.25	20.34	17.00	1.00	63.00
39	4	12	20	2007	-14.46	-11.99	-180.00	180.00	-58.69	-58.23	-90.00	-29.21	54.07	50.23	41.12	80.66	242.31	245.54	216.59	265.12	312.64	329.80	0.33	358.82	1.61	1.70	1.30	1.79	2.24	1.88	1.43	3.56	37.38	28.00	1.00	255.00
39	5	12	20	2007	-17.77	-19.45	-180.00	180.00	-53.61	-52.69	-90.00	-20.79	54.91	51.95	43.23	80.26	239.69	240.40	211.61	263.96	312.50	332.71	0.42	359.54	1.61	1.70	1.31	1.74	1.68	1.34	0.92	3.25	29.68	28.00	1.00	99.00
39	6	12	20	2007	11.35	11.16	-30.39	55.79	-35.97	-35.85	-53.38	-14.13	28.33	29.63	2.06	49.41	211.86	212.36	201.62	213.48	348.36	351.16	333.07	359.18	1.93	1.70	0.43	16.46	1.49	1.62	0.91	2.08	11.36	6.00	1.00	84.00
41	1	2	22	2008	104.23	104.07	55.31	153.50	-27.77	-27.63	-39.78	-12.55	25.40	24.83	12.37	42.74	85.33	6.61	0.00	360.00	87.89	89.64	58.82	109.96	0.39	0.35	0.23	1.48	0.42	0.29	0.23	1.76	6.22	7.00	1.00	12.00
41	2	2	22	2008	152.51	152.49	140.16	165.73	-25.46	-25.41	-37.17	-13.96	29.06	32.15	4.52	42.72	54.65	2.40	0.00	360.00	58.26	58.97	44.31	63.21	0.42	0.33	0.23	1.61	0.24	0.24	0.23	0.25	2.55	3.00	1.00	4.00
41	3	2	22	2008	194.15	194.46	165.27	221.40	-9.95	-9.99	-36.38	16.59	13.64	13.69	2.73	26.62	190.74	179.84	163.97	266.82	220.98	231.72	145.19	246.54	0.95	0.69	0.37	7.97	0.56	0.33	0.24	6.47	6.62	7.00	1.00	11.00
43	1	5	12	2008	144.22	141.39	70.18	222.75	4.63	9.14	-39.97	33.50	21.56	20.11	6.42	42.70	176.82	178.41	106.55	247.25	249.52	248.65	220.94	307.18	0.49	0.41	0.23	2.77	0.42	0.29	0.23	2.48	6.21	7.00	1.00	13.00
43	2	5	12	2008	102.38	103.96	52.77	146.95	-30.60	-30.38	-68.98	8.72	39.58	40.93	8.01	69.74	331.79	334.94	290.92	341.92	182.96	176.93	163.99	247.09	2.30	1.69	1.35	7.24	1.67	1.71	1.26	1.84	32.97	12.00	1.00	175.00
44	1	5	28	2008	159.43	158.28	91.08	227.53	-0.16	2.46	-37.09	26.54	18.92	19.11	8.70	29.01	178.38	179.91	129.33	246.81	248.75	246.61	211.46	289.49	0.50	0.46	0.36	2.11	0.38	0.27	0.23	2.04	5.01	5.00	1.00	10.00
48	1	12	5	2008	116.70	116.91	93.69	141.18	-25.47	-25.43	-34.90	-13.73	20.60	20.89	10.63	30.38	34.41	20.96	0.01	359.99	67.25	70.19	36.34	82.16	0.59	0.52	0.36	1.75	0.65	0.57	0.31	2.01	7.61	8.00	1.00	14.00
48	2	12	5	2008	128.19	128.17	113.12	146.23	-20.98	-20.94	-35.88	-5.85	32.70	30.71	15.18	67.81	34.51	38.01	0.49	54.31	45.30	42.04	25.88	77.87	0.33	0.33	0.19	0.53	0.35	0.34	0.30	0.42	3.99	4.00	1.00	29.00
48	3	12	5	2008	174.01	174.39	112.20	241.45	7.34	5.56	-34.06	55.21	41.95	39.97	30.51	75.85	179.40	293.77	0.01	359.99	56.94	52.85	21.63	125.70	0.26	0.26	0.18	0.31	0.30	0.28	0.24	0.72	2.27	2.00	1.00	19.00
48	4	12	5	2008	147.62	150.20	99.00	197.64	-53.66	-53.04	-78.90	-26.75	48.14	48.45	25.83	67.95	142.44	143.54	128.87	150.60	188.76	188.54	158.38	223.62	1.56	1.63	0.54	2.56	1.61	1.62	1.15	2.39	52.49	53.00	1.00	125.00
48	5	12	5	2008	105.14	105.12	92.58	118.62	-32.66	-32.66	-43.90	-21.06	12.78	12.76	1.56	24.07	45.42	48.55	23.90	49.53	50.81	49.27	47.83	68.65	2.34	0.96	0.55	19.74	1.46	1.44	1.22	2.10	5.51	5.00	1.00	20.00
49	1	12	21	2008	117.59	122.65	-180.00	180.00	-47.31	-45.25	-90.00	-10.57	20.87	19.55	1.72	69.46	150.42	156.56	20.21	180.31	195.47	287.48	0.13	360.00	0.83	0.60	0.18	24.46	0.82	0.62	0.31	23.71	6.02	7.00	1.00	11.00
49	2	12	21	2008	254.34	256.50	203.38	282.78	-21.59	-21.60	-75.00	33.09	22.17	20.93	4.18	39.64	185.28	179.80	170.60	252.90	195.03	198.06	135.71	213.81	0.47	0.38	0.25	2.53	0.41	0.27	0.24	2.87	6.51	7.00	1.00	15.00
49	3	12	21	2008	277.40	277.51	253.60	301.28	4.23	4.03	-15.81	28.34	36.84	37.17	19.46	51.40	64.74	65.98	52.18	73.84	243.52	243.24	233.80	253.64	1.64	1.77	0.61	3.51	1.83	1.83	1.13	2.61	95.78	93.00	1.00	255.00
50	1	2	7	2009	-34.02	-40.44	-67.00	21.04	-25.64	-28.23	-62.39	20.24	42.22	41.18	30.51	60.07	178.00	177.24	118.27	241.15	145.41	150.62	101.04	171.35	0.27	0.27	0.23	0.31	0.31	0.28	0.24	0.52	2.02	2.00	1.00	3.00
50	2	2	7	2009	16.38	23.08	-180.00	180.00	-46.16	-47.49	-90.00	0.61	44.65	46.42	13.61	76.74	118.34	113.90	101.65	245.76	49.23	43.83	1.81	359.49	1.65	1.54	1.30	36.73	3.94	3.04	1.32	53.26	71.46	9.00	1.00	255.00
50	3	2	7	2009	259.86	259.59	230.76	291.41	-1.27	-1.93	-23.83	29.79	53.56	53.75	36.01	64.30	70.61	67.95	45.93	96.65	283.06	284.77	266.11	300.79	1.62	1.59	1.40	2.05	2.03	1.98	0.91	4.00	75.33	65.00	1.00	255.00
50	4	2	7	2009	275.39	277.35	244.00	294.31	43.92	44.20	18.73	69.24	34.60	35.25	3.53	65.16	244.58	257.31	180.23	265.30	92.69	81.23	58.66	161.17	2.16	1.96	1.43	3.10	2.11	2.15	0.87	3.74	2.25	2.00	1.00	10.00
55	1	5	21	2009	176.60	166.90	116.99	297.26	-24.02	-25.67	-78.88	42.01	21.61	20.91	8.63	39.88	176.69	178.32	116.90	241.77	316.11	328.56	0.08	360.00	0.47	0.40	0.25	1.93	0.42	0.30	0.25	1.88	6.42	7.00	1.00	15.00
55	2	5	21	2009	119.20	118.82	81.27	164.80	28.46	26.92	-7.24	69.38	27.48	27.27	2.09	41.08	166.83	61.19	0.02	359.91	284.90	285.81	248.93	320.58	2.89	2.87	0.71	27.66	2.88	2.56	1.20	8.61	74.87	79.00	1.00	200.00
55	3	5	21	2009	-36.24	-67.90	-180.00	180.00	-66.08	-66.61	-90.00	-37.71	32.64	32.33	3.96	59.79	167.13	165.12	161.76	324.68	57.99	40.51	0.49	359.59	1.93	1.71	0.50	61.30	1.59	1.54	1.05	3.25	42.19	4.00	1.00	255.00
55	4	5	21	2009	134.79	134.68	118.45	151.20	33.50	33.31	20.17	47.34	12.20	12.11	1.55	23.06	122.32	121.77	117.40	129.64	356.60	356.73	354.23	356.93	1.86	0.95	0.54	14.09	1.46	1.45	1.25	1.95	4.16	4.00	1.00	12.00
55	5	5	21	2009	262.91	262.81	231.68	298.22	-65.17																											

# Cassini RADAR Users Guide

SWATH	SEGMENT	DATE			WEST LONGITUDE (DEG)				LATITUDE (DEG)				INCIDENCE (DEG)				POLARIZATION (DEG)				AZIMUTH (DEG)				SAR RANGE RESOLUTION (KM)				SAR AZIMUTH RESOLUTION (KM)				NUMBER OF LOOKS				
		T#	M	D	Y	MEAN	MEDIAN	MIN	MAX	MEAN	MEDIAN	MIN	MAX	MEAN	MEDIAN	MIN	MAX	MEAN	MEDIAN	MIN	MAX	MEAN	MEDIAN	MIN	MAX	MEAN	MEDIAN	MIN	MAX	MEAN	MEDIAN	MIN	MAX	MEAN	MEDIAN	MIN	MAX
61	6	8	25	2009	302.83	302.81	293.92	312.37	1.30	1.31	-9.63	12.23	27.66	27.55	22.51	33.13	336.89	336.85	326.52	347.27	90.74	90.83	79.70	101.57	0.38	0.38	0.30	0.47	1.01	1.00	1.00	0.97	1.03	1.77	2.00	1.00	4.00
64	1	12	28	2009	-90.25	-133.35	-180.00	180.00	55.67	59.30	10.66	90.00	27.13	23.86	9.02	55.71	99.27	7.24	0.00	360.00	208.99	187.87	162.57	307.75	0.43	0.36	0.24	1.90	0.40	0.32	0.25	1.66	5.04	5.00	1.00	13.00	
65	1	1	12	2010	-21.18	2.19	-180.00	180.00	-66.68	-68.49	-90.00	-37.85	30.68	31.94	2.10	48.02	181.40	169.52	0.00	359.93	78.77	59.12	0.00	359.95	0.57	0.33	0.26	14.18	0.29	0.27	0.25	1.40	2.85	3.00	1.00	11.00	
65	2	1	12	2010	186.86	187.01	165.19	201.61	-68.37	-68.36	-75.89	-60.96	32.14	32.23	17.44	45.04	41.96	44.48	1.99	74.03	327.89	333.43	0.09	359.83	0.35	0.35	0.26	0.47	0.44	0.43	0.30	0.65	5.96	5.00	1.00	26.00	
65	3	1	12	2010	227.46	227.42	175.26	279.57	-34.97	-34.96	-74.96	-0.75	40.64	39.93	17.27	71.69	139.49	134.61	83.53	202.83	215.30	215.59	124.86	308.87	0.69	0.39	0.18	9.10	1.65	1.06	0.58	17.18	2.19	2.00	1.00	13.00	
69	2	6	5	2010	4.30	0.17	-64.25	105.86	16.47	12.51	-28.82	78.18	37.10	36.17	12.06	69.95	235.99	236.78	0.06	359.98	140.03	133.94	0.05	359.89	2.77	2.43	1.33	34.16	3.26	2.61	0.84	32.31	58.15	43.00	1.00	255.00	
71	1	7	7	2010	-57.46	-45.68	-155.71	24.72	-54.65	-56.54	-76.23	-22.68	42.53	41.30	29.14	63.13	180.08	293.14	0.03	359.97	217.00	222.79	0.08	359.86	0.28	0.28	0.22	0.32	0.33	0.30	0.25	0.61	2.15	2.00	1.00	4.00	
77	1	6	20	2011	64.42	64.42	30.82	97.97	10.27	10.27	-0.93	21.40	22.47	22.85	3.71	32.71	120.03	24.44	0.00	360.00	86.12	92.14	44.05	99.11	0.49	0.43	0.31	1.74	0.46	0.36	0.25	1.46	6.61	7.00	1.00	12.00	
77	2	6	20	2011	131.92	131.92	94.96	169.04	-18.14	-18.14	-48.77	12.40	61.68	60.69	48.95	80.28	56.42	23.05	0.11	359.96	346.97	347.64	332.84	354.44	1.61	1.47	1.33	2.59	4.16	2.94	1.36	14.99	121.87	117.00	1.00	255.00	
77	3	6	20	2011	70.91	70.91	33.49	107.98	11.29	11.29	-28.90	51.40	55.50	55.69	36.84	72.09	295.43	295.06	256.59	313.16	163.30	164.29	146.02	190.81	1.84	1.62	1.36	18.89	4.46	3.67	1.91	55.21	82.18	87.00	1.00	210.00	
83	1	5	22	2012	-43.95	16.03	-180.00	180.00	55.60	57.40	11.76	90.00	27.10	24.12	8.99	60.56	188.46	309.45	0.03	360.00	169.36	153.65	0.00	359.98	0.42	0.32	0.23	3.20	0.39	0.30	0.25	1.99	4.90	4.00	1.00	23.00	
83	2	5	21	2012	57.53	59.51	5.09	105.40	21.95	19.21	-15.94	75.00	43.04	43.39	5.41	61.99	294.45	296.08	269.32	302.37	169.17	169.11	155.46	185.11	2.04	1.89	1.44	16.18	2.09	1.80	1.12	3.74	63.74	63.00	1.00	255.00	
83	3	5	22	2012	176.94	175.83	126.42	228.48	14.63	13.09	-23.95	66.78	40.84	43.01	4.30	60.51	245.23	246.92	227.65	255.50	15.23	13.54	1.06	41.69	2.33	1.87	1.48	32.20	1.46	1.30	0.89	2.99	25.89	25.00	1.00	125.00	
83	4	5	22	2012	201.69	201.68	194.16	208.98	18.51	18.51	12.48	24.43	8.77	8.78	1.57	15.35	315.55	315.68	314.14	316.39	204.95	204.85	204.46	206.52	3.35	2.01	0.86	13.75	1.39	1.41	1.29	1.53	2.76	3.00	1.00	9.00	
84	1	6	6	2012	-71.62	-77.62	-156.28	24.40	37.07	39.67	1.84	58.14	21.72	20.98	8.93	39.88	177.56	180.03	114.11	243.86	84.19	74.20	0.08	359.92	0.47	0.40	0.24	2.13	0.42	0.31	0.25	2.08	6.10	6.00	1.00	20.00	
84	2	6	6	2012	-20.56	-13.92	-180.00	180.00	46.53	46.16	-5.20	89.99	61.77	62.89	16.68	84.19	295.88	296.01	277.13	312.22	70.22	44.75	0.03	359.99	1.79	1.63	1.31	20.55	5.11	4.86	1.76	10.79	54.07	57.00	1.00	184.00	
84	3	6	7	2012	237.03	238.57	181.18	283.93	-10.49	-11.63	-54.39	44.21	36.76	38.30	3.87	56.44	154.02	155.55	140.93	164.57	200.70	199.55	188.96	215.43	2.50	2.09	1.52	33.23	1.13	1.12	0.82	1.61	20.54	18.00	1.00	102.00	
84	4	6	6	2012	6.80	6.79	-3.22	17.12	28.88	28.87	19.76	38.08	11.41	11.40	1.61	20.90	134.32	133.08	130.37	144.48	167.59	168.82	158.07	171.00	2.19	1.25	0.65	9.53	1.48	1.47	1.44	1.51	2.42	2.00	1.00	6.00	
84	5	6	7	2012	215.89	215.89	207.12	224.69	6.94	6.95	-1.93	15.79	10.59	10.60	1.58	19.09	227.91	227.66	227.51	229.59	9.28	9.34	8.33	9.73	2.16	1.32	0.68	8.34	1.34	1.34	1.30	1.37	2.23	2.00	1.00	6.00	
86	1	9	26	2012	-111.01	-133.80	-151.26	1.77	56.01	60.80	16.99	83.48	40.76	40.16	30.68	54.52	177.91	54.93	0.02	359.98	214.91	210.17	189.92	269.12	0.27	0.27	0.24	0.31	0.31	0.29	0.25	0.48	1.98	2.00	1.00	3.00	
86	2	9	26	2012	-58.17	-83.11	-180.00	180.00	68.78	68.71	44.77	90.00	60.23	60.12	54.86	64.21	310.54	311.41	301.33	319.71	308.85	311.14	296.02	321.50	0.21	0.21	0.20	0.21	2.29	2.48	1.13	3.29	8.89	6.00	1.00	56.00	
86	3	9	26	2012	-31.61	-20.31	-180.00	180.00	58.46	59.25	24.13	90.00	47.81	49.88	29.31	70.03	108.08	60.64	0.85	359.84	296.30	285.60	270.01	341.85	0.27	0.26	0.20	0.32	0.52	0.49	0.33	1.14	2.03	2.00	1.00	16.00	
86	4	9	26	2012	216.53	216.60	189.36	246.12	2.12	2.12	-36.37	40.63	65.15	64.11	50.68	79.70	298.26	298.90	283.58	305.09	241.76	241.33	236.60	253.97	0.24	0.24	0.19	0.26	0.58	0.52	0.43	1.43	1.53	1.00	1.00	3.00	
91	1	5	23	2013	247.80	247.69	239.53	260.70	26.27	26.29	3.92	49.12	26.79	27.42	2.85	39.09	180.83	13.05	0.00	360.00	177.40	177.08	153.72	187.77	0.36	0.33	0.26	1.96	0.28	0.27	0.25	0.36	3.69	4.00	1.00	6.00	
91	2	5	23	2013	107.76	100.35	68.09	189.14	69.36	70.14	52.10	85.34	22.06	22.42	12.76	31.90	159.28	160.90	126.06	180.41	236.53	233.82	220.37	268.16	0.54	0.47	0.34	1.34	0.63	0.57	0.34	1.48	7.66	8.00	1.00	12.00	
91	3	5	23	2013	34.27	144.38	-180.00	180.00	83.44	83.86	76.07	90.00	13.49	13.95	2.21	22.42	179.48	179.92	176.28	180.30	295.65	286.23	268.73	348.14	1.17	0.65	0.41	5.10	0.34	0.34	0.32	0.37	1.94	2.00	1.00	6.00	
91	4	5	23	2013	-22.78	-23.52	-180.00	180.00	55.18	53.78	23.47	89.99	53.71	54.74	5.01	75.78	295.22	295.38	279.67	316.08	310.49	310.77	0.09	359.31	1.68	1.48	1.30	24.29	3.71	2.82	1.12	11.83	87.93	87.00	1.00	255.00	
91	5	5	23	2013	221.67	221.28	175.42	268.98	-16.55	-16.27	-47.87	10.12	31.60	30.87	6.72	47.10	310.38	298.65	291.93	347.96	58.26	66.66	32.70	72.92	4.20	5.12	1.75	21.42	3.07	2.76	0.95	7.29	46.58	32.00	1.00	255.00	
91	6	5	23	2013	73.73	74.12	49.46	100.12	64.14	64.07	56.42	70.87	13.82	13.86	1.89	25.55	141.52	139.80	137.50	154.81	226.60	229.48	205.04	235.84	1.82	0.79	0.47	12.07	1.28	1.30	1.18	1.36	2.75	2.00	1.00	11.00	
91	7	5	23	2013	243.72	243.71	236.57	251.78	48.97	48.97	43.66	54.12	10.07	9.99	2.17	18.28	351.20	358.10	0.10	359.94	181.11	181.31	176.79	183.94	1.56	1.06	0.50	5.44	0.26	0.26	0.25	0.26	2.13	2.00	1.00	4.00	
91	8	5	23	2013	241.54	241.54	237.51	245.60	5.10	5.10	2.08	8.13	4.64	4.53	1.95	7.83	1.92	1.67	0.76	4.41	168.95	169.18	166.25	170.42	3.12	2.61	1.22	6.99	0.33	0.33	0.32	0.35	1.77	2.00	1.00	4.00	
91	9	5	23	2013	241.27	241.13	156.98	322.70	77.24	77.44	66.03	89.12	4.32	4.16	3.04	5.88	89.91	87.79	0.57	179.46	154.15	119.45	41.80	347.72	0.00	0.00	0.00	0.00	0.00	0.00	0.00	0.00	1.20	1.00	1.00	2.00	
92	1	7	10	2013	-85.45	-118.66	-180.00	180.00	33.91	38.79	-36.03	90.00	19.89	19.08	1.66	39.79	189.46	164.54	0.00	360.00	194.21	185.88	3.02	357.76	0.58	0.46	0.25	13.79	0.42	0.30	0.25	2.17	6.14	6.00	1.00	23.00	
92	2	7	10	2013	224.79	223.35	147.43	313.34	-19.36	-16.71																											

# Cassini RADAR Users Guide

SWATH	SEGMENT	DATE			WEST LONGITUDE (DEG)				LATITUDE (DEG)				INCIDENCE (DEG)				POLARIZATION (DEG)				AZIMUTH (DEG)				SAR RANGE RESOLUTION (KM)				SAR AZIMUTH RESOLUTION (KM)				NUMBER OF LOOKS							
		T#	M	D	Y	MEAN	MEDIAN	MIN	MAX	MEAN	MEDIAN	MIN	MAX	MEAN	MEDIAN	MIN	MAX	MEAN	MEDIAN	MIN	MAX	MEAN	MEDIAN	MIN	MAX	MEAN	MEDIAN	MIN	MAX	MEAN	MEDIAN	MIN	MAX	MEAN	MEDIAN	MIN	MAX			
108	2	1	11	2015	223.53	216.72	195.99	287.79	69.35	69.86	50.84	88.78	7.76	7.64	1.72	13.73	192.94	242.71	0.00	360.00	192.37	199.89	0.47	359.43	2.15	1.35	0.54	16.84	0.41	0.32	0.27	3.74	4.49	4.00	1.00	13.00				
108	3	1	11	2015	-9.88	-10.92	-60.31	47.88	0.36	-0.06	-47.26	53.13	42.07	42.67	4.58	61.63	228.48	229.77	207.72	285.54	41.81	39.80	1.23	61.04	2.14	1.89	1.43	24.75	2.41	2.45	1.00	4.12	51.93	37.00	1.00	255.00				
108	4	1	11	2015	17.15	17.15	12.06	22.24	0.59	0.59	-6.28	7.43	11.09	11.13	2.37	17.56	108.85	108.05	107.74	113.02	244.47	244.75	241.45	245.31	3.85	2.58	1.69	12.90	3.13	3.19	2.86	3.62	3.76	3.00	1.00	13.00				
108	5	1	11	2015	52.14	105.79	-180.00	180.00	55.63	54.34	22.34	89.99	65.77	65.56	56.19	77.43	11.88	11.93	9.75	16.35	46.30	39.84	0.55	359.84	1.70	1.79	1.36	1.82	6.21	6.17	5.31	6.95	48.66	34.00	1.00	218.00				
113	1	9	28	2015	65.89	65.90	-6.87	138.65	-10.09	-10.09	-19.79	-0.15	27.61	23.33	3.79	66.82	205.42	306.63	0.01	360.00	273.01	273.39	190.73	352.90	0.60	0.33	0.22	5.92	0.48	0.31	0.25	5.42	4.52	4.00	1.00	14.00				
113	2	9	28	2015	129.93	129.93	105.18	154.78	-3.75	-3.75	-27.54	20.07	10.56	10.54	1.78	18.68	62.00	63.22	55.15	63.56	211.52	210.35	210.00	218.17	3.27	1.82	1.08	15.78	2.05	2.04	1.97	2.65	2.70	2.00	1.00	8.00				
113	3	9	28	2015	322.77	322.74	294.11	351.27	-35.42	-35.42	-63.29	-7.56	62.85	62.61	52.82	75.03	249.40	249.47	246.03	252.51	318.91	318.27	317.25	322.86	0.21	0.21	0.17	0.25	1.82	1.80	1.76	2.05	1.21	1.00	1.00	2.00				
113	4	9	28	2015	-17.78	-17.78	-39.11	3.49	-11.18	-11.18	-32.44	10.10	24.25	24.27	21.90	26.56	230.59	230.57	230.37	230.83	319.49	319.46	319.06	319.99	0.63	0.63	0.59	0.66	2.15	2.15	2.13	2.17	1.29	1.00	1.00	2.00				
113	5	9	28	2015	9.90	9.90	-29.92	49.44	2.02	2.02	-21.78	25.98	40.90	41.56	16.21	51.65	284.92	284.86	282.87	287.06	175.56	175.46	174.10	177.57	1.87	1.42	0.42	5.28	23.14	22.71	18.52	28.61	1.09	1.00	1.00	3.00				
113	6	9	28	2015	31.04	31.05	-12.75	74.41	21.87	21.87	-10.78	54.74	54.40	53.98	37.54	86.15	297.96	294.25	286.41	314.99	160.44	163.11	143.91	174.39	1.64	1.55	1.26	2.49	4.60	4.13	2.22	10.25	67.52	50.00	1.00	255.00				
120	1	6	7	2016	140.62	161.24	4.36	213.04	-37.06	-43.71	-81.20	25.32	27.51	24.70	9.05	75.48	185.76	179.87	116.20	249.76	227.73	219.45	0.01	359.94	0.43	0.38	0.17	1.90	0.42	0.32	0.25	1.83	4.94	4.00	1.00	14.00				
120	3	6	7	2016	200.30	199.69	183.30	219.83	28.50	28.71	11.21	45.61	35.60	36.20	9.77	52.49	260.37	260.44	259.93	260.70	139.91	139.13	134.46	148.09	2.55	2.22	1.05	5.83	6.61	6.50	6.25	7.57	1.54	2.00	1.00	3.00				
120	5	6	7	2016	151.13	147.07	84.52	264.38	33.74	35.77	-34.99	89.91	37.23	36.87	10.52	64.84	257.71	260.03	157.10	301.28	249.47	330.60	0.01	359.99	2.90	2.86	1.36	14.23	3.02	2.57	1.52	10.14	45.42	36.00	1.00	255.00				
121	1	7	25	2016	126.00	128.08	49.97	200.09	-5.88	-7.13	-58.88	52.61	21.33	20.62	2.08	39.59	160.85	179.84	0.00	360.00	180.60	226.17	27.81	252.10	0.53	0.43	0.25	13.24	0.42	0.31	0.25	1.83	6.22	6.00	1.00	14.00				
121	2	7	25	2016	60.40	60.37	52.39	69.94	-35.49	-35.49	-43.77	-27.08	12.12	12.11	1.61	22.42	45.60	47.23	33.74	49.18	39.11	39.02	36.30	42.89	2.36	1.08	0.61	14.49	1.43	1.44	1.36	1.62	2.75	2.00	1.00	9.00				
121	3	7	25	2016	188.90	188.95	179.20	197.70	29.49	29.49	20.47	38.61	12.13	12.13	1.60	21.81	225.43	225.78	222.66	227.26	206.40	207.43	200.44	210.21	1.72	0.83	0.59	9.56	1.31	1.29	1.25	1.43	3.17	3.00	1.00	17.00				
121	5	7	25	2016	211.59	210.70	120.93	302.23	0.03	-1.42	-48.39	50.00	52.34	52.03	25.70	83.81	65.29	57.53	24.15	149.33	285.96	292.63	228.78	311.87	1.63	1.54	1.28	2.74	4.01	3.93	1.66	9.28	60.27	44.00	1.00	255.00				
121	6	7	25	2016	72.05	72.65	7.76	137.45	-18.56	-17.92	-61.00	26.50	40.61	39.25	4.44	64.43	218.34	217.04	189.59	260.04	123.24	125.03	96.58	139.60	2.23	2.05	1.63	24.19	2.06	1.69	0.94	4.87	42.03	46.00	1.00	130.00				
126	1	4	22	2017	-105.25	-114.80	-180.00	180.00	63.17	63.68	36.56	90.00	16.50	16.48	1.96	27.27	161.01	27.44	0.00	360.00	166.82	161.50	1.94	358.30	0.00	0.00	0.00	0.00	0.00	0.00	0.00	0.00	0.00	0.00	0.00	0.00	7.03	7.00	1.00	23.00
126	2	4	22	2017	81.26	78.47	46.07	138.81	52.35	52.57	21.17	83.49	35.20	35.74	2.14	51.94	91.89	34.07	0.00	360.00	201.09	316.44	0.01	359.99	0.00	0.00	0.00	0.00	0.00	0.00	0.00	0.00	0.00	0.00	0.00	0.00	2.35	2.00	1.00	4.00
126	3	4	22	2017	75.92	76.14	3.11	146.62	-0.55	-0.79	-52.59	52.30	32.10	32.50	3.81	55.98	147.23	141.11	67.33	265.22	122.03	130.45	14.91	187.25	0.00	0.00	0.00	0.00	0.00	0.00	0.00	0.00	0.00	0.00	0.00	0.00	32.86	19.00	1.00	255.00
126	4	4	22	2017	62.66	62.60	56.16	69.38	14.48	14.47	-0.73	29.32	60.10	60.37	48.02	71.08	63.97	64.04	58.09	69.48	306.30	306.18	301.54	311.68	0.00	0.00	0.00	0.00	0.00	0.00	0.00	0.00	0.00	0.00	0.00	0.00	1.91	2.00	1.00	3.00
126	5	4	22	2017	-43.95	-47.32	-180.00	180.00	35.39	33.77	-21.15	90.00	43.10	45.63	3.91	80.15	274.45	330.64	0.07	359.97	139.93	144.16	0.38	359.97	0.00	0.00	0.00	0.00	0.00	0.00	0.00	0.00	0.00	0.00	0.00	0.00	31.57	23.00	1.00	255.00

## 14 Appendix 5: Cassini RADAR Uplink/Downlink Spreadsheet through T77

Notes at the end of the spreadsheet describe column headings and define acronyms used.

**COLOR KEY:**

	Event occurred
	Event IEB delivery was skipped
	Typically minor issues
	Event ERROR

IEB	DTN	Seq #	BG vs SSR	IDAP	PSIV2 Delivery (Subseq)	EXECUTION			Duration Total (s)	~End of Downlink (PST/PDT)	Actual DV (kbit)	NOTES
						Date (UTC)	Julian Day	TIME (UTC)				
ph_000_1	31	S01	BG	no	04/20/2004	06/11/2004	163	11:08:36	10320	06/12/2004 by 4:46 pm	2705.6	WTK (4.0) files did not include all expected telemetry gaps. Total (ph1 & ph2)
ph_000_2	32	S01	SSR	YES Live IVP	04/20/2004	06/11/2004	163	14:08:52	41684	06/12/2004 by 4:46 pm	285030.4	287736
s04_engtest	33	S04	BG	no	08/17/2004	10/13/2004	287	22:50:00	3000	10/15/2004 by 3:58 am	289180	
ti_00a_1	34	S05	BG	YES	09/20/2004?	10/25/2004	299	0:01:00	21600	10/25/2004 at 10:45 am	476216	Missing 266 packets (15 gaps)
ta	35	S05	BG	YES	09/20/2004?	10/26/2004	300	10:20:39	36561	10/27/2004 at 3:30 am	562810	All packets recovered! All data are present!
ti_00a_2	36	S05	SSR	no	09/20/2004?	11/06/2004	311	16:53:00	19461	11/07/2004 at 9:02 am	99606	Missing 150 packets (4 gaps)
src_00b_1	37	S06	BG	no	10/19/2004	11/30/2004	335	16:25:00	35400	12/01/2004 at 9:04 am (or CO*)	35500	Handedit (shorttime by 1 minute) to meet DV
di_00b_1	38	S06	BG	YES Live IVP	10/19/2004	12/14/2004	349	21:57:30	18610	12/15/2004 at 8:36 am (or CO*)	0	S/C commanding error. THIS ACTIVITY DID NOT GET DOWNLINKED!
mi_00b_1	39	S06	BG	YES Live IVP	10/19/2004	12/15/2004	350	3:09:57	4023	12/15/2004 at 8:36 a+R33m (or CO*)	0	S/C commanding error. THIS ACTIVITY DID NOT GET DOWNLINKED!
ia_00b_1	40	S07 MIA	MIA-Mini	no	11/16/2004	12/31/2004	366	1:50:00	21900	12/31/2005 at 6:44 am (or CO)	318295.6	3 gaps: Total loss = 228 SABs
ia_00c_1	41	S07 MIA	MIA-Mini	no	11/16/2004	01/01/2005	001	13:05:00	38362	01/06/2005 at 5:07 am (last CO)	1259214	1 gap missing 2 SABs

# Cassini RADAR Users Guide

IEB	DTN	Seq #	BG vs SSR	IDAP	PSIV2 Delivery (Subseq)	EXECUTION			Duration Total (s)	~End of Downlink (PST/PDT)	Actual DV (kbit)	NOTES
						Date (UTC)	Julian Day	TIME (UTC)				
ti_00c_1	42	S08	BG	no	12/09/2004	01/26/2005	026	13:05:00	17400	01/27/2005 at 2:37 am	14280.4	Missing 46 (FIN5) during warm-up
ti_00c_2	43	S08	BG	no	12/09/2004	01/28/2005	028	13:05:00	13800	1/29/2005 at 2:22 am (or CO)	9887.6	No gaps
engtest	44	S08	BG	no	12/09/2004	01/29/2005	029	14:05:00	6600	1/30/2005 19:52 (or CO)	282902.4	Power State Error due to IEB duration longer than it should be . . . OK
t3	45	S08	BG	YES	12/09/2004	02/15/2005	046	2:17:53	20819	02/15/2005* at 8:18 pm	639844	Two gaps: First missed 3496 SABs (FIN8). This was expected due to S&ER3. A second critical gap of 171 SABs (FIN243-249) at +11 CPA (46 seconds for SAR). Incorrect ND setting
en_003_1	46	S08	Mini-Seq	no	12/09/2004	02/17/2005	048	8:21:30	11190	02/18/2005 at 1:57 am	495953.2	No gaps!
en_004_1	47	S09	BG	YES	02/01/2005	03/09/2005	068	12:06:41	13200	03/09/2005 at 20:00* (CO)	397586.4	Telem gap at FIN5 for telemetry mode (missed 1423 SABs), plus Fin 58 drop 3 SABs, plus FIN134 dropped 99 SABs
t4	48	S09	BG	YES	02/01/2005	03/31/2005	090	14:38:06	29100	04/01/2005 at 15:36	157092	T4—rad and scat only (plus attn test) (missed 2701 SABs due to telem). WTK2seqsasf DV calculation incorrect for scat_compress
engtest	49	S09	BG	no	02/01/2005	04/08/2005	098	8:30:35	17580	04/08/2005 at 22:29	154333.2	
rings_006_1	50	S10	BG	no	03/16/2005	04/12/2005	102	9:35:00	31799	04/12/2005 at xx:xx	31942.8	1 gap missing 9 SABs at FIN 18
ti_006_1	51	S10	BG	YES, -9 s	03/16/2005	04/17/2005	107	22:30:00	17729	04/18/2005 at 15:14 (or CO*2)	262899	Missing 9 SABs
src_006_1	52	S10	BG	no	03/16/2005	04/18/2005	108	3:28:45	24675	04/18/2005 at 15:14 (or CO*2)	70307.6	Missing 205 SABs

# Cassini RADAR Users Guide

IEB	DTN	Seq #	BG vs SSR	IDAP	PSIV2 Delivery (Subseq)	EXECUTION			Duration Total (s)	~End of Downlink (PST/PDT)	Actual DV (kbit)	NOTES
						Date (UTC)	Julian Day	TIME (UTC)				
ti_010_1	53	S12	BG	no	05/23/2005	06/19/2005	170	0:45:00	13800	06/19/2005 at 16:04	6148.4	38 missing SABs (DSN gap)
ti_011_1	54	S12	BG	no	05/23/2005	07/11/2005	192	23:35:00	14700	07/12/2005 at 16:44	3655.6	S&ER3: Expect to drop 2520 SABs
rh_011_1	55	S12	BG	YES	05/23/2005	07/14/2005	195	4:15:00	20401	07/15/2005 at 2:54	212123.6	S&ER3: Expect to drop ~3200 SABs
engtest	56	S13	Mini-Seq	no	06/29/2005	08/23/2005	235	19:40:00	10195	8/24/2005 at 15:36	250625.2	DSN drop of 30 seconds (70 SABs)
src_013_1	57	S13	Mini-Seq	no	06/29/2005	08/23/2005	235	23:40:00	35803	8/24/2005 at 15:36	31730	Minus S&ER3 gap
rings_014_1	58	S14	BG	no	08/04/2005	09/03/2005	246	5:00:00	33601	09/03/2005 at 19:44 (w CO?)	21987	Expect to drop ~11690 SABs due to S&ER3
t <sub>z</sub>	59	S14	BG	as expected 7:25:07	08/04/2005	09/07/2005	250	7:27:07	21720	09/09/2005 at ~11:00 (for RADAR)	179154.8	SSR problem lost data from -2 CPA until end. DSN problem lost data from start to -14:45. Plus multiple small gaps during downlink (one medium-size gap (~42 SABs) causes a gap in image. Incorrect ND & RL setting)
sa_015_1	60	S14	BG	no	08/04/2005	09/23/2005	266	11:30:00	47130	09/24/2005 at 18:34 (w CO?)	34291.2	Dropped 12036 SABs due to S&ER3. Second small gap of 122 SABs (OBS: Sat1&2)
te_015_1	61	S14	Mini-Seq	23:59:25	08/04/2005	09/23/2005	266	23:59:25	26895	same as above	248960.8	Planned/expected dropped 5364 SABs due to S&ER3
sa_015_2	62	S14	BG	no	08/04/2005	09/24/2005	267	5:04:00	9155	same as above	7942	OBS: Sat3. No dropped packets
hy_015_1	63	S14	BG	as expected 06:00:16	08/04/2005	09/26/2005	269	6:00:16	10306	09/26/2005 at 18:57 (w CO?)	392669.2	No gaps due to second downlink recovery!

# Cassini RADAR Users Guide

IEB	DTN	Seq #	BG vs SSR	IDAP	PSIV2 Delivery (Subseq)	EXECUTION			Duration Total (s)	~End of Downlink (PST/PDT)	Actual DV (kbit)	NOTES
						Date (UTC)	Julian Day	TIME (UTC)				
di_016_1	64	S15	BG	shift by -2 s to 19:12:00	09/07/2005	10/11/2005	284	19:12:02	15771	10/12/2005 at 12:59	314343.6	Dropped only the expected 90 minutes of data due to S&ER3
ti_016_1	65	S15	BG	Live Update 18:37:20	09/07/2005	10/27/2005	300	18:37:20	53085	10/28/2005 at 23:30 (for RADAR)	791304.4	Dropped 4290 SABs due to S&ER3, 1 at FIN 33 (inbound scat), 2 at FIN 249 (SAR+4.5)
ti_017_1	66	S15	BG	no	09/07/2005	11/01/2005	305	3:55:00	14661	11/02/2005 at 10:43	4187.6	Dropped only the 10493 SABs due to S&ER3
ti_017_2	67	S15	BG	no	09/07/2005	11/11/2005	315	20:58:00	13801	11/12/2005 at 10:15	6178.8	One CCSDS packet drop (equal 8 SABs drop. At 4 s BPD)
ti_017_3 / ia_017_1	68	S16	BG	as expected 17:50:25	10/18/2005	11/12/2005	316	17:50:25	24120	11/13/2005 at 11:16	321898	RMSS will create one IEB (ia_017_1). On downlink we will cut into two data files for the two targets and call the first one ti_017_3 FSIV: VIMS IEB load conflicts with our FSW load, shift our turn-on sequence by ~20 minutes. New IEB duration, therefore new IEB-required gap of 152 SABs observed
rh_018_1	69	S16	BG	as expected 00:39:09	10/18/2005	11/27/2005	331	0:39:09	17605	11/27/2005 at 1:49	698675.6	There is a 2:40:00 gap expected due to S&ER3 (~5980 SABs)
ti_019_1	70	S16	BG	no	10/18/2005	12/13/2005	347	17:05:00	13800	12/14/2005 at 8:04	6186.4	No gaps expected
ti_019_2	71	S16	BG	no	10/18/2005	12/15/2005	349	0:45:00	15960	12/15/2005 at 8:05	8192.8	1 gap of 161 s (160 SABs)
eng_019_1	72	S17	BG	no	11/15/2005	12/23/2005	357	15:42:10	10601	12/24/2005 at ~7:00	301773.2	Testbed had disk crash, so not tested on BB Two gaps, 65 s (144 SABs) & 7 s (14 SABs)
ti_021_1	73	S18	BG	no	12/15/2005	02/15/2006	046	10:42:00	13800	02/15/2006 at 21:00	6186.4	No gaps
ti_021_2	74	S18	BG	no	12/15/2005	02/16/2006	047	3:42:00	13800	02/17/2006 at 4:21	6186.4	No gaps
te_021_1	75	S18	BG	as expected 16:05:00	12/15/2005	02/25/2006	056	16:05:00	14670	02/26/2006 at 2:20	290570.8	Expected data drop of 9926 SABs during VIMS collection
src_021_1	76	S18	BG	no	12/15/2005	02/28/2006	059	13:26:00	35400	03/01/2006 at 2:03	27291.6	Two small gaps of 9 seconds and 138 seconds

# Cassini RADAR Users Guide

IEB	DTN	Seq #	BG vs SSR	IDAP	PSIV2 Delivery (Subseq)	EXECUTION			Duration Total (s)	~End of Downlink (PST/PDT)	Actual DV (kbit)	NOTES
						Date (UTC)	Julian Day	TIME (UTC)				
ti_022_1	77	S19	BG	no	02/09/2006	03/14/2006	073	8:11:11	18829	03/16/2006 at ~2:00 w/ CO	10160.2	No gaps
<u>T12</u>	78	S19	BG	NO IVP update. As expected 22:55:57	02/09/2006	03/18/2006	077	22:56:26	23670	03/19/2006 at 18:20	240334.8	High-res scat attempt. One expected gap due to telemetry
rh_022_1	79	S19	Mini-Seq	YES, live. with mini-seq	02/09/2006	03/21/2006	080	6:25:29	36571	03/22/2006 at ~2:00	738347.6	Stare, 5-point scat, raster
ti_023_1	80	S20	BG	no	03/29/2006	04/26/2006	116	17:29:00	17401	04/26/2006 at 22:15	9355.6	Rad (plus eng test)
ti_023_2	81	S20	BG	YES—OD-58 4/25/2006	03/29/2006	04/29/2006	119	17:14:00	17370	04/29/2006 at 22:00	159166.8	Scat (plus eng tests). 10 small gaps. Missing 129 SABs
<u>T13</u>	82	S20	BG	YES—OD-58 4/25/2006	03/29/2006	04/30/2006	120	20:23:15	33870	05/01/2006 at 14:30	610561.2	Full SAR pass, plus outbound Possibly an ITL test, so delivery required for SSG 1 gap: missing 1748 SABs
engtest	83	S20	BG	no	03/29/2006	05/12/2006	132	14:00:00	10200	05/12/2006 at 21:15	387554.4	Attn test. 6 small gaps
ti_024_1	84	S20	BG	no	03/29/2006	05/16/2006	136	9:30:00	15600	05/16/2006 at 22:00	9682.4	Rad (plus eng test). 1 gap of 69 SABs
ti_025_1	85	S21	BG	no	05/09/2006	07/01/2006	182	2:06:00	7200	07/01/2006 at 18:00	13452	Rad
T15	86	S21	BG	YES as expected 01:25:47	05/09/2006	07/02/2006	183	4:20:00	14400	07/03/2006 at 10:30:00	145144.8	Rad and scat

# Cassini RADAR Users Guide

IEB	DTN	Seq #	BG vs SSR	IDAP	PSIV2 Delivery (Subseq)	EXECUTION			Duration Total (s)	~End of Downlink (PST/PDT)	Actual DV (kbit)	NOTES
						Date (UTC)	Julian Day	TIME (UTC)				
T16	87	S22	BG	as expected 16:30:26	06/14/2006	07/21/2006	202	16:30:55	30269	07/22/06 Saturday 203 14:36P	779813.2	Inbound alt & full SAR. 4 unknown gaps
ti_026_1	88	S22	BG	no	06/14/2006	08/03/2006	215	0:09:59	19200	215 23:05U	13186.6	Gap of 9 s. Missing 8 SABs
ti_027_1	89	S22	BG	no	06/14/2006	08/13/2006	225	8:09:59	16320	225 22:12U	13915.6	No gaps
di_027_1	90	S22	mini	mini 228T08:10:00	08/04/2006	08/16/2006	228	8:10:29	15571	229 22:21U	147956.8	1 early gap of 40 seconds
rh_027_1	91	S22	mini	mini 229T03:30:00	08/04/2006	08/17/2006	229	3:30:29	11670	229 22:21U	157783.6	No gaps
ti_027_2	92	S23	BG	no	07/25/2006	08/22/2006	234	15:11:00	51600	235 21:51U	58611	Include source scan and eng test (on & off target)
T17 (rider)	93	S23	BG	YES (I=-20 s) 250T18:58:03	07/25/2006	09/07/2006	250	18:58:23	4910	09/08/06 Friday 251 13:06	62373.2	~4-5 minutes of SAR
en_028_1 (rings_028_1)*	94 95	S23	BG	IVP -3 252T21:06:07	07/25/2006	09/09/2006	252	21:06:40	31730	253 21:00U	152038	Includes rings_028_1 observation and eng test
rings_028_2	96	S23	BG	no	07/25/2006	09/11/2006	254	5:05:00	22800	254 21:00U	18065.2	Includes eng test
ti_029_1	97	S24	BG	no	08/22/2006	09/21/2006	264	4:50:00	17400	264T20:22U or 265T18:52U	111568	
T18 (rider)	98	S24	BG	IDAP 266T17:03:49	08/22/2006	09/23/2006	266	17:04:19	7980	267T20:00U	120885.6	~10 minutes of SAR
ti_030_1	99	S24	BG	no	08/22/2006	10/07/2006	280	5:05:00	16500	280T19:24U	87080.8	
T19	100	S24	BG	OD ~10/4 YES 282T09:15:07	08/22/2006	10/09/2006	282	9:15:37	48601	2006- 283T19:00U 10/10/2006 3:00-12:00	889686.4	X-only rolling (INMS ride-along)

# Cassini RADAR Users Guide

IEB	DTN	Seq #	BG vs SSR	IDAP	PSIV2 Delivery (Subseq)	EXECUTION			Duration Total (s)	~End of Downlink (PST/PDT)	Actual DV (kbit)	NOTES
						Date (UTC)	Julian Day	TIME (UTC)				
<u>T20</u>	101	S25	BG	OTM 78-OTM79-Sun22 YES	09/27/2006	10/25/2006	298	7:33:04	25800	299T11:15P	250169.2	High scat-SAR
ti_032_1/eng	102	S25	BG	no	09/27/2006	11/04/2006	308	18:17:00	15600	309T17:30	307466	
ti_032_2	103	S25	BG	no	09/27/2006	11/06/2006	310	17:35:00	15600	311T17:28	7532	
en_032_1	104	S25	mini	Mini	09/27/2006	11/08/2006	312	22:45:00	15000	UTC:313T17:28	144567.2	
ti_032_3	105	S25	BG	no	09/27/2006	11/13/2006	317	18:19:00	13800	UTC:318T16:59	3245	
di_033_1	106	S25	BG	OTM 80 YES, Mini	09/27/2006	11/20/2006	324	22:05:00	21000	UTC:326T09:15	163826	
ti_033_1	107	S26	BG	no	10/24/2006	11/25/2006	329	2:05:00	17400	UTC:329T16:30	6992	
<u>T21</u>	108	S26	BG	YES	10/24/2006	12/12/2006	346	9:02:01	23640	12/13/2006 at 5:30	541701	Double-bit errors (DBEs) on the SSR are corrupting the data, All data are present, but ~4 minutes of data have not gone into the preprocessor (scatmode) due to the DBEs (FYI: 2 ITL runs)
src_035_1/eng	109	S26	BG	no	10/24/2006	12/19/2006	353	15:23:00	35400	UTC:354T14:48	57243.2	
ti_037_1	110	S27	BG	YES +24seconds	11/30/2006	01/11/2007	011	23:09:02	17338	UTC:012T13:34	250465.6	Rad/eng or scat or HiSAR. Dropped 2 SABs
<u>T23</u>	111	S27	BG	YES	11/30/2006	01/13/2007	013	0:43:31	46140	UTC:014T13:34	804429.6	Full pass (0.5, 0.5, 2.0 pointing). Dropped 711 SABs; however, some expected ~561. Missing ~150
ti_037_2	112	S27	BG	YES	11/30/2006	01/14/2007	014	13:40:10	12770	UTC:015T05:36	133950	Rad/eng or scat or high SAR
ti_037_3	113	S27	BG	no	11/30/2006	01/15/2007	015	13:35:00	15600	UTC:016T05:36	3947.6	Rad
ti_037_4	114	S27	BG	no	11/30/2006	01/18/2007	018	17:25:00	15600	UTC:019T12:51	7448	Rad
ti_037_5	115	S27	BG	no	11/30/2006	01/20/2007	020	22:50:00	15600	UTC:021T12:36	6095.2	Rad
rings_038_1	116	S27	BG	no	11/30/2006	01/27/2007	027	13:41:02	46199	UTC:028T12:12	35910	Rings rad/eng, lot of little gaps, we did get hit by DBE
ti_038_1	117	S27	BG	no	11/30/2006	02/03/2007	034	6:15:00	13800	UTC:035T11:37	4658.8	Rad
rings_038_2	118	S27	BG	no	11/30/2006	02/04/2007	035	17:57:00	40800	UTC:036T12:37	32991.6	Rings rad/eng
hy_039_1	119	S27	BG	NO, just let BG trig go (+30) 2/7 OTM 93	11/30/2006	02/15/2007	046	20:00:00	19440	UTC:047T10:52	246278	Scat/eng

# Cassini RADAR Users Guide

IEB	DTN	Seq #	BG vs SSR	IDAP	PSIV2 Delivery (Subseq)	EXECUTION			Duration Total (s)	~End of Downlink (PST/PDT)	Actual DV (kbit)	NOTES
						Date (UTC)	Julian Day	TIME (UTC)				
<u>T25</u>	120	S28	BG	YES	01/24/2007	02/21/2007	052	19:17:24	45660	UTC:054T11:26:00 2/23-FRI@3:26 PST	555940	Some double-bit hits on SSR
rings_039_1	121	S28	BG	no	01/24/2007	02/23/2007	054	10:17:10	32390	UTC:055 10:22	28302.4	
ti_039_1	122	S28	BG	no	01/24/2007	02/26/2007	057	11:41:00	17400	UTC:058 02:36	9750.8	
ti_040_1	123	S28	BG	no	01/24/2007	03/05/2007	064	10:41:00	13801	UTC:065 02:21	6178.8	
ti_040_2	124	S28	BG	YES	01/24/2007	03/08/2007	067	15:26:00	15540	UTC:068 09:21	395298.8	Distant scat, with eng
ti_040_3	125	S28	BG	no	01/24/2007	03/13/2007	072	19:35:00	13800	UTC:073 09:06	3252.8	
<u>T28</u>	126	s29	BG	YES	02/28/2007	04/10/2007	100	15:03:30	30211	UTC: 101T16:00 - 102T7:00	742010.8	Use PDT kernel for RMSS runs for SSG runs
<u>T29</u>	127	s29	BG	YES	02/28/2007	04/26/2007	116	16:47:58	34461	PST: 117 6:15 117 15:45	871925	
src_043_1	128	s29	BG	no	02/28/2007	04/28/2007	118	10:20:00	35400		31289.2	
ti_043_1	129	s29	BG	no	02/28/2007	04/29/2007	119	8:50:00	13800		3260.4	
ti_043_2	130	s29	BG	no	02/28/2007	05/01/2007	121	22:06:10	13730		1140	
<u>T30</u>	131	s30	BG	no	04/10/2007	05/12/2007	132	12:24:58	44221	PST: 133: 05:30 133 14:30	819865.2	
ti_044_1	132	s30	BG	Missed IDAP! BG trig only	04/10/2007	05/13/2007	133	22:18:00	15600		197326.4	Possibly use altimeter instead of SAR
rh_045_1	133	s30	BG	YES	04/10/2007	05/27/2007	147	7:40:00	19800			
engtest	134	s30	BG	no	04/10/2007	06/08/2007	159	5:30:30	16500		292	
mi_047_1	135	s31	mini	Mini	06/23/2007	06/27/2007	178	23:48:00	15989	UTC 180 03:20	264.3	
rh_047_1	136	s31	mini	Mini	06/23/2007	06/28/2007	179	11:35:00	14070	UTC 180 03:20	224	
ti_048_1	137	s32	BG		06/13/2007	07/15/2007	196	11:41:00	13800		5183.2	
te_048_1	138	s32	mini	Mini	06/13/2007	07/20/2007	201	14:35:00	13800		206172.8	Dropped 47 SABs. FIN51-55

# Cassini RADAR Users Guide

IEB	DTN	Seq #	BG vs SSR	IDAP	PSIV2 Delivery (Subseq)	EXECUTION			Duration Total (s)	~End of Downlink (PST/PDT)	Actual DV (kbit)	NOTES
						Date (UTC)	Julian Day	TIME (UTC)				
ti_049_1	139	s33	BG		07/12/2007	08/26/2007	238	22:20:00	54001		573.8	
rh_049_1	140	s33	BG	YES, plus 4 s	07/12/2007	08/29/2007	241	19:32:00	43320	Thursday by 4:00pm	225157.6	
ia_049_1	141	s33	BG	YES, 0shift	07/12/2007	09/08/2007	251	21:50:00	53700		561237.2	
ia_049_2	142	s33	BG	YES, 0shift	07/12/2007	09/09/2007	252	21:34:00	30360		291482.8	
ia_049_3	143	s33	BG	YES, 0shift	07/12/2007	09/10/2007	253	8:44:00	40861		330888.8	
ia_049_4	144	s33	BG	YES, 0shift	07/12/2007	09/10/2007	253	22:20:00	25800		155397.2	
ia_049_5	145	s33	BG	YES, 0shift	07/12/2007	09/11/2007	254	20:25:00	58201		0	S/C safing incident: IEB did not execute
rings_050_1	146	s34	BG		08/27/2007	09/27/2007	270	22:11:00	46200		88403.2	Including engineering test
di_050_1	147	s34	BG	YES, 0shift	08/27/2007	09/29/2007	272	21:05:00	21000		274975.6	
en_050_1	148	s34	BG	YES, 0shift	08/27/2007	09/30/2007	273	3:03:15	48436		115178	Missing last 25 minutes in ROME file, but OK is SFDU. Double bit errors are confusing ROME SW
<u>T36</u>	149	s34	BG		08/27/2007	10/01/2007	274	18:32:43	53700		791684.4	Using new SAR ping-pong mode
ti_051_1	150	s34	BG		08/27/2007	10/20/2007	293	20:35:30	19200		187438.8	Including engineering test
rings_051_1	151	s34	BG		08/27/2007	10/23/2007	296	18:05:00	19200		8831.2	
ti_051_2	152	s34	BG		08/27/2007	10/27/2007	300	0:20:00	39000		310156	Source scan, might need to split the downlink
rings_052_1	153	s35	BG		10/02/2007	11/14/2007	318	18:02:15	37364		3576565	Engineering tests?
ti_052_1	154	s35	BG		10/02/2007	11/16/2007	320	0:05:00	15599		5183.2	
rings_052_2	155	s35	BG		10/02/2007	11/16/2007	320	18:35:00	19199		8626	
mi_053_1	156	s35	BG	Mini-Seq	10/02/2007	12/02/2007	336	21:05:00	21567		297965.6	
<u>T39</u>	157	s36	BG		11/12/2007	12/20/2007	354	15:17:53	44401	Saturday 12/22 @ 2:15 am	691159.2	
ti_057_1	158	s36	BG		11/12/2007	01/22/2008	022	21:05:00	13799		4294	
sa_058_1	159	s37	BG		12/12/2007	02/08/2008	039	19:19:14	38146		28690	
sa_059_1	160	s38	BG		01/22/2008	02/20/2008	051	1:12:07	54533		267398.4	
<u>T41</u>	161	s38	BG		01/22/2008	02/22/2008	053	7:22:07	40740		805919.2	
en_061_1	162	s38	BG	IDAP	01/22/2008	03/12/2008	072	3:21:12	46921		243815.6	Two parts or two IEBs?
en_061_2	163	s38	BG	IDAP	01/22/2008	03/12/2008	072	16:31:57	15495		199644.4	Two parts or two IEBs?

# Cassini RADAR Users Guide

IEB	DTN	Seq #	BG vs SSR	IDAP	PSIV2 Delivery (Subseq)	EXECUTION			Duration Total (s)	~End of Downlink (PST/PDT)	Actual DV (kbit)	NOTES
						Date (UTC)	Julian Day	TIME (UTC)				
mi_064_1	164	s39	BG	IDAP	02/20/2008	04/11/2008	102	9:24:30	6599		222700	
rings_066_1	165	s40	BG		03/25/2008	05/04/2008	125	7:51:00	46200		46420.8	Lots of small DSN gaps, ~450
<u>T43</u>	166	s40	BG		03/25/2008	05/12/2008	133	23:51:58	43019	Tue May 13 @4:30	930642.8	
<u>T44</u>	167	s40	BG		03/25/2008	05/28/2008	149	3:29:32	35699	Thurs May 29 @3:30	609056.4	
<b>***** EXTENDED MISSION ***** EXTENDED MISSION ***** EXTENDED MISSION ***** EXTENDED MISSION *****</b>												
sat rings en_088_1	168 169 170	s44	BG	IDAP	08/12/2008	10/10/2008	284	9:36:00	15940	10/11/2008 @6:00am	402131	
ti_092_1	171	s45	BG		09/08/2008	11/06/2008	311	12:05:00	19199	11/13/2008 2:00am	7508.8	
sa_095_1	172	s46	BG		10/20/2008	12/01/2008	336	5:21:00	31799		112001.2	
sa_095_2	173	s46	BG		10/20/2008	12/03/2008	338	0:02:08	27531		86784.4	
<u>T48</u>	174	s46	BG		10/20/2008	12/05/2008	340	5:15:45	34020		395025.2	
sa_097_1	175	s46	BG		10/20/2008	12/16/2008	351	23:53:00	34319		114592.8	
sa_097_2	176	s46	BG		10/20/2008	12/17/2008	352	23:04:08	31731		123758.3	Lots of small gaps
<u>T49</u>	177	s46	BG		10/20/2008	12/21/2008	356	10:04:52	29999	357 19:29	746631.1	9 one SAB gaps?
ti_098_1	178	s46	BG		10/20/2008	12/23/2008	358	19:35:00	15599		11840.8	
ti_099_1	179	s46	BG		10/20/2008	01/07/2009	007	15:22:08	14331		10624.8	
src_100_1	180	s47	BG		11/18/2008	01/18/2009	018	14:22:00	31431		218614	
<u>T50</u>	181	s47	BG		11/18/2008	02/07/2009	038	23:10:51	56099		696578	Dropped 3 SABs: FIN104*1, FIN227*2
ti_103_1	182	s47	BG		11/18/2008	02/11/2009	042	22:09:00	15599		5768.4	
ti_104_1	183	s48	BG		01/14/2009	02/20/2009	051	15:34:58	12602		6786.8	
ti_105_1	184	s48	BG		01/14/2009	03/13/2009	072	21:30:00	13799		0	LOST OBSERVATION due to the S/C thruster swap. The background sequence suspended for 10 days. Restarted the BG on day 78
ti_106_1	185	s48	BG		01/14/2009	03/19/2009	078	10:41:11	14928		6254.8	

# Cassini RADAR Users Guide

IEB	DTN	Seq #	BG vs SSR	IDAP	PSIV2 Delivery (Subseq)	EXECUTION			Duration Total (s)	~End of Downlink (PST/PDT)	Actual DV (kbit)	NOTES
						Date (UTC)	Julian Day	TIME (UTC)				
<u>T52</u>	186	s49	BG		02/19/2009	04/03/2009	093	16:52:45	20062		23620.8	Rad & compressed scat only
ti_108_1	187	s49	BG		02/19/2009	04/15/2009	105	18:27:58	15601		5707.6	
ti_108_2	188	s49	BG		02/19/2009	04/16/2009	106	10:32:58	41101		15975.2	
<u>T53</u>	189	s49	BG		02/19/2009	04/20/2009	110	22:50:43	26701		39428.8	Rad & compressed scat only: Dropped 11 unexpected SABs as FIN13
ti_109_1	190	s49	BG		02/19/2009	04/22/2009	112	18:00:00	15599		8443.6	Zero drops
ti_110_1	191	s50	BG		03/31/2009	05/08/2009	128	16:56:00	15599		11833.2	Zero drops
ti_110_2	192	s50	BG		03/31/2009	05/11/2009	131	16:11:00	15599		11377.2	Zero drops
<u>T55</u>	193	s50	BG		03/31/2009	05/21/2009	141	12:31:41	41060		956186.4	Full pass
ti_111_1	194	s50	BG		03/31/2009	05/24/2009	144	6:44:00	15599		11377.2	Zero drops
<u>T56</u>	195	s50	BG		03/31/2009	06/06/2009	157	11:05:01	33719		811239.2	Ends at +26 min, include rerouted chirp engineering test. Lots of one-second gaps?
ti_112_1	196	s50	BG		03/31/2009	06/11/2009	162	14:50:00	41060		11377.2	Zero drops
src_112_1	197	s51	BG		05/06/2009	06/16/2009	167	7:16:03	40800		30270.8	
ti_113_1	198	s51	BG		05/06/2009	06/18/2009	169	19:30:03	15601		5707.6	One 9-second gap (FIN11)
<u>T57</u>	199	s51	BG		05/06/2009	06/22/2009	173	18:11:58	20448		420044.4	Dropped 4 SABs (FIN:69, 69, 165, 168)
<u>T58</u>	200	s51	BG		05/06/2009	07/08/2009	189	11:54:06	19561		478359.2	Missing 2 packet (fin158)
<u>T59</u>	201	s52	BG		06/16/2009	07/24/2009	205	10:24:03	19199		134368	Ride-along SAR (+/-5.2 min only)
<u>T60</u>	202	s52	BG		06/16/2009	08/09/2009	221	5:08:53	33359		0	DSN problems, downlink dropped! NO DATA!
<u>T61</u>	203	s53	BG		07/22/2009	08/25/2009	237	7:31:38	20399		746639.2	~4 small gaps?
ti_117_1	204	s53	BG		07/22/2009	09/07/2009	250	14:38:00	15600		11787.6	Lots of little gaps
sa_119_1	205	s54	BG		09/01/2009	10/13/2009	286	20:00:03	55202		44718.4	2 gaps
ti_120_1	206	s54	BG		09/01/2009	10/29/2009	302	12:30:00	15599		11833.2	
en_120_1	207	s54	BG		09/01/2009	11/01/2009	305	22:18:58	29879		444828	Lots of gaps....in SAB report
sa_122_1	208	s55	BG		10/06/2009	12/09/2009	343	22:45:58	51722		51984	
<u>T63</u>	209	s55	BG		10/06/2009	12/11/2009	345	22:18:58	24302		42491.6	

# Cassini RADAR Users Guide

IEB	DTN	Seq #	BG vs SSR	IDAP	PSIV2 Delivery (Subseq)	EXECUTION			Duration Total (s)	~End of Downlink (PST/PDT)	Actual DV (kbit)	NOTES
						Date (UTC)	Julian Day	TIME (UTC)				
T64	210	s56	BG		11/16/2009	12/27/2009	361	19:21:59	20879		465659	Lots of gaps, even with dual downlink.
T65	211	s56	BG		11/16/2009	01/12/2010	012	18:00:36	19520		241140	All data present!
src_124_1	212	s56	BG		11/16/2009	01/18/2010	018	10:40:00	40800		368022.4	No gaps
mi_126_1	213	s57	BG		12/02/2000	02/13/2010	044	11:20:58	16081		190402.8	No gaps
rh_127_1	214	s58	BG		01/20/2010	03/02/2010	061	9:54:59	24937		428822.4	FIN 70 dropped 2 SABs
ti_128_1	215	s58	BG		01/20/2010	03/22/2010	081	2:53:59	15601		5791	
ti_130_1	216	s59	BG		03/02/2010	04/30/2010	120	5:01:59	15601		11833.2	Zero dropped
src_131_1	217	s60	BG		04/13/2010	05/25/2010	145	13:06:08	38872		540.3	No gaps
T69	218	s60	BG		04/13/2010	06/04/2010	155	17:13:27	31979		312808	4-minute radiometry gap only
ti_132_1	219	s60	BG		04/13/2010	06/07/2010	158	7:18:00	29219		5776	No gaps, only expected telem gap
T71	220	s61	BG	PSIV May 18	05/14/2010	07/06/2010	187	15:27:45	53400	7/8 @ 4am	352320	
sa_135_1	221	s61	BG	PSIV May 18	05/14/2010	07/24/2010	205	19:20:00	56939		50669	
ti_138_1	222	s63	BG		07/29/2010	09/26/2010	269	6:23:08	17331		10024	No gaps
ti_140_1	223	s64	BG		08/30/2010	11/13/2010	317	4:05:00	17399			LOST DUE TO S/C SAFING
sa_141_1	224	s64	BG		08/30/2010	11/21/2010	325	11:05:08	17399			Engineering and TWT health-check. LOST DUE TO S/C SAFING
ti_144_1	225	s66	BG		11/23/2010	01/29/2011	029	0:04:00	17400		11400	
sa_146_1	226	s67	BG		01/23/2111	03/20/2011	079					Only one off-target case. Stays on target at the end
ti_147_1	227	s67	BG		01/23/2111	04/20/2011	110					
eng_147_1	228	s67	BG		01/23/2111	04/21/2011	111					Next TWT turn on
T77	229	s68	BG			06/20/2011	171					
ti_150_1	230	s69	BG									
	231	s69	BG									
	232	s69	BG									

# Cassini RADAR Users Guide

IEB	DTN	Seq #	BG vs SSR	IDAP	PSIV2 Delivery (Subseq)	EXECUTION			Duration Total (s)	~End of Downlink (PST/PDT)	Actual DV (kbit)	NOTES
						Date (UTC)	Julian Day	TIME (UTC)				
	233	s70	BG									
	234	s70	BG									
	235	s70	BG									
	236	s71	BG									
	237	s71	BG									
	238	s71	BG									
	239	s72	BG									
	240	s72	BG									
	241	s72	BG									
	242	s73	BG									
	243	s73	BG									
	244	s73	BG									

Notes for uplink/downlink spreadsheet: column descriptions, acronym definitions, and other notes. Key columns of the Cruise worksheet are reproduced above.

HEAD	DESCRIPTION: NOTES, ACRONYMS
IEB	Instrument execution block: This column is really the name of the observation: Two letters for target, rev. number, times during the rev.
DTN	Datatake number: For cruise, we used 1–21; for tour we started at 31. Maximum value is 255, so it might roll over.
Seq #	Sequence number: Project-supplied number for uplink planning units. For cruise, we used 1–21; for tour we started at 31.
BG vs SSR	Background (sequence) vs solid-state recorder: Used to keep track of the location in S/C memory of where our IEB will reside until it is transferred to the RADAR. Typically part of the BG sequence, unless there were memory space issues.
IDAP	Immediate/Delayed Action Program: A method to “trigger” the IEB within the RADAR. Normally the trigger time of the IEB is placed in the BG sequence. However, to allow for late pointing adjustments, this “trigger” instruction can be placed in an IDAP. Note that BG sequence commands are determined months ahead of time. An IDAP timing can be adjusted within a few days of execution to account for target/timing changes. IVP = Inertial Vector Propagator PSIV = Preliminary Sequence Integration and Validation
PSIV2 Delivery (Subseq)	Preliminary sequence integration and validation delivery date (Port 2): There are various delivery windows that the RADAR team can use to deliver commands. Typically, we used the second port of the PSIV process.
Execution Date (UTC)	Date of execution: The UTC execute start date of the IEB, calculated from the Julian Day in Column M.
Execution Julian Day	The day of execution of the start time of the IEB.
Execution Time (UTC)	This is rounded typically to the nearest second of trigger time.
Duration Total (s)	Total seconds of IEB time (trigger to halt), converted to hours and minutes.
~End of Downlink (PST/PDT)	Date (and sometimes time, Pacific Standard/Daylight Time) when the downlink window is complete: This was used so that the IO Team would know the earliest time to query for the data. CO = Carryover, meaning that we might get only some of the data on that downlink and will have to wait for the rest on the next downlink.
Actual DV (kbit)	Actual amount of data volume allocation to RADAR for that observation DV = data volume
Acronyms	DBE = double-bit error FSIV = Final Sequence Integration and Validation ITL = Integrated Test Lab ND = noise diode RL = resistive load RMSS =RADAR Mapping Sequencing Software SAB = SAR-altimetry burst, where SAR = synthetic aperture radar SFDU = Standard Formatted Data Unit SSG = subsequence generation WTK = William T. K. Johnson data volume. The original command format for the IEBs was given the name “WTK” files for the lead scientist/engineer who developed the tools (and a large portion of the RADAR). This is a data volume estimator tool in bits.
COLOR	KEY
Green	Event occurred
Yellow	Event IEB delivery was skipped
Orange	Typically minor issues
Red	Event ERROR

## 15 Appendix 6: Example BIDR PDS Label, Primary Data Set, 32-Bit Data

Source: BIDR SIS, Appendix A. Note that this example is not based on actual flyby geometries for any particular Titan pass.

```

PDS_VERSION_ID = PDS3
/* FILE FORMAT AND LENGTH */
RECORD_TYPE = FIXED_LENGTH
RECORD_BYTES = 160
FILE_RECORDS = 183
LABEL_RECORDS = 23
/* POINTERS TO START RECORDS OF OBJECTS IN FILE */
^IMAGE = 24
/* IMAGE DESCRIPTION */
DATA_SET_ID = "CO-SSA-RADAR-5-BIDR-V1.0"
DATA_SET_NAME = "CASSINI ORBITER SSA RADAR 5 BIDR V1.0"
PRODUCER_INSTITUTION_NAME = "JET PROPULSION LABORATORY"
PRODUCER_ID = JPL
PRODUCER_FULL_NAME = "Inst Lead Charles Elachi contact Bryan Stiles"
PRODUCT_ID = BIFQI42N253_D035_T00A_V01
PRODUCT_VERSION_ID = 1
INSTRUMENT_HOST_NAME = "CASSINI ORBITER"
INSTRUMENT_HOST_ID = CO
INSTRUMENT_NAME = "CASSINI RADAR"
INSTRUMENT_ID = RADAR
TARGET_NAME = TITAN
START_TIME = YYYY-DOYThh:mm:ss.sss
STOP_TIME = YYYY-DOYThh:mm:ss.sss
SPACECRAFT_CLOCK_START_COUNT = nnnnnnnnnn
SPACECRAFT_CLOCK_STOP_COUNT = nnnnnnnnnn
PRODUCT_CREATION_TIME = YYYY-DOYThh:mm:ss.sss
SOURCE_PRODUCT_ID = LBDR_08_031_V01
MISSION_PHASE_NAME = TOUR
MISSION_NAME = "CASSINI-HUYGENS"
SOFTWARE_VERSION_ID = "V1.0"
/* DESCRIPTIONS OF OBJECTS CONTAINED IN FILE */
OBJECT = IMAGE
LINES = 160

```

```

LINE_SAMPLES = 40
SAMPLE_TYPE = "PC_REAL"
SAMPLE_BITS = 32
CHECKSUM = nnnnnnnnn
SCALING_FACTOR = 1.00000000
OFFSET = 0.00000000
MISSING_CONSTANT = 16#FF7FFFFB#
NOTE = "Data values in this Basic Image Data Record are SAR-normalized
backscatter cross-section values. The values are physical scale (not in dB) and have
been normalized in order to remove variations in the image due to incidence angle
variations among the measurements. The raw backscatter values are multiplied by the
function f(I) of incidence angle, I, in degrees of the form XXXXXXXXXX."
END_OBJECT = IMAGE
OBJECT = IMAGE_MAP_PROJECTION
^DATA_SET_MAP_PROJECTION = "DSMAP.CAT"
MAP_PROJECTION_TYPE = OBLIQUE_CYLINDRICAL
A_AXIS_RADIUS = 2575.000000 <km>
B_AXIS_RADIUS = 2575.000000 <km>
C_AXIS_RADIUS = 2575.000000 <km>
FIRST_STANDARD_PARALLEL = "N/A"
SECOND_STANDARD_PARALLEL = "N/A"
POSITIVE_LONGITUDE_DIRECTION = WEST
CENTER_LATITUDE = 0.000000 <deg>
CENTER_LONGITUDE = 0.000000 <deg>
REFERENCE_LATITUDE = 30.000000 <deg>
REFERENCE_LONGITUDE = 150.000000 <deg>
LINE_FIRST_PIXEL = 1
LINE_LAST_PIXEL = 160
SAMPLE_FIRST_PIXEL = 1
SAMPLE_LAST_PIXEL = 40
MAP_PROJECTION_ROTATION = 90.0
MAP_RESOLUTION = 8.0 <pix/deg>
MAP_SCALE = 5.61777853 <km/pix>
MAXIMUM_LATITUDE = 46.13792 <deg>
MINIMUM_LATITUDE = 37.160353 <deg>
EASTERNMOST_LONGITUDE = 93.703090 <deg>
WESTERNMOST_LONGITUDE = 120.701079 <deg>
LINE_PROJECTION_OFFSET = -240.500000

```

```
SAMPLE_PROJECTION_OFFSET = -80.500000
OBLIQUE_PROJ_POLE_LATITUDE = 58.525051 <deg>
OBLIQUE_PROJ_POLE_LONGITUDE = 310.574599 <deg>
OBLIQUE_PROJ_POLE_ROTATION = 157.535316 <deg>
OBLIQUE_PROJ_X_AXIS_VECTOR = ( -0.75000000, -0.43301270, 0.50000000 )
OBLIQUE_PROJ_Y_AXIS_VECTOR = ( 0.56759575, -0.80945648, 0.15038374 )
OBLIQUE_PROJ_Z_AXIS_VECTOR = ( 0.33961017, 0.39658568, 0.85286853 )
LOOK_DIRECTION = LEFT
COORDINATE_SYSTEM_NAME = "PLANETOGRAPHIC"
COORDINATE_SYSTEM_TYPE = "BODY-FIXED ROTATING"
END_OBJECT = IMAGE_MAP_PROJECTION
END
```

## 16 Appendix 7: SAR Coverage of Titan by Feature Names

Features are listed by their IAU names where available. This list is not exhaustive: For example, small portions of some features might be seen in adjacent swaths. For a complete list of named features on Titan, see <http://planetarynames.wr.usgs.gov/>

NAME (IF APPLICABLE)	CENTER LATITUDE	CENTER LONGITUDE	FEATURE TYPE	FEATURE DESCRIPTION	SWATH COVERAGE
Afekan	25.8	159.7	crater	largest crater in the Afekan region	T43, T83
Anbus Labyrinthus	39.2	145	labyrinth	labyrinth in north Afekan	T64, T86
Ara Fluctus	39.8	241.6	flow	radar bright crescent flow feature	Ta
Arrakis Planitia	-78.4	243	plains	radar bright plains in the south pole	T49
Aura Undae	13.79	133.14	dunes	dune field southwest of Afekan crater	T84
Belet	-5	105	dunes	Sand sea	T8, T49, T61, T84seg5, T50seg3, T92
Bermoothes Insula	67.1	42.9	island	island in Kraken Mare	T30, T84seg2, T91seg2
Bolsena Lacus	75.75	349.72	lake(s)	circular lake in the north pole with a diffuse shoreline	T16, T29
Bralgu Insulae	76.2	108.5	island	island in Ligeia Mare	T25, T28, T86, T92
Caladan Planitia	31	134	plains	undifferentiated plains west of Afekan crater	T84, T44
Celadon Flumina	-73.7	331.2	channel(s)	dark meandering channel coming off of Sikun Labyrinthus	T39
Coats Facula	-11.1	330.8	plains (?)	bright ISS feature; radar dark feature with a bright boundary	T28
Dilmun	15	185	mountain(s)	mountain range east of Afekan	T48, T44, T61
Doom Mons	-14.65	319.58	hummock	bright hummock dome in Quivira	T25
Ecaz Labyrinthus	-83	323.3	labyrinth	large labyrinth in the south pole	T39
Eir Macula	-24	245.3	dunes (?)	radar dark circular feature in south Xanadu	T44, T48
Elivagar Flumina	19.3	281.5	channel(s)	channel and fan system east of Menrva	T3, T77seg3
Forseti	25.53	349.6	crater	crater in T28	T23, T84, T113seg7
Gammu Labyrinthus	-77.9	110	labyrinth	labyrinth in the south pole incised by depressions	T58
Gandalf Colles	14.61	150.46	hummock	bulbous hummock bit south west of Afekan crater	T44, T84
Ganesa Macula	50	272.7	plains	radar dark feature north of Menrva with channels overlapping it	Ta
Gansireed Labyrinthus	-69.3	120.7	labyrinth	labyrinth south of the south belet region	T55, T56
Ginaz Labyrinthus	83	98.3	labyrinth	labyrinth next to ligeia mare	T25, T29, T92
Grumman Labyrinthus	-35.3	253.2	labyrinth	labyrinth in south Xanadu	T41
Guabonito	-10.9	209.2	crater	crater in Hobal, west of Xanadu	T13, T48seg3
Hagal Planitia	-60.59	15.05	plains	radar dark plains feature; partially SAR coverage	T71

# Cassini RADAR Users Guide

NAME (IF APPLICABLE)	CENTER LATITUDE	CENTER LONGITUDE	FEATURE TYPE	FEATURE DESCRIPTION	SWATH COVERAGE
Hano	40.3	14.9	crater	crater in Aaru	T16, T84, T104
Hobal Virga	-35	194	streak(s)	Large Hobal windstreaks	T55, T56, T57, T58, T120
Hotei Regio	-26	282	depression(s)	radar bright lobate features in Xanadu; ISS bright region	T41, T43, T121
Hufaidh Insulae	67	39.7	island	peninsula in Kraken Mare	T30, T91seg2
Jingpo Lacus	73	24	lake(s)	lake in the north pole	T28, T84seg2, T86, T91seg2
Junction Labyrinthus	-47.7	144.7	labyrinth	labyrinth in S Ching-Tu	T39, T71
Kaitain Labyrinthus	52.37	11.34	labyrinth	labyrinth in Aaru	T16, T84seg2
Karesos Flumen	-70.9	165.25	channel(s)	channel in a mountain near Ontario Lacus	T57
Kraken Mare	68	50	sea	Largest sea in the north pole	T30, T91seg2
Kronin Labyrinthus	-35.7	263.73	labyrinth	labyrinth in south Xanadu	T41
Ksa	14	294.6	crater	crater southeast of Menrva	T77, T77seg3
Lampadas Labyrinthus	-81.8	236	labyrinth	large, muted labyrinth in south pole	T49
Lankiveil Labyrinthus	-48.2	210.5	labyrinth	labyrinth in south Hobal	T59, T120
Leilah Fluctus	50.5	282.2	flow	fans north of Menrva	Ta, T23
Lernaeus Labyrinthus	-83.4	222	labyrinth	labyrinth in the south pole	T49
Ligeia Mare	79.7	112.1	sea	second largest sea in np	T25, T28, T86, T92
Mayda Insula	79.1	47.8	island	island in kraken mare	T25, T28, T86, T91
Menrva	20.1	272.8	crater	largest crater on Titan	T3, T77seg3
Misty Montes	56.8	297.56	mountain(s)	mountainous, potentially labyrinthic, features north of Menrva	T23
Mithrim Montes	-2.16	232.58	mountain(s)	parallel mountains in northwest Xanadu	T20seg3, T43
Momoy	11.6	315.4	crater	crater directly east of Ksa	T77
Moray Sinus	76.6	78.6	bay	bay in Kraken Mare	T25, T28, T91seg2
Muritan Labyrinthus	-68.8	140.8	labyrinth	labyrinth in the south pole	T55, T56
Mystis	0.07	165.14	crater	crater on border of Afekan and Adiri	T61, T36
Ontario Lacus	-72	177	lake(s)	largest lake in the south pole	T57, T58, T65, T98
Perkunas Virgae	-27	198	streak(s)	northern large Hobal windstreak	T55, T56, T57, T58, T120
Planctae Insulae	77.5	108.7	island	island in Ligeria Mare	T25, T28, T86, T92
Polelya Macula	50	304	plains	patch of dark irregular plains west of Winia Fluctus	Ta
Puget Sinus	82.4	118.9	bay	bay in Kraken Mare	T25, T29, T92
Punga Mare	85.1	20.3	sea	sea in the north pole	T29